Novel System Designs for Future mmWave Communication Networks

by

Mahmoud Raeisi

A Dissertation Submitted to the
Graduate School of Sciences and Engineering
in Partial Fulfillment of the Requirements for
the Degree of

Doctor of Philosophy

in

Electrical and Electronics Engineering

KOÇ ÜNİVERSİTESİ

January, 2025

Novel System Designs for Future mmWave Communication Networks

Koç University
Graduate School of Sciences and Engineering
This is to certify that I have examined this copy of a doctoral dissertation by

Mahmoud Raeisi

and have found that it is complete and satisfactory in all respects,
and that any and all revisions required by the final
examining committee have been made.

Committee Members:

Prof. Dr. Ertuğrul Başar (Advisor)

Prof. Dr. Alper Erdoğan

Prof. Dr. Sinem Çöleri

Prof. Dr. Hüseyin Arslan

Prof. Dr. Ali Emre Pusane

Date: ______________________

To my beloved family—my parents, for their unwavering encouragement, and my wife, for her steadfast support—thank you for being my strength throughout this journey.

ABSTRACT

Novel System Designs for Future mmWave Communication Networks
Mahmoud Raeisi
Doctor of Philosophy in Electrical and Electronics Engineering
January, 2025

The advent of next-generation communication systems, has spurred a demand for innovative approaches to overcome the limitations of traditional wireless technologies. This thesis investigates novel system designs for future millimeter-wave (mmWave) communication networks, focusing on improving bit error rate (BER), achievable rate, energy efficiency, and communication coverage. With mmWave technology promising enhanced bandwidth and data throughput, the challenges posed by severe path loss and signal attenuation in these high-frequency bands necessitate the use of advanced techniques, such as large antenna arrays, index modulation (IM), and reconfigurable intelligent surfaces (RISs).

The first part of this thesis introduces cluster index modulation (CIM), a novel IM scheme tailored for more realistic mmWave environments compared to existing IM schemes. CIM leverages the spatial separation of clusters and indexes distinct propagation paths to improve BER performance. This concept is extended with a hybrid beamforming architecture and further explored within an RIS-aided framework, demonstrating the potential of CIM to enhance spectral and energy efficiency in complex mmWave environments.

To address the high cost and power demands associated with large antenna arrays, this thesis proposes the Plug-In RIS, a fully passive and low-complexity solution tailored for blockage mitigation in mmWave networks. This standalone RIS operates without the need for decoupling end-to-end channel, providing a cost-effective alternative for coverage enhancement in dead zones. Additionally, a comprehensive design framework for both BS-side and UE-side RIS deployments is presented, offering insights into optimal placement strategies for different application scenarios and highlighting practical design considerations in RIS control and configuration.

The latter part of the thesis focuses on beyond-diagonal RISs (BD-RISs), an

advanced RIS structure integrated with the base station to enable efficient passive beamforming. A BD-RIS provides high beamforming gains comparable to those of active antenna arrays but with significantly lower energy consumption, making it a valuable solution for 6G applications requiring enhanced coverage and energy efficiency. Although primarily focused on communication performance, BD-RIS is also shown to support applications in single-anchor localization, where high beamforming gain is crucial for accurate positioning.

In summary, this thesis contributes to the development of novel system designs for mmWave networks by presenting innovative modulation schemes, energy-efficient RIS designs, and advanced beamforming techniques. The findings provide a foundation for future research in scalable, cost-effective solutions that meet the stringent requirements of next-generation wireless networks.

ÖZETÇE

Doktora Tez Başlığı
Mahmoud Raeisi
Elektrik ve Elektronik Mühendisliği, Doktora
Kasım 2024

Yeni nesil iletişim sistemlerinin ortaya çıkışı, geleneksel kablosuz teknolojilerin sınırlamalarının üstesinden gelmek için yenilikçi yaklaşımlara olan talebi artırmıştır. Bu tez, bit hata oranını (BER), ulaşılabilir hızı, enerji verimliliğini ve iletişim kapsamını iyileştirmeye odaklanarak gelecekteki milimetre dalga (mmWave) iletişim ağları için yeni sistem tasarımlarını araştırmaktadır. Gelişmiş bant genişliği ve veri çıkışı vaat eden mmWave teknolojisiyle birlikte, bu yüksek frekanslı bantlarda ciddi yol kaybı ve sinyal zayıflamasının yarattığı zorluklar, büyük anten dizileri, indeks modülasyonu (IM) ve yeniden yapılandırılabilir akıllı yüzeyler (RIS'ler) gibi gelişmiş tekniklerin kullanılmasını gerektirmektedir.

Bu tezin ilk bölümünde, mevcut IM şemalarına kıyasla daha gerçekçi mmWave ortamları için uyarlanmış yeni bir IM şeması olan küme indeks modülasyonu (CIM) tanıtılmaktadır. CIM, kümelerin uzamsal ayrımından yararlanır ve BER performansını iyileştirmek için farklı yayılma yollarını indeksler. Bu konsept, hibrit bir hüzmeleme mimarisi ile genişletilmiş ve RIS destekli bir çerçevede daha fazla araştırılmış ve CIM'in karmaşık mmWave ortamlarında spektral ve enerji verimliliğini artırma potansiyelini göstermiştir.

Büyük anten dizileriyle ilişkili yüksek maliyet ve güç taleplerini karşılamak için bu tez, mmWave ağlarında blokaj azaltma için özel olarak tasarlanmış tamamen pasif ve düşük karmaşıklıkta bir çözüm olan Plug-In RIS'i önermektedir. Bu bağımsız RIS, uçtan uca kanal ayrıştırmaya ihtiyaç duymadan çalışmakta ve ölü bölgelerde kapsama alanının iyileştirilmesi için uygun maliyetli bir alternatif sunmaktadır. Ek olarak, hem BS tarafı hem de UE tarafı RIS dağıtımları için kapsamlı bir tasarım çerçevesi sunulmakta, farklı uygulama senaryoları için en uygun yerleştirme stratejilerine ilişkin içgörüler sunulmakta ve RIS kontrolü ve yapılandırmasında pratik tasarım hususları vurgulanmaktadır.

Tezin ikinci bölümü, verimli pasif hüzmeleme sağlamak için baz istasyonu ile entegre edilmiş gelişmiş bir RIS yapısı olan diyagonal ötesi RIS'lere (BD-RIS'ler) odaklanmaktadır. Bir BD-RIS, aktif anten dizileriyle karşılaştırılabilir yüksek hüzmeleme kazançları sağlar, ancak önemli ölçüde daha düşük enerji tüketimi ile, gelişmiş kapsama alanı ve enerji verimliliği gerektiren 6G uygulamaları için değerli bir çözüm haline getirir. Öncelikli olarak iletişim performansına odaklanmış olsa da, BD-RIS'in yüksek hüzmeleme kazancının doğru konumlandırma için çok önemli olduğu tek çıpalı yerelleştirme uygulamalarını da desteklediği gösterilmiştir.

Özet olarak, bu tez yenilikçi modülasyon şemaları, enerji tasarruflu RIS tasarımları ve gelişmiş hüzmeleme teknikleri sunarak mmWave ağları için yeni sistem tasarımlarının geliştirilmesine katkıda bulunmaktadır. Bulgular, yeni nesil kablosuz ağların katı gereksinimlerini karşılayan ölçeklenebilir, uygun maliyetli çözümler konusunda gelecekteki araştırmalar için bir temel oluşturmaktadır.

ACKNOWLEDGMENTS

First and foremost, I would like to express my deepest gratitude to my esteemed advisor, Professor Ertugrul Basar. The opportunity to pursue my Ph.D. under his supervision has been a transformative experience, one that would not have been possible without his unwavering support and belief in my potential. His invaluable guidance, insightful feedback, and patient encouragement have been the foundation of all my achievements throughout this journey. I am sincerely thankful to him for his mentorship, which has not only shaped this work but also profoundly influenced my personal and professional growth.

I am also incredibly grateful to my dear friends, Dr. Asil Koc and Dr. Ibrahim Yildirim, whose kindness, support, and contributions were instrumental during my Ph.D. studies. Their camaraderie and collaboration enriched my experience, and I am thankful for their friendship.

A special thanks goes to Dr. Aymen Khaleel for his kind support, and to Professor Tho Le-Ngoc at McGill University for his generous assistance and guidance. I would also like to extend my appreciation to Dr. Mehmet Cagri Ilter and Dr. Majid Gerami for their valuable contributions throughout my research.

I am deeply grateful to Professor Henk Wymeersch and Dr. Hui Chen at Chalmers University of Technology for their support and collaboration, which contributed significantly to the depth and impact of my research.

I am grateful to members of my thesis committee, Professor Alper Erdoğan and Professor Semiha Tedik Başaran, for their encouragement and insightful feedback.

I would like to acknowledge the Scientific and Technological Research Council of Turkey (TUBITAK) for its financial support, and Huawei Technologies for their generous funding, both of which were essential to the completion of this work.

Words cannot fully express my gratitude to my beloved parents, Farideh and Salman. Their unwavering encouragement and faith in me to pursue my dreams, including this Ph.D., have been my greatest source of strength. Their boundless material and spiritual support, day and night, not only during my Ph.D. but throughout my entire life, made these achievements possible. I am forever indebted to them for their love, sacrifices, and belief in me.

I would also like to sincerely thank my beloved wife, Fatma, for her support, patience, and for providing a nurturing environment that allowed me to focus on my studies. Her kindness and love made this journey possible, and I am deeply grateful for her presence every step of the way.

TABLE OF CONTENTS

LIST OF TABLES

LIST OF FIGURES

ABBREVIATIONS

BS	Base Station
UE	User Equipment
RIS	Reconfigurable Intelligent Surface
IM	Index Modulation
CIM	Cluster Index Modulation
Tx	Transmitter
Rx	Receiver
BER	Bit Error Rate
ULA	Uniform Linear Array
UPA	Uniform Planar Array
mmWave	Millimeter-Wave
CSI	Channel State Information
AoA	Angle of Arrival
AoD	Angle of Departure
MIMO	Multiple-Input Multiple-Output
OFDM	Orthogonal Frequency Division Multiplexing
QAM	Quadrature Amplitude Modulation
6G	Sixth Generation
SNR	Signal-to-Noise Ratio
LoS	Line of Sight
NLoS	Non Line of Sight
AWGN	Additive White Gaussian Noise
PEP	Pair-wise Error Probability

Chapter 1

INTRODUCTION

With the rapid advancement of data-intensive applications and the increasing demand for high-speed and reliable connectivity, spectrum availability remains a central challenge in every generation of wireless communication [1]. To support higher data rates, the evolution of mobile communication technologies has progressively extended the use of the spectrum to higher frequency bands. Fifth-generation (5G) systems introduced the use of millimeter-wave (mmWave) bands, leveraging their abundant spectrum resources and large bandwidth in targeted deployments. However, their commercial adoption has been limited due to coverage constraints and the significant infrastructure requirements associated with mmWave technology. Building upon this, sixth-generation (6G) networks are envisioned to further exploit even higher frequencies, such as the sub-terahertz (sub-THz) and terahertz (THz) bands, to address the growing need for ultra-high data rates [1].

In the context of 6G wireless systems, low- and mid-frequency bands remain indispensable for achieving broad coverage across wide areas. However, to meet the escalating demands of next-generation applications, a more comprehensive frequency band architecture is envisioned, as depicted in Figure 1.1. This architecture harmonizes the unique advantages offered by different frequency ranges, facilitating both broad coverage and exceptional capacity to ensure seamless connectivity. Among these, the mmWave spectrum emerges as a cornerstone for 6G innovation, offering capabilities that other bands cannot match. Foremost, the vast amount of available bandwidth in mmWave frequencies is vital for delivering the extremely high data rates anticipated in future networks. Additionally, mmWave bands are uniquely suited for achieving centimeter-level sensing accuracy, an essential require-

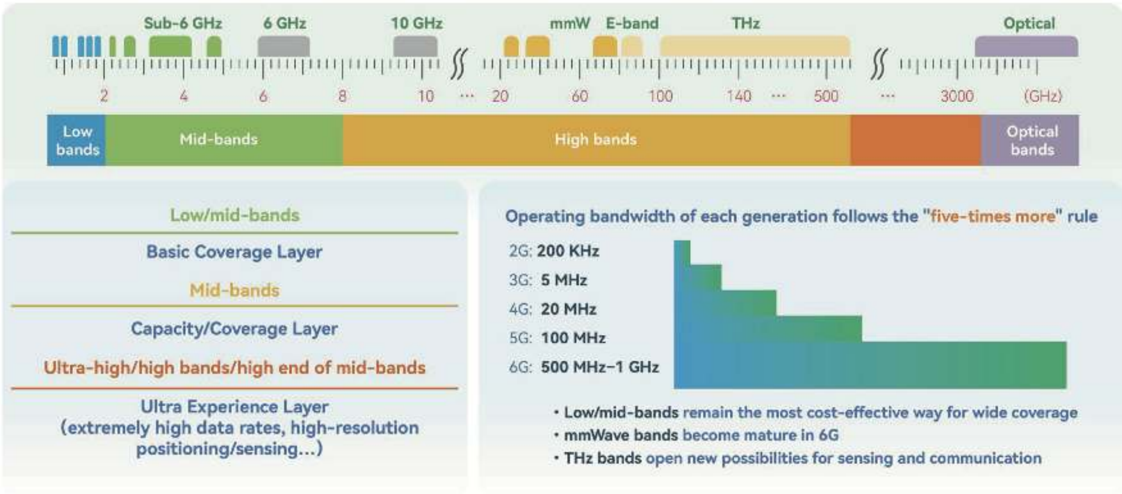

Figure 1.1: Multilayered frequency band framework [1].

ment for precision mapping and situational awareness through networked infrastructures. These levels of accuracy are challenging for mid-band frequencies due to constraints such as narrower bandwidths and smaller antenna apertures. Furthermore, advancements in radio technologies, such as enhanced beamforming techniques and dynamic spectrum management, are expected to significantly improve the efficient use of mmWave resources, maximizing their contribution to next-generation wireless systems. This multi-layered approach highlights the critical role of mmWave frequencies in 6G, effectively complementing lower frequency bands to enable groundbreaking performance and functionality.

MmWave signals, as discussed earlier, are highly susceptible to severe path loss, signal attenuation, and penetration loss [3], particularly in dense urban and indoor environments. These challenges limit the range and reliability of mmWave communications. As a result, mmWave channels are commonly modeled using a sparse scattering framework, often referred to as the 3D geometric channel model, which is widely adopted in the literature [4, 5, 6, 7, 8, 9]. Figure 1.2 illustrates this geometric channel model, which characterizes the propagation environment between a base station (BS) and a user. Due to the significant penetration loss, mmWave signals

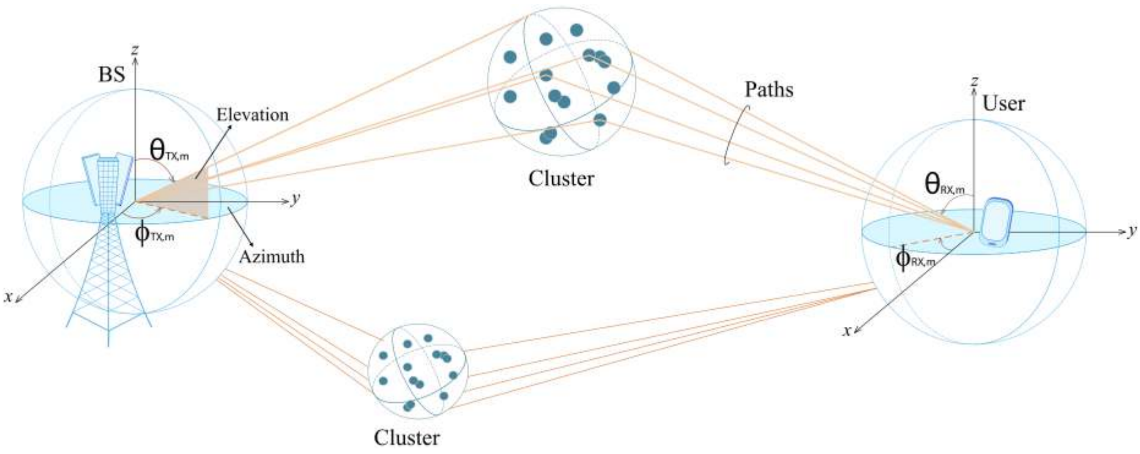

Figure 1.2: 3D geometric channel model [2].

are predominantly reflected by a limited number of scatterers in the environment. These reflected paths are grouped into clusters, where each cluster represents a set of closely spaced propagation paths. For simplicity and to avoid complicating the figure, only non-line-of-sight (NLOS) clusters are shown in Figure 1.2. As depicted, each path is characterized by its azimuth and elevation angles of departure (AoD) at the BS, denoted by ϕ_{Tx} and θ_{Tx}, respectively, and its azimuth and elevation angles of arrival (AoA) at the user, denoted by ϕ_{Rx} and θ_{Rx}, respectively. The resulting geometric channel model can be mathematically expressed as:

$$\mathbf{H} = \sqrt{\frac{N_t N_r}{CL+1}} \left(\alpha \mathbf{a}_r(\phi^0_{Rx}, \theta^0_{Rx}) \mathbf{a}_t^H(\phi^0_{Tx}, \theta^0_{Tx}) + \sum_{c=1}^{C} \sum_{l=1}^{L} \beta \mathbf{a}_r(\phi^{c,l}_{Rx}, \theta^{c,l}_{Rx}) \mathbf{a}_t^H(\phi^{c,l}_{Tx}, \theta^{c,l}_{Tx}) \right), \tag{1.1}$$

where N_t and N_r denote the number of antenna elements at the transmitter and receiver, respectively; C represents the number of clusters; L indicates the number of paths per cluster; α and β are the path gains for the line-of-sight (LOS) and NLOS components, respectively; and $\mathbf{a}_t(.)$ and $\mathbf{a}_r(.)$ are the array response vectors at the BS and the user, respectively. The superscript 0 represents the LOS component, while the indices $\{c, l\}$ correspond to the l-th path within the c-th NLOS cluster. This model effectively captures the sparse and clustered nature of mmWave

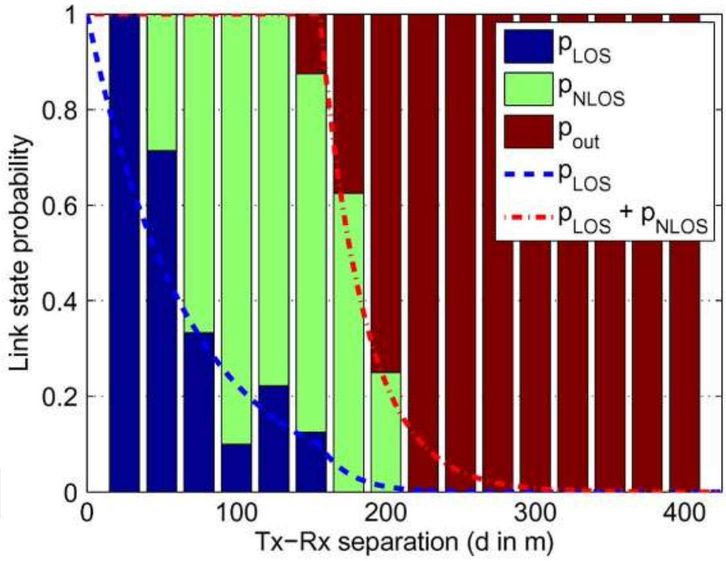

Figure 1.3: The fitted curves and the empirical values of $p_{\mathrm{LOS}}(d)$, $p_{\mathrm{NLOS}}(d)$, and $p_{\mathrm{out}}(d)$ as a function of the distance d. Measurement data is based on 42 TX-RX location pairs with distances from 30 m to 420 m at 28 GHz [4].

propagation, providing a realistic representation of the channel characteristics in challenging environments.

The empirical study in [4] demonstrates that, in urban environments at a carrier frequency of 28 GHz, the probability of establishing a LOS link decreases sharply as the separation between the transmitter (Tx) and receiver (Rx) increases. Beyond approximately 150 meters, this probability approaches zero. Similarly, the likelihood of a NLOS link also diminishes with distance, becoming negligible beyond 200 meters. Figure 1.3 presents both the fitted curves and empirical values for the LOS probability $p_{\mathrm{LOS}}(d)$, the NLOS probability $p_{\mathrm{NLOS}}(d)$, and the outage probability $p_{\mathrm{out}}(d)$ as functions of distance d. These findings underscore the challenges posed by severe path loss and signal attenuation in mmWave frequencies, which restricts the effective range and coverage of mmWave communication systems.

In order to address the severe path loss in mmWave band, large antenna arrays have become essential. By leveraging the short wavelengths of mmWave signals, large arrays can form narrow, highly directional beams, which enhance sig-

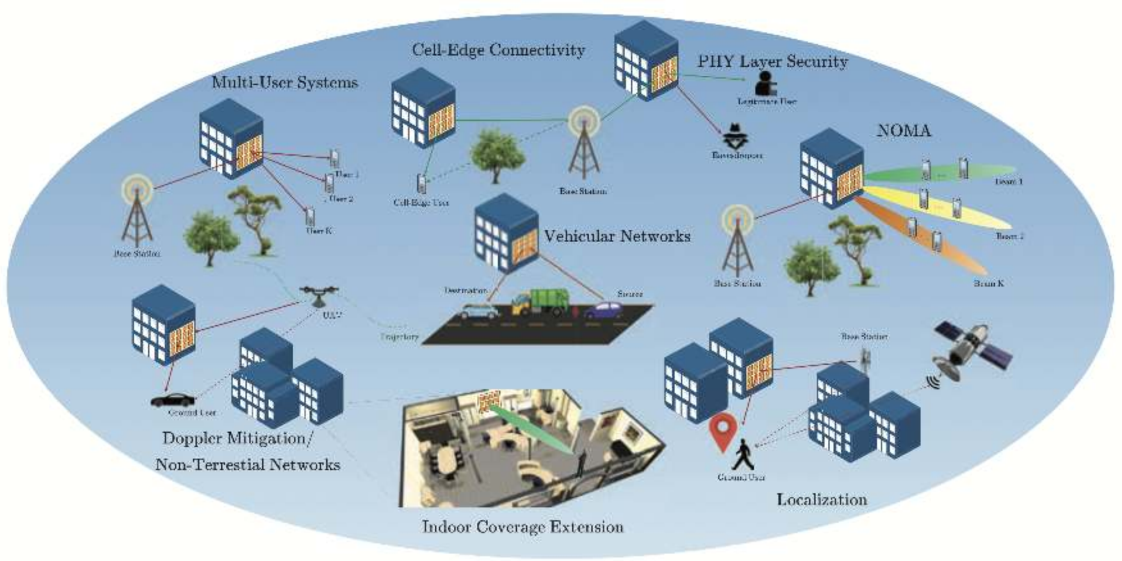

Figure 1.4: Emerging applications and use-cases of RIS-assisted communication systems in future wireless networks [11].

nal strength and mitigate path loss. This beamforming capability allows mmWave systems to maintain robust links over greater distances. However, scaling up to large arrays also introduces new challenges, such as increased implementation costs, higher power consumption, and complexity in hardware, particularly for fully-digital beamforming systems. As a result, hybrid and analog beamforming techniques have gained traction as more hardware-efficient alternatives, reducing the number of required RF chains while still achieving significant beamforming gains. Additionally, designs such as fixed phase shifters (FPS) have been explored to provide near-optimal performance with minimal complexity [10].

Addressing the challenges of enhancing mmWave communication performance while minimizing hardware complexity and cost has become a focal point in the development of next-generation wireless systems. This has spurred interest in innovative transceiver designs and system architectures that strike a balance between efficiency and affordability. Technologies such as index modulation (IM) [12, 13] and reconfigurable intelligent surfaces (RISs) [14] have emerged as promising solutions.

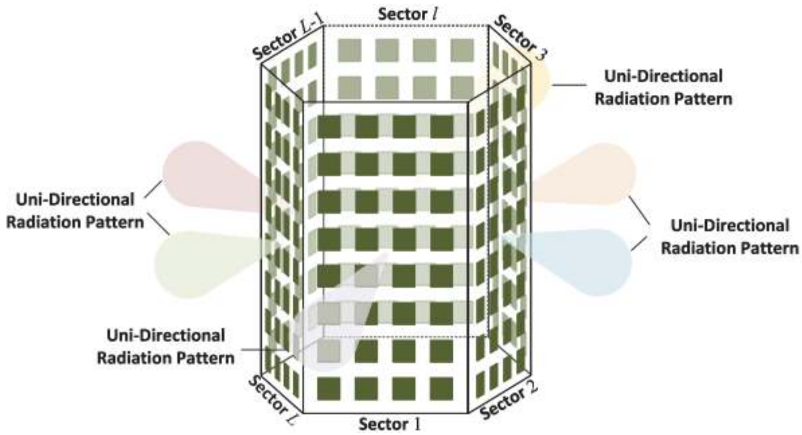

Figure 1.5: A multi-sector BD-RIS modeled as a polygon[16].

IM achieves higher spectral and energy efficiency by encoding additional information into system components like antenna arrays and clusters, thereby reducing the reliance on costly RF chains and enhancing overall throughput [12, 13]. On the other hand, RIS technology offers a transformative approach to signal propagation, enabling dynamic control over the reflective properties of surfaces to mitigate path loss and improve coverage in challenging environments, such as urban or indoor settings [14, 11]. These advancements hold the potential to not only optimize resource usage but also expand the capabilities of mmWave systems. Figure 1.4 illustrates the wide-ranging applications of RIS, emphasizing its role in diverse scenarios for future wireless networks.

Moreover, the practical deployment of RIS in real-world scenarios presents unique design opportunities and challenges. By placing RIS near the BS or user equipment (UE), distinct benefits arise [15]. BS-side RIS provides robust control and configuration, suitable for high-demand areas, whereas UE-side RIS can improve coverage in dead zones or high-interference areas. These deployment strategies underscore the need for carefully tailored RIS designs to meet the diverse requirements of 6G.

A significant advancement in system design for mmWave systems is the introduction of beyond-diagonal RIS (BD-RIS), which facilitate efficient passive beamforming without relying on costly active components [17, 18, 19]. Unlike conventional

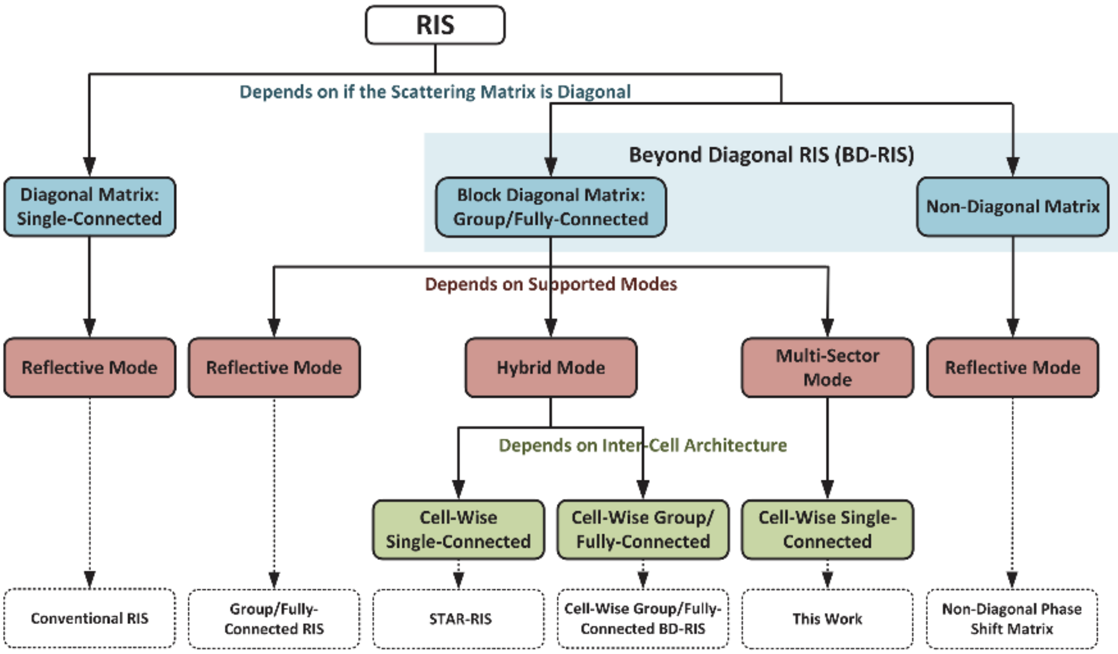

Figure 1.6: RIS classification tree [16].

diagonal RIS configurations, BD-RIS enhances beamforming capabilities by offering simultaneous control over the phase and amplitude of reflected signals [17, 18, 19]. This is achieved through the novel interconnection of RIS elements, forming beyond-diagonal scattering matrices that enable signal impingement on one reconfigurable element while reflecting from another [16]. Such a design not only broadens the scope of RIS functionality but also allows for the development of multi-sector RIS structures. These multi-sector configurations enable full environmental coverage, overcoming the half-coverage limitation commonly associated with traditional RIS designs. Figure 1.5 illustrates a multi-sector BD-RIS modeled as a polygon, showcasing its potential to enhance coverage capabilities. Additionally, Figure 1.6 presents an RIS classification tree based on the type of scattering matrix, further contextualizing the evolution of RIS technologies. The BD-RIS paradigm thus represents a transformative step forward in the design of intelligent surfaces, significantly advancing the performance and versatility of mmWave systems.

By utilizing BD-RIS at the transmitters, mmWave systems can achieve high beamforming gains comparable to those of active antenna arrays, but with lower operational costs and energy demands. This design approach not only advances the potential of RIS technology as a cost-effective alternative to active beamforming but also meets the rigorous performance requirements of applications needing precise control over signal direction and strength.

1.1 Thesis Contributions

This thesis presents several contributions to the field of mmWave communication systems, as detailed below:

1. **Introduction of cluster index modulation for mmWave Communications:** Developed a novel cluster index modulation (CIM) technique specifically designed to mitigate inter-beam interference. By utilizing well-separated clusters, CIM effectively reduces interference, enhancing bit error rate (BER) performance compared to beam index modulation (BIM) under realistic channel conditions. This scheme was extended to a hybrid beamforming architecture that combines analog RF and digital baseband precoding, further mitigating interference effects and optimizing performance.

2. **Investigation of antenna array structures for enhanced CIM performance:** Analyzed the impact of various antenna array structures, such as uniform linear, rectangular, circular, and concentric circular arrays, on the performance of CIM in mmWave systems. By examining the characteristics of these arrays, including radiation pattern, side lobe levels, and directivity, the study identified optimal array configurations that minimize inter-cluster interference and improve BER performance in CIM-enabled systems. This work also introduced a hardware-efficient FPS design to examine CIM performance under reducing system complexity.

3. **Integration of CIM with RIS:** Proposed a CIM scheme that leverages RIS

technology in a mmWave massive MIMO system. This integration introduces an optimized cluster selection mechanism, beam-gain cluster selection CIM (BGCS-CIM), which indexes clusters rather than individual paths, utilizing the spatial diversity within each cluster to improve communication reliability.

4. **Standalone Plug-In RIS Design for mmWave coverage enhancement:** Designed a plug-in RIS with standalone operation that requires minimal control and configuration. This fully passive RIS consists of sub-RIS planes with fixed phase profiles that cover specific spatial segments in dead zones, allowing mmWave systems to overcome signal blockage without the need for complex cascaded channel decoupling. The plug-in RIS is shown to be both energy-efficient and compatible with traditional end-to-end channel estimation methods, addressing key challenges in large-scale, passive RIS implementations.

5. **Design and evaluation of RIS deployments on BS-side and UE-side:** Conducted an in-depth analysis of RIS configurations at both BS and UE sides, exploring their unique applications and effectiveness under various deployment constraints. BS-side RIS configurations provide robust, centralized control ideal for dense environments, while UE-side RIS designs focus on energy efficiency and simplicity, catering to user mobility and extended coverage. This work contributes to identifying optimal RIS deployment strategies tailored to different 6G applications.

6. **Advanced BD-RIS Structure for efficient passive beamforming:** Introduced a beyond-diagonal RIS (BD-RIS) structure, integrated in the BS, that enhances passive beamforming capabilities without requiring active components. BS-integrated BD-RIS provides a high beamforming gain comparable to active antenna arrays, but with lower energy and cost.

7. **BS-Integrated BD-RIS for efficient localization:** Proposed the integration of BD-RIS at the BS to enable passive beamforming, offering an efficient solution for single-anchor localization scenarios. This approach ensures high

beamforming gain, which is crucial for precise positioning with minimal deployment of additional infrastructure.

8. **Analytical and simulation-based performance analysis:** Across each proposed system, comprehensive analytical derivations and simulations were performed to validate performance metrics such as achievable rate, bit error rate (BER), and coverage. The results demonstrate that the proposed systems achieve performance improvements over existing benchmarks, with the plug-in RIS and BD-RIS systems providing energy-efficient solutions that retain strong signal quality and localization accuracy in practical mmWave scenarios.

The findings of this Ph.D. thesis have been shared across various academic platforms, encompassing publications and submissions in four journals, a magazine, and two conference proceedings. This includes publishing in two prestigious IEEE journals and a widely recognized IEEE magazine, as detailed below:

1. **M. Raeisi**, A. Koc, E. Basar, and T. Le-Ngoc, "Cluster index modulation for mmWave communication systems," *Frontiers Commun. Netw.*, vol. 2, Feb. 2022, Art. no. 803007, doi: 10.3389/frcmn.2021.803007.

2. **M. Raeisi**, A. Koc, I. Yildirim, E. Basar, and T. Le-Ngoc, "Antenna array structures for enhanced cluster index modulation," in *Proc. Joint Eur. Conf. Netw. Commun. 6G Summit (EuCNC/6G Summit)*, Gothenburg, Sweden, Jun. 2023, pp. 102–107, doi: 10.1109/EuCNC/6GSummit58263.2023.10188340.

3. **M. Raeisi**, A. Koc, I. Yildirim, E. Basar, and T. Le-Ngoc, "Cluster index modulation for reconfigurable intelligent surface-assisted mmWave massive MIMO," *IEEE Trans. Wireless Commun.*, vol. 23, no. 2, pp. 1581–1591, Jul. 2023, doi: 10.1109/TWC.2023.3290618.

4. **M. Raeisi**, I. Yildirim, M. C. Ilter, M. Gerami, and E. Basar, "Plug-in RIS: A novel approach to fully passive reconfigurable intelligent surfaces," *IEEE*

Trans. Wireless Commun., vol. 23, no. 10, pp. 14776-14789, Jul. 2024. doi: 10.1109/TWC.2024.3418969.

5. **M. Raeisi**, A. Khaleel, M. C. Ilter, M. Gerami, and E. Basar, "A comprehensive design framework for UE-side and BS-side RIS deployments," *IEEE Wireless Commun.*, [accepted for publication], doi: 10.1109/MWC.001.2400142.

6. **M. Raeisi**, H. Chen, H. Wymeersch, and E. Basar, "Efficient localization with base station-integrated beyond diagonal RIS," in *Proc. IEEE Int. Conf. Commun. (ICC)*, Montreal, Canada, 2025, [submitted].

7. **M. Raeisi**, H. Chen, H. Wymeersch, and E. Basar, "Modern base station architecture: Enabling passive beamforming with beyond diagonal RIS," *IEEE Trans. Wireless Commun.*, [to be submitted], 2025.

1.2 Thesis Organization

The rest of this thesis is organized as follows: In Chapter 2, we introduce and explore the concept of CIM, presenting its relevance and applications in mmWave communication systems. Chapter 3 extends this discussion to antenna array structures for enhanced CIM, where different array configurations are analyzed for their impact on CIM performance. In Chapter 4, we investigate CIM for RIS-assisted mmWave massive MIMO, detailing how CIM can be integrated with RIS to enhance communication reliability in challenging environments. Chapter 5 focuses on Plug-In RIS, presenting a design that simplifies RIS deployment without compromising performance. Chapter 6 provides a comprehensive design framework for UE-side and BS-Side RIS deployments, offering insights into optimal RIS placement strategies for different applications. Chapter 7 introduces a novel BS design with integrated BD-RIS, enabling passive beamforming through large arrays that are cost and power-efficient. In Chapter 8, we examine efficient localization with base station-integrated BD-RIS, discussing the potential of BD-RIS for precise localization with high beamforming gain. Finally, Chapter 9 concludes the thesis, summarizing the key contributions and suggesting directions for future research.

Notation: Bold uppercase and lowercase letters are used to denote matrices and vectors, respectively. The operators $(.)^{\mathsf{T}}$, $(.)^{*}$, $(.)^{\mathsf{H}}$, $||.||$, $|.|$, $\angle$, diag(.),and blkdiag(.) denote transpose, conjugate, Hermitian, norm, absolute value, phase of a complex number, diagonalization, and block-diagonalization, respectively. $\mathbb{C}$ represents the set of complex numbers while $\odot$ denotes the Hadamard (element-wise) product. The operator $\mathbb{E}_X[.]$ indicates the expectation taken over the random variable X, while $\mathbb{P}(.)$ represents the probability of an event. The notation $[.]_i$ refers to the i-th element of a vector, while $\boldsymbol{v}_{[i:j]}$ defines a sub-vector containing elements from position i to j. Furthermore, $[a : \Delta : b]$ denotes a discrete sequence ranging from a to b with increments of Δ. $\mathcal{CN}(\mu, \sigma^2)$ denotes a complex Gaussian distribution with mean μ and variance σ^2, $\mathcal{L}(\varpi, \varsigma)$ refers to a Laplace distribution with location parameter ϖ and scale parameter ς, and $\mathcal{U}(a, b)$ denotes a uniform distribution within the interval $[a, b]$. $Q(x) = \frac{1}{\sqrt{2\pi}} \int_x^{\infty} \exp{(-\frac{u^2}{2})} du$ is the Q-function, and $\Gamma(n) = (n-1)!$ represents the gamma function. Ultimately, $\boldsymbol{I}_n$ signifies the $n \times n$ identity matrix.

Chapter 2

CLUSTER INDEX MODULATION

2.1 Introduction

With increasing demands for higher data rate and spectrum usage, new technologies and novel techniques for future wireless systems are needed. One of the most promising technologies with a large available spectrum is millimeter wave (mmWave) communication ([20, 21, 22, 23]). Nonetheless, mmWave signals suffer from significant path loss due to sparse-scattered environment ([24, 25]). To compensate the effect of path loss, mmWave systems should employ large antenna arrays in both transmitter and receiver to leverage beamforming gain. Deployment of large antenna arrays in a compact size is possible thanks to short wavelength of mmWave communications ([26, 3]). Normally in sub-6 GHz systems, MIMO arrays are fully digital where each antenna element connects to a single RF chain. However, for mmWave systems with large antenna arrays, it is costly and power consuming to have a huge number of RF chains ([27]), which necessitates the use of novel techniques to decrease implementation costs. Hybrid beamforming is a key technology to deal with this problem and to reduce the mmWave implementation costs ([28]). It is shown that hybrid beamforming achieves a spectral efficiency close to the fully-digital beamforming, also it greatly enhances energy efficiency for mmWave communication systems with large antenna arrays by significantly reducing the number of RF chains ([29]). While hybrid beamforming is known as an energy- and cost-efficient method to decrease the number of RF-chains, there is still a need for a tremendous number of high precision phase shifters. To decrease the number of phase shifters implemented in the analog network, ([10]) proposed a novel hardware efficient structure by adopting a network of fixed phase shifters. A network of dynamic switches implemented in order to adapt the analog network to the channel states.

Index modulation (IM) is another promising technology with high spectral and energy efficiencies, in which the transmitter performs indexing building blocks, e.g., antenna arrays, paths, sub-carriers and so on, to convey additional bits ([12, 13]). In ([30]), the authors investigated array IM in a mmWave communication system. In this study, the considered system consists of several arrays, an index in each array is specified. Therefore, according to the spatial symbols, one array is selected and traditional symbols are transmitted through that array. Here each receiver has to resolve traditional constellation and array index. In ([31]), the authors proposed a scheme named spatial scattering modulation (SSM) by indexing spatial directions of scattering clusters. It has been shown that the SSM scheme can perform better than maximum beamforming and random beamforming in the ideal condition of orthogonal paths, in terms of bit error rate (BER). However, this work did not consider realistic conditions such that the paths are randomly distributed in the environment and the orthogonality is not guaranteed. ([32]) proposed a hybrid beam index modulation (BIM) scheme by adopting a layer of digital precoding to solve the problem of inter-beam interference in mmWave communication systems. The authors showed that the proposed scheme can boost the system performance in comparison with pure analog BIM, due to cancellation of inter-beam interference. ([33]) proposed an anti-Doppler IM for wideband mmWave systems. They proposed a Doppler precompensator to assist IM in order to decrease the complexity of maximum likelihood (ML) detector. With such a scheme, they indicate that error performance enhances. A spatial modulation scheme for uplink mmWave system proposed in ([34]). In this scheme, the authors considered a power iteration algorithm to obtain spatial symbols. With such a spatial codebook, it is possible to find the optimal transmission mode, by obtaining a trade off between spatial domain and signal domain. On the other hand, at the base station (BS), they adopt a round-robin path selection algorithm to ensure that selected paths are separated enough with respect to angle of arrival (AoA). Generalized beamspace modulation (GBM) is proposed in ([35]) to enhance multiplexing gain and spectral efficiency. Theoretical analysis and numerical simulations demonstrate that this scheme can perform better than non-GBM schemes in terms of BER and spectral efficiency. Finally ([24]) studies receive spatial modulation (RSM) for indoor line-of-sight (LOS) mmWave systems. To minimize symbol error probability (SEP), they derive optimal channel conditions; and based on this optimization, they propose a simple structure for transmitter and receiver.

In this chapter, a mmWave communication scenario in which the paths are uniformly distributed in the environment is studied, and normally, these paths are not orthogonal. In our proposed scheme, named cluster index modulation (CIM), the best path from each cluster is chosen for IM. Due to the well separation of clusters in terms of their angular distribution, the selected paths are also separated. It is worth mentioning that, when two paths are physically separated enough, they become near orthogonal. Extensive computer simulations evaluate superiority of the proposed CIM scheme against traditional mmWave communication. Our contributions are summarized as follows:

- A novel IM scheme based on indexing separated clusters in the mmWave communication environment is proposed. Simulation results reveal that our proposed scheme can perform better than traditional mmWave communication in terms of BER in the presence of non-orthogonal paths.

- We propose a hybrid architecture in the transmitter, which benefits from a digital ZF precoder to further mitigate inter-beam interference. Simulation results demonstrate the superiority of our proposed hybrid scheme in comparison with the BIM scheme.

- We study our scheme in the case of analog and hybrid architectures at the transmitter, derive our semi-analytical derivations, and closed-form analytical unconditional pairwise error probability (UPEP) expressions for both architectures, which prove the validity of our proposed scheme. We further note that our derivations based or semi-analytical models provide useful approximation on the actual BER.

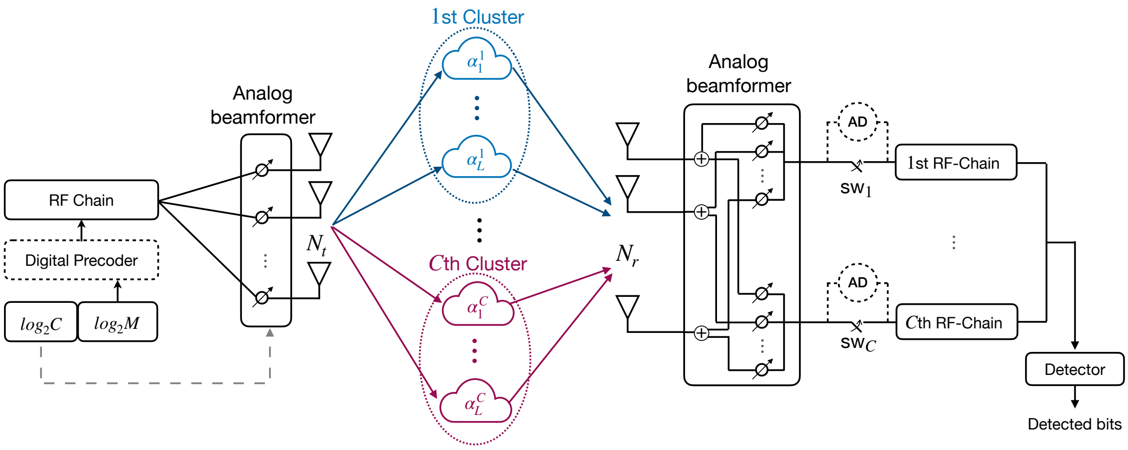

Figure 2.1: CIM system model with analog and hybrid beamforming architecture

The rest of this chapter is organized as follows. In Section 2.2, our channel model has been introduced. BER performance analysis is given in Section 2.3. Simulation results are provided in Section 2.4; and the conclusion of this work can be found in Section 2.5.

2.2 System Model

In this section, we present the proposed system and its generic architecture. Fig. 2.1 illustrates the proposed system model with C clusters in the environment. It is assumed that each cluster consists of several paths with uniformly distributed angle-of-arrival (AoA) or departure (AoD) within a predefined interval. We consider that the clusters have non-overlapping angular support (i.e., AoA and AoD). Hence, they are well separated from each other. As shown in Fig. 2.1, the number of transmit and receive antennas are assumed as N_t and N_r, respectively. At both transmitter and receiver, each antenna element is connected to a phase shifter for the purpose of analog beamforming to compensate the effect of path loss. A point-to-point communication scenario is considered; hence, at the transmitter, we have a single RF chain. At the receiver side, C beams should be formed simultaneously, where

C is the number of indexed clusters; hence, C RF chains is needed at the receiver. With taking into consideration M as the constellation order, the spectral efficiency is given as $\eta = \log_2 C + \log_2 M$ bits per channel use (bpcu).

We adopt Saleh-Valenzuela channel model to characterize a mmWave non-line-of-sight (NLOS) channel in an indoor environment ([7, 4]). The channel matrix $\mathbf{H} \in \mathbb{C}^{N_r \times N_t}$ is expressed as follows:

$$\mathbf{H} = \sqrt{N_t N_r} \sum_{i=1}^{C} \sum_{l=1}^{L_i} \alpha_l^i \mathbf{a}_R(\phi_l^i) \mathbf{a}_T^H(\theta_l^i), \tag{2.1}$$

where α_l^i shows l-th path gain in the i-th cluster that follows $\alpha_l^i \sim \mathcal{CN}(0,1)$ distribution; L_i is the number of available paths in the i-th cluster, $\mathbf{a}_R(.) \in \mathbb{C}^{N_r \times 1}$ and $\mathbf{a}_T(.) \in \mathbb{C}^{N_t \times 1}$ are the receive and transmit antenna array responses, respectively; ϕ_l^i and θ_l^i are the azimuth AoA and AoD corresponding to l-th path in the i-th cluster, respectively. Considering both transmitter and receiver equipped with uniform linear arrays, the array responses $\mathbf{a}_R(.)$ and $\mathbf{a}_T(.)$ are respectively defined as follows:

$$\mathbf{a}_T(\theta_l^i) = \frac{1}{\sqrt{N_t}} \begin{bmatrix} 1 & e^{j\Theta_l^i} & \dots & e^{j\Theta_l^i(N_t-1)} \end{bmatrix}^T, \tag{2.2}$$

$$\mathbf{a}_R(\phi_l^i) = \frac{1}{\sqrt{N_r}} \begin{bmatrix} 1 & e^{j\Phi_l^i} & \dots & e^{j\Phi_l^i(N_r-1)} \end{bmatrix}^T, \tag{2.3}$$

where $\Theta_l^i = 2\pi \frac{d_t}{\lambda} \sin(\theta_l^i)$, $\Phi_l^i = 2\pi \frac{d_r}{\lambda} \sin(\phi_l^i)$, d_t and d_r are the distances between antenna elements at the transmitter and receiver respectively, and λ is the signal wavelength. In this chapter, half-wavelength separation between antenna elements is assumed (i.e., $d_t = d_r = \frac{\lambda}{2}$). In the following, we describe the proposed analog and hybrid beamforming architecture.

2.2.1 Analog Beamforming Architecture

In this setup, completely analog architectures are considered at the transmitter and receiver; hence, there is no digital signal processing in the system. The received signal vector $\mathbf{y} \in \mathbb{C}^{N_r \times 1}$ at the receiver can be expressed as follows:

$$\mathbf{y} = \mathbf{H}\mathbf{f}_{i^*} s + \mathbf{n}, \tag{2.4}$$

where $\mathbf{f}_{i^*} \in \mathbb{C}^{N_t \times 1}$ is the analog beamformer of the best path of the selected cluster, i.e., cluster i^*, at the transmitter, and $\mathbf{n} \in \mathbb{C}^{N_r \times 1}$ is the noise vector which has the circularly symmetric complex Gaussian distribution with variance σ^2, i.e., $\mathbf{n} \sim \mathcal{CN}(\mathbf{0}, \sigma^2 \boldsymbol{I}_{N_r})$. s is the traditional transmitted data symbol. In this chapter, the best path in each cluster is considered to be the path with strongest path gain. The transmitter selects one of the indexed clusters according to the spatial symbol, and conveys the conventional constellation through the best path of that cluster. For the sake of statement simplicity, when we mention indexed cluster, we mean the best path of that cluster. Analog beamformer $\mathbf{f}_{i^*}$ at the transmitter can be expressed as follows ([36, 37]):

$$\mathbf{f}_{i^*} = \frac{1}{\sqrt{N_t}} \begin{bmatrix} 1 & e^{j\tilde{\Theta}_{l^*}^{i^*}} & \dots & e^{j\tilde{\Theta}_{l^*}^{i^*}(N_t-1)} \end{bmatrix}^T, \tag{2.5}$$

where $\tilde{\Theta}_{l^*}^{i^*} = 2\pi \frac{d_t}{\lambda} \sin(\tilde{\theta}_{l^*}^{i^*})$, and $\tilde{\theta}_{l^*}^{i^*}$ is the angle-of-transmission (AoT) of the beam corresponding to the selected cluster. The receiver uses analog combiners to resolve the spatial symbol. To do so, the receiver searches among all indexed clusters by multiplying corresponding vectors of analog combiners $\mathbf{w}_i$. Hence, the received signal after analog combiner can be shown as:

$$y_i = \mathbf{w}_i^H \mathbf{H} \mathbf{f}_{i^*} s + \mathbf{w}_i^H \mathbf{n}, \tag{2.6}$$

Analog combiner of l-th path of the i-th cluster can be expressed as follows:

$$\mathbf{w}_i = \frac{1}{\sqrt{N_r}} \begin{bmatrix} 1 & e^{j\tilde{\Phi}_l^i} & \dots & e^{j\tilde{\Phi}_l^i(N_r-1)} \end{bmatrix}^T, \tag{2.7}$$

where $\tilde{\Phi}_l^i = 2\pi \frac{d_r}{\lambda} \sin(\tilde{\phi}_l^i)$, and $\tilde{\phi}_l^i$ is the angle-of-reception (AoR) of the beam corresponding to the i-th cluster. In (2.6), i^* shows the correct index that is adopted by the transmitter; however, receiver should resolve the index used at the transmitter. Therefore, we use the unknown index i for the combiner to emphasis this fact. In this chapter, it is assumed that AoT and AoR are equal to AoD and AoA of the strongest path of the indexed cluster, respectively; unless specified otherwise. As shown in Fig. 2.1, the receiver consists of C RF chains connecting to a network of phase shifters, and each of them forms the received beam toward the strongest path of a specific indexed cluster for the received signal. In this way, all analog combiners work simultaneously to resolve the spatial symbol.

In this chapter, we study both brute-force and two-stage greedy-maximum likelihood (ML) detector to analyze the performance of the proposed CIM. To use brute-force detector, all switches (i.e. $\mathrm{SW}_i, i = 1, 2, \ldots, C$) should be closed. Afterwards, the receiver jointly detects indexed and M-ary bits as follows:

$$[\hat{i}, \hat{m}] = \arg \min_{\substack{i=1,\ldots,C \\ m=1,\ldots,M}} \left| y_i - \mathbf{w}_i^H \mathbf{H} \mathbf{f}_i s_m \right|^2. \tag{2.8}$$

For the case of greedy-ML detector, amplitude detectors (AD) measure the received power of signals from each cluster to detect the one with the most power; henceforth, the corresponding switch to that path is closed while the other switches remain open. Therefore, we have the first stage detection to resolve indexed bits as follows:

$$\hat{i} = \arg \max_{i=1,\ldots,C} |y_i|^2. \tag{2.9}$$

At the second stage, we adopt ML detector to detect M-ary symbols as follows:

$$\hat{m} = \arg \min_{m=1,\ldots,M} \left| y_{\hat{i}} - \mathbf{w}_{\hat{i}}^H \mathbf{H} \mathbf{f}_{\hat{i}} s_m \right|^2. \tag{2.10}$$

2.2.2 Hybrid Beamforming Architecture

In the hybrid architecture, a digital precoder is adopted at the transmitter to further suppress inter-beam interference and boost the system performance. By applying ZF criterion to the indexed clusters, the transmitter can null the inter-beam interference. The received signal vector $\mathbf{y}$ can be expressed as follows:

$$\mathbf{y} = \mathbf{HFDx} + \mathbf{n}. \tag{2.11}$$

Notice $\mathbf{D} = [\mathbf{d}_1 \ldots \mathbf{d}_C] \in \mathbb{C}^{C\times C}$ is the digital zero-forcing (ZF) precoder, wherein $\mathbf{d}_i \in \mathbb{C}^{C\times 1}$ is digital precoder vector related to i-th indexed cluster. $\mathbf{F} = [\mathbf{f}_1 \ldots \mathbf{f}_C] \in \mathbb{C}^{N_t\times C}$ contains analog beamforming vectors of all indexed clusters, and $\mathbf{x} = [0 \ldots 0\ s\ 0 \ldots 0]^T \in \mathbb{C}^{C\times 1}$ whose i^*-th element is s, i.e., M-ary constellation symbol. To define ZF precoder, first we define effective channel $\mathbf{H}_e \in \mathbb{C}^{C\times C}$ as follows:

$$\mathbf{H}_e = \mathbf{W}^H \mathbf{HF}, \tag{2.12}$$

where $\mathbf{W} = [\mathbf{w}_1 \dots \mathbf{w}_C] \in \mathbb{C}^{N_r \times C}$ includes all analog combiner vectors of all indexed clusters. Next, $\mathbf{D}$ is defined as

$$\mathbf{D} = \varepsilon \mathbf{H}_e^H (\mathbf{H}_e \mathbf{H}_e^H)^{-1}, \tag{2.13}$$

where ε is the normalization scalar and can be obtained as

$$\varepsilon = \sqrt{\frac{1}{\mathrm{tr}(\mathbf{F}^H \mathbf{F} \mathbf{H}_e^H (\mathbf{H}_e \mathbf{H}_e^H)^{-2} \mathbf{H}_e)}}, \tag{2.14}$$

wherein tr(.) is the trace operation. It is worth mentioning that, channel characteristics at the transmitter can be obtained via both online and offline approaches ([38, 39, 40]). The received signal vector after analog combiner can be stated as follows:

$$\mathbf{y}^c = \mathbf{W}^H \mathbf{HFDx} + \mathbf{W}^H \mathbf{n}, \tag{2.15}$$

in which $\mathbf{y}^c = [y_1^c \dots y_C^c]^T \in \mathbb{C}^{C \times 1}$. It is worth mentioning that y_i^c is the received signal from the i-th indexed cluster after the analog combiner that can be expressed as follows:

$$y_i^c = \mathbf{w}_i^H \mathbf{HFd}_i s_m + \mathbf{w}_i^H \mathbf{n} \tag{2.16}$$

Finally, in order to jointly detect indexed and M-ary bits, the brute-force detector is defined as follows:

$$[\hat{i}, \hat{m}] = \arg \min_{\substack{i=1,\dots,C \\ m=1,\dots,M}} \left| y_i^c - \mathbf{w}_i^H \mathbf{HFd}_i s_m \right|^2. \tag{2.17}$$

2.3 BER Performance Analysis

In this section, the BER performance of the proposed analog and hybrid beamforming schemes are derived. We use i^* and s^* to present the true cluster index and symbol; whereas, $\hat{i}$ and $\hat{s}$ are used to represent detected cluster index and symbol.

2.3.1 Analog Beamforming Architecture

Using brute-force detector, conditional pairwise error probability (CPEP) can be stated as follows:

$$\mathbb{P}(\{i^*, s^*\} \to \{\hat{i}, \hat{s}\} | \alpha_1^1, \dots, \alpha_L^C) = \mathbb{P}(|y_{i^*} - \mathbf{w}_{i^*}^H \mathbf{Hf}_{i^*} s^*|^2 > |y_{\hat{i}} - \mathbf{w}_{\hat{i}}^H \mathbf{Hf}_{\hat{i}} \hat{s}|^2), \tag{2.18}$$

wherein

$$|y_{i^*} - \mathbf{w}_{i^*}^H \mathbf{H}\mathbf{f}_{i^*} s^*|^2 = |\mathbf{w}_{i^*}^H \mathbf{n}|^2. \tag{2.19}$$

To solve CPEP expression, we consider two cases, correct cluster index detection ($\hat{\imath} = i^*$) and erroneous cluster index detection ($\hat{\imath} \neq i^*$). In this chapter, we do not consider the case of erroneously index detection and correct symbol detection because when the detector resolve the cluster erroneously, the error spreads to the symbol.

Correct Cluster Index Detection $\hat{\imath} = i^*$

When the cluster index is detected correctly, by using (2.6) and right-hand side of (2.18), we can derive the following:

$$|y_{\hat{\imath}} - \mathbf{w}_{\hat{\imath}}^H \mathbf{H}\mathbf{f}_{\hat{\imath}} \hat{s}|^2 = |\mathbf{w}_{i^*}^H \mathbf{n} + \mathbf{w}_{i^*}^H \mathbf{H}\mathbf{f}_{i^*}(s^* - \hat{s})|^2. \tag{2.20}$$

Therefore, by substituting (2.19) and (2.20) into (2.18), CPEP expression can be as follows:

$$\mathbb{P}(\{i^*, s^*\} \to \{\hat{\imath}, \hat{s}\} | \alpha_1^1, \ldots, \alpha_L^C) = \mathbb{P}(\zeta < 0), \tag{2.21}$$

where

$$\zeta = 2\mathcal{R}e\{\mathbf{n}^H \mathbf{w}_{i^*} \mathbf{w}_{i^*}^H \mathbf{H}\mathbf{f}_{i^*}(s^* - \hat{s})\} + |\mathbf{w}_{i^*}^H \mathbf{H}\mathbf{f}_{i^*}(s^* - \hat{s})|^2. \tag{2.22}$$

Hence, ζ follows Gaussian distribution with mean μ_ζ and variance σ_ζ^2. These mean and variance values can be calculated as follows:

$$\mu_\zeta = |\mathbf{w}_{i^*}^H \mathbf{H}\mathbf{f}_{i^*}(s^* - \hat{s})|^2, \tag{2.23}$$

$$\sigma_\zeta^2 = 2\sigma^2 ||\mathbf{H}\mathbf{f}_{i^*}(s^* - \hat{s})||^2. \tag{2.24}$$

Accordingly, we can calculate CPEP for this case as follows:

$$\mathbb{P}(\{i^*, s^*\} \to \{i^*, \hat{s}\} | \alpha_1^1, \ldots, \alpha_L^C) = Q\left(\sqrt{\frac{||\mathbf{H}\mathbf{f}_{i^*}(s^* - \hat{s})||^2}{2\sigma^2}}\right), \tag{2.25}$$

where $Q(.)$ is the Q-function and defined as follows:

$$Q(x) = \frac{1}{\sqrt{2\pi}} \int_x^\infty \exp\left(-\frac{u^2}{2}\right) du. \tag{2.26}$$

Let us define M_A as follows

$$M_A = \frac{||\mathbf{Hf}_{i^*}(s^* - \hat{s})||^2}{2\sigma^2}. \tag{2.27}$$

Unfortunately, due to complicated distribution of $\mathbf{Hf}_i^*$, we cannot obtain UPEP analytically. To obtain semi-analytical results, we generate and store S samples of M_A as $M_A(t), t = 1, 2, ..., S$ for each given SNR, and take the mean over all the random samples as follows to obtain UPEP ([41]):

$$\mathbb{P}(\{i^*, s^*\} \to \{i^*, \hat{s}\}) = \frac{1}{S} \sum_{t=1}^{S} Q\big(\sqrt{M_A(t)}\big). \tag{2.28}$$

As an alternative to above approach, we can obtain approximate analytical results by using Distribution Fitter tool in MATLAB. For this purpose, one can obtain probability density function (PDF) of the random part in (2.25). Let us define

$$X = ||\mathbf{Hf}_{i^*}(s^* - \hat{s})||^2. \tag{2.29}$$

Subsequently, (2.25) can be rewritten as:

$$g(X) = Q\Big(\sqrt{\frac{X}{2\sigma^2}}\Big), \tag{2.30}$$

wherein $g(X)$ is a function of random variable X. In order to calculate UPEP, we need to take an expectation over $g(X)$, given that X has a PDF of $f_X(x)$. Hence, by applying the expectation operation, we can write

$$\mathbb{P}(\{i^*, s^*\} \to \{i^*, \hat{s}\}) = E[g(X)] = \int g(x) f_X(x) dx. \tag{2.31}$$

In Section 2.4, the PDF of X (i.e., $f_X(x)$) is obtained by using Distribution Fitter tool; then, by adopting (2.30) and (2.31), we acquire approximate analytical results for UPEP.

Erroneous Cluster Index Detection $\hat{i} \neq i^*$

Considering erroneous detection of the cluster index, by using (2.6) and (2.18), the following expression can be derived:

$$|y_{\hat{i}} - \mathbf{w}_{\hat{i}}^H \mathbf{H} \mathbf{f}_{\hat{i}} \hat{s}|^2 = |\mathbf{w}_{\hat{i}}^H \mathbf{H}(\mathbf{f}_{i^*} s^* - \mathbf{f}_{\hat{i}} \hat{s}) + \mathbf{w}_{\hat{i}}^H \mathbf{n}|^2. \tag{2.32}$$

Accordingly, substituting (2.19) and (2.32) into (2.18) results into following CPEP expression:

$$\mathbb{P}(\{i^*, s^*\} \rightarrow \{\hat{i}, \hat{s}\} | \alpha_1^1, \ldots, \alpha_L^C) = \mathbb{P}(|\mathbf{w}_{\hat{i}}^H \mathbf{H}(\mathbf{f}_{i^*} s^* - \mathbf{f}_{\hat{i}} \hat{s}) + \mathbf{w}_{\hat{i}}^H \mathbf{n}|^2 - |\mathbf{w}_{i^*}^H \mathbf{n}|^2 < 0). \tag{2.33}$$

Let us define

$$\xi_1 = |\mathbf{w}_{\hat{i}}^H \mathbf{H}(\mathbf{f}_{i^*} s^* - \mathbf{f}_{\hat{i}} \hat{s}) + \mathbf{w}_{\hat{i}}^H \mathbf{n}|^2, \tag{2.34}$$

$$\xi_2 = |\mathbf{w}_{i^*}^H \mathbf{n}|^2. \tag{2.35}$$

Further, we define $\chi_1 \triangleq \frac{\xi_1}{\sigma^2/2}$ and $\chi_2 \triangleq \frac{\xi_2}{\sigma^2/2}$. Notice that, χ_1 is a non-central chi-square random variable with two degrees of freedom and non-centrality parameter Λ_A:

$$\Lambda_A = \frac{2|\mathbf{w}_{\hat{i}}^H \mathbf{H}(\mathbf{f}_{i^*} s^* - \mathbf{f}_{\hat{i}} \hat{s})|^2}{\sigma^2}. \tag{2.36}$$

Similarly, χ_2 is a central chi-square random variable with two degrees of freedom, which has an exponential distribution with the parameter of $\frac{1}{2}$. To tackle the analytical calculations, it is necessary to have $\mathbf{w}_{i^*}^H \times \mathbf{w}_{\hat{i}} = 0$. To do so, we select AoRs from a discrete Fourier transform (DFT) bin. When we select AoRs from a DFT bin, the corresponding analog combiners $\mathbf{w}_i$ are orthogonal; consequently, they can satisfy $\mathbf{w}_{i^*}^H \times \mathbf{w}_{\hat{i}} = 0$. Therefore, in this section AoR and AoA are not equal. As selection criteria for AoR, we select an AoR from DFT bin which constitute the minimum distance with the best path of the selected indexed cluster. While the formed beams at the receiver are orthogonal, paths are still non-orthogonal. Though with this assumption the system performance decreases, but it does not violate feasibility of the system, because it is possible for the receiver to form the orthogonal beams. Regarding indipendency of $\mathbf{w}_{i^*}^H\mathbf{n}$ and $\mathbf{w}_{\hat{i}}^H\mathbf{n}$, we have to calculate the following:

$$\mathbb{P}(\{i^*, s^*\} \rightarrow \{\hat{i}, \hat{s}\}|\alpha_1^1, \ldots, \alpha_L^C) = \mathbb{P}(\chi_1 < \chi_2) = \int_0^{+\infty}\int_{x_1}^{+\infty} f_{\chi_1}(x_1)f_{\chi_2}(x_2)dx_1dx_2, \tag{2.37}$$

where $f_{\chi_1}(x_1)$ and $f_{\chi_2}(x_2)$ are PDF of χ_1 and χ_2, respectively. After some manipulations, we obtain

$$\begin{aligned}\mathbb{P}(\{i^*, s^*\} \rightarrow \{\hat{i}, \hat{s}\}|\alpha_1^1, \ldots, \alpha_L^C) &= \mathbb{P}(\chi_1 < \chi_2)\\ &= \frac{1}{2}\exp\Big(-\frac{|\mathbf{w}_{\hat{i}}^H\mathbf{H}(\mathbf{f}_{i^*}s^* - \mathbf{f}_{\hat{i}}\hat{s})|^2}{2\sigma^2}\Big) = \frac{1}{2}\exp\big(-\frac{\Lambda_A}{4}\big).\end{aligned} \tag{2.38}$$

To acquire semi-analytical results, we can use the following expression

$$\mathbb{P}(\{i^*, s^*\} \rightarrow \{\hat{i}, \hat{s}\}) = \frac{1}{2S}\sum_{t=1}^{S}\exp(-\frac{\Lambda_A(t)}{4}), \tag{2.39}$$

where $\Lambda_A(t)$ is the t-th random sample of Λ_A and S stands for number of random realizations.

To obtain UPEP by using Distribution Fitter tool, the random part of (2.38) can be considered as

$$Y = |\mathbf{w}_{\hat{i}}^H\mathbf{H}(\mathbf{f}_{i^*}s^* - \mathbf{f}_{\hat{i}}\hat{s})|^2. \tag{2.40}$$

Hence, we can rewrite (2.38) as

$$h(Y) = \frac{1}{2}\exp\big(-\frac{Y}{2\sigma^2}\big). \tag{2.41}$$

By taking expectation over $h(Y)$ given that Y has a PDF of $f_Y(y)$, we can derive UPEP as

$$\mathbb{P}(\{i^*, s^*\} \rightarrow \{\hat{i}, \hat{s}\}) = E[h(Y)] = \int h(y)f_Y(y)dy. \tag{2.42}$$

In Section 2.4, we obtain the PDF of Y for the deployed scenario; subsequently, UPEP can be calculated by using (2.41) and (2.42).

2.3.2 Hybrid Beamforming Architecture

By following the same procedure, we can easily calculate CPEP for the hybrid beamforming architecture. Therefore, for the case of $\hat{i} = i^*$ and $\hat{i} \neq i^*$, CPEP can be expressed as follows, respectively:

$$\mathbb{P}(\{i^*, s^*\} \rightarrow \{i^*, \hat{s}\} | \alpha_1^1, \ldots, \alpha_L^C) = Q\Bigg(\sqrt{\frac{||\mathbf{HFd}_{i^*}(s^* - \hat{s})||^2}{2\sigma^2}}\Bigg), \tag{2.43}$$

$$\mathbb{P}(\{i^*, s^*\} \rightarrow \{\hat{i}, \hat{s}\} | \alpha_1^1, \ldots, \alpha_L^C) = \frac{1}{2}\exp\Big(-\frac{\Lambda_H}{4}\Big), \tag{2.44}$$

where

$$\Lambda_H = \frac{2\Big|\mathbf{w}_{\hat{i}}^H\mathbf{HF}\Big(\mathbf{d}_{i^*}s^* - \mathbf{d}_{\hat{i}}\hat{s}\Big)\Big|^2}{\sigma^2}. \tag{2.45}$$

Regarding (2.43), let us define M_H as follows

$$M_H = \frac{||\mathbf{HFd}_{i^*}(s^* - \hat{s})||^2}{2\sigma^2}. \tag{2.46}$$

Semi-analytical results can be obtained by using the following

$$\mathbb{P}(\{i^*, s^*\} \rightarrow \{i^*, \hat{s}\}) = \frac{1}{S}\sum_{t=1}^{S} Q\Big(\sqrt{M_H(t)}\Big), \tag{2.47}$$

in which $M_H(t)$ is the t-th random sample of M_H. Similarly, we can calculate semi-analytical UPEP for the case of $\hat{i} \neq i^*$ as follows

$$\mathbb{P}(\{i^*, s^*\} \rightarrow \{\hat{i}, \hat{s}\}) = \frac{1}{2S}\sum_{t=1}^{S} \exp\big(-\frac{\Lambda_H(t)}{4}\big), \tag{2.48}$$

where $\Lambda_H(t)$ is the t-th random sample of Λ_H.

To obtain approximate UPEP, the same approach as the analog architecture can be adopted; hereby, we define $\tilde{X}$ and $\tilde{Y}$ as random variables for (2.43) and (2.44) as follows, respectively:

$$\tilde{X} = ||\mathbf{HFd}_{i^*}(s^* - \hat{s})||^2. \tag{2.49}$$

$$\tilde{Y} = \Big|\mathbf{w}_{\hat{i}}^H\mathbf{HF}\Big(\mathbf{d}_{i^*}s^* - \mathbf{d}_{\hat{i}}\hat{s}\Big)\Big|^2. \tag{2.50}$$

Subsequently, we can rewrite CPEP expressions of (2.43) and (2.44) as follows, respectively:

$$\mathbb{P}(\{i^*, s^*\} \rightarrow \{i^*, \hat{s}\}|\alpha_1^1, \ldots, \alpha_L^C) = g(\tilde{X}) = Q\Big(\sqrt{\frac{\tilde{X}}{2\sigma^2}}\Big), \tag{2.51}$$

$$\mathbb{P}(\{i^*, s^*\} \rightarrow \{\hat{i}, \hat{s}\}|\alpha_1^1, \ldots, \alpha_L^C) = h(\tilde{Y}) = \frac{1}{2}\exp\big(-\frac{\tilde{Y}}{2\sigma^2}\big). \tag{2.52}$$

Finally, by taking the expectation over $g(\tilde{X})$ and $h(\tilde{Y})$, and having the PDF of $f_{\tilde{X}}(\tilde{x})$ and $f_{\tilde{Y}}(\tilde{y})$, we can calculate analytical UPEP for the cases of $i^* = \hat{i}$ and $i^* \neq \hat{i}$ as follows, respectively:

$$\mathbb{P}(\{i^*, s^*\} \rightarrow \{i^*, \hat{s}\}) = E[g(\tilde{X})] = \int g(\tilde{x}) f_{\tilde{X}}(\tilde{x}) d\tilde{x}. \tag{2.53}$$

$$\mathbb{P}(\{i^*, s^*\} \rightarrow \{\hat{i}, \hat{s}\}) = E[h(\tilde{Y})] = \int h(\tilde{y}) f_{\tilde{Y}}(\tilde{y}) d\tilde{y}. \tag{2.54}$$

It is worth noting that, in the Section 2.4, we obtain a PDF for $\tilde{X}$ and $\tilde{Y}$ based on implemented system. Therefore, we can acquire UPEP by adopting (2.51) to (2.54).

2.3.3 BER Derivation

We can derive BER using union bound as follows:

$$p_b \leq \frac{1}{N_b N(i^*, s^*)} \sum_{i^*, s^*} \sum_{\hat{i}, \hat{s}} E_b\big(\{i^*, s^*\} \rightarrow \{\hat{i}, \hat{s}\}\big) A, \tag{2.55}$$

where N_b is the total number of transmitted bits, $N(i^*, s^*)$ is the total number of realizations of i^* and s^*, and $E_b\big(\{i^*, s^*\} \rightarrow \{\hat{i}, \hat{s}\}\big)$ is the number of erroneous bits when i^* and s^* are transmitted but $\hat{i}$ and $\hat{s}$ are detected. As it is mentioned earlier, there are two cases of errors, i.e., both index and symbol are erroneous, or just only symbol is erroneously detected. To obtain semi-analytical results, we define $A = \mathbb{P}(\{i^*, s^*\} \rightarrow \{\hat{i}, \hat{s}\}|\alpha_1^1, \ldots, \alpha_L^C)$, which can be obtained by using (2.28) and (2.39) for analog beamforming architecture, or by using (2.47) and (2.48) for hybrid beamforming architecture. It is worth mentioning that, $S = 10^4$ has been considered during numerical expectation. On the other hand, to obtain approximate analytical results with Distribution Fitter tool, we can define $A = \mathbb{P}(\{i^*, s^*\} \rightarrow \{\hat{i}, \hat{s}\})$, which can be acquired by (2.31) and (2.42) for the analog beamforming architecture, and (2.53) and (2.54) for the hybrid beamforming architecture.

Table 2.1: AoA/AoR interval ranges for cluster index modulation (CIM).

	First cluster	Second cluster	Third cluster	Forth cluster
AoD/AoA intervals	$\left[-\frac{41\pi}{120}, -\frac{31\pi}{120}\right]$	$\left[-\frac{17\pi}{120}, -\frac{7\pi}{120}\right]$	$\left[\frac{7\pi}{120}, \frac{17\pi}{120}\right]$	$\left[\frac{31\pi}{120}, \frac{41\pi}{120}\right]$

2.4 Simulation Results

Two architectures are considered for the proposed scheme, i.e., analog, and hybrid scheme. First, we provide computer simulation results for the analog scheme. Then, hybrid scheme, which includes a ZF precoder block to suppress inter-beam interference, is analyzed.

2.4.1 Analog Beamforming Architecture

The number of antenna elements at the transmitter and receiver is considered to be 128. The total number of paths in all clusters is considered to be 20, i.e., $\sum_{i=1}^{C} L_i = 20$. In this chapter, it is assumed that the number of paths in each cluster is the same. We studied scenarios with one and two extra bits thanks to IM. It is further assumed that, the number of clusters is four (i.e., $C = 4$), and the distance between central angles of two adjacent clusters is $\pi/5$. It is worth mentioning that, in each cluster, AoD/AoA are uniformly distributed in an interval with a length of $\pi/12$. Detailed information on AoD/AoA interval is provided in Table 2.1, which shows the range of angles in each cluster. In this chapter, unit transmit power is assumed; hence, signal to noise ratio is defined as $\mathrm{SNR} = \frac{1}{\sigma^2}$.

In this section, we provide BER comparison of the proposed CIM scheme with traditional mmWave communication while our system uses two-stage greedy-ML detector. Our motivation for designing this detector is the insufficient performance of the brute-force detector in terms of BER. Fig. 2.2 illustrates the performance of greedy-ML detector in comparison with brute-force detector. In a mmWave system,

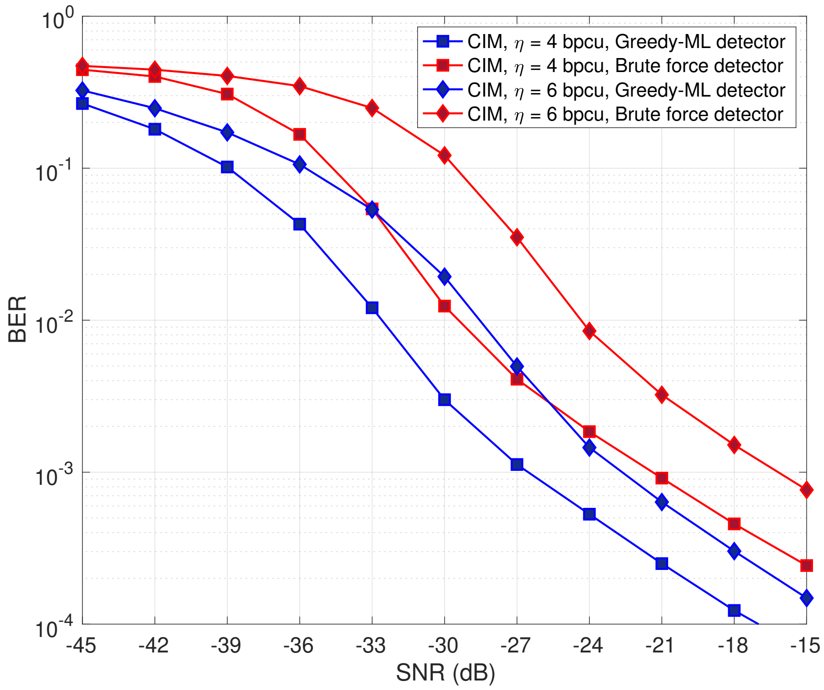

Figure 2.2: BER performance for greedy-ML detector (1 bit CIM)

Table 2.2: Simulation parameters

	CIM 1 extra bit	CIM 2 extra bits	Traditional communication
$\eta = 3$ bpcu	4-QAM	—	—
$\eta = 4$ bpcu	8-QAM	QPSK	16-QAM
$\eta = 5$ bpcu	16-QAM	8-QAM	—
$\eta = 6$ bpcu	32-QAM	16-QAM	64-QAM

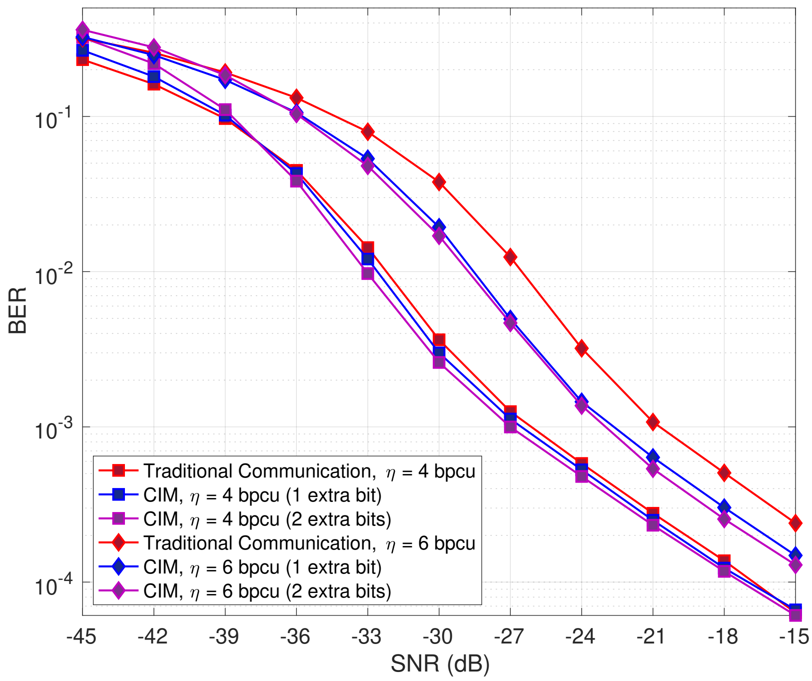

Figure 2.3: BER performance for analog architecture with greedy-ML detector

analog combiners at the receiver can result into different effective noises for each indexed cluster. This results into more errors in brute-force detector in comparison with greedy-ML detector. Let us assume a system with two indexed clusters, and cluster one is the correct cluster. Under these circumstances, if the effective noise of the first cluster is more powerful, the greedy-ML detector benefits from it, while the brute-force detector may not detect the symbol correctly. Fig. 2.3 depicts the superiority of the proposed scheme in comparison with traditional communication, wherein the system uses two-stage greedy-ML detector. The corresponding computer simulation configurations are provided in Table 2.2. It is noticeable that, in the traditional mmWave communication, one can transmit through the best path regarding path gain strength, without considering any IM. As shown in Fig. 2.3, computer simulations for 4 bpcu and 6 bpcu spectral efficiency have been provided. In each case, we compare traditional mmWave communication with one extra bit and two extra bits provided by the proposed scheme, i.e., CIM. As we can see,

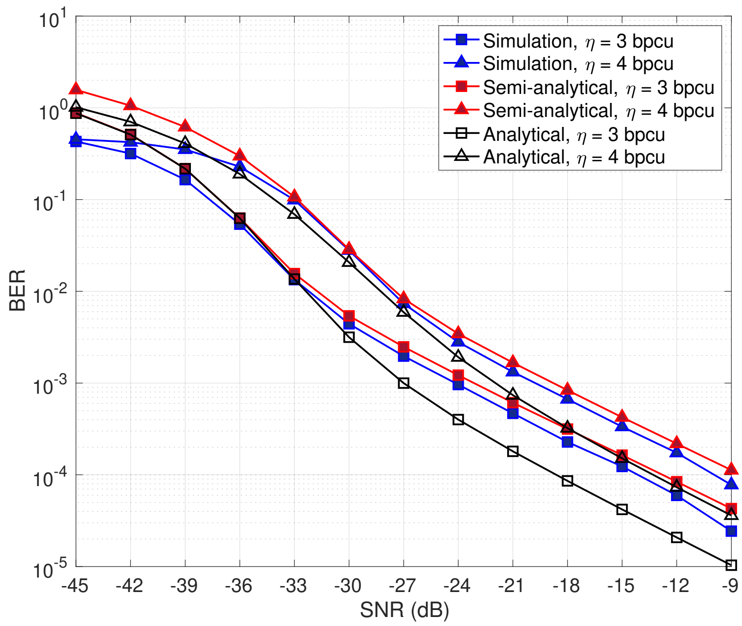

Figure 2.4: Theoretical and simulation performance comparison for the analog architecture

when we adopt our scheme to transmit one extra bit, the performance is better in comparison with traditional mmWave communication. We can improve the BER performance further by transmitting two extra bits. However, when we increase the spectral efficiency, BER increases as well. This is because with increasing spectral efficiency, the distance between M-ary constellation symbols, and the distance among indexed paths decreases; therefore, the receiver has more difficulty to resolve both conventional and spatial symbols.

Fig. 2.4 illustrates BER performance of the proposed scheme and derived theoretical bound on the BER. As shown in Fig. 2.4, our semi-analytical results behave as an upper bound on the computer simulation results and confirms their validity. Table 2.2 shows detailed information on the used M-ary constellations. In all cases one extra bit is modulated with CIM.

As aforementioned earlier, to have analytical results with Distribution Fitter, we have to obtain the PDF of random components in CPEP. We consider the random

Table 2.3: PDF approximation parameters

	ξ_X	s_X	μ_X	ξ_Y	s_Y	μ_Y
$\eta = 3$ bpcu	0.22	48776.2	107306	0.01	15226.8	29021.8
$\eta = 4$ bpcu	0.73	43470.9	55581.1	0.61	15326.2	17274.7

variables X and Y in (2.29) and (2.40), for two cases of $\hat{i} = i^*$ and $\hat{i} \neq i^*$, respectively. Distribution Fitter tool in MATLAB shows that X and Y can be approximated to have the generalized extreme value distribution with parameters described in Table 2.3. If a random variable Z has generalized extreme value, the PDF of Z can be calculated as follows ([42])

$$f_Z(z) = \frac{1}{s_Z}\left[\big(1+\xi_Z(\frac{z-\mu_Z}{s_Z})\big)^{-\frac{1}{\xi_z}}\right]^{\xi_Z+1} \exp\Bigg(-\big(1+\xi_Z(\frac{x-\mu_Z}{s_z})\big)^{-\frac{1}{\xi_Z}}\Bigg). \quad (2.56)$$

Therefore, UPEP can be calculated as in (2.31) and (2.42), for the case of $\hat{i} = i^*$ and $\hat{i} \neq i^*$, respectively. As the shape parameter is positive for all cases, i.e., $\xi_Z > 0$, we have to satisfy $z \geq \mu_Z - \frac{s_Z}{\xi_Z}$. On the hand, from (2.29) and (2.40), we have to have $z \geq 0$. These two constraints determines the lower bound of integrals given in (2.31) and (2.42). We calculate integral numerically with the upper bound of infinity using MATLAB. The results are shown in Fig.2.4. As we can see, the results are approximately match with simulation and semi-analytical results which confirms validity of our simulations. As an example, the outputs of Distribution Fitter tool for $\eta = 3$ bpcu are illustrated in Fig. 2.5.

2.4.2 Hybrid Beamforming Architecture

For this architecture, we assume the same parameters with the analog architecture. Fig. 2.6 shows the accuracy of our semi-analytical derivations. We consider scenarios with 3 and 4 bpcu spectral efficiency with 1 extra bit modulated by CIM. Table 2.2 shows detailed information at the selected M-ary constellation used for each case.

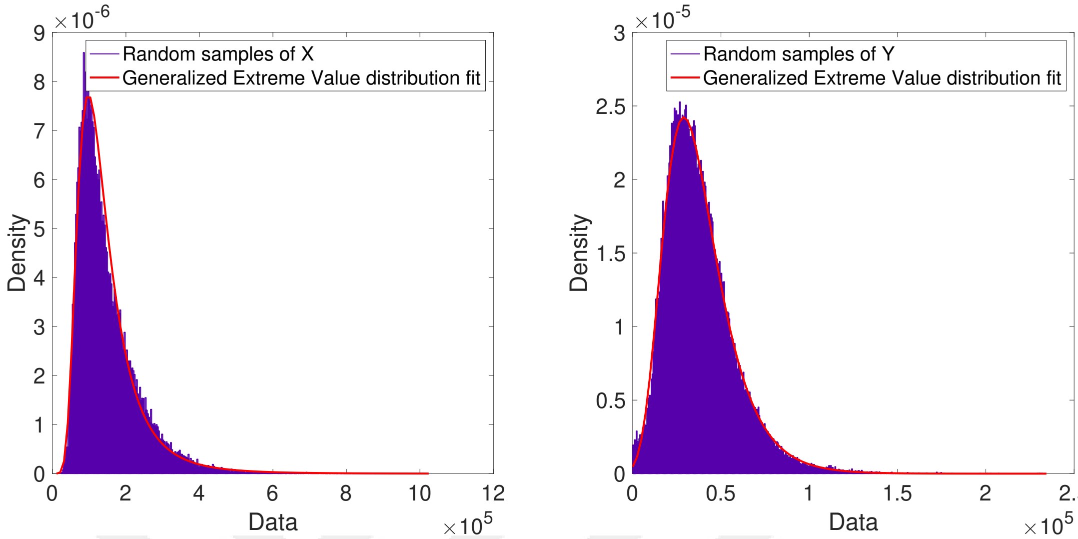

Figure 2.5: Distribution fit for variables X and Y

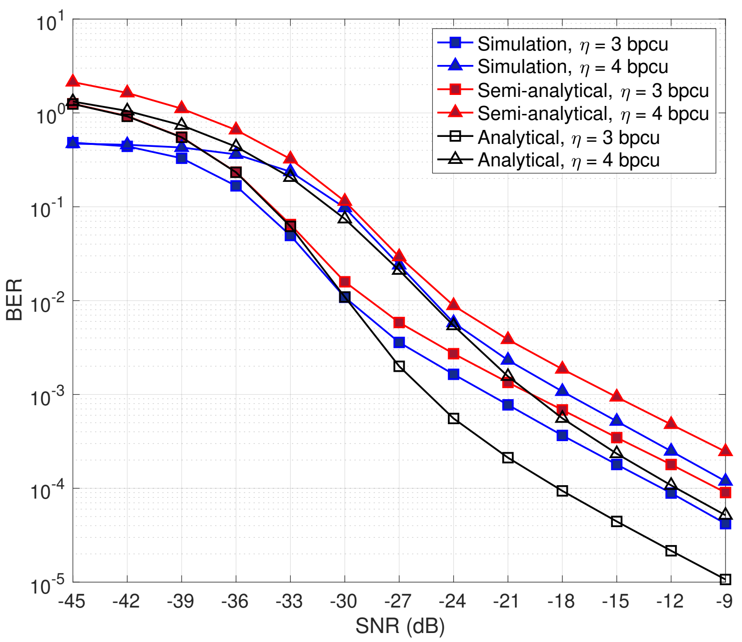

Figure 2.6: Theoretical and simulation performance comparison for hybrid architecture

Table 2.4: PDF approximation parameters for the hybrid architecture

	ξ_X	s_X	μ_X	ξ_Y	s_Y	μ_Y
$\eta = 3$ bpcu	0.12	26326.1	51460.8	-0.09	6184.42	13953.1
$\eta = 4$ bpcu	0.62	22473.4	27279.4	0.60	6910.19	8093.7

As we can see, the derived semi-analytical expressions provide an upper bound for the BER. To achieve analytical results, we need to obtain the PDF of random variables $\tilde{X}$ and $\tilde{Y}$ in (2.51) and (2.52), respectively. Distribution Fitter tool in MATLAB reveals that $\tilde{X}$ and $\tilde{Y}$ have generalized extreme value distribution with the PDF given in (2.56), and parameters described in Table 2.4. As depicted in Fig. 2.6, analytical results based on PDF derivation can provide an approximation on computer simulation results. It is noticeable that, when the shape factor is negative (i.e., $\xi_Z < 0$), we have to satisfy $z \in (-\infty, \mu_Z - \frac{s_Z}{\xi_Z}]$. On the other hand, (2.49) and (2.50) necessitate us to have $z \geq 0$. These two constraints determine the lower and upper bounds of the integrals given in (2.53) and (2.54).

In Fig. 2.7, we show the superiority of the proposed scheme in a hybrid architecture in comparison with BIM structure proposed in ([32]). In the BIM structure, the dominant paths have been selected for indexing purposes. However, correlation among indexed paths can increase the BER. Hence, in the proposed CIM structure, dominant paths have been selected from the well separated clusters to decrease correlation among them. Simulation results illustrate BER for the spectral efficiency of 4 bpcu with 2 bits IM. We provide computer simulations for both BIM and CIM with different number of paths distributed uniformly in four clusters. As illustrated in Fig.2.7, when there are 4 paths in the environment, the performance of two schemes are identical because there is only one path in each cluster. However, with increasing the number of paths, the performance of CIM increases significantly, while BIM performs worse. This is because in BIM, indexed paths can be selected

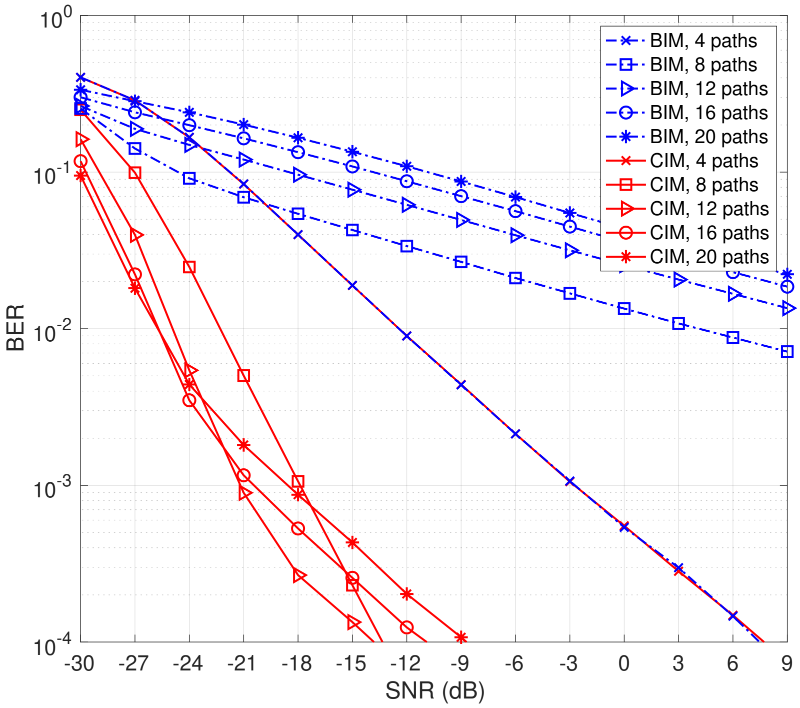

Figure 2.7: CIM and BIM performance comparison

from the same clusters which leverage the huge correlation on the selected paths, while CIM guarantees that selected paths are far enough to decrease the effect of inter-beam interference. However, the improvement in the performance of CIM is not permanent with increasing the number of paths, and after a specific number of paths, it decreases. This is because with increasing number of paths, the transmitted signal experiences leakage on the neighboring paths, which decreases the effective transmitted power in the selected path.

2.5 Conclusion

In this chapter, we have proposed a novel IM scheme for future mmWave communication systems, which takes into consideration well separated clusters for indexing purpose. With adopting these separated clusters, the indexed paths become near orthogonal; hence, the inter-beam interference, which is one of the biggest problems in the mmWave communication, decreases significantly. Furthermore, we have studied an architecture of hybrid precoder and considered a ZF precoder at the transmitter to further suppress the inter-beam interference. With such an architecture, we have assumed and studied the system in more realistic conditions. Computer simulation results reveal that CIM can perform better than traditional mmWave communication, and hybrid CIM performs better than BIM in terms of BER. We derived semi-analytical and analytical error probability expression for the proposed scheme, which have proven the superiority of our scheme. Our future work might focus on multi-user systems with randomly distributed clusters in the mmWave communication environments to study scenarios under more realistic circumstances.

Chapter 3

ANTENNA ARRAY STRUCTURES FOR ENHANCED CLUSETER INDEX MODULATION

3.1 Introduction

Millimeter-wave (mmWave) communications is a promising technology for future wireless communications due to its large spectrum availability, high bandwidth, and high data rate that can respond to the stringent demands of 6G communications. However, there are some challenges that mmWave communication encounters, e.g., severe path loss and attenuation, costly hardware equipment, and energy consumption. By exploiting the short wavelength of mmWave signals, we can pack large antenna arrays and utilize them in practical massive multiple-input multiple-output (mMIMO) communications systems. Large antenna arrays in mmWave systems compensate for the severe path loss by forming high directivity beams [43, 44]. Fully-digital beamforming (FDBF) is widely considered in conventional MIMO communications systems; however, it requires a power-hungry and expensive RF chain per antenna. Likewise, as the antenna array size increases, FDBF is not feasible for mMIMO systems due to the extremely high hardware cost/complexity [45]. Analog beamforming (ABF) has recently received significant attention in the literature to be adopted in mmWave mMIMO communications systems since it needs only a single RF chain to perform the beamforming for a large antenna array [45]. Nonetheless, implementing high-precision/coarsely-quantized[1] single phase shifters (SPS) per each RF chain-antenna pair is still needed in the analog network structure,

[1]High-precision phase shifters are assumed to obtain near-optimal performance; however, it might be impractical. On the other hand, practical phase shifters have coarsely quantized phases; but they still should be implemented in large numbers to support mMIMO [10].

which entails a costly and high energy consumption drawback in mmWave systems. A fixed phase shifter (FPS) structure is proposed in [10] to reduce the number of phase shifters with quantized phases. It is shown that only a few phase shifters are required to implement the FPS structure in the analog network.

Index modulation (IM) is a promising technique to use in mmWave communications due to its ability to decrease the cost and energy consumption by decreasing the number of radio-frequency (RF) chains and increasing the spectral efficiency by conveying additional information bits [12, 13, 46]. The spatial scattering modulation (SSM) method, which provides additional information transmission by indexing orthogonal paths, is investigated in [31, 47, 46]. However, SSM might be im- practical for most mmWave environments due to the orthogonality assumption among paths. More recently, we proposed cluster index modulation (CIM) in [48] for mmWave mMIMO communications systems to enhance system performance by transmitting additional bits through indexing spatial clusters in the sparse mmWave environment. It has been demonstrated in [48] that under practical circumstances of non-orthogonal paths, CIM performs better than SSM in terms of bit error rate (BER).

In a sparse mmWave environment, clusters are typically located at large distances from each other, making them more suitable for indexing than paths, e.g., SSM scheme. The larger difference in physical distance results in less correlation among indexed entities, i.e., clusters in the CIM scheme, enhancing error performance. Nevertheless, interference from non-intended indexed clusters, potentially located far from the target cluster, is still expected at the receiver. Since inter-cluster interference is the primary source of interference in the CIM scheme, reducing such interference is of great importance. Accordingly, it is essential to form narrow beams in the steering direction and reduce side lobes in the other spatial angles to improve the error performance. Most of the works in the literature investigated the effect of different array structures on spectral/energy efficiency and/or data rate [49, 50, 51, 6, 52, 53, 54]. It is indicated that various array structures show different behaviors under different communication systems; hence, the results of a study with a specific communication method cannot be extended here. Besides, the effect of different antenna arrays on BER is less studied in the literature. The aforementioned gaps motivate us to have a more detailed look at the behavior of newly introduced CIM-enabled mmWave communication systems with various antenna array structures that are more adopted in the literature [49, 50, 51, 6, 52, 53, 54].

In this chapter, we investigate the effect of various antenna array structures, i.e., uniform linear array (ULA), uniform rectangular array (URA), uniform circular array (UCA), and concentric circular array (CCA), which are more considered in the literature [49, 50, 51, 6, 52, 53, 54], on the error performance of the CIM-enabled mMIMO mmWave communications systems. More specifically, we study the radiation pattern characteristics of different antenna arrays and their effect on the system BER performance. We show that an efficient radiation pattern significantly influences the BER performance by reducing inter-cluster interference among the indexed clusters. We also reveal that a hardware-efficient (HE) analog network (beamformer/combiner) with a few FPSs can perform near the ideal analog networks when the studied antenna arrays are adopted. Adopting the HE structure reduces the cost and energy consumption significantly. To the best of our knowledge, the performance of different array structures on SSM/CIM-enabled mmWave communications systems with FPS analog networks has not been investigated in the existing literature.

The rest of this chapter is organized as follows. Section 3.2 illustrates the system model. Analog beamforming with different antenna array structures are discussed in Section 3.3. Illustrative results are presented in Section 3.4, and Section 3.5 concludes this work.

3.2 System Model

This section presents the system model of the considered mMIMO system with ABF in a sparse mmWave environment, as illustrated in Fig. 3.1. The number of antenna elements at the transmitter (Tx) and receiver (Rx) is assumed to be N_t and N_r, respectively. For ease of analysis, we consider a point-to-point scenario in

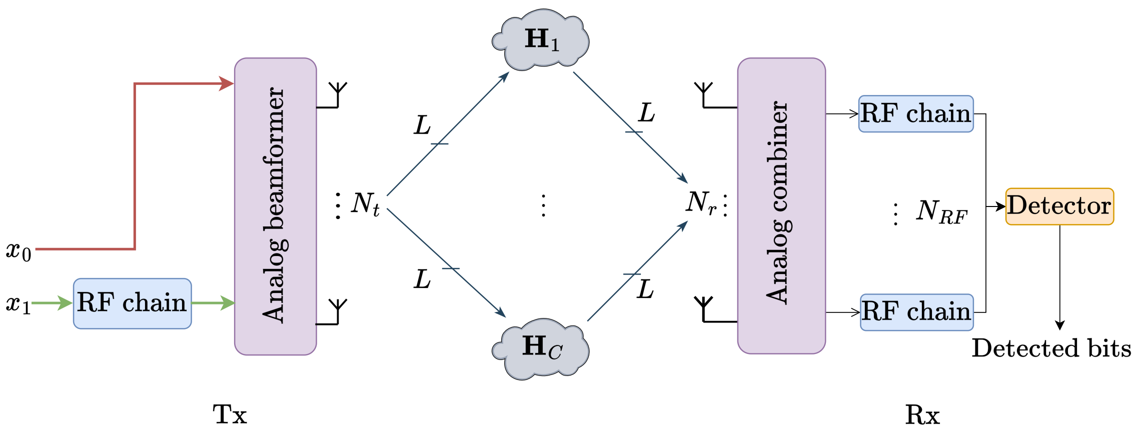

Figure 3.1: System model.

which only one RF chain is adopted at the Tx[2]. By considering mMIMO at both terminals as a back-haul link, there are N_{RF} RF chains at the Rx ($N_{RF} \ll N_r$) to form the receive beams toward the indexed clusters. Thanks to the CIM scheme, the Tx conveys an extra stream denoted by x_0 as spatial domain information without using an extra RF chain [55]. Due to the vulnerability of the mmWave signal to the blockage, we assume there is no line-of-sight (LoS) link between the Tx and the Rx [44]. Consequently, the transmission between them relies on non-line-of-sight (NLoS) channels, i.e., $\mathbf{H}_i \in \mathbb{C}^{N_r \times N_t}$, $i = 1, \ldots, C$, where C is the total number of clusters in the sparse environment. Besides, there are L paths within each cluster.

3.2.1 Channel model

We consider Saleh-Valenzuela (SV) channel model as follows [43, 44, 45, 7, 48]:

$$\mathbf{H} = \sqrt{\frac{N_t N_r}{CL}} \sum_{c=1}^{C} \sum_{l=1}^{L} \alpha_{c,l} \mathbf{a}_r(\varphi^r_{c,l}, \vartheta^r_{c,l}) \mathbf{a}_t^H(\varphi^t_{c,l}, \vartheta^t_{c,l}), \tag{3.1}$$

[2]This system model can be generalized to a multi-user/stream scenario with K users/streams; hence, at least K RF chains are needed at the Tx.

where $\alpha_{c,l}$ is the NLoS complex channel gain of the lth path in the cth cluster, $\mathbf{a}_t(.)$ and $\mathbf{a}_r(.)$ are transmit and receive array response vectors[3], respectively, $\varphi^t_{c,l}$ and $\vartheta^t_{c,l}$ are the azimuth and elevation angle-of-departure (AoD) at the Tx, respectively, $\varphi^r_{c,l}$ and $\vartheta^r_{c,l}$ are the azimuth and elevation angle-of-arrival (AoA) at the Rx, respectively. $\alpha_{c,l}$ follows complex Gaussian distribution with zero-mean and variance σ^2, i.e., $\alpha_{c,l} \sim \mathcal{CN}(0, \sigma^2)$, wherein $\sigma^2 = 10^{-0.1PL(d)}$. Notice that the path loss between the Tx and the Rx is shown by $PL(d)$, and d is the distance between the terminals. Each cluster is specified by its azimuth and elevation mean angles at Tx (Rx), i.e., $\varphi^t_m(\varphi^r_m)$ and $\vartheta^t_m(\vartheta^r_m)$, which are uniformly distributed[4]. Within each cluster, the paths are spread according to Laplacian distribution with associated azimuth/elevation mean angles and the angular spread of azimuth/elevation domains, i.e., $\sigma_{\varphi^t_m}, \sigma_{\vartheta^t_m}, \sigma_{\varphi^r_m}, \sigma_{\vartheta^r_m}$ [52, 26].

3.2.2 Signal model and cluster index modulation

The proposed system model transmits two information streams; x_0 is the CIM symbol including $\log_2(B)$ bits, and x_1 is the M-ary symbol including $\log_2(M)$ bits. Here M is the M-ary constellation order while B is the CIM codebook order. In other words, B ($B \leq N_{RF}$) is the number of indexed clusters. Accordingly, the spectral efficiency is $\eta = \log_2(B) + \log_2(M)$ bits per channel use (bpcu). The received signal $\mathbf{y} \in \mathbb{C}^{N_r \times 1}$ at the receive antenna array terminal is

$$\mathbf{y} = \sqrt{P} G_t G_r \mathbf{H} \mathbf{f} s + \mathbf{n}, \tag{3.2}$$

where $\mathbf{f} \in \mathbb{C}^{N_t \times 1}$ is the analog beamformer vector, s is the modulated symbol using the M-ary constellation, $\mathbf{n} \in \mathbb{C}^{N_r \times 1} \sim \mathcal{CN}(0, \sigma^2_N)$ is the additive noise component at the Rx with variance σ^2_N, P is the transmit power, and G_t (G_r) [43, 56] is the Tx (Rx) antenna array gain. The Rx forms multiple receive beams toward the indexed clusters by adopting multiple analog combiners in order to resolve the spatial CIM symbol, i.e., x_0, [31, 48]. Therefore, the received signal $\mathbf{z} \in \mathbb{C}^{B \times 1}$ after processing

[3]Section 3.3 defines the array response vector for each array structure.

[4]A uniform distribution with parameters β_1 and β_2 is shown as $\mathcal{U}(\beta_1, \beta_2)$.

by analog combiner block is obtained as

$$\mathbf{z} = \sqrt{P} G_t G_r \mathbf{W}^H \mathbf{H} \mathbf{f} s + \mathbf{W}^H \mathbf{n}, \tag{3.3}$$

where $\mathbf{W} = [\mathbf{w}_1, \ldots, \mathbf{w}_B] \in \mathbb{C}^{N_r \times B}$ is the analog combiner matrix block, with $\mathbf{w}_i \in \mathbb{C}^{N_r \times 1}$ being the analog combiner vector associated with the ith ($i = 1, \cdots B$) indexed cluster. A maximum-likelihood detector is adopted to jointly resolve the CIM and M-ary symbols as follows:

$$[\hat{c}, \hat{s}] = \arg\min_{c,s} \left| \mathbf{z}(c) - \sqrt{P} G_t G_r \mathbf{w}_c^H \mathbf{H} \mathbf{f} s \right|^2, \tag{3.4}$$

where the estimated CIM and M-ary symbols are shown as $\hat{c}$ and $\hat{s}$, respectively, and $\mathbf{z}(c)$ represents the cth element in the received signal vector $\mathbf{z}$.

Analog beamformer $\mathbf{f}$ is selected from a pre-defined CIM codebook according to the CIM symbol x_0. Once the CIM codebook is constructed, the analog combiner matrix block can be constructed accordingly[5]. In order to build a pre-defined codebook, each transmit array response vector associated with the corresponding indexed cluster is mapped to the corresponding CIM codeword. Hence, CIM codebook $\mathcal{B}$ includes B codewords that specify the directions of indexed clusters. In each cluster, the best effective path is considered to steer the beam toward it. The best effective path in the cth cluster is defined as follows:

$$p_c = \arg\max_{l=1,\ldots,L} |\mathbf{w}_{c,l}^H \mathbf{H} \mathbf{f}_{c,l}|^2, \ c = 1, \ldots, C, \tag{3.5}$$

where $\mathbf{f}_{c,l} \in \mathbb{C}^{N_t \times 1}$ and $\mathbf{w}_{c,l} \in \mathbb{C}^{N_r \times 1}$ are respectively the beamformer and combiner to steer the beam toward the lth path within the cth cluster, defined as follows:

$$\mathbf{f}_{c,l} = \mathbf{a}_t(\varphi_{c,l}^t, \vartheta_{c,l}^t), \tag{3.6}$$

$$\mathbf{w}_{c,l} = \mathbf{a}_r(\varphi_{c,l}^r, \vartheta_{c,l}^r). \tag{3.7}$$

[5]In this chapter, we assume that the channel state information (CSI) is perfectly known at the Tx and the Rx [57]. Therefore, all path gains, AoDs, and AoAs associated with the paths/clusters are available at the Tx and Rx.

Algorithm 1: $\mathcal{B}$ and $\mathbf{W}$ construction algorithm.

Input: $\mathbf{H}, \mathbf{a}(.)$

Output: $\mathcal{B}$, $\mathbf{W}$

Find the best effective path for each cluster using (3.5).

Construct vector $\mathcal{P} = \{p_1, \ldots, p_C\}$.

for $k \leftarrow 1$ *to* B **do**

  calculate kth codeword as $\mathbf{b}_k = \mathbf{f}_{b_k, p_{b_k}}$ via (3.6) and (3.8).

  calculate kth combiner as $\mathbf{w}_k = \mathbf{w}_{b_k, p_{b_k}}$ via (3.7) and (3.8).

  Update $\mathcal{P}$: $\mathcal{P} = \mathcal{P} - \{b_k\}$.

Construct CIM codebook: $\mathcal{B} = \{\mathbf{b}_1, \ldots, \mathbf{b}_B\}$.

Construct analog combiner: $\mathbf{W} = [\mathbf{w}_1, \ldots, \mathbf{w}_B]$.

Henceforth, we show the set of indexed clusters as $\mathcal{P} = \{p_1, \ldots, p_C\}$. Ultimately, each codeword of the CIM codebook is achieved consecutively as follows:

$$\mathbf{b} = \mathbf{f}_{b,p_b}, \quad b = \arg \max_{c=1,\ldots,C} |\mathbf{w}^H_{c,p_c} \mathbf{H} \mathbf{f}_{c,p_c}|^2, \tag{3.8}$$

where $\mathbf{b} \in \mathbb{C}^{N_t \times 1}$ is the CIM codeword. Algorithm 1 summarizes the instructions to construct $\mathcal{B}$ and $\mathbf{W}$.

3.3 Analog Beamforming with Different Array Structures

This section describes different array structures and corresponding antenna array response vectors. Afterward, we propose implementing an HE structure for the analog network to be adopted in the practical mmWave mMIMO systems.

3.3.1 Different antenna array structures

In [49, 51], it has been revealed that the proper array configuration effectively generates narrower beams. Here, besides narrower beams, reducing side lobes is also important. The general expression for the array response vector is [52]

$$\mathbf{a}(\omega^{az}, \omega^{el}) = \frac{1}{\sqrt{N}} [e^{j\mathbf{k}^T \mathbf{p}_0}, e^{j\mathbf{k}^T \mathbf{p}_1}, ..., e^{j\mathbf{k}^T \mathbf{p}_{N-1}}]^T, \tag{3.9}$$

where $\omega^{az} \in \{\varphi^t_{c,l}, \varphi^r_{c,l}\}(\omega^{el} \in \{\vartheta^t_{c,l}, \vartheta^r_{c,l}\})$ is the corresponding angle of azimuth (elevation), $N \in \{N_t, N_r\}$ is the total number of antenna elements, $\mathbf{p}_n$ specifies the location of nth antenna element, and $\mathbf{k}$ is the wave-number defined as [52]

$$\mathbf{k} = \frac{2\pi}{\lambda}\left[\sin(\omega^{el})\cos(\omega^{az}),\ \sin(\omega^{el})\sin(\omega^{az}),\ \cos(\omega^{el})\right]^T,$$

where λ is the signal wavelength. The vector $\mathbf{p}_n$ is unique for each structure and specifies the array geometry. The corresponding $\mathbf{p}_n$ for ULA, URA, UCA, and CCA are given as follows, respectively [52]:

$$\mathbf{p}_{n_z} = \left[0,\ 0,\ n_z d_z\right]^T, \tag{3.10}$$

$$\mathbf{p}_{n_x,n_y} = \left[n_x d_x,\ n_y d_y,\ 0\right]^T, \tag{3.11}$$

$$\mathbf{p}_{n_c} = R\left[\cos\omega^{az}_{n_c},\ \sin\omega^{az}_{n_c},\ 0\right]^T, \tag{3.12}$$

$$\mathbf{p}_{n_{c'},n_c} = R_{n_{c'}}\left[\cos\omega^{az}_{n_{c'},n_c},\ \sin\omega^{az}_{n_{c'},n_c},\ 0\right]^T, \tag{3.13}$$

where $0 \leq n_x \leq N_x - 1$, $0 \leq n_y \leq N_y - 1$, $0 \leq n_z \leq N_z - 1$ depict the location of antenna elements spanned on the x, y, z directions, respectively, $0 \leq n_c \leq N_c - 1$ is the location of antenna elements spanned on each circle of corresponding antenna structures; $1 \leq n_{c'} \leq N_{c'}$ is the $n_{c'}$th circle corresponding to CCA structure with radius $R_{n_{c'}}$; R is the antenna array radius in UCA structure; and d_x, d_y and d_z are the space between two adjacent antenna elements along x, y, and z direction, respectively. Furthermore, $\omega^{az}_{n_c}$ and $\omega^{az}_{n_{c'},n_c}$ are depicted in Figs. 3.2(c) and 3.2(d), respectively, and are defined as $\omega^{az}_{n_{c'},n_c} = \omega^{az}_{n_c} = \frac{2\pi n_c}{N_c}$. The geometries of the aforementioned array structures are depicted in Fig. 3.2.

3.3.2 Hardware-efficient analog network structure

In order to perform analog beamforming/combining to the intended direction, each RF chain is connected to the antenna array through a network of phase shifters at both terminals. In this chapter, we investigate two structures for the analog network, i.e., near-optimal (OP) single phase shifters (SPS) structure with high-resolution phase shifters (as shown in Fig. 3.3(a)) and HE fixed phase shifters (FPS)

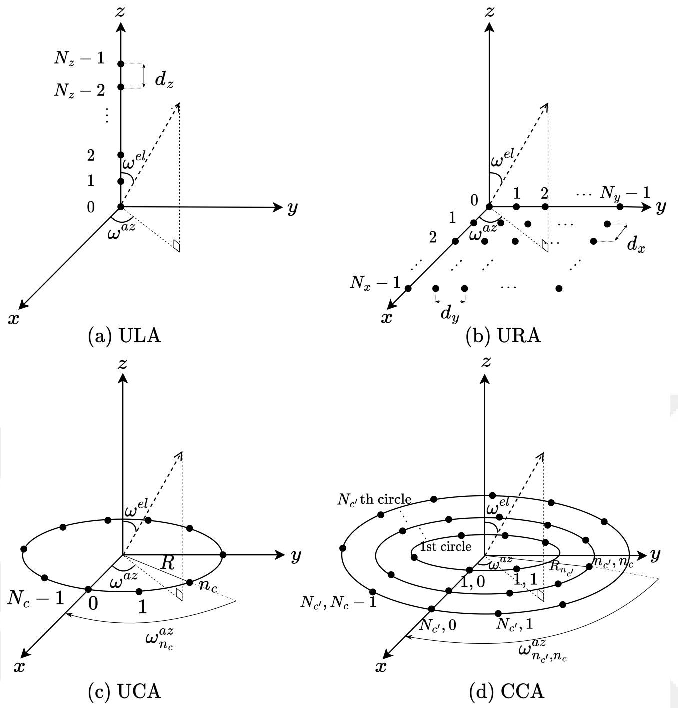

Figure 3.2: Different array geometries.

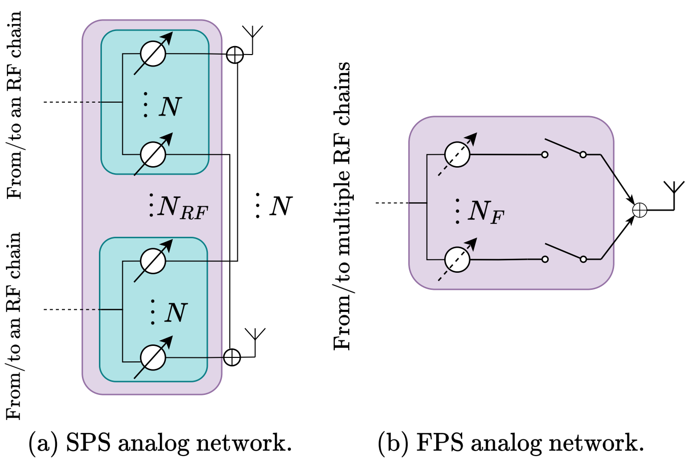

Figure 3.3: Analog network structures.

structure with fixed and quantized phase shifters (as given in Fig. 3.3(b)). The SPS structure is widely used in the literature to achieve near-optimal performance [43, 44, 45, 46, 31, 48, 52]; however, it requires implementing a phase shifter per each RF chain-antenna pair. In order to implement the OP analog network, the phase shifters should have high-precision resolution and match with the continuous phases of antenna array response vectors. Hence, (3.6) and (3.7) can be adopted as the beamformer and combiner, respectively.

In order to realize the HE analog network with a few numbers of phase shifters, the FPS structure is proposed in [10]. As depicted in Fig. 3.3(b), the number of adopted phase shifters is not dependent on the other parameters, i.e., the number of antenna elements and RF chains. Instead, a network of adaptive switches is implemented to provide dynamic connections between phase shifters and antenna elements. It is worth mentioning that Fig. 3.3(b) focuses on a single pair of RF chain-antenna to describe the FPS structure clearly. Therefore, for each RF chain-antenna pair, deploying N_F switches is required. Assume that we want to compose an analog beamformer/combiner to steer a beam toward the lth path of the cth cluster with antenna array response vector $\mathbf{a} = \frac{1}{\sqrt{N}}[e^{j\Theta_0}, e^{j\Theta_1}, \ldots, e^{j\Theta_{N-1}}]$, where Θ_i is the continuous phase corresponding to the ith antenna. The signal flow passes through the N_F fixed phase shifters and generates N_F signals with different phases. To compose the signal with an approximation of a certain phase, a subset of N_F signals can be combined by determining the statuses of N_F adaptive switches. The quantized phase of each RF chain-antenna pair can be expressed as follows:

$$\Omega = \mathbf{l}^T\mathbf{v}, \tag{3.14}$$

where $\mathbf{l}$ is the vector of switches status including N_F binary elements, and $\mathbf{v}$ is the FPS vector including N_F fixed phase shifters values. By adopting N_F FPSs, obtaining $N_F - 1$ bits resolution is possible if we define $\mathbf{v}$ as follows:

$$\mathbf{v} = \frac{2\pi}{2^{N_F-1}}[0, 2^0, 2^1, \ldots, 2^{N_F-2}]^T, \;\; N_F \geq 2. \tag{3.15}$$

Accordingly, adopting (3.14) allows the Tx/Rx to compose a desired quantized phase shift by combining appropriate FPSs. Therefore, the associated quantized beam-

Algorithm 2: Switch vector composition algorithm.

Input: Θ

Output: $\mathbf{l}$

Initialize $\mathbf{l}$ to zero vector (open all switches).

Wrap the phase shift Θ to 2π.

$t \leftarrow \Theta$.

$i \leftarrow \log_2 N_F + 2$.

while $i \neq 0$ **do**

  if $\mathbf{v}(i) \leq t$ **then**

    $\mathbf{l}(i) \leftarrow 1$ (close the ith switch).

    $t \leftarrow t - \mathbf{v}(i)$

  $i \leftarrow i - 1$.

former (combiner) can be obtained as $\mathbf{f} = \frac{1}{\sqrt{N}}[e^{j\Omega_0}, e^{j\Omega_1}, \ldots, e^{j\Omega_{N-1}}]$, where Ω_i is the quantized phase shift corresponding to the ith antenna element (quantized combiner can be composed similarly). Algorithm 2 states how to determine switches status to compose quantized phase shift Ω associated with Θ.

3.4 Illustrative Results

This section presents computer simulation results in terms of BER performance. Subsection 3.4.1 describes the simulation setup for a real-world deployment in New York City [4]. After that, we discuss BER performance regarding different array structures in subsection 3.4.2.

3.4.1 Simulation setup

We consider a dense urban area of New York City in which the distance between the Tx and Rx is large enough that LoS link is blocked, and the channel model is given as (3.1) [4]. Parameters of considered scenario in this section are given in Table 3.1. It is considered that both the Tx and the Rx are equipped with the

Table 3.1: Simulation setup parameters.

Parameter	**value**
Tx location	(25 m, 25 m, 9 m)
Rx location	(25 m, 175 m, 9 m)
σ_N^2 [44, 43]	-90 dBm
$G_t = G_r$ [56]	$4 + 10\log_{10}(\sqrt{N})$
a, b, σ_ξ [4]	72, 2.92, 8.7 dB
f_c [4]	28 GHz
$d_x = d_y$	$\lambda/2$
L, C [52, 26]	10, 8
N(Except URA)	82
N(Only URA)	9×9
R	$N\lambda/4\pi$
φ_m^t, φ_m^r	$\mathcal{U}[0, 2\pi)$
$\vartheta_m^t, \vartheta_m^r$	$\mathcal{U}[0, \pi)$
σ_ω [52, 26]	7.5°

same antenna geometry/size ($N = N_t = N_r$)[6]. Regarding ULA, URA, and UCA, the separation between antenna elements is $\frac{\lambda}{2}$; consequently, in the case of UCA, the radius of the antenna array is $R = \frac{N\lambda}{4\pi}$. For the CCA, the structure is slightly different because the antenna elements are not uniformly distributed. We assume a CCA structure with optimized ring spacing and number of elements in each ring as introduced in [58]. The radius and number of elements of the $n_{c'}$th ring is assumed to be $R_{n_{c'}} \in \{0.76\lambda, 1.36\lambda, 2.09\lambda, 2.99\lambda\}$ and $N_{n_{c'}} \in \{9, 17, 25, 31\}$, respectively [58]. With this type of structure, 82 antenna elements can be arranged in 4 rings. We define path loss in dB as follows [4]:

$$PL(d) = a + 10b\log_{10}(d) + \xi \text{ [dB]}, \tag{3.16}$$

[6]In this chapter, we investigate half-duplex (HD) link with the same array geometry in both terminals. In an HD scenario, a terminal is a transmitter at a specific time slot, while in the next time slot, it can receive data and serve as a receiver; hence, this assumption is reasonable. In a full-duplex (FD) scenario, we can adopt different array structure combinations at Tx/Rx.

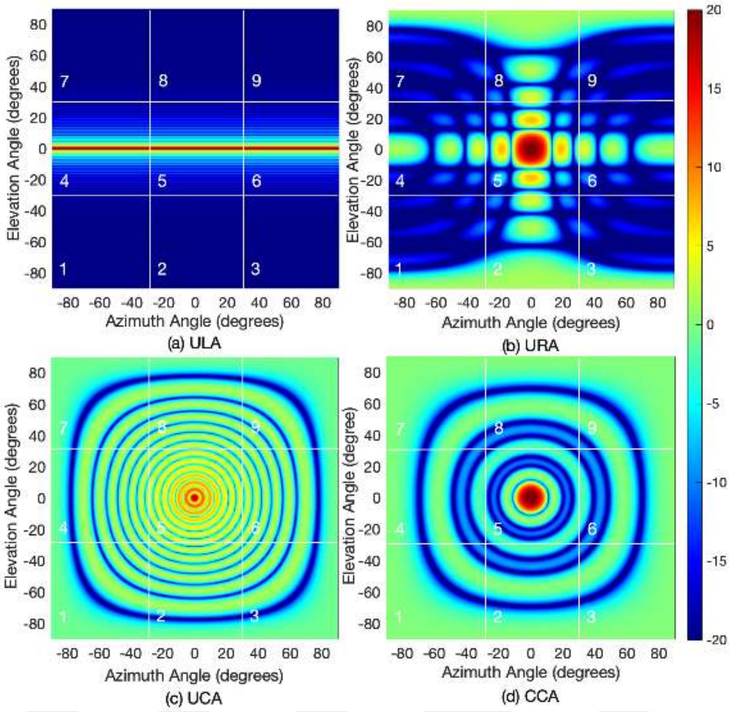

Figure 3.4: Antenna directivity patterns for different array architectures.

where ξ is the effect of large-scale shadow fading and it has a normal distribution with zero mean and standard deviation σ_ξ, i.e., $\xi \sim \mathcal{N}(0, \sigma_\xi^2)$.

3.4.2 BER Performance

This subsection demonstrates the BER comparison for different antenna array structures by presenting the Monte Carlo simulation results of BER performance. For the sake of analysis, we define a new radiation characteristic named side lobe directivity (SLD) which states the directivity of a side lobe emitted by an antenna array. Afterward, taking the geometrical mean of SLD gives us the average SLD (ASLD), which helps us to investigate the behavior of different array structures on a CIM-based system. Hence, we can define ASLD as ASLD $= \sqrt[m]{\prod_{i=1}^{m} \mathrm{SLD}}$, where m is the number of selected SLDs[7]. The following explains BER performance using array characteristics, i.e., directivity, HPBW, and ASLD. In order to have a detailed look

[7] m should be large enough to give us an acceptable measure of ASLD.

Table 3.2: Array characteristics for different array structures.

	Parameter	**Value**	
		Steered at 0° *Az;* 0° *El*	*Steered at* 15° *Az;* 30° *El*
ULA	*Directivity (dBi)*	19.14	19.14
	HPBW	360° Az; 1.24° El	360° Az; 1.28° El
	ASLD (dB)	−23.52	−18.94
URA	*Directivity (dBi)*	20.67	19.97
	HPBW	11.34° Az; 11.34° El	13.56° Az; 13.00° El
	ASLD (dB)	−16.52	−18.36
UCA	*Directivity (dBi)*	19.32	19.16
	HPBW	3.16° Az; 3.16° El	3.76° Az; 3.59° El
	ASLD (dB)	−3.90	−4.42
CCA	*Directivity (dBi)*	21.13	19.72
	HPBW	9.20° Az; 9.20° El	11.00° Az; 10.51° El
	ASLD (dB)	−5.91	−6.63

at the aforementioned array characteristics, we provide numerical values in Table 3.2 and the corresponding antenna array directivity patterns in Fig. 3.4.

Fig. 3.5 illustrates BER performance for two different signalings, i.e., (a) binary CIM (BCIM) with QPSK and (b) quadrature CIM (QCIM) with QPSK. As expected, BER improves from linear arrays to 2D arrays due to the ability of 2D arrays to illuminate azimuth and elevation dimensions simultaneously. Regarding 2D arrays, URA has the best BER performance. To explain this superiority, we notice the ASLD mentioned in Table 3.2. Among the 2D arrays, URA has provided significantly lower ASLD. At the Tx, lower side lobes result in less power leakage into the non-intended directions, which in turn reduces inter-cluster interference at the receiver. At the Rx, lower side lobes reduce collected interference from the non-intended indexed clusters. Fig. 3.4 illustrates the side lobes effect on the non-intended angles for different array structures.

To explain the effect of side lobes, let us give an example of the studied CIM system. First, we divide each pattern in Fig. 3.4 into 9 areas. Without loss of generality, let us assume the Tx is going to transmit a signal toward a cluster located

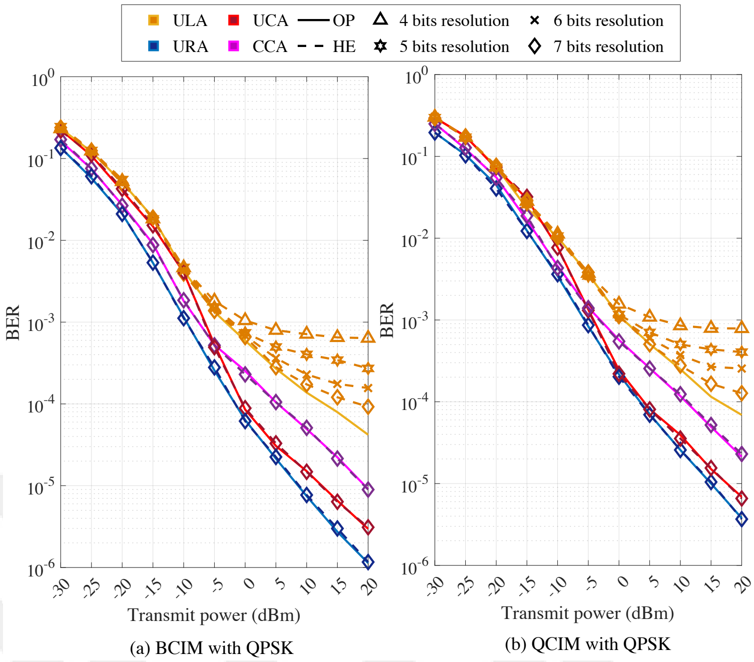

Figure 3.5: BER comparison of different array structures.

in origin; therefore, the main lobe emitted by the antenna array is steered toward the origin, as depicted in Fig. 3.4. Hereupon, we call area 5 as the intended area and all the other areas as interference areas. Under such circumstances, any power leakage (signal collection) to (from) the interference areas at the Tx (Rx) contributes to performance degradation by leveraging more inter-cluster interference. As is depicted in Fig. 3.4, UCA and CCA have higher side lobes directivity compared with URA in the interference areas. More specifically, URA has extremely low directivity side lobes in areas 1, 3, 7, and 9, i.e., lower than −15 dB, while this value for UCA and CCA is around 0 dB. Assume that the CIM algorithm indexes some clusters in the mentioned areas; hence, UCA and CCA entail more interference in the system compared with URA. This example explains the superiority of URA over UCA and CCA well.

In comparison between UCA and CCA, CCA performs better than UCA in low transmit powers. This behavior can be explained by comparing of directivity and ASLD between two arrays. As expressed in Table 3.2, CCA has higher directivity and less ASLD than the UCA, which has the dominant effect on the BER performance and results in better performance of CCA in low transmit powers. However, with increasing transmit power, UCA performs better, as illustrated in Fig. 3.5. Here, the effect of narrower beam width of UCA becomes dominant with increasing transmit power and causes better BER performance. As is provided in Table 3.2, the HPBW of UCA is approximately three times less than CCA.

HE analog network with implementing FPSs is adopted to reduce cost and energy consumption. As it is shown in Fig. 3.5, by adopting the HE structure with only 7 bits resolution, i.e., 8 quantized fixed phase shifters, we can achieve the same BER performance with OP structure for 2D antenna arrays. This is while, to implement OP analog network, we need to adopt N_t SPSs at the Tx and $N_{RF} \times N_r$ SPSs at the Rx. Knowing that each SPS costs around a hundred US dollars and consumes around 50 milliwatts of power shows the superiority of implementing the HE structure well [10]. When we increase the resolution bits, the HE BER performance can approach the OP structure more. We also depict the BER performance for different resolution bits, i.e., 4, 5, 6, and 7, for the ULA structure in Fig. 3.5. As is expected, the BER performance of the HE structure approaches the OP structure with increasing resolution bits (number of adopted FPSs). It is worth mentioning that BER performance has an error floor when the HE structure is adopted. However, increasing the resolution of the HE structure reduces the error floor because the detector can resolve the symbols more precisely.

3.5 Conclusion

This chapter has investigated the effect of different array structures on CIM-enabled mMIMO mmWave communications systems. We have studied the different array characteristics, i.e., directivity, HPBW, and ASLD, to show their effect on the BER performance of the CIM-enabled system. Our illustrative results revealed that URA has the best BER performance among its counterparts, thanks to the lower side lobes. It has been shown that the higher side lobes directivity results in stronger inter-cluster interference, which is detrimental to the CIM-based systems. We have also proposed an algorithm for the HE analog network to decrease cost and energy consumption significantly. It is shown that the HE structure can perform similarly to the OP structure by adopting a few numbers of FPS. As a potential direction for future work, an intelligent CIM algorithm can be designed to intelligently index clusters and limit the effect of inter-cluster interference by considering the antenna array directivity pattern.

Chapter 4

CLUSTER INDEX MODULATION FOR RECONFIGURABLE INTELLIGENT SURFACE-ASSISTED MMWAVE MASSIVE MIMO

4.1 Introduction

The intriguing applications of next-generation wireless networks demand more bandwidth, which is already scarce in the sub-6 GHz communication band [59]. A promising solution is adopting the millimeter wave (mmWave) band, which spans from 30 GHz to 300 GHz [59, 43]. On the other hand, mmWave signals suffer from high path loss and attenuation. Thanks to the short wavelength of mmWave signals, it is possible to pack a large antenna array and form a high directivity beam to compensate for the severe path loss [43, 44]. Nevertheless, high directivity beams are vulnerable to blockage, especially in a dense urban area or indoor environment. Reconfigurable intelligent surfaces (RISs) can be installed in the environment to handle the blockage problem and increase the coverage area by providing additional transmission paths [43, 44, 7, 14, 11]. Another problem encountered in mmWave transmission compared to sub-6 GHz systems is its higher hardware cost and power consumption [60, 9]. These drawbacks necessitate wireless researchers to consider intelligent and efficient schemes that decrease the cost and power consumption. Moreover, index modulation (IM) is considered a promising solution to obtain a lower hardware cost with a reduced number of radio-frequency (RF) chains and enhanced spectral efficiency performance by transmitting extra information bits [46, 12, 13]. In IM systems, additional information bits can be transmitted by indexing different building blocks such as antenna elements, subcarriers, paths, and clusters [46, 31, 48, 52].

4.1.1 Related works

RIS-empowered communication can be considered a promising technology to extend the coverage area in mmWave communication systems. The optimal placement for RIS implementation in mmWave systems has been investigated in [59, 61]. It is shown that an increased achievable rate is obtained when an RIS is located in the proximity of the transmitter or receiver due to the multiplicative path loss of the RIS-assisted path. The authors in [44] proposed a framework to extend the coverage area by adopting several RISs to assist communication from the base station to the single antenna user. Specifically, they proposed a joint active and passive precoding design to maximize the received signal power. By introducing such a scheme, the proposed RIS-assisted scheme in [44] can effectively increase the robustness of the mmWave system against blockage. In [43], the authors investigated a mmWave communication system that adopted large antenna arrays at both transmitter and receiver. An optimization problem is formulated to jointly adjust reflection coefficients at the RIS and the hybrid precoder/combiner at the transmitter/receiver to maximize spectral efficiency. Guo *et al.* study a power minimization problem in [60] by jointly optimizing digital and analog beamforming matrices at the transmitter and reflection coefficients at the RIS under a given signal-to-interference-plus-noise-ratio (SINR) constraint.

Spatial scattering modulation (SSM) is introduced in [31] by indexing a set of orthogonal paths in the mmWave environment. However, the authors assume that there is only one cluster in the environment in [31], this approach might be impractical for most the mmWave transmission environment. Another drawback of the SSM scheme is the orthogonality assumption among paths. Generalized SSM (GSSM) is also proposed in [47] by indexing a set of paths instead of a single path. Both works of [31] and [47] adopt linear arrays at the transmitter and receiver, which are not capable of resolving scattering paths in both azimuth and elevation directions. Moreover, in [46], the authors investigated a generalization three dimensions (3D) SSM scheme to facilitate the problem of path resolution in both azimuth and elevation dimensions. They also proposed a whitening filter to deal with correlated noises at the receiver. Against this background, the authors of the current work recently introduced cluster index modulation (CIM) in [48] in order to efficiently index the clusters in the environment. The well-known Saleh-Valenzuela channel model with multiple clusters is assumed in the CIM scheme, and scattering clusters in the environment are indexed instead of paths. It has been demonstrated in [48] that under non-orthogonal path conditions, SSM could not perform well because the paths are generally close to each other, which results in interference on the other indexed paths. Since there is a considerable physical distance between the clusters, indexing clusters is a more reasonable idea, and the superiority of CIM over SSM is shown in terms of bit error rate (BER) in [48].

More recently, [62] introduced a twin-RIS structure to perform a beam-index modulation scheme using two RISs between the terminals. The first RIS is located close to the transmitter, while the second one is close to the receiver. The reflecting elements on the second RIS are indexed for the IM purpose and reflect the received beam to the receiver. According to the IM symbol, the first RIS adjusts the phases of the received beam from the transmitter to ensure that only the target element on the second RIS receives the beam.

4.1.2 Motivations and contributions

The state-of-the-art of IM schemes in mmWave communications assumed orthogonality among paths when the array size is large [46, 31, 63, 47, 64]. Nonetheless, this orthogonality assumption is unrealistic, and in practice, there is a correlation among each couple of paths that is not ignorable for indexing paths [48]. In the realistic channel model, which includes correlation among paths, power leakage into undesired paths can result in interference, making IM detection more difficult. Hence, a practical IM scheme should be appropriately designed to prevent interference between the paths and even exploit this leakage to enhance the system performance. Although [48] demonstrates the superiority of the CIM scheme compared to traditional SSM, the performance of the CIM scheme under the situation that clusters are randomly distributed in both azimuth and elevation dimensions has not been studied before.

As we mentioned earlier, the mmWave channel is vulnerable to blockage due to the intrinsic characteristics of the mmWave signals. Adopting an RIS to the transmission can potentially combat this blockage problem [43, 44, 7, 14, 11]. Incorporating IM into RIS-assisted mmWave communications systems is also interesting due to its potential to enhance the coverage, energy efficiency, achievable rate performance, and to decrease the overall cost. From this point of view, an RIS-assisted mmWave communications system model should be designed delicately to make the IM effective. Accordingly, the location of terminals and the IM entities should be selected precisely. In the existing literature, there is a need for a comprehensive IM-based RIS-assisted scheme that considers all of these concerns.

Based on the aforementioned gaps and main motivation, our contributions in this chapter are summarized as follows:

- This chapter proposes an advanced CIM scheme by creating a synergy between the CIM scheme (introduced in [48]) and the RIS technology. The proposed scheme is investigated in a realistic propagation environment in the presence of inter-cluster interference. At the same time, the available clusters are distributed randomly in both azimuth and elevation directions by adopting two-dimensional (2D) antenna arrays at all terminals to demonstrate the effectiveness of the proposed scheme in real channel conditions. In the proposed beam-gain optimized cluster selection CIM (BGCS-CIM) scheme, instead of indexing paths, clusters are indexed; consequently, by selecting the best effective path associated with each cluster and by considering the spatial diversity gain of other paths within the indexed cluster, the effect of inter-cluster interference can be reduced to construct an efficient CIM codebook. It is also shown that the entire cascaded channel is effective in achieving the optimal codebook even though one of the cascaded channels is completely shared between all the indexed entities. Extensive computer simulations reveal that the BGCS-CIM scheme outperforms the existing benchmarks.

- We also integrate the CIM technique into an RIS-assisted transmission in mmWave massive MIMO systems to provide a virtual channel between the transmitter and receiver when the direct channel between them is blocked. For this purpose, we design a novel IM framework in which the clusters between the RIS and Rx get involved in the IM process. We also consider an outdoor scenario to make our analyses more practical.

- We consider a practical system model in which the channel between transmitter and RIS is line-of-sight (LOS), and the channel between the RIS and receiver is non-LOS (NLOS). In this proposed system model, we index clusters in the NLOS channel between the RIS and receiver to transmit extra information bits without adopting an extra RF chain. To the best of our knowledge, this system model for the RIS-assisted mmWave communication systems has not been studied before.

- We adopt a whitening transformation to perform decorrelation among the effective noises. Thanks to the whitening filter, the filtered noises corresponding to the different indexed clusters are independent; thus, we can constitute a joint probability density function (PDF) to calculate the conditional pairwise error probability (CPEP) in the case of erroneous cluster index detection. Therefore, we derive a closed-form expression for the average bit error rate (ABER) using the union upper bound. Our extensive computer simulations demonstrate the validity of the derived ABER expression by providing an upper bound to the simulation results.

The remainder of this chapter is organized as follows. Section 4.2 describes the system and channel model of a practical RIS-assisted mmWave massive MIMO. Then, ABER performance analysis is discussed in Section 4.3 to obtain a closed-form expression for the proposed scheme. In Section 4.4, we provide computer simulation results to validate the ABER performance of the proposed BGCS-CIM scheme and compare it with the available benchmarks. Finally, Section 4.5 concludes this work.

Table 4.1: List of frequently-used mathematical symbols.

$\mathbf{G}$	S-V channel between Tx and RIS
$\mathbf{R}$	S-V channel between RIS and Rx
N_i	Number of antenna elements at $i \in \{\text{Tx, Rx}\}$
N	Number of reflectors at RIS
G_t (G_r)	Transmitter (receiver) antenna array gain
C_i (L_i)	Number of clusters (paths), where $i \in \{G, R\}$
α (β)	Complex channel gain of $\mathbf{G}$ ($\mathbf{R}$)
ϕ^t (ϕ^r)	Azimuth angle of departure (arrival) associated with the RIS
θ^t (θ^r)	Elevation angle of departure (arrival) associated with the RIS
φ^t (φ^r)	Azimuth angle of departure (arrival) associated with the transmitter (receiver)
ϑ^t (ϑ^r)	Elevation angle of departure (arrival) associated with the transmitter (receiver)
$\mathbf{a}_i(.)$	Antenna array response associated with the $i \in \{\text{Tx, Rx}\}$.
$\mathbf{a}_{i,ris}(.)$	$i \in \{$ Transmit, Receive$\}$ antenna array response associated with the RIS
P	Transmit power
$\boldsymbol{\Psi}$	RIS phase shift matrix
$\mathbf{f_t}$	Analog beamformer vector at the Tx
$\mathbf{W}$	Analog combiner matrix
$\mathbf{y}$	Receive signal vector before combiner
$\mathbf{z}$	Receive signal vector after combiner
$\mathbf{z_F}$	Filtered receive signal with whitened noise
$\mathcal{B}$	CIM codebook
B	CIM codebook order

For improving the clarity, a list of frequently-used mathematical symbols and a list of acronyms are provided in Tables 4.1 and 4.2, respectively.

4.2 System Model

Fig. 4.1 shows the proposed system model of the RIS-assisted mmWave transmission. Here, the transmitter (Tx) and receiver (Rx) are equipped with N_t and N_r antenna elements, respectively. In the mmWave band, due to the high penetration loss, blockages/outages occur frequently [57]. Besides, it is shown that some corners

Table 4.2: List of acronyms.

IM	Index modulation
CIM	Cluster index modulation
SSM	Spatial scattering modulation
Tx	Transmitter
Rx	Receive
LOS	Line of sight
NLOS	Non-line of sight
RIS	Reconfigurable intelligence surface
BGCS	Beam-gain optimized cluster selection
InF	Inside factory
CSI	Channel state information
PEP	Pairwise error probability
CPEP	Conditional pairwise error probability
UPEP	Unconditional pairwise error probability
ABER	Average bit error rate
ZCA	Zero-phase components analysis
ULA	Uniform linear array
UPA	Uniform planar array

and holes are challenging to cover in outdoor environments [65]. Instead of implementing extra base stations, an RIS would be a cost-effective alternative to extend the communication range and cover such areas. Hence, in this chapter, it is assumed that the direct channel between the Tx and Rx is completely blocked [65, 43, 60, 9, 57, 66, 67, 59]. Thus, an RIS with N reconfigurable reflecting elements is implemented to assist the mmWave communication system. Due to the rank-deficiency of the cascaded channels and inherent characteristics of the mmWave signals [44], the Tx can only transmit a single stream. Hence, only one RF chain is available at the Tx, while $N_{RF}^{r} \ll N_r$ RF chains are available at the Rx. Thanks to the IM technique applied through clusters, the RIS can transmit an extra stream, i.e., the spatial domain information represented by x_0, without using an extra RF chain

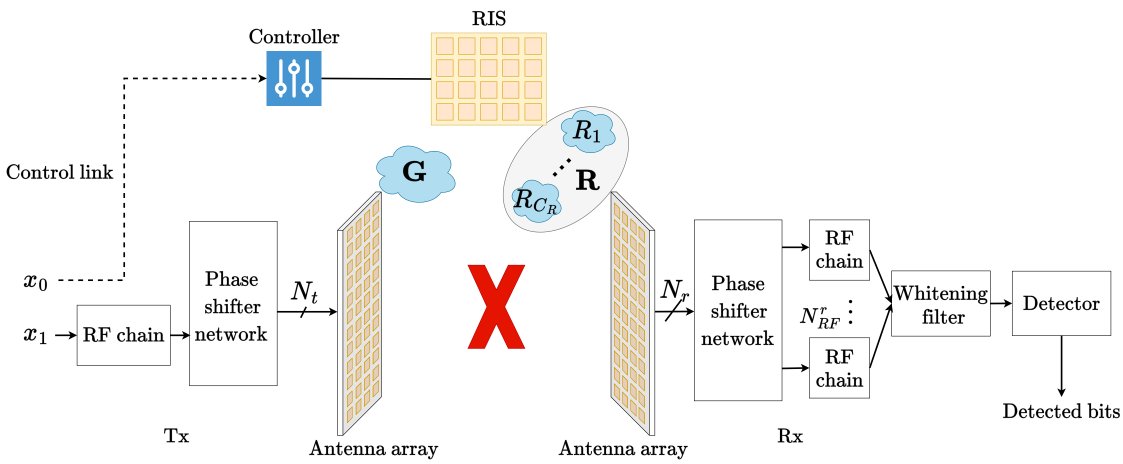

Figure 4.1: System Model.

[55][1]. Since the RF chain is a costly and energy-consuming component in a communication system, decreasing the number of RF chains saves tremendous cost and energy. $\mathbf{G} \in \mathbb{C}^{N \times N_t}$ is the channel between the Tx and RIS, and $\mathbf{R} \in \mathbb{C}^{N_r \times N}$ is the channel between the RIS and Rx. In [59] and [61], it is observed that the optimal placement for the RIS is the proximity of the Tx or Rx. In this chapter, it is assumed that RIS is located close to the Tx. Since the Tx has a fixed location, the RIS can be positioned in the sight of Tx; accordingly, there is a robust LOS link between the Tx and the RIS [44, 4]. On the other hand, the Rx is located far from the Tx; hence, due to the vulnerability of mmWave to blockage [44], we cannot guarantee a LOS link between the RIS and Rx. Therefore, assuming a NLOS dominant channel between the RIS and Rx is more reasonable[2][4].

---

[1]The proposed system model can be generalized for adopting K RISs; consequently, the transmitter and the RIS can transmit $2K$ streams by adopting only K RF chains.

[2]As illustrated in [4], in a dense urban area when the carrier frequency is 28 GHz, for distances less than 25 m, the channel is almost LOS-dominant, while for distances more than 100 m, the channel is NLOS-dominant with probability more than 80%.

4.2.1 Channel model

In this chapter, we adopt the well-known Saleh-Valenzuela (S-V) channel model for mmWave communication systems as follows [43, 44, 7, 60]:

$$\mathbf{G} = \alpha_0 \mathbf{a}_{r,ris}(\phi_0^r, \theta_0^r)\mathbf{a}_t^H(\varphi_0^t, \vartheta_0^t), \tag{4.1}$$

$$\mathbf{R} = \sqrt{\frac{NN_r}{C_R L_R}} \sum_{c=1}^{C_R} \sum_{l=1}^{L_R} \beta_{c,l} \mathbf{a}_r(\varphi_{c,l}^r, \vartheta_{c,l}^r)\mathbf{a}_{t,ris}^H(\phi_{c,l}^t, \theta_{c,l}^t), \tag{4.2}$$

where C_R is the number of clusters, and L_R is the number of paths in each cluster in the channel $\mathbf{R}$. The complex channel gain for the lth path within the cth cluster of channel $\mathbf{R}$ is represented by $\beta_{c,l} \sim \mathcal{CN}(0, 10^{-0.1PL(d)})$, wherein $PL(d)$ is the corresponding path loss dependent to the distance between two associated terminals, i.e., d, $\varphi_{c,l}^t(\varphi_{c,l}^r)$ and $\vartheta_{c,l}^t(\vartheta_{c,l}^r)$ are the azimuth and elevation angles of departure (arrival) of the Tx (Rx), and $\phi_{c,l}^t(\phi_{c,l}^r)$ and $\theta_{c,l}^t(\theta_{c,l}^r)$ are the azimuth and elevation angles of departure (arrival) associated with the RIS. α_0 stands for the complex channel gain of the LOS path of channel $\mathbf{G}$. Moreover, $\mathbf{a}_t(.)$ and $\mathbf{a}_r(.)$ represent the array response vectors associated with the Tx and Rx, respectively; $\mathbf{a}_{t,ris}(.)$ and $\mathbf{a}_{r,ris}(.)$ show the transmit and receive array response vector associated with the RIS, respectively. In this chapter, we adopt uniform planar array (UPA) at all terminals (i.e., Tx, Rx, and RIS); therefore, the normalized antenna array response in each terminal with azimuth angle ω^{az} and elevation angle ω^{el} is expressed as follows [52, 68]:

$$\mathbf{a}(\omega^{az}, \omega^{el}) = \frac{1}{\sqrt{N_a}}[1, e^{j\mathbf{k}^T\mathbf{p}_1}, e^{j\mathbf{k}^T\mathbf{p}_2} ..., e^{j\mathbf{k}^T\mathbf{p}_{N_a-1}}]^T, \tag{4.3}$$

where $N_a = N_x \times N_y$ is the total number of antenna elements/reflectors; N_x is the number of antenna elements/reflectors in x-axis, and N_y is the number of antenna elements/reflectors in y-axis; $\mathbf{p}_n$ specifies the location of nth antenna element/reflector, and $\mathbf{k}$ is the wave-number defined as [52]:

$$\mathbf{k} = \frac{2\pi}{\lambda}\Big[\sin(\omega^{el})\cos(\omega^{az}),\ \sin(\omega^{el})\sin(\omega^{az})\Big]^T, \tag{4.4}$$

$$\mathbf{p}_{n_x,n_y} = \Big[n_x d_x,\ n_y d_y\Big]^T, \tag{4.5}$$

where λ is the wavelength, $0 \leq n_x \leq N_x - 1$, and $0 \leq n_y \leq N_y - 1$ denote the location of antenna elements/reflectors; d_x and d_y are the separation between two adjacent antenna elements/reflectors along x and y direction, respectively.

4.2.2 Signal model

As illustrated in Fig. 4.1, the incoming bits constitute two information streams; x_0 is CIM symbol, while x_1 is modulated using M-ary constellation. Accordingly, the total spectral efficiency is $\eta = \log_2 M + \log_2 B$ bits per channel use (bpcu), where B is the CIM codebook order. The M-ary constellation symbol s is transmitted to the RIS through the wireless channel $\mathbf{G}$. Besides, the Tx maps each CIM symbol into a phase vector from a pre-defined CIM codebook, i.e., $\mathcal{B} \in [\mathbf{b}_1, \ldots, \mathbf{b}_B] \in \mathbb{C}^{N \times B}$, which is defined in Section 4.2.3. Each phase vector $\mathbf{b}_i$ represents a specific direction associated with a specific cluster. Afterward, based on the CIM bits and with the help of a smart controller [43, 44, 7], the corresponding phase vector will be sent to the RIS to adjust the phases of the received signal at each element of the RIS [62]. In other words, the RIS is exploited as a beamformer to reflect the signal passively over a specific cluster in the mmWave channel [62]. Denoting ψ_i as the phase shift associated with the ith passive element of the RIS, the RIS phase shift matrix associated with vector $\mathbf{b}$, i.e., $\mathbf{\Psi_b} \in \mathbb{C}^{N \times N}$, is defined as:

$$\mathbf{\Psi_b} \triangleq \mathrm{diag}(e^{j\psi_1}, \ldots, e^{j\psi_N}) = \mathrm{diag}(\mathbf{b}), \tag{4.6}$$

where $\mathbf{b} \in \mathcal{B}$ is the codeword corresponding to the transmitted CIM symbol. For the notation simplicity, we represent the effective channel associated with vector $\mathbf{b}$ as $\mathbf{H}^{\mathbf{b}}_{\mathbf{eff}} = G_t G_r \mathbf{R} \mathbf{\Psi_b} \mathbf{G}$, where G_t and G_r are the transmitter and receiver antenna gains, respectively. The received signal at the Rx can be expressed as:

$$\mathbf{y} = \sqrt{P} \mathbf{H}^{\mathbf{b}}_{\mathbf{eff}} \mathbf{f}_t s + \mathbf{n}, \tag{4.7}$$

where $\mathbf{n} \in \mathbb{C}^{N_r \times 1} \sim \mathcal{CN}(0, \sigma^2)$ is the additive noise component at the Rx, $\mathbf{f}_t \in \mathbb{C}^{N_t \times 1}$ is the analog beamformer at the Tx, and P is the transmit power. The Tx transmits the signal through the LOS path due to its dominance in channel $\mathbf{G}$; thus, we can consider $\mathbf{f}_t = \mathbf{a}_t(\varphi_0^t, \vartheta_0^t)$. In this chapter, we assume that the perfect channel state information (CSI) is available [43, 44, 60]. More specifically, channel estimation for the RIS-assisted mmWave systems is discussed in [57][3], [67, 66]. The received signal $\mathbf{z} \in \mathbb{C}^{B\times 1}$ after applying analog combiner is given as:

$$\mathbf{z} = \sqrt{P}\mathbf{W}^H \mathbf{H}_{\mathbf{eff}}^{\mathbf{b}} \mathbf{f}_t s + \mathbf{W}^H \mathbf{n}, \tag{4.8}$$

where $\mathbf{W} = [\mathbf{w}_1, \ldots, \mathbf{w}_B] \in \mathbb{C}^{N_r\times B}$ is the analog combiner matrix wherein $\mathbf{w}_i \in \mathbb{C}^{N_r\times 1}$ is the analog combiner vector associated with the ith indexed cluster. Section 4.2.3 discusses the method to determine $\mathbf{W}$.

It is important to note that even though $\mathbf{n}$ is a white noise vector, the effective noise $\mathbf{W}^H\mathbf{n}$ is colored; consequently, the effective noises of different clusters are correlated. To derive a closed-form expression for CPEP in Section 4.3, we need to whiten the effective noise through a whitening filter[4].

Lemma 1. *The whitening filter for the proposed system can be obtained as follows:*

$$\mathbf{B} = \mathbf{P}^{-\frac{1}{2}}\mathbf{V}^{-\frac{1}{2}}, \tag{4.9}$$

where $\mathbf{P}$ and $\mathbf{V}$ are the correlation matrix and diagonal variance matrix corresponding to the effective noise $\mathbf{W}^H\mathbf{n}$, respectively.

Proof. Please see Appendix A.1. □

Hence, by applying whitening filter to the received signal $\mathbf{z}$, the filtered signal $\mathbf{z}_{\mathbf{F}} \in \mathbb{C}^{B\times 1}$ is as:

$$\mathbf{z}_{\mathbf{F}} = \sqrt{P}\mathbf{F}_r^H \mathbf{H}_{\mathbf{eff}}^{\mathbf{b}} \mathbf{f}_t s + \mathbf{F}_r^H \mathbf{n}. \tag{4.10}$$

[3]Authors in [57] proposed a low-complexity channel estimation using semi-passive RIS. In this algorithm, few simplified receiver units with only 1-bit quantization at the RIS are randomly connected to a small fraction of reflectors; therefore, the RIS actively gets involved in the channel estimation procedure.

[4]It is worth mentioning that the designed pre-whitening filter whitens the effective noises for theoretical derivations. Accordingly, the whitening process does not get involved in the codebook construction procedure.

where $\mathbf{F}_r = \mathbf{W}\mathbf{B}^H = [\mathbf{f}_{r,1}, \ldots, \mathbf{f}_{r,B}]$. We adopt maximum-likelihood (ML) detector to resolve the transmitted symbols from the received filtered signal as follows[5]:

$$[\hat{c}, \hat{s}] = \arg\min_{c,s} \left| \mathbf{z}_{\mathbf{F}}(c) - \sqrt{P}\mathbf{f}_{r,c}^H \mathbf{H}_{\mathbf{eff}}^{\mathbf{b}} \mathbf{f}_t s \right|^2, \tag{4.11}$$

where $\hat{c}$ and $\hat{s}$ are the estimated CIM and M-ary symbols, respectively; and $\mathbf{z}_{\mathbf{F}}(c)$ is the cth element in $\mathbf{z}_{\mathbf{F}}$.

4.2.3 Constructing CIM codebook and analog combiner

This subsection presents a scheme for constructing CIM codebook, i.e., $\mathcal{B}$, and analog combiner, i.e., $\mathbf{W}$, for the RIS-assisted mmWave communication systems. Let us define the effective path gain of the vth path in the uth cluster as follows:

$$\mathcal{G}_{u,v} = \frac{\sqrt{P}G_t G_r}{\sqrt{N}} \mathbf{a}_r^H(\varphi_{u,v}^r, \vartheta_{u,v}^r) \mathbf{R} \,\mathrm{diag}(\mathbf{a}_{t,ris}(\phi_{u,v}^t, \theta_{u,v}^t)) \mathbf{G}\mathbf{f}_t. \tag{4.12}$$

We assume each cluster is represented by the best effective path as follows:

$$p_c = \arg\max_{i=1,\ldots,L_R} |\mathcal{G}_{c,i}|^2, \tag{4.13}$$

where $p_c, c = 1, \ldots, C_R$, is the best path index in the cth cluster. Henceforth, we show the set of all clusters with their representative path as $\mathcal{P} = \{p_1, \ldots, p_{C_R}\}$.

Thereupon, the BGCS-CIM scheme constructs the CIM-codebook consecutively by adopting the following criteria:

$$b = \arg\max_{i=1,\ldots,C_R} |\mathcal{G}_{i,p_i}|^2. \tag{4.14}$$

Notice that b gives the best choice among all possible options of the corresponding scheme. To construct the CIM codebook, we need to choose B out of C_R clusters for indexing. It is worth noting that the codewords carry the information to adjust RIS phase shifts. The Tx should select a codeword according to the CIM symbol

[5] It is worth mentioning that although the ML detector is the best option in terms of BER-vs-transmitted power performance, it leads to a high-complexity receiver. In order to decrease the detector's complexity, sub-optimal detectors should be designed by considering different use cases of the CIM scheme, which is beyond the scope of this thesis and is left for future works.

Algorithm 3: CIM codebook and analog combiner construction algorithm according to the BGCS-CIM scheme.

Input: $\mathbf{R}, \mathbf{G}, \mathbf{f}_t, \phi, \theta, \varphi, \vartheta, \mathbf{a}(.)$

Output: $\mathcal{B}$

```
Calculate the effective path gain for all paths using (4.12).
Find the best effective path for each cluster using (4.13).
Construct CIM codeword index candidates: P = {p_1, ..., p_{C_R}}.
for k ← 1 to B do
    Calculate the best cluster b_k among P by adopting BGCS-CIM scheme in (4.14).
    calculate kth codeword using b_k = a_{t,ris}(φ^t_{b_k,p_{b_k}}, θ^t_{b_k,p_{b_k}}).
    calculate kth combiner vector using w_k = a_r(φ^r_{b_k,p_{b_k}}, ϑ^r_{b_k,p_{b_k}}).
    Update P: P = P − {b_k}.
Construct CIM codebook: B = {b_1, ..., b_B}.
Construct analog combiner: W = [w_1, ..., w_B].
```

---

and transfer it to the RIS through the control link. Finally, analog combiner vector associated with ith indexed cluster can be determined as $\mathbf{w}_i = \mathbf{a}_r(\varphi^r_{i,p_i}, \vartheta^r_{i,p_i})$. Algorithm 3 presents the CIM codebook and analog combiner construction procedure according to the BGCS-CIM scheme[6].

4.3 ABER Performance Analysis

In this section we derive a closed-form expression for the upper bound on ABER to validate performance of the proposed system. The upper bound on ABER can be stated as:

$$\text{ABER} \leq \frac{1}{\eta M B} \sum_{c^*, s^*} \sum_{\hat{c}, \hat{s}} E_b(\{c^*, s^*\} \rightarrow \{\hat{c}, \hat{s}\})\text{UPEP}, \tag{4.15}$$

---

[6] The primary purpose of the BGCS-CIM algorithm is to index the clusters in an RIS-assisted mmWave system and reduce the interference among the indexed entities. The correlation among paths and clusters is an inseparable characteristic of the mmWave channel. Nevertheless, the essential point is exploiting them concurrently while decreasing the entailed interference. BGCS-CIM proposes an algorithm to reduce this interference in the analog stage without involving a baseband process.

where $E_b(\{c^*, s^*\} \rightarrow \{\hat{c}, \hat{s}\})$ is the total number of erroneous bits of both M-ary and CIM symbols, and UPEP is the unconditional pairwise error probability. To obtain the upper bound, we first state the CPEP as follows:

$$\begin{aligned} \mathbb{P}(\{c^*, s^*\} \rightarrow \{\hat{c}, \hat{s}\} | \alpha_0, \beta_{1,1}, \ldots, \beta_{C_R,L_R}) &= \mathbb{P}(|\mathbf{z_F}(c^*) \\ - \sqrt{P}\mathbf{f}_{r,c^*}^H \mathbf{H}_{\mathbf{eff}}^{\mathbf{b}^*} \mathbf{f}_t s^*|^2 &> |\mathbf{z_F}(\hat{c}) - \sqrt{P}\mathbf{f}_{r,\hat{c}}^H \mathbf{H}_{\mathbf{eff}}^{\hat{\mathbf{b}}} \mathbf{f}_t \hat{s}|^2), \end{aligned} \tag{4.16}$$

where $(.)^*$ and $\hat{(.)}$ depict the transmitted and detected symbols, respectively. By substituting $\mathbf{z_F}(c^*)$ from (4.10) into (4.16), we can rewrite the CPEP expression as:

$$\mathbb{P}(\{c^*, s^*\} \rightarrow \{\hat{c}, \hat{s}\} | \alpha_0, \beta_{1,1}, \ldots, \beta_{C_R,L_R}) = \mathbb{P}(|\mathbf{f}_{r,c^*}^H \mathbf{n}|^2 > |\mathbf{z_F}(\hat{c}) - \sqrt{P}\mathbf{f}_{r,\hat{c}}^H \mathbf{H}_{\mathbf{eff}}^{\hat{\mathbf{b}}} \mathbf{f}_t \hat{s}|^2). \tag{4.17}$$

In the following, we consider two cases of correct cluster index detection, i.e., $\hat{c} = c^*$, and erroneous cluster index detection, i.e., $\hat{c} \neq c^*$.

4.3.1 Correct Cluster Index Detection $\hat{c} = c^*$

In the case of correct cluster index detection, we assume that the detector resolves the CIM symbol correctly; hence, the error comes from the M-ary symbol. To obtain the CPEP expression for this case, (4.17) can be updated as:

$$\begin{aligned} &\mathbb{P}(\{c^*, s^*\} \rightarrow \{c^*, \hat{s}\} | \alpha_0, \beta_{1,1}, \ldots, \beta_{C_R,L_R}) \\ &= \mathbb{P}(|\mathbf{f}_{r,c^*}^H \mathbf{n}|^2 > |\mathbf{f}_{r,c^*}^H \mathbf{n} + \sqrt{P}\mathbf{f}_{r,c^*}^H \mathbf{H}_{\mathbf{eff}}^{\mathbf{b}^*} \mathbf{f}_t (s^* - \hat{s})|^2). \end{aligned} \tag{4.18}$$

Lemma 2. *In the case of correct cluster index detection, the analytical expression for* UPEP *is as follows:*

$$\mathbb{P}(\{c^*,s^*\} \rightarrow \{c^*, \hat{s}\}) = \mathbb{E}\Bigg[Q\Bigg(\frac{|\mathbf{f}_{r,c^*}^H \mathbf{H}_{\mathbf{eff}}^{\mathbf{b}^*} \mathbf{f}_t (s^* - \hat{s})|^2}{\sqrt{2}\sigma ||\mathbf{f}_{r,c^*} \mathbf{f}_{r,c^*}^H \mathbf{H}_{\mathbf{eff}}^{\mathbf{b}^*} \mathbf{f}_t (s^* - \hat{s})||}\Bigg)\Bigg]. \tag{4.19}$$

Proof. Please see Appendix A.2. □

4.3.2 Erroneous Cluster Index Detection $\hat{c} \neq c^*$

When the detector resolves the CIM symbol erroneously, error can propagate to the M-ary symbol. In this case, (4.17) can be rewritten as follows:

$$\begin{aligned}\mathbb{P}(\{c^*, s^*\} \to \{\hat{c}, \hat{s}\}|\alpha_0, \beta_{1,1}, \ldots, \beta_{C_R,L_R}) = \mathbb{P}(|\mathbf{f}_{r,c^*}^H \mathbf{n}|^2 \\ - |\mathbf{f}_{r,\hat{c}}^H \mathbf{n} + \sqrt{P}\mathbf{f}_{r,\hat{c}}^H (\mathbf{H}_{\mathbf{eff}}^{\mathbf{b}^*} s^* - \mathbf{H}_{\mathbf{eff}}^{\hat{\mathbf{b}}} \hat{s})\mathbf{f}_t|^2 > 0).\end{aligned} \tag{4.20}$$

Lemma 3. *In the case of erroneous cluster index detection, the analytical expression for* UPEP *can be obtained as:*

$$\mathbb{P}(\{c^*, s^*\} \to \{\hat{c}, \hat{s}\}) = \mathbb{E}\left[\frac{1}{2}\exp\left(-\frac{|\sqrt{P}\mathbf{f}_{r,\hat{c}}^H (\mathbf{H}_{\mathbf{eff}}^{\mathbf{b}^*} s^* - \mathbf{H}_{\mathbf{eff}}^{\hat{\mathbf{b}}} \hat{s})\mathbf{f}_t|^2}{2\sigma^2}\right)\right]. \tag{4.21}$$

Proof. Please see Appendix A.3. □

Using (4.19) and (4.21), we can express UPEP as:

$$\text{UPEP} = \begin{cases} \mathbb{E}\left[Q\left(\frac{|\mathbf{f}_{r,c^*}^H \mathbf{H}_{\mathbf{eff}}^{\mathbf{b}^*} \mathbf{f}_t (s^* - \hat{s})|^2}{\sqrt{2}\sigma ||\mathbf{f}_{r,c^*} \mathbf{f}_{r,c^*}^H \mathbf{H}_{\mathbf{eff}}^{\mathbf{b}^*} \mathbf{f}_t (s^* - \hat{s})||}\right)\right], \text{if } \{c^*, s^*\} \to \{c^*, \hat{s}\}, \\ \\ \mathbb{E}\left[\frac{1}{2}\exp\left(-\frac{|\sqrt{P}\mathbf{f}_{r,\hat{c}}^H (\mathbf{H}_{\mathbf{eff}}^{\mathbf{b}^*} s^* - \mathbf{H}_{\mathbf{eff}}^{\hat{\mathbf{b}}} \hat{s})\mathbf{f}_t|^2}{2\sigma^2}\right)\right], \text{if } \{c^*, s^*\} \to \{\hat{c}, \hat{s}\}. \end{cases} \tag{4.22}$$

4.4 Simulation Results

This section provides computer simulation results for the proposed BGCS-CIM scheme for the RIS-assisted mmWave system. We first describe the simulation setup for a practical scenario in an outdoor environment. Then, we validate our simulation results with the derived analytical upper bound. We also compare the proposed scheme with the simple CIM scheme introduced in [48], the SSM-based scheme proposed in [46], the orthogonal match pursuit (OMP) method proposed in [26], and the random cluster selection (RCS) scheme in which a cluster is randomly selected for transmitting the conventional M-ary signaling. Furthermore, we investigate the proposed system performance for different antenna elements/reflectors and different channel sparsity. Ultimately, we examine the robustness of the proposed scheme with respect to the angular information change.

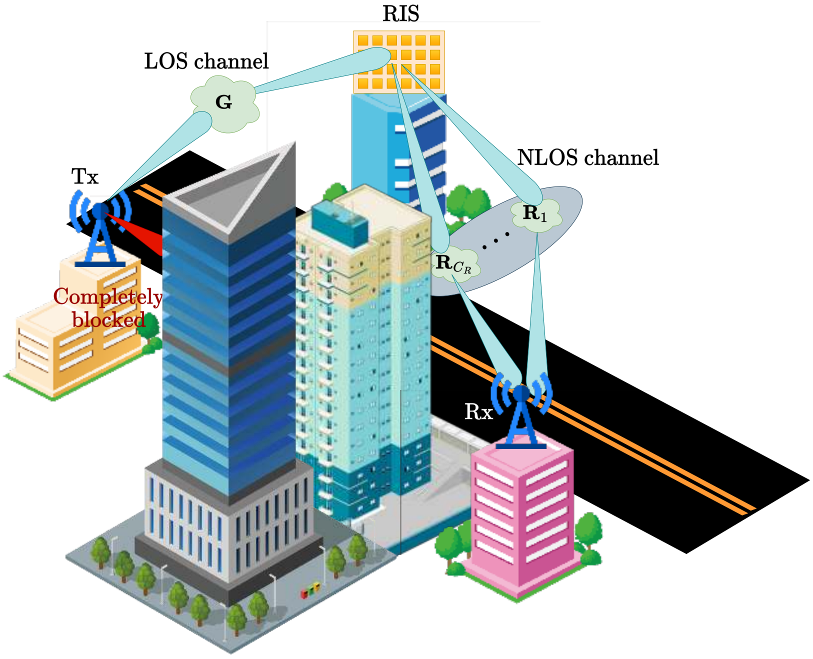

Figure 4.2: Considered outdoor scenario with RIS deployment on top of the roof of a neighboring building.

4.4.1 Simulation setup

In this subsection, we investigate a communication scenario between two BSs (backhaul scenario) in an urban area [4]. The coordinates of the Tx, RIS, and Rx are $(3 \text{ m}, 0, 12 \text{ m})$, $(0, 3 \text{ m}, 15 \text{ m})$, and $(3 \text{ m}, 103 \text{ m}, 6 \text{ m})$ in 3D Cartesian coordinate system, respectively. It is worth emphasizing that the channel between Tx and Rx is completely blocked and communication is possible only through a cascaded channel via an RIS. As depicted in [4], in a dense urban area and for a carrier frequency of 28 GHz, the channel is almost LOS-dominant when the distance is less than 25 m. On the other hand, if the distance between transmit and receive terminal is more than 100 m, it is shown that the channel is NLOS-dominant. Therefore, in this chapter, we assume that the Tx-RIS channel, which is a short-range link, is LOS-dominant, while the long-range link between the RIS and Rx is NLOS-dominant. Fig. 4.2 depicts a scheme of considered scenario. The path loss model is as follows [4]:

$$PL(d)\ [dB] = a + 10b\log_{10}(d) + \xi, \tag{4.23}$$

Table 4.3: Simulation parameters.

Parameter		Assumed value	Parameter	Assumed value
Tx location		$(3\text{ m}, 0, 12\text{ m})$	f	28 GHz
RIS location		$(0, 3\text{ m}, 15\text{ m})$	BW	100 MHz
Rx location		$(3\text{ m}, 103\text{ m}, 6\text{ m})$	L_R	10
PSD		-174 dBm	C_R	8
$G_t = G_r$		24.5 dBi	N	10×10
LOS	a	61.4	$N_t = N_r$	8×8
	b	2	$d_x = d_y$	$\lambda/2$
	σ_ξ	5.8	ϕ_m^t, φ_m^t	$\mathcal{U}[0, 2\pi)$
NLOS	a	72	$\theta_m^t, \vartheta_m^t$	$\mathcal{U}[0, \pi)$
	b	2.92	$\sigma_{\phi_m^t}, \sigma_{\theta_m^t}$	$7.5°$
	σ_ξ	8.7	$\sigma_{\varphi_m^r}, \sigma_{\vartheta_m^r}$	$7.5°$

where $\xi \sim \mathcal{N}(0, \sigma_\xi^2)$, and d is the distance between the Tx and RIS (or the RIS and Rx). The parameters a, b, and σ_ξ are given according to Table 4.3 which are collected from experimental measurements at 28 GHz carrier frequency[7] [4]. In this chapter, the noise power spectral density (PSD) is assumed to be -174 dBm/Hz [69], and the bandwidth (BW) is supposed to be 100 MHz [70]; hence, the noise power can be calculated as $\sigma^2 = \text{PSD} + 10\log_{10}(BW) = -94$ dBm.

Regarding the channel $\mathbf{R}$, we assume that there are $C_R = 8$ clusters in the mmWave propagation environment; and in each cluster, there exists $L_R = 10$ paths [52, 26]. Each cluster has departure/arrival azimuth and elevation mean angles $(\phi_m^t, \theta_m^t, \varphi_m^r, \vartheta_m^r)$, which are distributed uniformly in an interval of $[0, 2\pi)$ and $[0, \pi)$, respectively; and the angular spread (standard deviation) of departure/arrival of

[7]In (4.23), ξ is a random variable that describes large-scale shadow fading with a zero mean Gaussian distribution and standard deviation σ_ξ.

both azimuth and elevation $(\sigma_{\phi^t_m}, \sigma_{\theta^t_m}, \sigma_{\varphi^r_m}, \sigma_{\vartheta^r_m})$ domains are supposed to be 7.5°. Within each cluster, the azimuth and elevation angles corresponding to each path follow Laplacian distribution [52, 26]. The transmitter and receiver antenna gains (G_t and G_r) are assumed to be 24.5 dBi [43, 56]. Table 4.3 shows a summary of the assumed values of the system parameters.

4.4.2 Analytical validation and benchmark comparison

In this subsection, we validate our simulations with the derived analytical upper bound and compare the proposed scheme with four benchmarks, i.e., simple CIM [48], SSM [31, 46], OMP [26], and RCS, for the RIS-assisted mmWave systems. It is worth noting that the simple CIM is designed to index the clusters in a sparse channel between transmit and receive terminals. Since we need to index the clusters in the RIS-Rx channel, we apply the simple CIM in that channel. However, BGCS-CIM creates a synergy between the CIM scheme and the RIS technology. In the BGCS-CIM scheme, we consider the entire cascaded channel in the construction procedure of the codebook. Fig. 4.3 illustrates the ABER performance versus the transmit power (P) for four different signaling schemes: (a) binary IM (B-IM) with binary phase-shift keying (BPSK), (b) B-IM with quadrature PSK (QPSK), (c) quadrature IM (Q-IM) with BPSK, and (d) Q-IM with quadrature PSK (QPSK). It is worth mentioning that, spatial information domain includes one bit and two bits for B-IM and Q-IM, respectively. As shown in the Fig. 4.3, the analytical expression is an upper bound on the BGCS-CIM scheme, which validates the simulation results[8]. The simulation results reveal that BGCS-CIM scheme can outperform the benchmark schemes. Regarding Benchmark 1, i.e., simple CIM, at first glance, it seems that we should have a similar performance because the Tx-RIS LOS channel is shared among all the clusters in the RIS-Rx channel. However, simulation re-

[8]The gap between the upper bound and simulation results increases with the increasing spectral efficiency. Since the upper bound is an approximation, with increasing the spectral efficiency, the accuracy of the approximation decreases. Nonetheless, for higher transmit powers, we will see that the theoretical upper bound approaches the simulation curve.

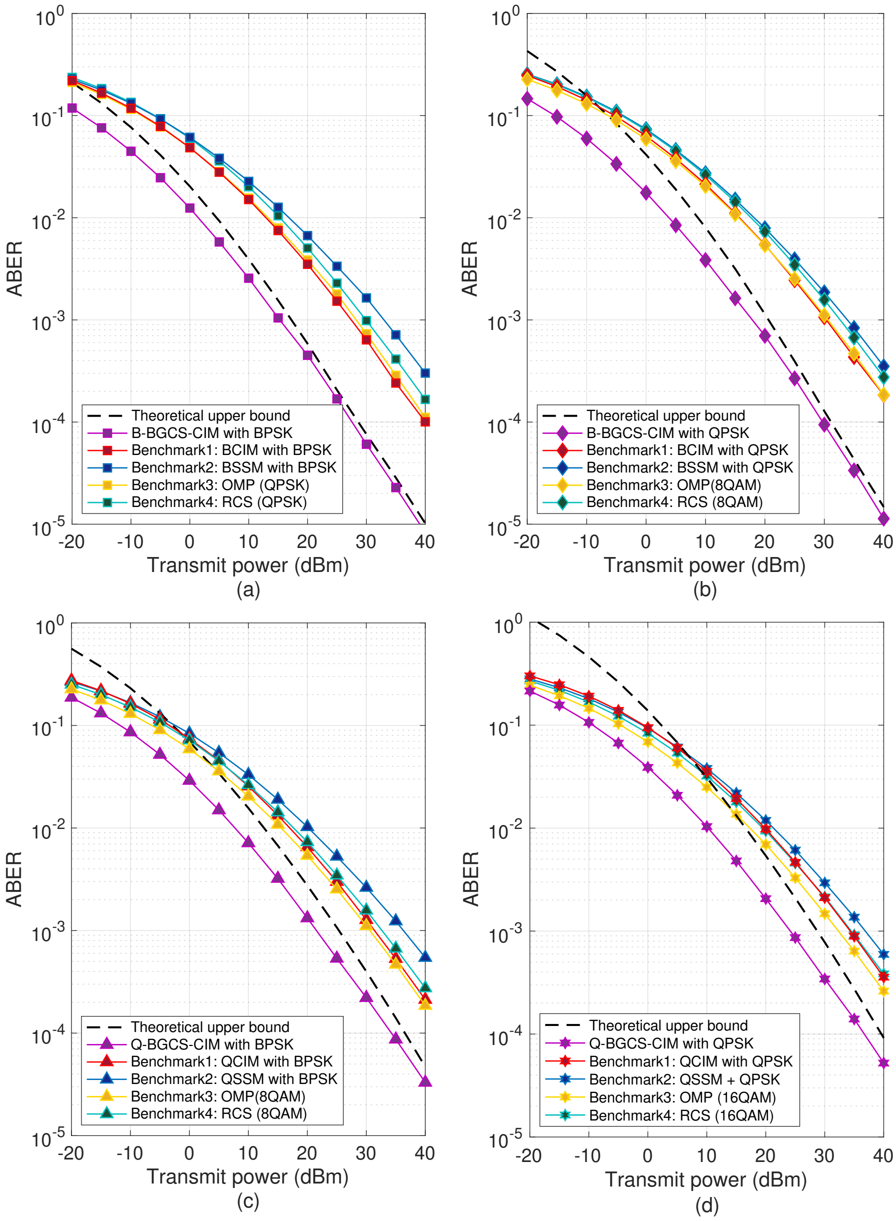

Figure 4.3: ABER performance, analytical validation and benchmarks comparison: (a) B-IM with BPSK, (b) B-IM with QPSK, (c) Q-IM with BPSK, (d) Q-IM with QPSK.

sults reveal that the BGCS-CIM scheme can boost ABER performance significantly. These results prove the importance of the entire cascaded channel in constructing an effective CIM codebook. On the other hand, the superiority of CIM-based schemes,

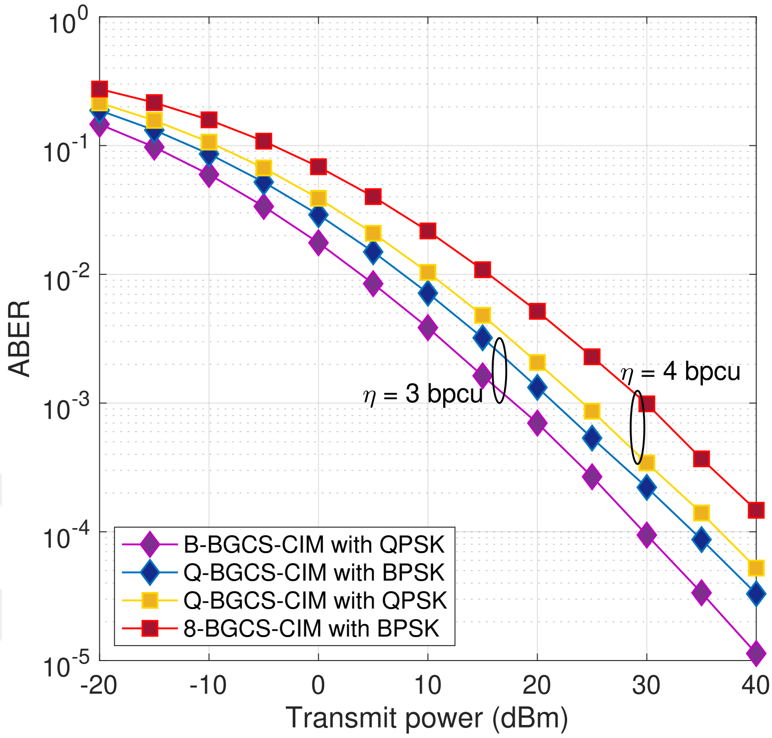

Figure 4.4: ABER performance for different CIM orders.

i.e., simple CIM and BGCS-CIM, over SSM is due to the inherent characteristic of CIM-based schemes in indexing clusters instead of paths. In other words, in the SSM scheme, under realistic circumstances of correlation among paths, two indexing paths can be near to each other, which results in power leakage in unfavorable paths; while by indexing clusters instead of paths, we can reduce the possibility of indexing highly correlated paths.

We also consider different CIM orders to investigate the effect of Euclidean distance among the indexed clusters. As illustrated in Fig. 4.4, the increasing number of CIM bits results in degraded ABER performance. This performance loss is due to the shorter Euclidean distance between CIM symbols in Q-BGCS-CIM as compared with B-BGCS-CIM and 8-BGCS-CIM as compared with Q-BGCS-CIM, for the spectral efficiency of 3 and 4 bpcu, respectively. Besides, for higher orders of CIM symbols, spreading error[9] from the CIM symbol to M-ary symbol is more likely,

[9]When the CIM symbol is detected erroneously, the detector resolves the signal received from

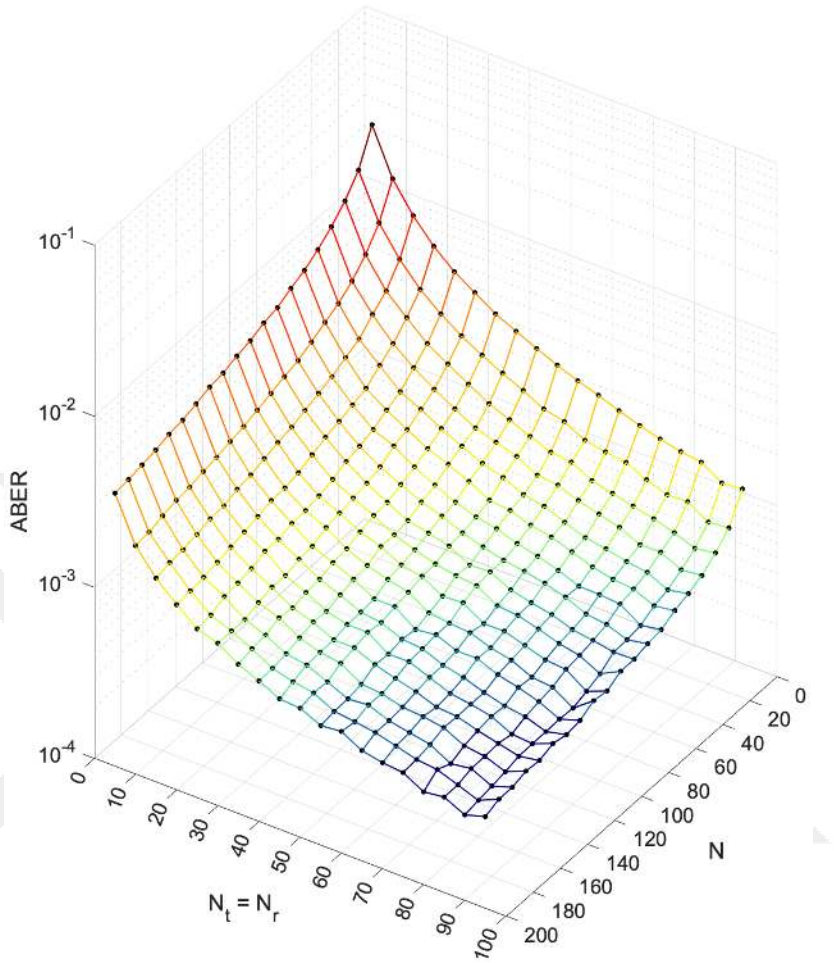

Figure 4.5: ABER for different numbers of antenna elments and RIS reflectors for B-BGCS-CIM with QPSK signaling.

which also contributes to the deteriorated ABER performance.

4.4.3 BGCS-CIM performance in S-V channel model

This subsection studies the proposed scheme performance for different numbers of antennas/reflectors and channel sparsity. Fig. 4.5 plots the ABER versus the num-

the corresponding cluster; consequently, the detected signal does not carry any information unless noise. In other words, in this situation, the detector tries to resolve noise which leads to erroneous M-ary symbol detection as well. This phenomenon is called spreading error from the IM symbol to the M-ary symbol.

Table 4.4: Array characteristics for different array sizes at 0° azimuth and 0° elevation.

Array size	**Parameter**	**Values**
8×8	Array directivity	19.74 dBi
	HPBW	12.80° Az; 14° El
	SLL	12.80 dB Az; 12.80 dB El
12×12	Array directivity	23.34 dBi
	HPBW	8.48° Az; 10° El
	SLL	13.06 dB Az; 13.07 dB El
20×20	Array directivity	27.85 dBi
	HPBW	5.08° Az; 6° El
	SLL	13.19 dB Az; 13.26 dB El

bers of antenna elements and reflectors for B-BGCS-CIM with QPSK signaling and transmit power $P = 20$ dBm. With the increasing number of antenna elements and reflectors, the ABER performance improves due to narrower beams, higher array directivity, and lower radiation sidelobes. These characteristics of larger arrays decrease the power leakage into undesirable indexed clusters, resulting in less inter-cluster interference. Hence, the detector can resolve CIM symbols more accurately, and the effect of spreading errors from CIM symbols into M-ary symbols is limited. As we mentioned earlier, increasing array size results in higher array directivity, narrower half-power bandwidth (HPBW), and higher side lobe level (SLL). The values for these parameters are summarized in Table 4.4. Higher array directivity gain results in more SINR, while with narrower HPBW (or beams), most of the transmitted signal concentrates in the desired cluster, resulting in less interference in the undesired clusters. On the other hand, higher SLL also prohibits wasting signal power on the undesired directions. All of these benefits from larger arrays result into ABER performance improvement as illustrated in Fig. 4.5.

Fig. 4.6 illustrates the ABER performance of different IM schemes under the effect of channel sparsity for one-bit IM with QPSK signaling. Fig. 4.6(a) indi-

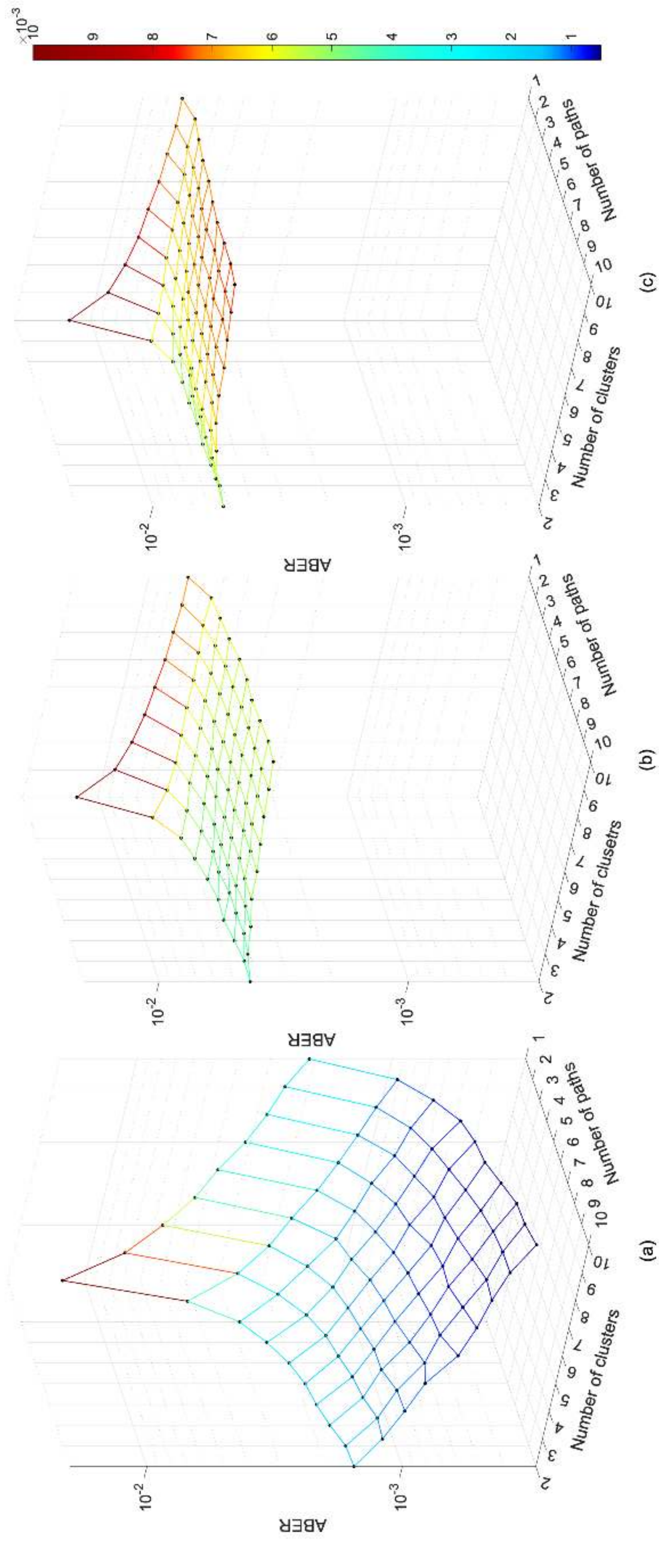

Figure 4.6: ABER performance for different IM schemes with respect to different channel sparsity: (a) B-BGCS-CIM with QPSK, (b) B-CIM with QPSK, (c) B-SSM with QPSK.

cates that the proposed BGCS-CIM scheme performs better with increasing paths and clusters since the detector can resolve the received signal more precisely in rich scattered channels. More specifically, with the increasing number of paths in each cluster, BGCS-CIM exploits this enriching in the channel as spatial diversity. On the other hand, increasing the number of clusters gives more opportunity to the BGCS-CIM scheme to index the clusters with higher gains. Consequently, increasing channel sparsity boosts ABER performance in the proposed BGCS-CIM scheme. However, this performance improvement is not observable in the simple CIM and SSM schemes. As explained earlier, in the simple CIM scheme, $\mathbf{G}$ is not involved in the indexing algorithm, while it is shared among all the indexed clusters. Specifically, $\mathbf{G}$ is a LOS channel and does not play any role in the illustrated channel sparsity. Nevertheless, the comparison between Figs. 4.6(a) and 4.6(b) perfectly shows the superiority of BGCS-CIM over simple CIM and indicates that the BGCS-CIM scheme owes its superiority to counting the entire cascaded channel in the codebook construction procedure. On the other hand, Fig. 4.6(c) shows the worst ABER performance of the SSM scheme among its counterparts. Since the SSM scheme indexes the paths without considering the clusters, by increasing channel sparsity, i.e., the number of paths and clusters, there is more potential correlation among the indexed paths.

This chapter assumes that the channel state information remains the same during a coherent block[10]. Nonetheless, in realistic conditions, the angular information slowly changes in time. This change in angular information can cause performance degradation in the proposed scheme. Fig. 4.7 depicts the performance degradation with respect to the angular information change for B-BGCS-CIM with QPSK signaling. As it is illustrated in Fig. 4.7, for $\Delta = 1^{\circ}$ and $\Delta = 2^{\circ}$ changes in the cluster

[10]In realistic channel conditions, CSI is divided into two parts, slow and fast time-varying CSI [71]. While angular information is slow time-varying information, path gains are fast time-varying CSI. In a realistic channel, angular information changes after several time intervals while the path gains change from one interval to another. However, in this chapter, for the sake of simplicity, we ignore this characteristic and assume that both angular information and path gains change from one interval to another [46, 43].

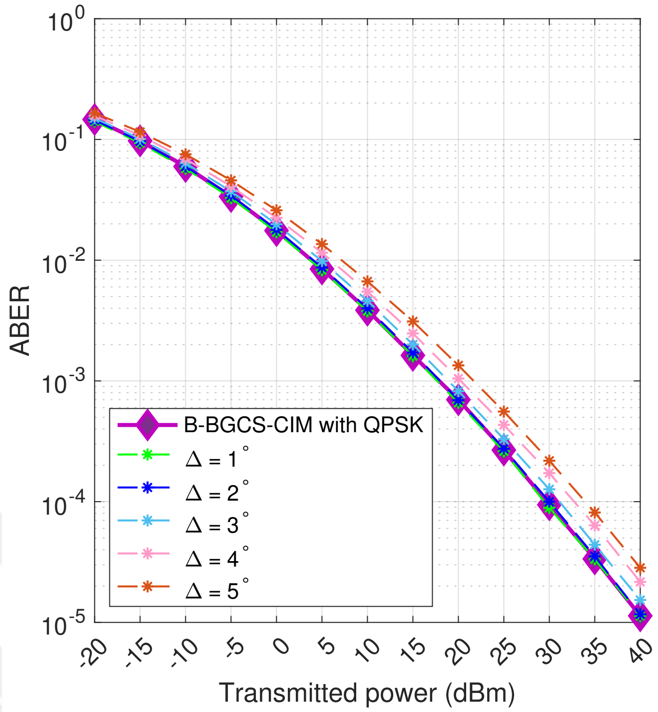

Figure 4.7: ABER performance degradation with respect to the angular information change for B-BGCS-CIM with QPSK signaling.

position, the performance is almost the same, while for $\Delta = 5°$ changes in the cluster location, the performance degrades by about 4 dB. It is worth mentioning that the angular spread of each cluster is assumed to be 7.5°; hence, 2° change in the cluster location is equivalent to more than 26% of the angular spread, while 5° is equivalent to more than 66% of the angular spread. In other words, the BGCS-CIM scheme can withstand about 26% of the angular spread variation in the cluster location without specific ABER performance degradation.

Ultimately, we analyze the computational complexity of our detector. First, the detector should calculate the effective channel $\mathbf{H}_{\text{eff}} = \mathbf{R}\mathbf{\Psi}\mathbf{G}$ which requires $\sim N^2N_t + NN_tN_r$ operations, where $\sim N^2N_t$ operations should be done to calculate $\mathbf{\Psi}\mathbf{G}$ and $\sim NN_tN_r$ operations requires to obtain $\mathbf{H}_{\text{eff}}$ completely. Next, the transmit beamformer should be multiplied in the effective channel, i.e., $\mathbf{H}_{\text{eff}}\mathbf{f}_t$, which requires $\sim N_rN_t$ operations. The whitening combiner $\mathbf{f}_r$ should be multiplied to build

$\mathbf{f}_r^H \mathbf{H}_{eff} \mathbf{f}_t$ which needs $\sim N_r$ operations. This procedure should be repeated MB times where M and B are the orders of M-ary and CIM constellations, respectively. Hence, the detector has a complexity order of $\mathcal{O}\big(MB(N^2N_t + NN_tN_r + N_tN_r + N_r)\big)$. By ignoring the lower-order terms $N_tN_r + N_r$, the complexity expression can be simplified as $\mathcal{O}\big(MBNN_t(N + N_r)\big)$.

4.5 Conclusion

This chapter has proposed a novel transmission mechanism for RIS-assisted mmWave systems named BGCS-CIM. We have considered a practical RIS-assisted system model, in which CIM has been delicately integrated to enhance system performance. The simulation results have revealed the superiority of the proposed scheme over the existing benchmarks. We have also derived an analytical upper bound for the proposed scheme, validating our simulations. Maximizing the Euclidean distance among indexed clusters can help the system to further boost performance due to minimizing inter-cluster interference, which we will investigate in our future work.

Chapter 5

PLUG-IN RIS: A NOVEL APPROACH TO FULLY PASSIVE RECONFIGURABLE INTELLIGENT SURFACES

5.1 Introduction

The requirements posed by the next generation of communication networks, including massive connectivity, ultra-reliability, low latency, and energy efficiency, necessitate exploring innovative strategies and technologies to enhance existing communication systems, enabling the deployment of ubiquitous connected devices. Reconfigurable intelligent surfaces (RISs), a promising technology that has acquired substantial attention from the research community, has emerged as a potential candidate for incorporation into the next-generation wireless communication networks [14]. By intelligently manipulating incident signals, RISs enable a smart environment through controlled scattering paths, significantly improving performance. The RIS-aided virtual channel between the terminals, making the channel adaptable for boosting communication performance in various scenarios or circumventing blockages that impede communication, a common occurrence in millimeter-wave (mmWave) communication systems due to signal vulnerability to the blockage and severe path loss. These blocked regions, termed dead zones, can be addressed by properly configuring the RIS phase shifts based on channel state information (CSI), allowing the RIS to redirect signals around obstructions and serve users within the dead zones. It is worth mentioning that CSI acquisition and phase shift configuration are key limiting factors significantly affecting the RIS design and system performance. Hence, the following sub-section elaborates on different RIS designs in the existing literature, mostly focusing on CSI acquisition methods for RIS phase adjustment [72, 67, 73, 74, 75, 76, 77, 78, 79, 57, 80, 81, 82].

5.1.1 Related Works

Two critical aspects distinguishing RIS deployment are its passive nature and ease of implementation, as highlighted in [14]. Specifically, it is assumed that an ideal RIS does not require an external power source and can be easily adapted for implementation in various environments. By taking these attributes into account, we classify the existing RIS structures into two main categories: Fully passive RIS and semi-passive RIS.[1]

Fully passive RIS

The RIS configuration depends on CSI availability for both the base station (BS)-RIS and RIS-user equipment (UE) channels, as assumed in most RIS studies in the literature. In a fully passive RIS setup, where the RIS lacks baseband processing capability, either the BS or the UE needs to estimate the end-to-end channel and decouple two parts of it, i.e., BS-RIS and RIS-UE. Numerous studies in the existing literature have addressed the channel estimation problem for fully passive RIS systems [72, 67, 73, 74, 75, 76, 77, 78, 79].

In [72], the authors proposed a channel estimation method for passive RIS-assisted power transfer systems, assuming that the power beacon manages all computational tasks due to constraints in UE. Besides, the RIS is deployed near the UE, and its controller is connected to the power beacon for programming and operating; therefore, a relatively long-distance dedicated control link is required to guarantee error-free control signaling. In [67], the authors studied channel estimation in an RIS-assisted mmWave communication system, aiming for joint active and passive beamforming for single-antenna UEs; nevertheless, dealing with multi-antenna UEs

[1] In the literature, there is a type of RIS called active RIS. However, active RIS is not equipped with baseband components like RF chains; it possesses the added capability of signal amplification [83]. In respect of the channel estimation methodology, it is not different from the fully passive RIS.

adds extra computational load for CSI acquisition and passive phase shift vector optimization. The study of [73] proposed a two-step channel estimation protocol for acquiring two parts of the end-to-end channel within a multi-user (MU) mmWave MIMO system, in which the BS is responsible for channel estimation. In addition, the authors also considered time allocation and RIS phase shift adjustment for the uplink channel estimation phase. Meanwhile, the study of [74] dives into channel estimation problem within a point-to-point (P2P) RIS-assisted mmWave communication system. Under the suggested protocol, the UE undertakes a non-convex optimization problem to obtain BS-RIS and RIS-UE channels. Similarly, a channel estimation algorithm for passive large intelligent metasurfaces (LIM) (which is a very large RIS) is introduced in [75], employing sparse matrix factorization and matrix completion. It is worth noting that running an algorithm in one of the transceivers is necessary to obtain BS-LIM and LIM-UE channels. In [76], the authors considered UE mobility and proposed a two-time scale channel estimation framework, leveraging the quasi-static BS-RIS channel while the RIS-UE is a low-dimensional mobile channel. Accordingly, the BS-RIS channel with a large dimension needs to be estimated less frequently, while the small dimension RIS-UE channel must be estimated frequently. Consequently, the pilot overhead is reduced in a long-term perspective. The study of [77] investigated channel estimation for broadband RIS-aided mmWave massive MIMO systems utilizing compressive sensing (CS) method. Specifically, the authors assumed that the line-of-sight (LOS) dominated BS-RIS channel is known; hence, in order to jointly estimate BS-UE and RIS-UE channels, the pilot signals can be designed accordingly. The study of [78, 79] proposed a novel framework for low-complex channel estimation and passive beamforming for both single-user and MU scenarios. The authors proposed that the composed superposed channel is estimated simultaneously instead of obtaining each direct link and reflective link separately. Additionally, a set of pre-adjusted training phase profiles can be adopted to acquire passive beamforming at the RIS.

This literature review reveals that significant efforts have been made to estimate the end-to-end channel and separate it into BS-RIS and RIS-UE components in RIS-assisted mmWave communication systems. It is worth emphasizing that in fully passive RIS design, channel estimation/decoupling and optimizing phase shifts are done at one of the endpoints, which necessitates two key considerations. Firstly, establishing a dedicated control link is essential to facilitate the transmission of configuration information from the responsible endpoint to the RIS. Secondly, allocating sufficient resources to accommodate the computational tasks associated with channel estimation/decoupling and RIS phase shift optimization at the responsible endpoint is essential. However, it is worth noting that both of these requirements have potential drawbacks. Introducing a dedicated control link can add complexity to the system and potentially increase the overall latency stemming from reconfiguration latency [84], while allocating substantial resources, particularly at the UE, may not be a cost/power-efficient solution. Similarly, if the BS assumes the responsibility for computational tasks, extending this approach to an MU scenario can significantly elevate system complexity and overhead, potentially posing challenges to the overall feasibility of the system.

Semi-passive RIS

Despite extensive endeavors to acquire individual cascaded channels for fully passive RIS configurations, challenges arise from the inefficient cascaded channel decoupling process due to the passive nature of RIS elements [57]. In order to address this issue, semi-passive RIS structure is introduced in [80]. In the semi-passive RIS design, a fraction of RIS elements are connected to baseband components, enabling the RIS to perform channel estimation through its integrated baseband components. Consequently, the RIS can accurately estimate BS-RIS and RIS-UE channels separately and adjust itself without being controlled by other terminals, i.e., the transmitter (Tx) or the receiver (Rx) [80]. In [57], the authors proposed an algorithm for semi-passive RIS channel estimation, leveraging sparsity in both spatial and frequency domains of mmWave channels. As shown in [57], connecting only 8% of RIS elements to the baseband components yields more accurate channel estimation than the considered benchmarks. The study of [81] proposed two practical residual neural networks to accurately estimate the channel for semi-passive RIS-aided communication systems. Similarly, the authors in [82] proposed a channel estimation method for semi-passive RIS-assisted systems based on super-resolution neural networks. It is worth noting that even though the studies of [81, 82] exploit semi-passive RIS, a significant portion of the computational load for channel estimation is carried out by the transceivers to simplify the RIS structure. Consequently, they inherit some of the drawbacks associated with both fully passive and semi-passive RIS designs.

Table 5.1 provides an overview of the structural characteristics of various RIS designs discussed above. The principal advantage of the semi-passive RIS design results from its reduced reliance on establishing a dedicated control link. Moreover, this approach eliminates the additional overhead and complexity imposed on the transceivers, as the RIS efficiently handles the computational tasks. Nonetheless, the semi-passive RIS configuration deviates from two fundamental characteristics highlighted previously: The passive nature of the RIS and its simplicity of implementation. While it is evident that the semi-passive RIS does not adhere to the passive attribute, it is crucial to remember that including baseband components introduces a costly and power-intensive structure, which, in turn, hinders easy and widespread deployment.

5.1.2 Motivations and contributions

As summarized in Table 5.1, both fully passive and semi-passive RIS configurations exhibit drawbacks that pose challenges to their practical implementation. Based on the existing literature, it becomes evident that there is a clear and pressing need within academia to create a novel RIS structure that fulfills the two fundamental attributes emphasized in [14], which strongly motivates us to introduce a fresh and innovative design, named *plug-in RIS*, with the specific aim of simplified deployment and operation within mmWave communication environments. In this system, the RIS can be conveniently plugged into the environment to operate with fixed phase shift profiles, which are adjusted based on the location of the BS and dead zones. Specifically, initially, the dead zone in the mmWave environment is defined to the

Table 5.1: Comparison among different RIS structures available in the existing literature and the proposed plug-in RIS. (**Abbreviations**: Y = yes; N = no; FP = fully passive; SP = semi-passive; H = high; M = medium; L = low.)

	[72]	[67]	[73]	[74]	[75]	[76]	[77]	[78]	[79]	[57]	[80]	[81]	[82]	**Plug-in RIS**
RIS type:	FP	FP	FP	FP	FP	FP	FP	FP	FP	SP	SP	SP	SP	FP
Channel estimation carries out by:	BS	UE	BS	UE	UE	BS	UE	BS	BS	RIS	RIS	BS/UE	BS/UE	BS
Control link availability:	Y	Y	Y	Y	Y	Y	Y	Y	Y	N	N	Y	Y	N
Implementation complexity:	M	M	H	H	H	M	H	M	M	H	H	M	M	L
Signalling overhead:	M	M	H	M	M	M	H	M	M	L	L	M	M	L

BS (because the BS is initially not aware of which area is the dead zone) and divided into spatial segments; each spatial segment is considered to be served via a part of divided RIS, named sub-RIS. Next, we examine the location of each spatial segment and assign a fixed phase shift profile to the corresponding sub-RIS. Since both the BS and dead zone have fixed locations, the sub-RISs are not required to be configured frequently. For activation, the BS obtains the UE's spatial segment and employs beamforming techniques to illuminate the corresponding sub-RIS, enabling control over signal reflection towards desired directions and offering a user-centric approach to enhance wireless communication performance.

Based on the aforementioned motivations, we outline our contributions as follows:

- *Plug-in RIS with standalone operation:* In contrast to the fully passive and semi-passive RIS designs, this study introduces an innovative approach—a plug-in RIS configuration with standalone operation—for extending communication coverage in mmWave systems. Specifically, since mmWave communication is vulnerable to blockages, it can encounter several limited-space dead zones. In this context, developing an RIS design that facilitates widespread RIS implementation while keeping cost and complexity low and maintaining high-quality communication is essential for mmWave communication systems. The proposed structure aligns with key attributes of RIS technology, such as, its passive nature and ease of implementation. The plug-in RIS consists of multiple sub-RIS planes, each pre-configured with fixed phase shifts, intended to cover distinct spatial segments within the dead zone. Leveraging the high beamforming gain at the BS in the mmWave communication systems, only one sub-RIS plane is activated in each transmission period to establish a virtual link toward the UE. This approach innovatively integrates the control mechanism within the transmitting beam, eliminating the necessity for implementing traditional control links and the associated overheads, which enhances the overall user experience by increasing the ease of implementation of the RIS in different environments.

- *Compatibility with existing end-to-end channel estimation methods:* The preconfigured phase shift design of the suggested plug-in RIS eliminates the necessity for decoupling two parts of the end-to-end channel, which alleviates the additional burden of channel decoupling on the participating terminals, enabling the easy deployment of fully passive RIS in mmWave communication systems. In other words, in the proposed plug-in RIS, obtaining the conventional end-to-end channel estimation is enough, and decoupling it into BS-RIS and RIS-UE channels is not required.

- *Reliability analysis:* We derive a closed-form expression for the upper bound of the average bit error rate (ABER) for the proposed plug-in RIS. Our analytical methodology employs the union-bound and pairwise error probability (PEP) to validate the precision of our simulation outcomes. Our results illustrate that these analytical derivations offer a tight upper bound on the ABER.

- *Simulation insights:* We conduct extensive simulations to evaluate the performance of the proposed plug-in RIS in terms of coverage performance, ABER, achievable rate, energy efficiency, and detector complexity. Computer simulation outcomes indicate that the plug-in RIS exhibits promising coverage performance, showing close ABER and achievable rate results to the semi-passive design. Moreover, the plug-in RIS outperforms the benchmark designs in terms of energy efficiency and detector complexity, highlighting the superiority of our proposed approach, taking a step forward to the practical implementation of fully passive RIS. Furthermore, analyzing received signal-to-interference-plus-noise-ratio (SINR) in an MU scenario reveals that plug-in RIS can also be adapted to serve more than a single UE without considerable performance loss compared to semi-passive RIS.

The rest of this chapter is organized as follows. Section 5.2 outlines the system, channel, and signal models. The design of the proposed plug-in RIS is elaborated in Section 5.3. Analytical expression as an upper bound for ABER performance

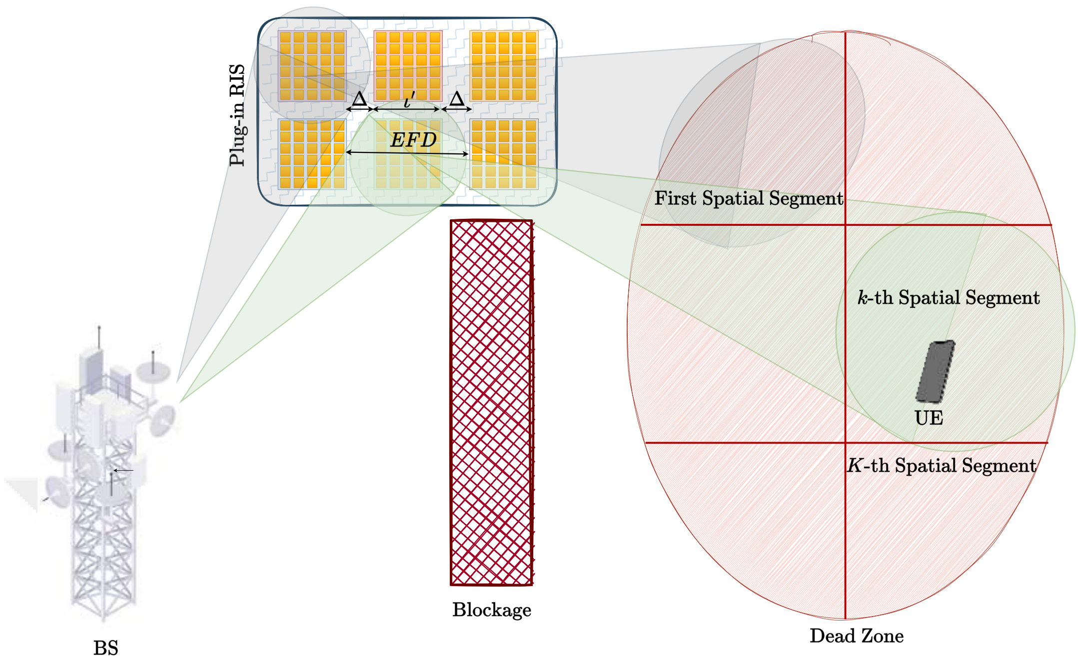

Figure 5.1: System model for proposed plug-in RIS.

is derived in Section 5.4. Simulation results are displayed in Sections 5.5 and 5.6 for single-user and multi-user cases, respectively, followed by the conclusion of this study in Section 5.7.

5.2 System, Channel, and Signal Model

This section describes the system model for the mmWave massive MIMO communication system aided by the proposed plug-in RIS. Afterward, we present the utilized channel model and the foundational assumptions supporting our suggested design. Next, we elaborate on the signal model and introduce a suitable maximum likelihood (ML) detector. Lastly, the proposed plug-in RIS is extended to an MU scenario considering inter-user interference and a baseband (BB) precoding stage to combat this interference.

5.2.1 System Model

As depicted in Fig. 5.1, we investigate a P2P mmWave communication system aided by a set of sub-RIS planes with pre-configured fixed phase shifts. Due to propagation loss challenges, the direct BS-UE link is assumed to be blocked, causing dead zones in the environment; therefore, the sub-RIS planes are plugged into the surrounding environment to assist UEs located in the dead zone, ensure constant connectivity and guarantee LOS links in the BS-RIS and RIS-UE channels. Specifically, a dead zone can be covered using one or more sub-RISs, each covering a distinct spatial segment of the dead zone with a fixed beam. The set of sub-RISs constitutes the plug-in RIS entity. During implementation, each sub-RIS is assigned to a spatial segment in the dead zone; therefore, they are adjusted according to the angular information of BS and the spatial segments. Specifically, for each spatial segment, we consider fixed angular information that represents it, and since this angular information is constant, the sub-RISs are not required to be adjusted frequently. During the transmission, based on the UE's location and with the aid of massive MIMO's beamforming gain at the BS, the transmitted beam footprint only activates the corresponding sub-RIS. Both the BS and UE are equipped with uniform rectangular arrays (URA); N_t and N_r denote the number of antenna elements at the BS and UE, respectively. To address severe path loss while minimizing the need for costly RF chains, analog beamformers/combiners are employed at the BS/UE. This approach allows a single RF chain at the BS and UE, supporting a single stream [85]. Our proposed plug-in RIS comprises K sub-RISs, each containing M_k $(k = 1, \dots, K)$ passive reflecting elements.

5.2.2 Channel Model

In this chapter, we adopt the three-dimensional (3D) geometry-based channel model for the BS-RIS and RIS-UE channels as follows [43, 44, 7, 48, 86]:

$$\mathbf{G}_k = \sqrt{N_t M_k}\alpha_k \mathbf{a}_{r,ris}(\varphi^k_{r,ris}, \vartheta^k_{r,ris})\mathbf{a}_t^H(\varphi_t, \vartheta_t), \tag{5.1}$$

$$\mathbf{R}_k = \sqrt{M_k N_r}\beta_k \mathbf{a}_r(\varphi_r, \vartheta_r)\mathbf{a}_{t,ris}^H(\varphi_{t,ris}^k, \vartheta_{t,ris}^k), \tag{5.2}$$

where $\mathbf{G}_k \in \mathbb{C}^{M_k \times N_t}$ ($\mathbf{R}_k \in \mathbb{C}^{N_r \times M_k}$) is the channel between BS and k-th sub-RIS (k-th sub-RIS and UE). The parameter α_k (β_k) is the LOS channel gain of $\mathbf{G}_k$ ($\mathbf{R}_k$) and follows a complex normal distribution $\mathcal{CN}(0, 10^{-0.1PL(d)})$, with $PL(d)$ representing path loss and d indicating the distance between the associated terminals. The array response (steering) vector is denoted as $\mathbf{a}(.)$, while $\varphi \in \mathcal{U}(a_\varphi, b_\varphi)$ and $\vartheta \in \mathcal{U}(a_\vartheta, b_\vartheta)$ stand for azimuth and elevation angles, respectively. Specifically, φ_t (ϑ_t) represents the azimuth (elevation) angle of departure (AoD) at the BS, and φ_r (ϑ_r) indicates the azimuth (elevation) angle of arrival (AoA) at the UE. Besides, $\varphi_{t,ris}^k$ ($\vartheta_{t,ris}^k$) shows azimuth (elevation) AoD associated with the k-th sub-RIS, and $\varphi_{r,ris}^k$ ($\vartheta_{r,ris}^k$) is the azimuth (elevation) AoA at the k-th sub-RIS. Here, it is assumed that each channel is LOS dominated due to the presence of LOS component [87]. Thus, non-LOS (NLOS) components are omitted, allowing for a focused investigation of the proposed plug-in RIS performance. The normalized antenna array response is defined as follows [85, 87]:

$$\mathbf{a}(\varphi, \vartheta) = \frac{1}{\sqrt{N}}[e^{j\mathbf{k}^T\mathbf{p}_0}, e^{j\mathbf{k}^T\mathbf{p}_1}, \ldots, e^{j\mathbf{k}^T\mathbf{p}_{N-1}}]^T, \tag{5.3}$$

where N represents the total number of antenna elements/reflectors at the corresponding terminal, calculated as $N = N_x \times N_y$. Here, N_x (N_y) refers to the number of antenna elements/reflectors along the x-axis (y-axis). The symbol $\mathbf{k}$ denotes the wave number, and $\mathbf{p}_n$ is associated with the structure of the antenna array, specifying the location of the n-th antenna element. We establish $n = n_y N_x + n_x$, where $0 \leq n_x \leq N_x - 1$ ($0 \leq n_y \leq N_y - 1$) represents the location of the antenna element/reflector along the x-axis (y-axis). For the URA configuration, the definitions of $\mathbf{k}$ and $\mathbf{p}_n$ are outlined as follows [85, 87]:

$$\mathbf{k} = \frac{2\pi}{\lambda}[\sin\vartheta\cos\varphi \quad \sin\vartheta\sin\varphi]^T, \tag{5.4}$$

$$\mathbf{p}_n = [n_x\delta_x \;\; n_y\delta_y]^T, \tag{5.5}$$

where δ_x (δ_y) represents the separation between adjacent antennas/reflectors along the x-axis (y-axis), and λ denotes the signal wavelength. Note that to calculate the antenna array response for each terminal, we need to substitute its corresponding φ and ϑ values into (5.3) and (5.4). The effective end-to-end channel between the BS and UE through the k-th sub-RIS, denoted as $\mathbf{H}_{\text{eff},k} \in \mathbb{C}^{N_r \times N_t}$, can be defined as follows:

$$\mathbf{H}_{\text{eff},k} = \mathbf{R}_k \mathbf{\Psi}_k \mathbf{G}_k, \tag{5.6}$$

where $\mathbf{\Psi}_k \in \mathbb{C}^{M_k \times M_k}$ is the k-th sub-RIS phase shift matrix and is defined as

$$\mathbf{\Psi}_k \triangleq \text{diag}\left(e^{j\psi_1}, e^{j\psi_2}, \ldots, e^{j\psi_{M_k}}\right), \tag{5.7}$$

where ψ_i is the phase shift associated with the i-th reflector of the corresponding sub-RIS. As mentioned earlier, the sub-RISs can be adjusted using the location of BS and dead zones. Lemma 4 gives a mathematical expression for sub-RISs phase shift adjustment.

Lemma 4. *The phase shift matrix for the k-th sub-RIS can be calculated as follows:*

$$\mathbf{\Psi}_k = \sqrt{M_k}\,\text{diag}\left(\mathbf{f}_{b,k} \circ \mathbf{a}^*_{r,ris}(\varphi^k_{r,ris}, \vartheta^k_{r,ris})\right), \tag{5.8}$$

where $\mathbf{f}_{b,k}$ represents the fixed beam formed by the k-th sub-RIS with azimuth and elevation AoD as $\phi_{b,k}$ and $\theta_{b,k}$, respectively. $\mathbf{f}_{b,k}$ is expressed as

$$\mathbf{f}_{b,k} = [e^{\mathbf{k}^T\mathbf{p}_0}, e^{\mathbf{k}^T\mathbf{p}_1}, \ldots, e^{\mathbf{k}^T\mathbf{p}_{M_k-1}}],$$

where $\mathbf{k}$ is calculated as (5.4) by substituting $\varphi = \phi_{b,k}$ and $\vartheta = \theta_{b,k}$.

Proof. See [7, Section III-C]. □

5.2.3 Signal Model

As mentioned earlier, the dead zone is divided into distinct spatial segments based on its geometric shape. Given that the dead zone's location remains fixed, the spatial segments also maintain constant positions. Consequently, each spatial segment is defined by a pair of unchanging azimuth and elevation angular values. Thus, sub-RISs are adjusted according to the constant angular information of BS and spatial segments in order to cover that segment. For starting transmission, end-to-end CSI and the spatial segment of the UE should be obtained. Since the BS and sub-RISs have fixed positions, the angular information at the BS is constant and known to the BS; therefore, after transmitting pilot signals, the BS can easily find the spatial segment in which the UE is located and its associated sub-RIS. Furthermore, by estimating end-to-end channel, both the BS and UE can adjust their analog beamformers/combiners accordingly. The effective end-to-end channel can be described as (5.6). Therefore, the received signal after passing through the combiner is represented as

$$y = \sqrt{P} G_t G_r \mathbf{f}_r^H \mathbf{H}_{\text{eff},k} \mathbf{f}_t s + \mathbf{f}_r^H \mathbf{n}, \tag{5.9}$$

where P stands for the transmit power, $G_i = g_e + 10 \log_{10}(N_i)$, wherein $i \in \{t, r\}$, represents the array gain, with g_e denoting the gain of each antenna element [88, 89]. The symbol s corresponds to the transmitted $\mathcal{M}$-ary symbol, and $\mathbf{n} \in \mathbb{C}^{N_r \times 1} \sim \mathcal{CN}(0, \sigma^2)$ is the additive noise component. Moreover, $\mathbf{f}_t \in \mathbb{C}^{N_t \times 1}$ denotes the analog beamformer at the BS, while $\mathbf{f}_r \in \mathbb{C}^{N_r \times 1}$ represents the analog combiner at the UE. For simplification, continuous phase shifters are assumed at the BS and UE; thus, analog beamformer/combiner can be adjusted as $\mathbf{f}_t = \mathbf{a}_t(\varphi_t, \vartheta_t)$ and $\mathbf{f}_r = \mathbf{a}_r(\varphi_r, \vartheta_r)$. Utilizing the ML detector at the UE, the estimated symbol is expressed as

$$\hat{s} = \arg\min_{\forall s \in \mathcal{S}} |y - \sqrt{P} G_t G_r \mathbf{f}_r^H \mathbf{H}_{\text{eff},k} \mathbf{f}_t s|^2, \tag{5.10}$$

where $\mathcal{S}$ is the set of $\mathcal{M}$-ary constellation points.

5.2.4 MU Plug-in RIS

This subsection investigates exploiting of plug-in RIS in MU scenarios to serve J single antenna UEs. We introduce the channel model for the MU-plug-in RIS-assisted system, then present the signal model and ultimately derive the SINR term.

The overall effective channel matrix, denoted as $\mathbf{H} \in \mathbb{C}^{J \times N_t}$, can be obtained as follows:

$$\mathbf{H} = \left[\mathbf{h}_{\text{eff},1}^T, \ldots, \mathbf{h}_{\text{eff},J}^T\right]^T, \tag{5.11}$$

where $\mathbf{h}_{\text{eff},j} \in \mathbb{C}^{1\times N_t}$, $(j \in \{1,\dots,J\})$, represents the end-to-end effective channel between the BS and the j-th UE. This can be computed according to (5.6), considering single antenna UEs, i.e., $N_r = 1$. It is worth mentioning that for clarity, we do not include sub-RIS index k in this subsection; however, each UE initiates the communication through a sub-RIS, which can be the same or different from other UEs. The effective channel seen from the BS's BB stage can be represented as $\boldsymbol{\mathcal{H}} = \mathbf{H}\mathbf{F_t}$, where $\mathbf{F_t} = [\mathbf{f}_{t,1},\dots,\mathbf{f}_{t,J}]$ is the transmit analog active beamforming matrix. Here, $\mathbf{f}_{t,j} \in \mathbb{C}^{N_t\times 1}$ denotes the transmit analog beamforming vector corresponding to the j-th UE. Accordingly, the BB precoding matrix is calculated as $\mathbf{B} = \varepsilon\mathbf{W}\boldsymbol{\mathcal{H}}^H$ where $\mathbf{W} = (\boldsymbol{\mathcal{H}}^H\boldsymbol{\mathcal{H}} + J\alpha\mathbf{I}_J)^{-1}$ [90]. Here, $\alpha = \sigma^2/P$ is the regularization parameter, and $\varepsilon = \sqrt{P_T/\operatorname{Tr}\left(\boldsymbol{\mathcal{H}}\mathbf{W}^2\boldsymbol{\mathcal{H}}^H\right)}$ is the normalization scalar [90]. Therefore, the received signal in the j-th UE is given by:

$$y_k = \underbrace{\varepsilon\mathbf{H}_{\text{eff},j}\mathbf{F_t}\mathbf{W}\mathbf{F}^H\mathbf{H}^H_{\text{eff},j}s_j}_{\text{Desired Signal}} + \underbrace{\varepsilon\sum_{q=1}^{J}\mathbf{H}_{\text{eff},j}\mathbf{F_t}\mathbf{W}\mathbf{F}^H\mathbf{H}^H_{\text{eff},q}s_q}_{\text{Interference}} + \underbrace{\mathbf{n}_j}_{\text{Noise}}. \tag{5.12}$$

Finally, the SINR can be derived as follows:

$$\text{SINR} = \frac{|\mathbf{H}_{\text{eff},j}\mathbf{F_t}\mathbf{W}\mathbf{F}^H\mathbf{H}^H_{\text{eff},j}|^2}{||\mathbf{H}_{\text{eff},j}\mathbf{F_t}\mathbf{W}\boldsymbol{\mathcal{H}}_{[j]}||^2 \; + \; \mathbf{n}_j}, \tag{5.13}$$

where $\boldsymbol{\mathcal{H}}_{[j]} = [\mathbf{h}^T_{\text{eff},1},\dots,\mathbf{h}^T_{\text{eff},j-1},\mathbf{h}^T_{\text{eff},j+1},\dots,\mathbf{h}^T_{\text{eff},J}]^T\mathbf{F_t}$ is the reduced-sized effective interference channel matrix.

5.3 Proposed Plug-in RIS Structure

This section illustrates the structure of the proposed plug-in RIS. In the plug-in RIS structure, sub-RIS units are placed with appropriate spacing, each pre-configured to cover a specific spatial segment within a known dead zone. Based on environmental blockage and path loss conditions, the sub-RIS units can be positioned on either the BS or UE side. The spacing between sub-RIS units should increase as they are deployed farther from the BS. We subsequently formulate the minimum spacing between sub-RIS units.

Maintaining an appropriate spacing between sub-RIS units is crucial for reducing power leakage to other segments within the dead zone, which is particularly beneficial in MU scenarios as it leads to decreased interference. Leveraging the beamforming gain offered by the large antenna array at the BS, forming a narrow beam precisely directed to a specific spatial area becomes feasible. This beam's coverage area, termed footprint, is determined by the distance from the BS and the emitted signal's beamwidth. Exploiting this property of large arrays enables the BS to illuminate only the corresponding sub-RIS based on the UE's location. In Fig. 5.1, an illustration of adjacent sub-RISs separated by Δ is shown. To establish a closed-form expression for Δ, we initially define the length of each side of the sub-RIS along the i-axis (where $i \in \{x, y\}$) as $\iota_i = M_i\delta_i$. Note that M_i represents the number of reflectors across the i-axis, and for simplicity in notation, we eliminated the sub-RIS's index. The footprint of the received beam should exclusively cover the intended sub-RIS. Assuming uniform spacing between sub-RISs, the effective footprint diameter (EFD) can be computed as $\text{EFD} = 2\Delta + \iota$. Consequently, Δ can be derived as follows:

$$\Delta = \frac{\text{EFD} - \iota}{2}. \tag{5.14}$$

In order to determine the EFD, we consider half-power beamwidth (HPBW) that encompasses an effective portion of the radiated power [62]. It is worth mentioning that an antenna can differentiate between two adjacent sources if the angular separation between them exceeds half of the first-null beamwidth (FNBW), which is approximately equivalent to HPBW, i.e., $\text{HPBW} \approx \frac{\text{FNBW}}{2}$ [36]. The HPBW of an antenna array along the i-axis ($i \in \{x, y\}$) can be calculated using the following formula [91]:

$$\text{HPBW} \approx 0.891 \frac{\lambda}{N_i \delta_i}. \tag{5.15}$$

Lemma 5. *The EFD of the transmitted beam from the Tx at a distance of d can be computed as follows:*

$$EFD = 2d \times \frac{\sin\left(\frac{HPBW}{2}\right)}{\cos\left(\frac{HPBW}{2} + \theta_0\right)}, \tag{5.16}$$

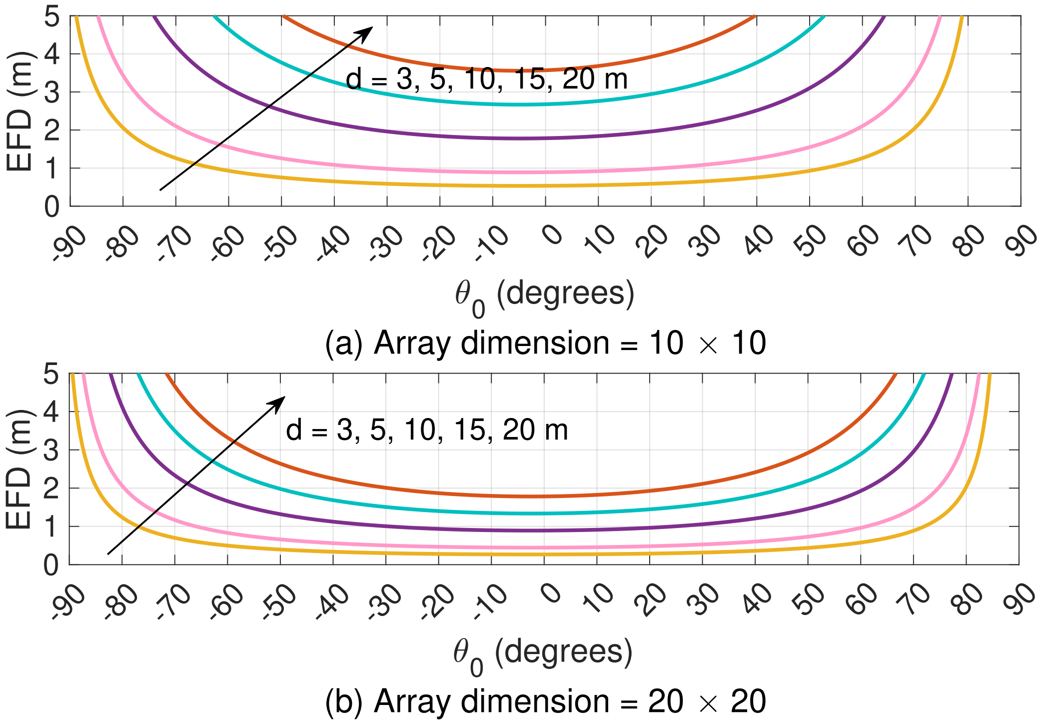

Figure 5.2: EFD versus different amounts of incident angle.

where θ_0 represents the angle of the incident signal at the RIS with respect to the RIS broadside direction.

Proof. See [59, Appendix B]. □

Corollary 1. *In the case where $\theta_0 = 0$, indicating that the received beam at the RIS is perpendicular to the RIS plane, the EFD can be approximated as*

$$EFD \approx HPBW \times d. \tag{5.17}$$

Proof. See Appendix B.1. □

Fig. 5.2 illustrates the precise EFD for various values of d and θ_0. Notably, in Figs. 5.2(a) and 5.2(b), a distinct pattern emerges: within a limited range centered around $\theta_0 = 0°$, the EFD remains constant; the extent of this interval diminishes with higher values of d. Conversely, as it is illustrated in Fig. 5.2(b), adopting a larger antenna array leads to expanding the interval.

Substituting EFD into (5.14), sub-RISs inter-spacing, i.e., Δ, can be calculated as

$$\Delta = \frac{\text{HPBW} \times d - \iota}{2}. \tag{5.18}$$

Notably, Δ defines the minimum distance that needs to be maintained between two neighboring sub-RIS units to mitigate power leakage to the other spatial segments.

5.4 Theoretical Analysis

In this section, we begin by presenting a mathematical expression to validate the accuracy of our ABER simulation results. Following that, we provide expressions for computing the detector's complexity for both plug-in and semi-passive RIS designs.

5.4.1 ABER Theoretical Upper Bound

Obtaining ABER involves calculating PEP, which denotes the likelihood of detecting $\hat{s}$ when transmitting s^*. Initially, we consider the channel as a known entity for both cascaded channels. This allows us to express the conditional PEP (CPEP) as follows:

$$\mathcal{P}(s^* \to \hat{s}|\alpha_k, \beta_k) = \mathcal{P}(|y - \sqrt{P}G_tG_r\mathbf{f}_r^H\mathbf{H}_{\text{eff},k}\mathbf{f}_t s^*|^2 > |y - \sqrt{P}G_tG_r\mathbf{f}_r^H\mathbf{H}_{\text{eff},k}\mathbf{f}_t\hat{s}|^2). \tag{5.19}$$

Lemma 6. *The mathematical expression for CPEP is as*

$$\mathcal{P}(s^* \to \hat{s}|\alpha_k, \beta_k) = Q\Big(\frac{\sqrt{P}G_tG_r|\mathbf{f}_r^H\mathbf{H}_{\textit{eff},k}\mathbf{f}_t(s^* - \hat{s})|^2}{\sqrt{2}\sigma||\mathbf{f}_r\mathbf{f}_r^H\mathbf{H}_{\textit{eff},k}\mathbf{f}_t(s^* - \hat{s})||}\Big). \tag{5.20}$$

Proof. See Appendix B.2. □

Lemma 6 provides a closed-form expression for the CPEP. To compute the unconditional PEP (UPEP), we take the expectation of CPEP over a sufficient number of channel realizations, denoted as UPEP $= \mathbb{E}[\text{CPEP}]$. Furthermore, to establish an upper bound for the ABER, we utilize the union-bound approach as follows:

$$\text{ABER} \leq \frac{1}{\eta\mathcal{M}}\sum_{s^*}\sum_{\hat{s}} E_b(s^* \to \hat{s})\text{UPEP}, \tag{5.21}$$

where $E_b(s^* \to \hat{s})$ is the total number of erroneous bits and $\mathcal{M}$ is the order of $\mathcal{M}$-ary constellation.

5.4.2 Detector Complexity

This subsection discusses the computation of detector complexity for the proposed plug-in RIS and semi-passive RIS designs. Both designs employ the same ML detector given in (5.10), but the main difference lies in obtaining $\mathbf{H}_{\text{eff}}$. In the semi-passive RIS design, $\mathbf{G}$ and $\mathbf{R}$ are computed separately, and the phase shift matrix $\boldsymbol{\Psi}$ is also calculated by the RIS in each transmission period. The detector then uses these matrices to calculate $\mathbf{H}_{\text{eff}}$, affecting the detector's complexity. However, in the plug-in RIS design, $\mathbf{H}_{\text{eff}}$ is directly acquired without the need for separate calculations of $\mathbf{G}$, $\mathbf{R}$, and $\boldsymbol{\Psi}$ due to the pre-adjusted sub-RIS configuration. Considering this point, we compute each RIS systems's detector complexity as follows. In this subsection, for the sake of notation simplicity, we show the number of RIS/sub-RIS elements engaged in the communication with M; hence, the index of sub-RISs has been ignored.

1. ***Semi-passive RIS:*** To compute $\mathbf{H}_{\text{eff}}$, the detector calculates $\boldsymbol{\Psi}\mathbf{G}$, involving $\sim M^2N_t$ operations. Subsequently, $\mathbf{R}\boldsymbol{\Psi}\mathbf{G}$ demands $\sim N_rMN_t$ operations. Thus, for computing $\mathbf{H}_{\text{eff}}$, $\sim M^2N_t + N_rMN_t$ operations are needed. Moreover, $\mathbf{H}_{\text{eff}}\mathbf{f}_t$ entails $\sim N_rN_t$ operations, and obtaining $\mathbf{f}_r^H\mathbf{H}_{\text{eff}}\mathbf{f}_t$ takes $\sim N_r$ operations. With this procedure repeated $\mathcal{M}$ times, the detector's complexity is $\mathcal{O}(\mathcal{M}(M^2N_t + N_rMN_t + N_tN_r + N_r))$. However, by neglecting the lower-order terms $N_tN_r + N_r$, the complexity of the semi-passive RIS detector can be simplified to $\sim \mathcal{O}(\mathcal{M}MN_t(M + N_r))$.

2. ***Plug-in RIS:*** In the plug-in RIS design, the detector has direct access to $\mathbf{H}_{\text{eff}}$ as explained earlier. Thus, in the initial step, it computes $\mathbf{H}_{\text{eff}}\mathbf{f}_t$, requiring $\sim N_rN_t$ operations. Following this, to calculate $\mathbf{f}_r^H\mathbf{H}_{\text{eff}}\mathbf{f}_t$, the detector performs $\sim N_r$ operations. This process is repeated $\mathcal{M}$ times, resulting in a detector complexity of order $\mathcal{O}(\mathcal{M}(N_rN_t + N_r))$. By omitting the lower-order term N_r, the plug-in RIS complexity can be simplified to $\sim \mathcal{O}(\mathcal{M}N_rN_t)$.

The complexity analysis conducted for both the semi-passive and plug-in RIS detectors demonstrates that the semi-passive RIS detector is more computationally complex, which is numerically shown in Section 5.5.6.

5.5 Illustrative Results - Single User Case

This section evaluates the proposed plug-in RIS for single-user scenarios using five performance metrics: received signal-to-noise-ratio (SNR) for coverage performance, ABER, achievable rate, energy efficiency (EE), and detector complexity. We also validate the ABER performance of the plug-in RIS via the theoretical upper bound. The assessment is conducted in practical scenarios, both indoors (office) and outdoors (street canyon), implementing RIS at the BS and UE sides, respectively. The effectiveness of the plug-in RIS is compared with four benchmarks, which are:

- **Benchmark 1**: *Semi-passive RIS* [80, 57]. This structure has been proposed in the literature as a practical approach that eliminates the need for cascaded channel decoupling [57]. Besides, semi-passive RIS can perform online (real-time) configuration based on the current channel characteristics.

- **Benchmark 2**: *Blind RIS* [92].[2] In the blind RIS configuration, the phase adjustments occur fully randomly; accordingly, there is no necessity for cascaded channel decoupling or control link establishment, like the proposed plug-in RIS.

- **Benchmark 3**: *Amplitude and forward (AF) relay* [93]. AF relay is a traditional method to extend the coverage to the dead zones.

- **Benchmark 4**: *Codebook-based RIS* [94, 95]. This scheme aims to reduce the pilot overhead and streamline the implementation process compared to conventional RIS schemes.

[2] In [92], the blind RIS suggests setting all RIS elements' phase shifts to zero. However, to enhance the performance of the blind RIS in the mmWave communication systems, we set random phase shift adjustments to increase diversity.

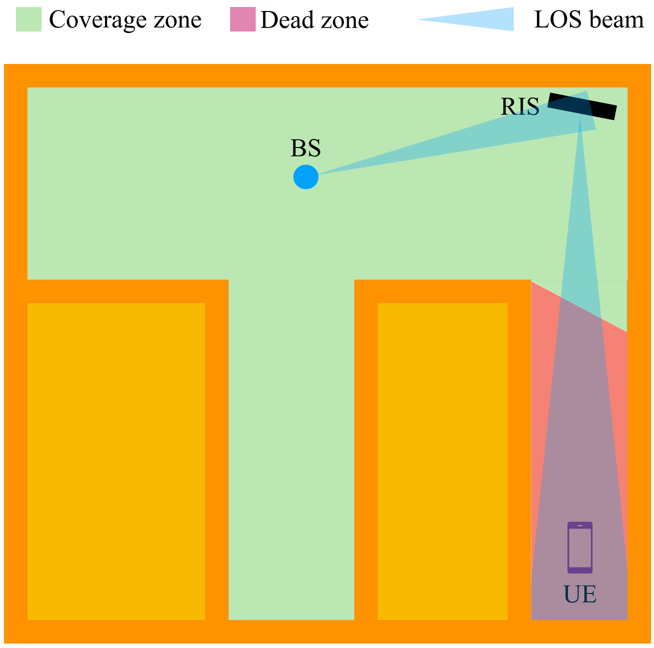

Figure 5.3: Indoor office for BS-side RIS.

5.5.1 Simulation Setup

In this subsection, we describe two wireless communication scenarios to evaluate the performance of the proposed plug-in RIS in enhancing the coverage. These scenarios have also presented in [96] as practical options for RIS implementation.

1. ***Indoor Office (BS-side RIS):*** The first scenario involves an indoor environment with two parallel hallways, as illustrated in Fig. 5.3. In practical situations, the BS is optimally installed to cover maximum areas, but due to mmWave vulnerability to blockage, certain spots and zones become challenging to cover, for instance, one of the parallel hallways in this scenario. Instead of deploying additional costly and inefficient BS, the RIS can be implemented to extend coverage to these dead zones. Here, the distance between the BS (RIS) and the RIS (UE) is 2.5 m (10 m).

2. ***Street Canyon (UE-side RIS):*** For the second scenario, we consider a street canyon environment, shown in Fig. 5.4, where the BS is installed on

Figure 5.4: Street canyon scenario for UE-side RIS.

the rooftop of one building on one side of the street. UEs positioned along the same side of the street experience signal deficiency owing to their placement within the dead zone. While an alternative could involve deploying another BS on top of a building on the opposite side of the street, adopting RIS proves to be a more cost/energy-effective way to cover the dead zone. In this scenario, we assume that the distance between the BS (RIS) and the RIS (UE) is 20 m (10 m).

The carrier frequency is designated as 28 GHz, and the path loss model is employed as follows [100]:

$$PL(d) = a + 10b\log_{10}(d) + 20\log_{10}(f_c), \tag{5.22}$$

where the values of a and b are given in Table 5.2. The analysis assumes a noise power spectral density (PSD) of -174 dBm/Hz, with a bandwidth (B) of 100 MHz [87]. This results in a noise power calculation of $\sigma^2 = -94$ dBm [87]. The antenna gain of each element is considered to be $g_e = 0$ dBi, signifying the utilization of om-

Table 5.2: Simulation parameters.

Parameter	Description	Value
f_c	Carrier frequency	28 GHz
B	Bandwidth	100 MHz
N_t	BS antenna array size	10×10
N_r	UE antenna array size	1
$\delta_x = \delta_y$	Antenna element separation	$\lambda/2$
Noise PSD	Noise power spectral density	-174 dBm
g_e	Antenna element gain	0 dBi
φ_t ($\varphi_{r,ris}$)	Azimuth Tx AoD (RIS AoA)	$\mathcal{U}[-\pi, \pi]$
$\varphi_{t,ris}$	Azimuth RIS AoD	$\mathcal{U}[-\pi, \pi]$
ϑ_t ($\vartheta_{r,ris}$)	Elevation Tx AoD (RIS AoA)	$\mathcal{U}[-\pi/3, \pi/3]$
$\vartheta_{t,ris}$	Elevation RIS AoD	$\mathcal{U}[-\pi/16, \pi/16]$
$(\phi_{b,k}, \theta_{b,k})$	Azimuth and elevation AoD for a two sub-RIS system	$\{(\frac{\pi}{2}, \frac{\pi}{32}),(-\frac{\pi}{2}, \frac{\pi}{32})\}$
$(\phi_{b,k}, \theta_{b,k})$	Azimuth and elevation AoD for a four sub-RIS system	$\{(\frac{\pi}{4}, \frac{\pi}{32}),(\frac{3\pi}{4}, \frac{\pi}{32}),$ $(-\frac{\pi}{4}, \frac{\pi}{32}),(-\frac{3\pi}{4}, \frac{\pi}{32})\}$
$P_{\text{controller}}$	RIS controller power consumption	1.5 W [97]
P_{PA}	Power amplifier power consumption	20 mW [98]
N_{rf}	Number of RF chain	1
M_{active}	Number of RIS active elements	$0.08 \times M$ [57]
P_{PS}	Phase shifter power consumption	30 mW [98]
$P_{\text{RF-chain}}$	RF chain power consumption	40 mW [99, 98]
P_{BB}	Baseband processor power consumption	200 mW [99, 98]
P_{LNA}	Low noise amplifier power consumption	20 mW [99, 98]
$P_{\text{PA\_RIS}}$	RIS element power consumption	10 mW [80]
FOM_W	Walden's figure-of-merit	46.1 fJ/conversion-step [80]
Indoors (a, b)	Path loss parameters	$(32.4, 1.73)$ [100]
d_{BR}	Distance between BS and RIS	2.5 m
d_{RU}	Distance between RIS and UE	10 m
Outdoors (a, b)	Path loss parameters	$(32.4, 2.1)$ [100]
d_{BR}	Distance between BS and RIS	20 m
d_{RU}	Distance between RIS and UE	10 m

nidirectional antennas for every element. The assumed values for system parameters are summarized in Table 5.2.

In the simulation, we consider a limited and known dead zone [96], as depicted in Figs. 5.3 and 5.4, which leads to an assumption that the elevation AoDs of the sub-RISs are constrained within a limited range. Consequently, we consider that the azimuth and elevation AoDs of the sub-RISs are $\varphi_{t,ris} \in \mathcal{U}[-\pi, \pi]$ and $\vartheta_{t,ris} \in \mathcal{U}[-\pi/16, \pi/16]$, respectively. With such assumptions and by adopting a sub-RIS of size 10×10, the sub-RIS can cover a circular area with a diameter of 4 m which is located 10 m away from the sub-RIS. Furthermore, given the fixed position of BS and sub-RISs, we can align the sub-RISs optimally with the BS [87] to meet the desired minimum sub-RISs separation requirements. Based on our discussion in Section 5.3 and as given in Fig. 5.2(a), we assume that $\varphi_t, \varphi_{r,ris} \in \mathcal{U}[-\pi, \pi]$ and $\vartheta_t, \vartheta_{r,ris} \in \mathcal{U}[-\pi/3, \pi/3]$, considering the BS is equipped with a 10×10 antenna array. In other words, we assume that if the incident angle θ_0 is confined to an interval of $[-\pi/3, \pi/3]$, the EFD remains constant.[3] We can consider the maximum amount of EFD in this interval to calculate Δ.

Fig. 5.5 depicts sub-RIS inter-spacing versus different system parameters. As shown in Fig. 5.5, with increasing BS antenna array size, the minimum spacing among sub-RISs Δ decreases due to narrower beams emitted through BS. On the other hand, with increasing the distance between BS and RIS, the EFD increases, which means that the sub-RISs inter-space should be increased to avoid power leakage to the non-targeted sub-RISs. Nevertheless, since the RIS is a passive device, we can increase the number of reflecting elements in each sub-RIS to decrease Δ. This is specifically feasible in the proposed plug-in RIS since increasing the number of elements does not entail more complexity in the system. It is worth emphasizing that since the sub-RISs in the plug-in RIS exploit fixed beams, only traditional end-to-

[3] Note that different antenna arrays' and RISs' sizes, and the use of beam widening techniques, as discussed in [101], can lead to the definition of different AoD and AoA intervals at the terminals. Nevertheless, these aspects are beyond the scope of this thesis and are left for future research directions.

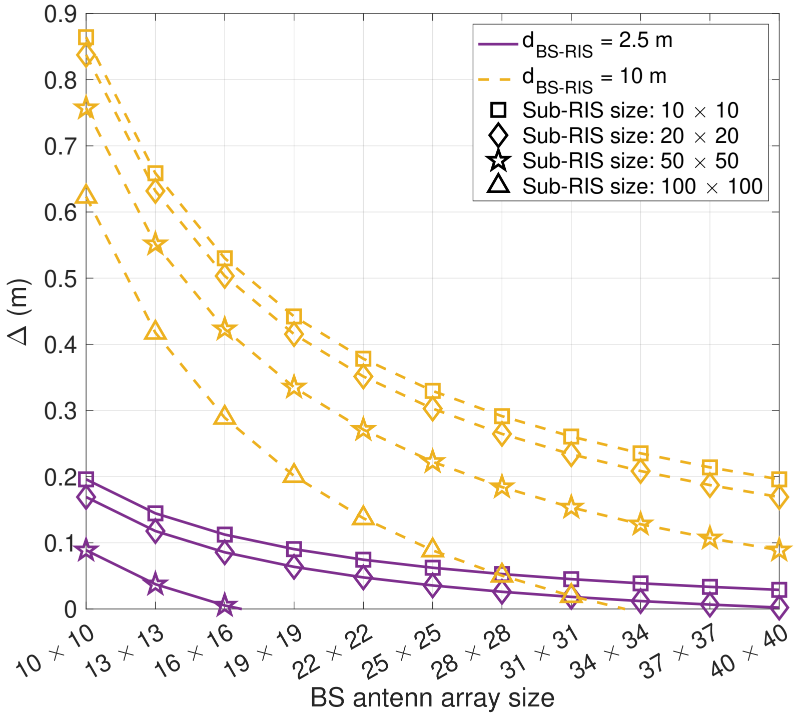

Figure 5.5: The variations of sub-RIS inter-spacing (Δ) with respect to different BS antenna array sizes for different distances and sub-RIS sizes.

end channel estimation is enough, and cascaded channel decoupling is not required in the practical plug-in RIS system, resulting in significant complexity reduction in comparison with semi-passive and fully passive RIS structures, which allows us to easily increase the number of reflectors in the plug-in RIS structure. Fig. 5.5 shows that with increasing the sub-RIS size, the sub-RISs inter-space decreases. Note that in this chapter, we consider BS antenna array and sub-RISs of size 10×10 to prevent high computational burden in the computer simulations, since in the computer simulations, we need to construct the cascaded channels separately for the sake of analysis.

As depicted in Fig. 5.6, various segments within the dead zone are represented in polar coordinates for both two and four divisions. The fixed beam orientation for each segment and several potential UE positions within the dead zone are also illustrated in Fig. 5.6. It is worth mentioning that the information given in Fig.

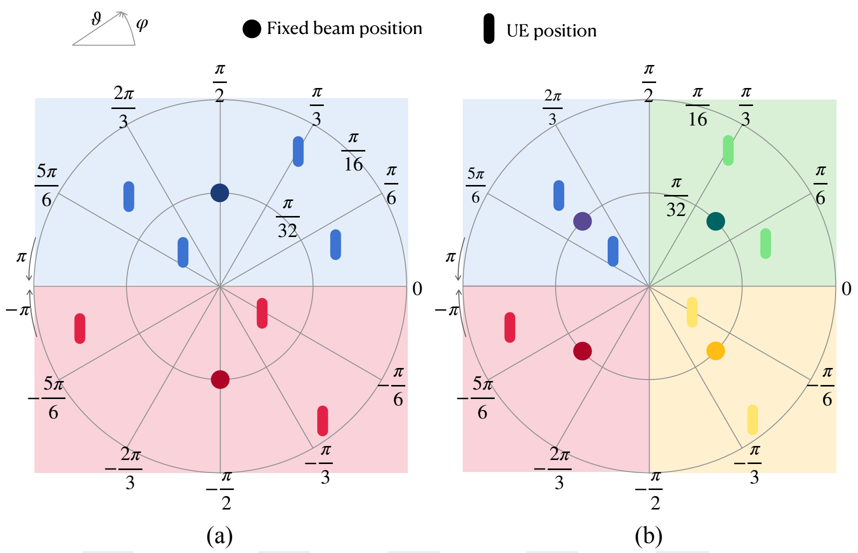

Figure 5.6: Dead zone divisions, fixed beams, and possible UE positions for (a) two segments and (b) four segments.

5.6 is used for plug-in RIS configuration and dead zone segmentation in this chapter. Specifically, for two and four spatial segments, $(\phi_{b,i}, \theta_{b,i}) \in \{(\pi/2, \pi/32), (-\pi/2, \pi/32)\}$ and $(\phi_{b,i}, \theta_{b,i}) \in \{(\pi/4, \pi/32), (3\pi/4, \pi/32), (-\pi/4, \pi/32), (-3\pi/4, \pi/32)\}$, respectively. As the number of segments increases, the average distance between the UE positions and the corresponding fixed beam orientations decreases; consequently, the UEs can receive signals via more favorable beams, which enhances overall system performance. It is important to mention that although Fig. 5.6 shows dead zone division only along the azimuth angle, such division can also be applied along the elevation angle. However, for clarity and simplicity, we have opted not to illustrate more complex divisions in the figures.

It is noteworthy that in this chapter, the system performance analysis is carried out using two and four sub-RIS configurations. For single-user scenarios, only one sub-RIS is used during each transmission period while the rest remain idle. On the other hand, the semi-passive RIS utilizes all implemented elements for maximum performance. In other words, the plug-in RIS uses only a portion of deployed elements, potentially sacrificing passive beamforming gain compared to the semi-passive RIS.

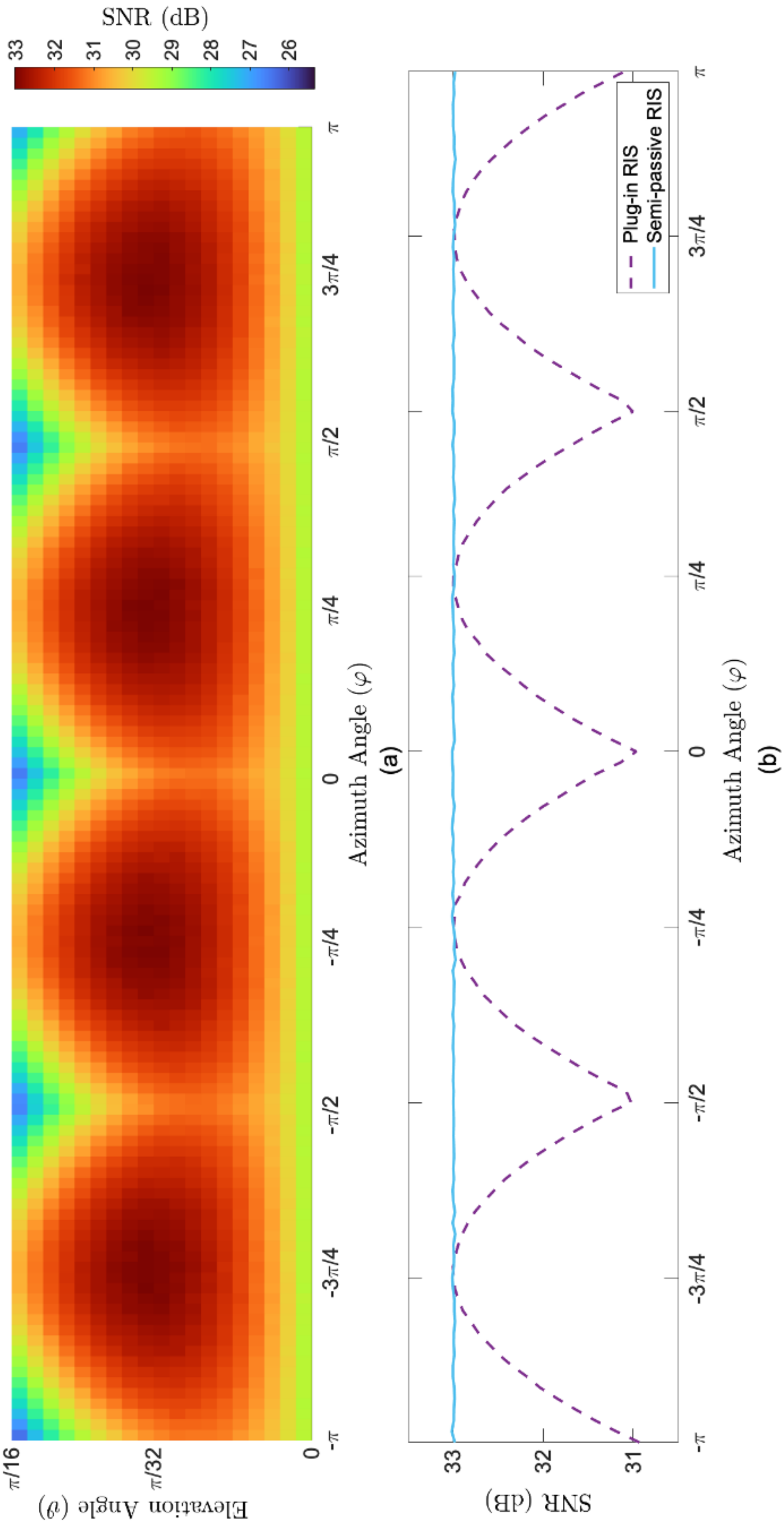

Figure 5.7: Coverage performance of the plug-in RIS; (a) considering all angular locations of the UE, (b) compared to the semi-passive RIS.

However, the semi-passive RIS employs baseband components to estimate the cascaded channels and adjust its phase shifts autonomously, while the proposed plug-in RIS remains fully passive. Therefore, the plug-in RIS offers a favorable trade-off between system performance and EE/cost/complexity. Likewise, for the blind RIS, all implemented elements are engaged in each transmission cycle.

5.5.2 Coverage Performance

This subsection evaluates the plug-in RIS's coverage performance and compares it with the coverage performance of semi-passive RIS in the street canyon scenario. To do this, we calculate the received SNR for all UE's angular locations throughout the dead zone via Monte-Carlo simulation, as illustrated in Fig. 5.7(a). The received SNR can be calculated as follows:

$$\mathrm{SNR} = \frac{|\sqrt{P} G_t G_r \mathbf{f}_r^H \mathbf{H}_{\mathrm{eff},k} \mathbf{f}_t|^2}{\sigma^2}. \tag{5.23}$$

It is worth mentioning that, for this simulation, we considered four sub-RISs, each of size 10×10, along with $P = 10$ dBm. According to Fig. 5.7(a), when UE is located at the center of each segment, the received SNR has its maximum amount of 33 dB. The received SNR decreases as UE moves to the edges of each segment. By counting all the pixels given in Fig. 5.7(a), it has been revealed that for around 85% of the UE's location spots, the received SNR is higher than 30 dB (i.e., within 3 dB of the SNR peak). Furthermore, as illustrated in Fig. 5.7(a), the worst location for UE is the corner of each segment, as expected.

Fig. 5.7(b) demonstrates the coverage performance of plug-in RIS compared to the benchmark, semi-passive RIS. For this simulation, we assumed $\vartheta = \frac{\pi}{32}$ for all the azimuth angles, and the semi-passive RIS is supposed to have a size of 10×10; hence, it has the same beamforming gain with the plug-in RIS in each transmission period. Due to the online configuration, the semi-passive RIS can provide a constant SNR of 33 dB at the UE for all angular locations. The plug-in RIS performance is the same as semi-passive RIS only at the center of each spatial segment. By moving UE to the segment edges, the coverage performance degrades approximately 2 dB and achieves 31 dB at the cell edges.

5.5.3 ABER Performance

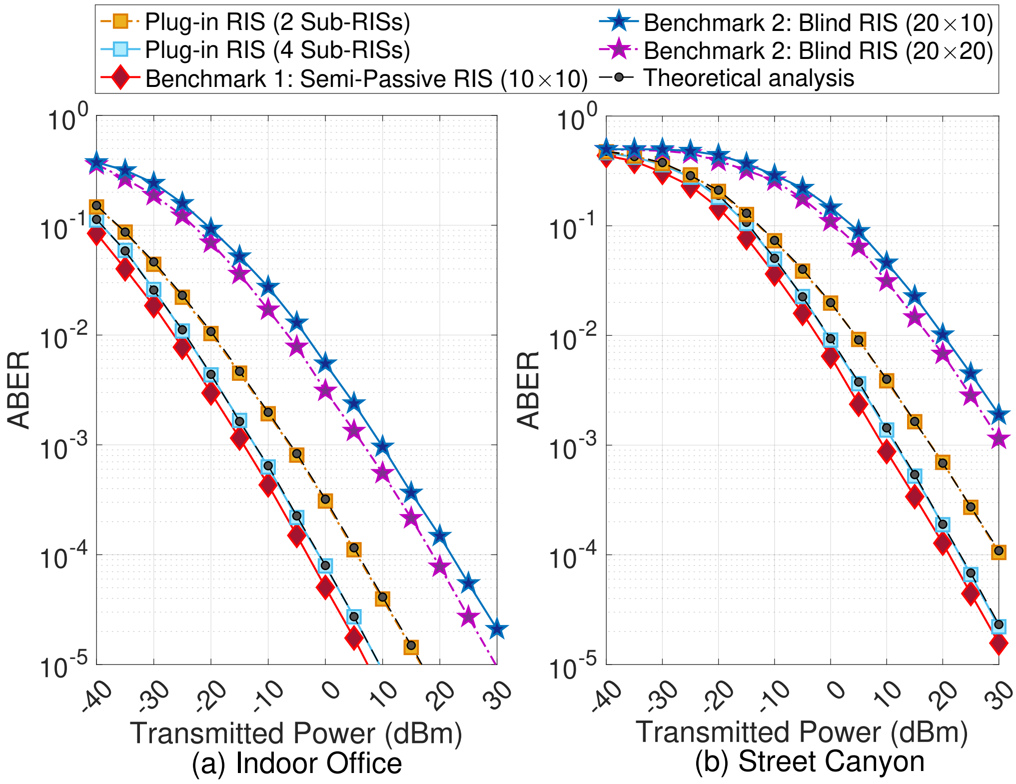

Figure 5.8: ABER performance analysis for (a) the BS-side RIS-aided system in the indoor office environment, (b) the UE-side RIS-aided system in the street canyon environment.

This subsection displays simulation results for the ABER performance of the proposed plug-in RIS. We further verify these results via the analytical upper bound derived in Lemma 6. Here, we utilize a 10×10 RIS for the semi-passive RIS structure to match the passive beamforming gain with the proposed plug-in RIS in each transmission period (since in each transmission period, only one sub-RIS of size 10×10 is used). In contrast, for the blind RIS design, we consider RIS sizes of 20×10 and 20×20 to highlight the superiority of the plug-in RIS over blind RIS.

As depicted in Fig. 5.8, our simulations closely align with the upper bound, confirming the accuracy of the conducted simulations for both indoor office and street canyon scenarios. Notably, we utilized a binary phase shift keying (BPSK) signaling scheme for this simulation. Fig. 5.8 illustrates a substantial performance improvement exhibited by the proposed plug-in RIS when compared with the blind RIS design, even though the blind RIS configuration considered here offers a larger beamforming gain due to its bigger size. Additionally, results in Fig. 5.8 reveal that adopting a plug-in RIS with two sub-RISs results in roughly 9 dB higher ABER compared to the semi-passive RIS. On the other hand, employing four sub-RISs leads to performance enhancement, causing only a 2 dB ABER degradation compared to the semi-passive RIS in both scenarios. It is important to recall that each sub-RIS corresponds to a segment within the dead zone, as shown in Fig. 5.6. Therefore, increasing the number of sub-RISs is equivalent to increasing the number of segments. Consequently, when we increase the sub-RISs from two to four, the ABER performance improves by about 7 dB because the UE has more chance to receive a stronger signal. These outcomes underline the efficacy of the proposed plug-in RIS structure, which proves to be more cost-effective than the semi-passive alternative with a few degradations in ABER.

Fig. 5.9 illustrates the ABER performance with the increasing number of passive elements in each sub-RIS in the plug-in RIS. For this simulation, we assumed that four sub-RISs have been deployed in the street canyon scenario, and the transmit power is considered to be $P = 20$ dBm. With the increasing number of passive elements, passive beamforming gain enhances, resulting in decreasing ABER.

5.5.4 Achievable Rate Performance

In this subsection, we examine the achievable rate performance of the proposed plug-in RIS and compare it with benchmarks. For this subsection, alongside the RIS sizes explored in the previous subsection, we consider an RIS of size of 10×10 for the blind RIS scheme. The achievable rate can be calculated as

$$R = \mathbb{E}[\log_2(1 + \text{SNR})]. \tag{5.24}$$

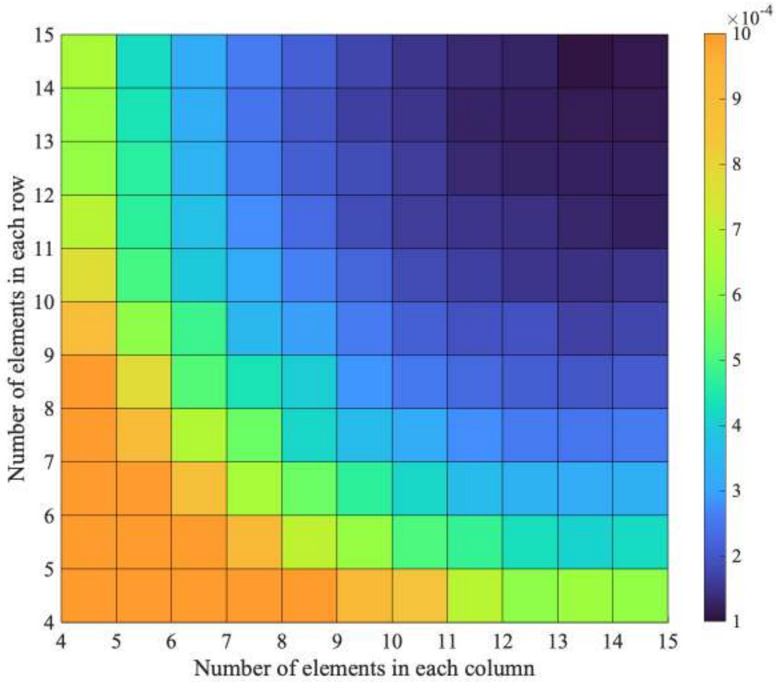

Figure 5.9: ABER performance with increasing number of passive elements in each sub-RIS.

Fig. 5.10 depicts the plug-in RIS performance in terms of achievable rate compared to the three considered benchmark schemes. Similar to the ABER performance, the plug-in RIS exhibits satisfactory achievable rate performance compared to the three benchmark schemes under consideration. Compared with the blind RIS configuration, our novel plug-in RIS configuration significantly improves the achievable rate performance. Likewise, similar to the ABER performance outcomes, even larger-scale blind RIS configurations, which provide more significant beamforming gains, fail to reach the achievable rate performance offered by the plug-in RIS configuration. In comparison to the semi-passive RIS, the proposed plug-in RIS shows a performance degradation of 5 dB with 2 sub-RISs. This degradation decreases to 2 dB when using 4 sub-RISs, demonstrating the impact of higher SNR at the UE due to increased segments in the dead zone. Ultimately, AF relay performance is also given in Fig. 5.10 as another benchmark. In this regard, we consider an AF relay equipped with a single antenna replaced with RIS in both indoor and outdoor

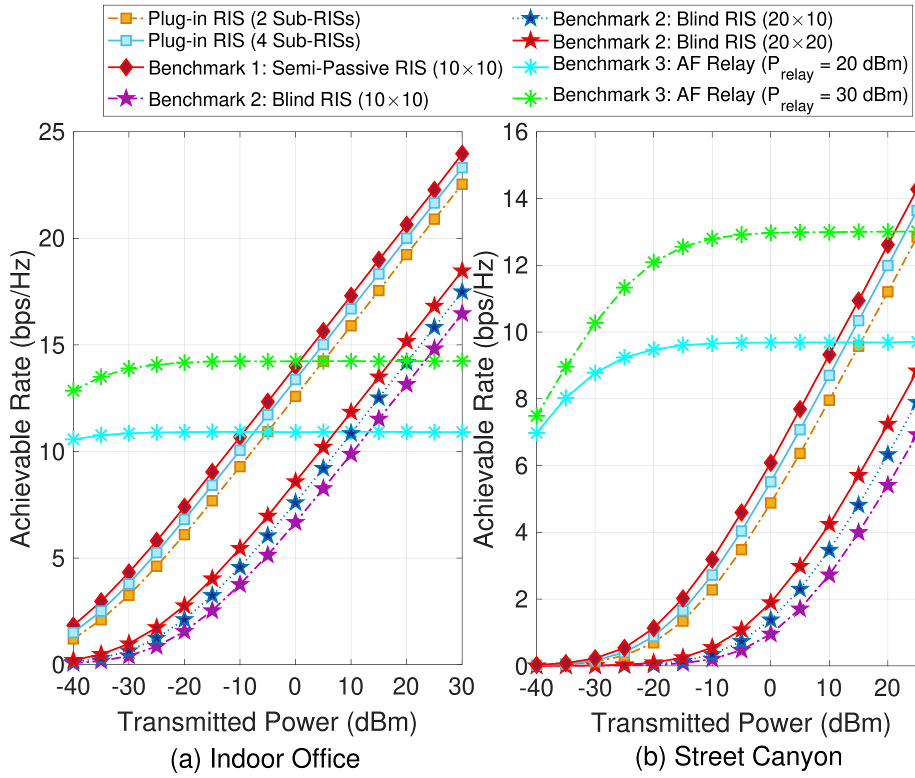

Figure 5.10: Achievable rate performance for (a) the BS-side RIS-aided system in the indoor office environment, (b) the UE-side RIS-aided system in the street canyon environment.

scenarios. As illustrated in Fig. 5.10, for a fixed relay power P_r, with increasing BS transmitted power P, the achievable rate increases; however, after a certain level of P, the achievable rate remains constant. To explain this behavior, we refer to the relay's SNR, which can be calculated as follows [102]:

$$\mathrm{SNR}_{\mathrm{relay}} = \frac{P_r G_t^2 P ||\mathbf{G}||^2 |\mathbf{R}|^2}{P_r |\mathbf{R}|^2 \sigma^2 + G_t^2 P ||\mathbf{G}||^2 \sigma^2 + \sigma^4}. \tag{5.25}$$

By increasing transmitted power P, term $G_t^2 P ||\mathbf{G}||^2 \sigma^2$ prevails over $P_r |\mathbf{R}|^2 \sigma^2 + \sigma^4$. Therefore, in high transmitted power P, we can write $\mathrm{SNR}_{\mathrm{relay}} \approx \frac{P_r G_t^2 P ||\mathbf{G}||^2 |\mathbf{R}|^2}{G_t^2 P ||\mathbf{G}||^2 \sigma^2} = \frac{P_r G_t^2 ||\mathbf{G}||^2 |\mathbf{R}|^2}{G_t^2 ||\mathbf{G}||^2 \sigma^2}$; hence, BS transmitted power has no effect on the AF relay's SNR when surpasses a specified level. On the other hand, with increasing relay's power P_r, the achievable rate increases, as shown in Fig. 5.10. Nonetheless, due to the constant achievable rate performance of the AF relay at the high BS transmitted power, it cannot surpass plug-in RIS in such power levels.

Computer simulation results in this subsection emphasize the effectiveness of our plug-in RIS compared to the benchmarks. While the plug-in RIS may not outperform the semi-passive RIS, its cost-effective passive design merits consideration.

5.5.5 Energy Efficiency

In this subsection, we focus on the strength point of the plug-in RIS design, which is its EE. We also highlight the trade-offs between EE and ABER/achievable rate. The EE is computed as follows:

$$\eta_{EE} = \frac{R \times B}{P_c} \text{ bits/Joule}, \tag{5.26}$$

where P_c signifies the power consumption within the system and can be determined as follows [80]:

$$P_c = P_{\text{Tx}} + P_{\text{Rx}} + P_{\text{RIS}}, \tag{5.27}$$

where P_i ($i \in \{\text{Tx, Rx, RIS}\}$) denotes the power consumption of the respective terminal and can be calculated as follows [98, 99]:

$$P_{\text{Tx}} = P + N_t P_{\text{PA}} + N_{\text{rf}}(N_t P_{\text{PS}} + P_{\text{RF-chain}} + 2P_{\text{DAC}}) + P_{\text{BB}}, \tag{5.28}$$

$$P_{\text{Rx}} = N_r P_{\text{LNA}} + N_{\text{rf}}(N_r P_{\text{PS}} + P_{\text{RF-chain}} + 2P_{\text{ADC}}) + P_{\text{BB}}, \tag{5.29}$$

$$P_{\text{Plug-in RIS}} = P_{\text{Blind RIS}} = M P_{\text{PA\_RIS}}, \tag{5.30}$$

$$P_{\text{Codebook-based RIS}} = P_{\text{controller}} + M P_{\text{PA\_RIS}}, \tag{5.31}$$

$$\begin{aligned} P_{\text{Semi\_Passive RIS}} &= P_{\text{controller}} + M P_{\text{PA\_RIS}} \\ &+ M_{\text{active}}(P_{\text{LNA}} + P_{\text{RF-chain}} + 2P_{\text{ADC(RIS)}}) + P_{\text{BB}}, \end{aligned} \tag{5.32}$$

where M represents for number of RIS/sub-RIS elements engaged in the communication and P_{ADC} (P_{DAC}) is the consumption power of analog-to-digital (ADC) (digital-to-analog (DAC)) converter at the receive (transmit) terminal and can be computed as follows [80, 99]:

$$P_{\text{ADC}} = P_{\text{DAC}} = FOM_W \times f_s \times 2^b, \tag{5.33}$$

where FOM_W corresponds to Walden's figure-of-merit for assessing ADC power efficiency, the variable f_s stands for the Nyquist sampling frequency, while b represents the ADC resolution bits. Our assumption employs $FOM_W = 46.1$ fJ/conversion-step for a 100 MHz bandwidth [80]. We utilize ADCs with 1 bit and 4 bits resolution for the semi-passive RIS [57] and transceivers [99], respectively. We also consider 8% of elements in the semi-passive RIS being connected to baseband components as suggested in [57]. All other parameters align with those defined in Table 5.2.

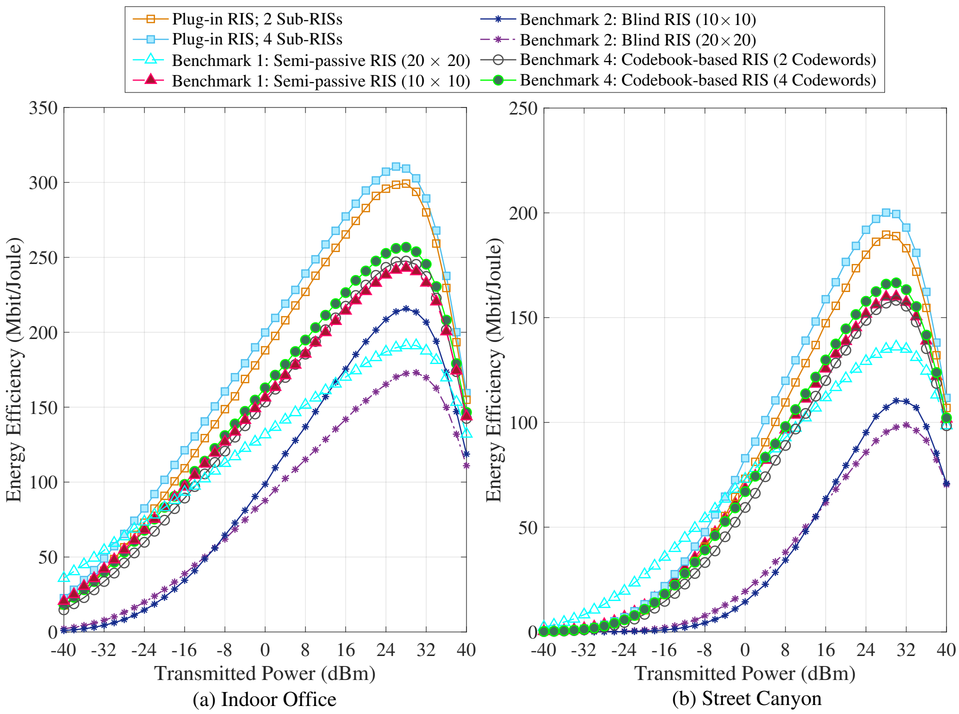

Figure 5.11: Energy efficiency comparison for (a) the BS-side RIS-aided system in the indoor office environment, (b) the UE-side RIS-aided system in the street canyon environment.

As illustrated in Fig. 5.11, the plug-in RIS performs better than all benchmarks in indoor and outdoor scenarios. The performance of the plug-in RIS improves as the number of sub-RISs increases, benefiting from higher SNR and the power-efficient nature of passive elements. Essentially, increasing the number of sub-RISs allows for increasing the number of segments within the dead zone. Consequently, each segment becomes smaller, leading to improved received SNR and better η_{EE}. On the contrary, increasing the number of elements in the semi-passive RIS negatively affects EE and leads to performance deterioration. It is important to note that although enlarging the RIS size in the semi-passive RIS configuration increases received SNR due to enhanced beamforming gain, it also involves more baseband components in the RIS structure, resulting in higher power consumption. In this case, power consumption primarily impacts EE performance and leads to decreased EE.

Similarly, in the case of the blind RIS, increasing the number of elements reduces EE due to the dominant effect of power consumption by passive elements. In other words, in the blind RIS, increasing the passive elements has a more negative effect on power consumption than its positive effect on beamforming gain. It is worth mentioning that a notable EE performance gap exists between blind RIS and the proposed plug-in RIS, primarily due to the enhanced SNR provided by the plug-in RIS without a proportional increase in power consumption. The EE performance of the codebook-based RIS is also depicted in Fig. 5.11, which is worse than the plug-in RIS due to the controller power consumption of codebook-based RIS. It is worth mentioning that the higher the number of codewords, the more the EE performance is enhanced, similar to the plug-in RIS, which indicates better performance with increasing the number of sub-RISs.

5.5.6 Detector Complexity

The detector complexity for different numbers of transmit antennas, RIS elements, and constellation orders is depicted in Fig. 5.12. As shown in Fig. 5.12(a), it is evident that the plug-in RIS's detector exhibits significantly lower computational complexity compared to the semi-passive RIS's detector. It is worth noting that the increase in the number of RIS elements (M) has a more significant impact on the complexity of the semi-passive RIS detector compared to the increase in the number of antennas (N_t); this is attributed to the quadratic relationship between M and the detector complexity in the semi-passive detector expression, while the plug-in RIS design remains unaffected by the increase in M. Note that in Fig.

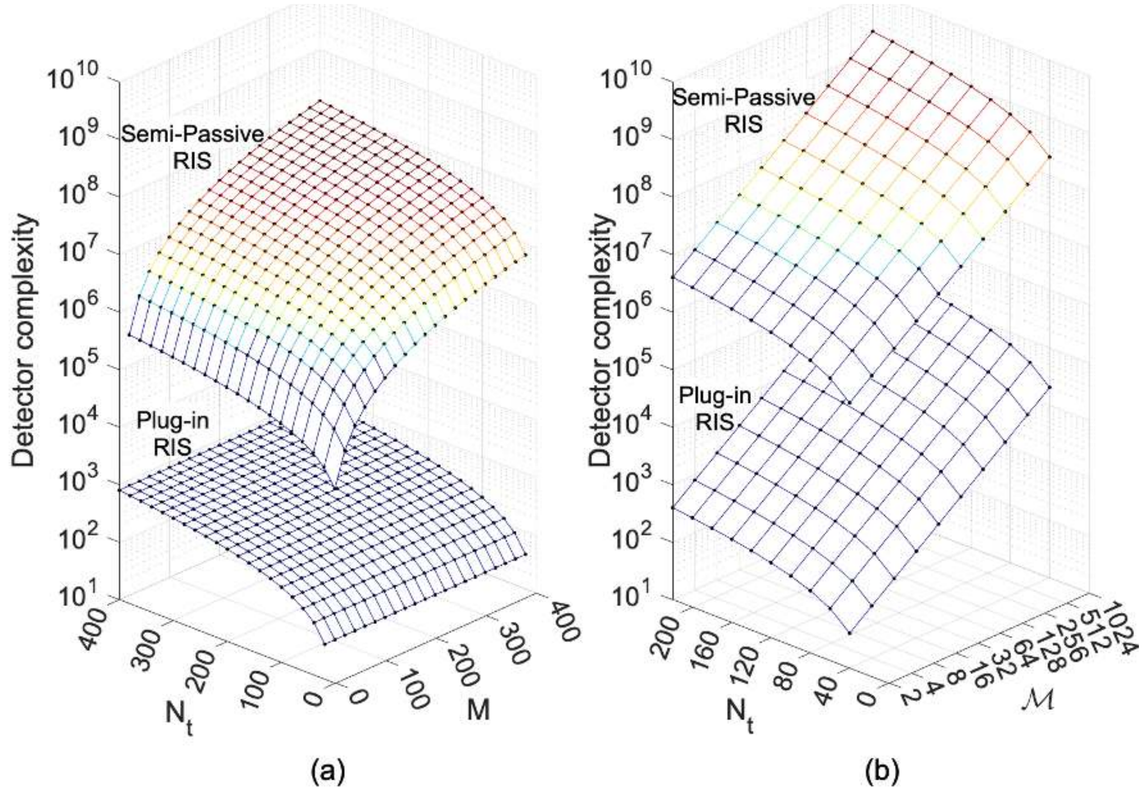

Figure 5.12: Detector complexity comparison as a function of (a) number of transmit antennas, N_t, and number of RIS elements, M, (b) number of transmit antennas, N_t, and constellation order, $\mathcal{M}$.

5.12(a), we have considered $\mathcal{M} = 2$. Fig. 5.12(b) further illustrates how variations in N_t and $\mathcal{M}$ affect detector complexity while maintaining a constant number of RIS elements ($M = 100$), emphasizing the superiority of the proposed plug-in RIS over semi-passive RIS design.

5.6 Illustrative Results - Multi User Case

This section investigates the SINR performance of the proposed plug-in RIS in an MU scenario. We consider a system setup with two UEs, two spatial segments, and the street canyon environment and investigate two different cases to ensure a more precise analysis: in case 1, both UEs are located in the same segment, while

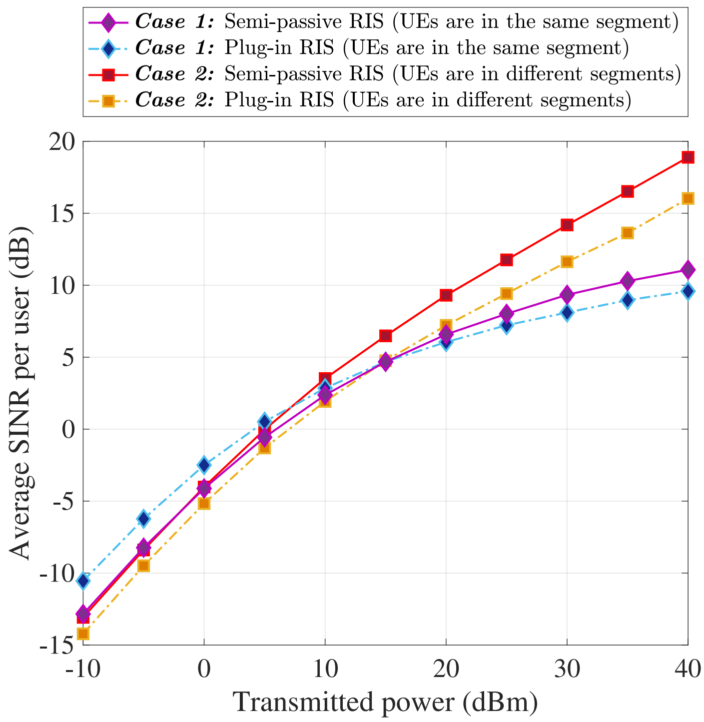

Figure 5.13: Average SINR performance of the plug-in RIS compared to the semi-passive RIS for a two-UE scenario.

in case 2, they are situated in different segments. Note that, for a fair comparison, we consider the same RIS size for semi-passive RIS and each sub-RIS, i.e., 10×10; hence, in each transmission period, the same number of reflectors engaged in the communication for both schemes, resulting in the same passive beamforming.

Fig. 5.13 compares the SINR performance of MU-plug-in RIS and MU-semi-passive RIS. It is important to highlight that, in the case of MU-semi-passive RIS, we employed one RIS for each UE to ensure effective passive beamforming. Sharing a single semi-passive RIS among two UEs results in the beamforming gain of the RIS being divided between them, thereby declining the effectiveness of passive beamforming. As shown in Fig. 5.13, at high transmitted power levels, plug-in RIS experiences 1.5 dB and 3 dB performance loss compared to the benchmark for case 1 and case 2, respectively. The lower performance loss of case 1 can be attributed to the better performance of plug-in RIS in this scenario. The plug-in

RIS in case 1 only exploits one sub-RIS for serving both UEs; hence, there is only interference in the BB stage, while in the other scenarios, two RISs/sub-RISs are adopted, which entails interference in the analog stage as well. Accordingly, the regularized zero-forcing (RZF) BB precoder works more efficiently in plug-in RIS under case 1's setup. In order to cancel interference in both analog and BB stages, more sophisticated precoder designs like joint-group-processing (JGP) and common-group-processing (CGP) are required, as described in [90, 71]. The interference effect at the analog stage is more dominant at the low power levels; hence, plug-in RIS under case 1's setup performs better than the other setups.

5.7 Conclusion

This chapter has introduced a practical RIS structure, the plug-in RIS, for mmWave communication systems to enhance coverage to the dead zones. The plug-in RIS operates passively, cleverly integrating the control mechanism within the transmitted beam to the RIS, eliminating the need for conventional reliable control links. It also relaxes the channel estimation process by eliminating complex cascaded channel decoupling, a common challenge in RIS-assisted systems. In this approach, dead zones are divided into segments, each served by a dedicated sub-RIS with a fixed beam. Computer simulation results have shown that deploying four sub-RISs causes only slight degradation in ABER and achievable rates, making fully passive operation feasible. We have also compared the EE of the plug-in RIS with benchmarks. While the semi-passive RIS slightly outperforms the plug-in RIS in terms of ABER and achievable rate, its EE performance is worse than the proposed plug-in RIS due to active baseband components. Besides, the plug-in RIS detector exhibits superior complexity performance compared to the semi-passive RIS thanks to the conventional channel estimation mechanism. Ultimately, extending the plug-in RIS into an MU scenario has also been investigated by studying the average SINR performance compared to the semi-passive RIS. It has been revealed that adopting plug-in RIS in an MU scenario only results in a few dB of performance loss compared to the semi-passive RIS. Nevertheless, MU solutions to mitigate interference can be future research directions that require more sophisticated design scenarios by considering advanced algorithms.

In summary, our plug-in RIS proves to be a compelling solution, performing closely to the semi-passive RIS regarding ABER and achievable rate performances, surpassing the benchmarks in terms of EE performance and detector complexity, and addressing challenges in mmWave systems.

Chapter 6

A COMPREHENSIVE DESIGN FRAMEWORK FOR UE-SIDE AND BS-SIDE RIS DEPLOYMENTS

6.1 Introduction

Reconfigurable intelligent surfaces (RISs) represent an emerging technology with significant potential for sixth-generation (6G) communication networks. RISs offer the capability to actively mitigate the detrimental effects of the propagation environment, such as multipath fading [14]. In other words, RISs pave the way for the realization of *smart radio environments*, where the environment itself becomes an active participant in wireless transmission by dynamically managing signal reflection/refraction across different locations [14].

One of the most compelling applications of RISs is their deployment in close proximity to either the base station (BS) or the user equipment (UE). This strategic placement, known as BS-side and UE-side RIS [15], offers distinct advantages tailored to specific network requirements. However, what exactly do these terms mean, and why are they critical for future networks?

BS-side RIS refers to a scenario where the RIS is positioned near the BS, enabling a reliable control link as the wireless service provider can efficiently establish and maintain control links between the BS and its RIS units. This setup simplifies the configuration process by leveraging the BS's advanced hardware capabilities. On the other hand, UE-side RIS involves placing the RIS near the UE, which can significantly enhance signal quality in challenging environments, such as areas with poor coverage or high interference. However, establishing reliable control links between BS and UE-side RISs can be challenging as these RIS units may be distant from the BS without a strong line-of-sight (LOS) connection. Additionally, a high number of

UE-side RIS units could impose substantial control signaling overhead on the BS. Hence, the wireless service provider cannot efficiently control UE-side RISs.

By understanding the unique benefits and challenges associated with each deployment strategy, we can better tailor RIS designs to meet the specific demands of 6G networks. The following sections explore how these strategies can be optimized to achieve the best performance in various scenarios.

Fig. 6.1 showcases diverse RIS applications tailored to address specific challenges in wireless communications systems. As a *BS-side* application, RISs can simplify the hardware design of BS by using passive elements instead of active power-hungry components, reducing both power consumption and overall system cost (scenario 1 in Fig. 6.1) [103, 104]. On the other hand, the *UE-side RIS* shines in scenarios where user mobility and varying coverage conditions (like dead zones and cell edges which may encompass a various range of conditions, such as Scenarios 4–7 illustrated in Fig. 6.1) present significant challenges. This challenge is particularly pronounced in high-frequency communication systems like millimeter-wave (mmWave) and terahertz bands. Traditionally, covering entire environments requires deploying additional BSs or relays, but this can be costly and inefficient. RISs offer a cost/energy-efficient solution as a programmable reflector network within the environment, addressing the coverage dilemma [105, 106]. The UE-side RISs can also realize the implementation of large arrays in the UE in a more compact and cost-efficient manner (Scenario 8 in Fig. 6.1) [107].

While BS/UE-side RIS deployments are particularly effective in the scenarios mentioned above, their applications extend far beyond these examples. These deployments are poised to play a crucial role in a wide range of emerging 6G technologies, including non-terrestrial networks (Scenarios 5 and 6), localization and sensing (Scenario 2), vehicular networks (Scenarios 5, 7, and 8), and more.

Although current literature considers both BS-side and UE-side RIS system designs, it is still unclear how their design parameters change from one to another. In particular, design parameters related to the RIS, such as its size, phase shift adjustment, control link, placement and deployment, and elements type (passive/active),

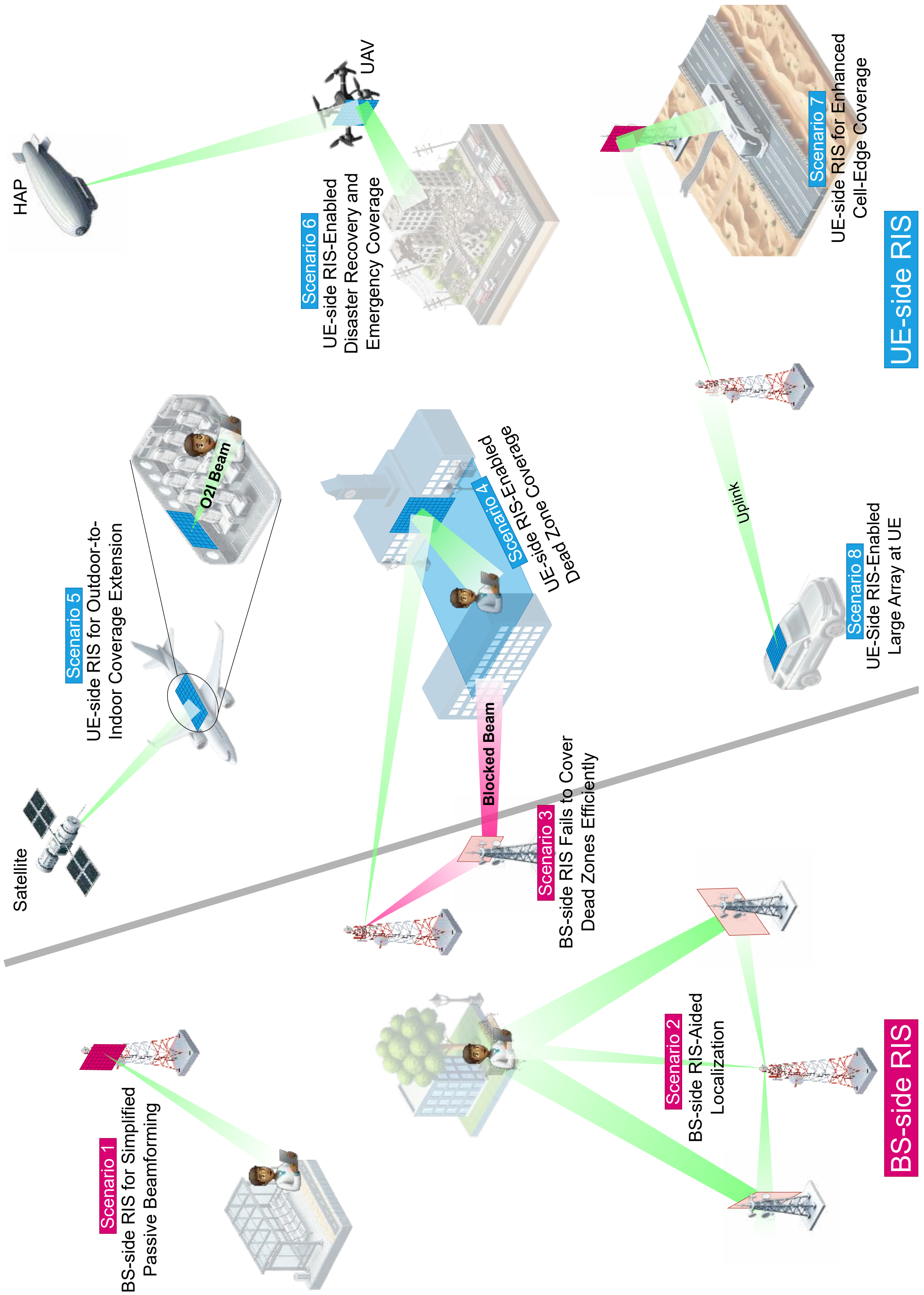

Figure 6.1: BS-side and UE-side RIS deployments within a generic RIS-assisted wireless network.

are yet to be differentiated among the two scenarios (BS-side and UE-side). Overlooking these parameters' differences while designing the RIS-assisted system affects their implementation feasibility, leading to a big gap between theoretical research and industry. For instance, when we examine the control link as an essential design parameter, it becomes apparent that the BS-side RIS system benefits from a more reliable control link. This advantage arises from the static positioning of both the BS and the RIS, enabling the utilization of a robust LOS wireless backhaul link or even a fiber optic cable. In contrast, ensuring a similarly robust control link in the UE-side RIS system is challenging, primarily attributed to resource constraints and UE's mobility. Extending this discussion to the other design parameters can reveal critical issues between the theoretical assumptions and implementation restrictions, which motivates this study.

In this chapter, we investigate the RIS-related design parameters for the BS/UE-side scenarios, shedding light on the critical differences that need to be considered by system designers. Specifically, by considering these parameters individually, we discuss how each scenario has different requirements/settings for that parameter. Accordingly, we provide a practical guideline to distinguish between these two scenarios from the system design and implementation perspectives.

6.2 Key Aspects of RIS Deployment Framework

Optimizing RIS deployment strategies is crucial for enhancing performance across various communication scenarios. Understanding the differences between BS-side and UE-side implementations is essential to address practical deployment considerations. This section explores these deployment strategies and highlights the key design parameters influencing their effectiveness.

6.2.1 Deployment Strategies: BS-side and UE-side RIS

An RIS deployment is considered BS-side when the RIS is located near the BS. In this case, the wireless service provider establishes a backhaul control link between the BS and RIS. When phase shift reconfiguration is required, the BS computes

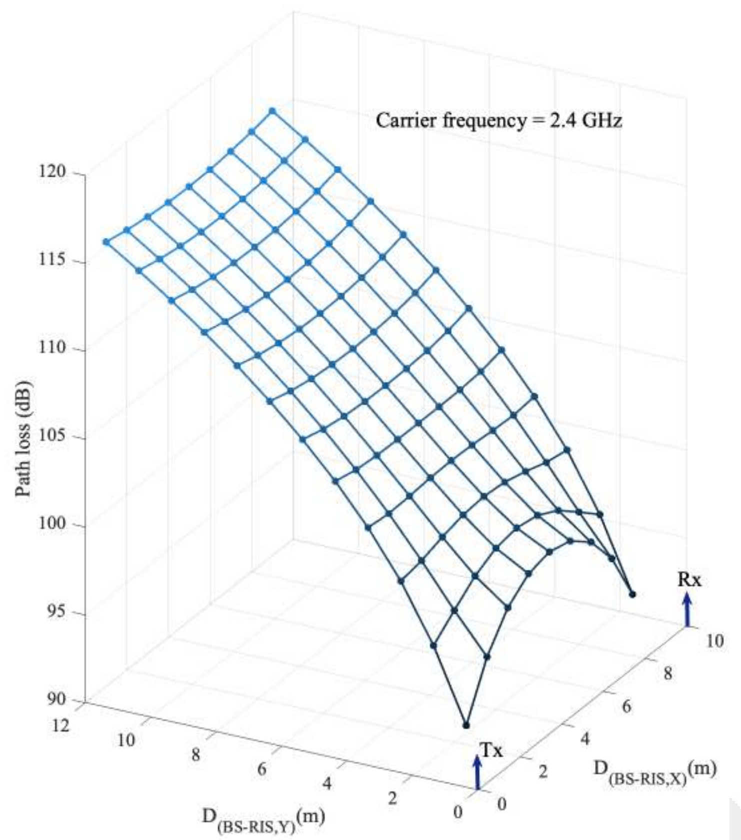

Figure 6.2: Two-way path loss in an RIS-assisted system over different RIS locations.

the optimal phase profile based on the current channel state information (CSI) and communicates this profile to the RIS control unit.

Conversely, in a UE-side RIS deployment, the RIS is positioned near the UE. As discussed earlier, in this case, the practical issues like lack of reliable control link and heavy signaling overhead preventing BS to control the RIS. Hence, in this case, UE is responsible for optimizing and controlling the RIS. Additionally, the RIS design should prioritize simplicity and energy efficiency, reflecting the UE's limited computational resources and mobility constraints.

In principle, the potential for RIS placement is virtually limitless, with the possibility of deploying these surfaces across diverse locations within the environment; however, practical limitations narrow down these possibilities. The primary constraint related to deploying RIS lies in the significant path loss associated with the signals imping and reflecting from its surface. Fig. 6.2 suggests that integrating the RIS within the transceivers minimizes free-space multiplicative path loss and offers optimal placement; nevertheless, it does not count the effect of other factors like, shadowing, large/small scale fading, space limitation, UE movement, and environmental obstacles. Such factors result in optimal RIS placement separated from the BS/UE. This leads to classifying each deployment strategy into two categories. When the RIS is closely integrated with the BS or UE, it is termed a BS/UE-side integrated RIS. If the RIS is deployed separately and not physically attached to the BS/UE, it is called a BS/UE-side separated RIS.

Note that in Fig. 6.2, the BS and UE are positioned at the coordinates $(0, 0)$ and $(10, 0)$, respectively. The RIS is deployed within the same 2D plane, with the projection of each simulated point onto the XY plane representing the location of the RIS. $D_{(\text{BS-RIS,i})}$ represents the distance between BS and RIS along $i \in \{X, Y\}$ axis while $D_{\text{BS-UE}}$ is the distance between BS and UE. Although path loss generally increases as the RIS is deployed farther from the terminals, exceptions do exist. Some cases necessitate us to consider $D_{(\text{BS-RIS,Y})}$ constant. In such cases, when $D_{(\text{BS-RIS,Y})} \geq D_{\text{BS-UE}}/2$, the best placing for RIS is $D_{(\text{BS-RIS,X})} = D_{\text{BS-UE}}/2$, as shown in Fig. 6.2 and discussed in [108]. However, this is an exceptional case that does not happen frequently.

6.2.2 Key Design Parameters

The performance and efficiency of RIS deployments are determined by several key design parameters that must be carefully balanced to achieve optimal results. These parameters—such as reliable control link, RIS size, phase shift adjustment, and element type—are not independent; rather, they are interconnected and jointly influence critical aspects like channel estimation overhead, resource allocation, and system complexity. A comprehensive understanding of these interrelations is crucial for developing a robust deployment strategy, whether in BS-side or UE-side scenarios.

1. *Control Link:* Establishing a reliable control link is essential for dynamically

adjusting the phase shifts of the RIS elements based on CSI. Depending on the deployment, this link can be either wired or wireless. In BS-side RIS, the proximity to the BS allows for more stable and reliable control link, often facilitated by a LOS connection or even a wired backhaul. This leads to reduced channel estimation overhead since the statistical CSI (S-CSI) dominates over instantaneous CSI (I-CSI), allowing for a less frequent estimation process. Conversely, in UE-side RIS, the wireless control link faces greater challenges due to the mobility of the UE, the increased likelihood of obstacles, and the potential for a more dynamic channel, all of which require more frequent CSI updates.

2. *Phase Shift Adjustment:* The flexibility and resolution of RIS phase shift adjustments are crucial for performance. BS-side RIS levera ges the BS's advanced capabilities for high-resolution/continuous adjustments to optimize performance. In contrast, UE-side RIS relies on simpler, low-complexity configurations suited to the UE's limited resources to balance precision and efficiency.

3. *RIS Size:* The physical dimensions of the RIS directly affect its beamforming capabilities and overall effectiveness. Larger RIS panels provide greater beamforming gain and are more feasible in BS-side deployments, where space, stable mounting points, and complex hardware for resource allocation are available. In contrast, UE-side deployments face size constraints and limited resources, restricting the use of large-scale RIS and requiring more compact designs that still ensure sufficient performance in mobile contexts.

4. *Element Type:* The choice between passive and active elements in RIS design depends on deployment strategy and performance needs. Passive elements, being more energy-efficient, are preferred in BS-side RIS due to the available space for larger implementations. In contrast, UE-side RIS may require active elements to amplify signal strength, though this comes with higher complexity

and power consumption.

6.3 BS-Side RIS Deployment

This section presents an overview of the BS-side RIS deployment, including its importance and potential applications.

In practice, the BS maintains a fixed location, allowing for strategic placement/orientation of the RIS to establish a LOS link with the BS. Furthermore, the proximity and immobility of the BS and the RIS in this design simplify channel estimation and enable a reliable control link from the BS to the RIS, as discussed in Section 6.2. Besides, owing to the more resources and sophisticated hardware available on its side (compared to the UE side), the BS can support advanced functionalities such as cascaded channel estimation/decoupling and joint active and passive beamforming optimization with high-resolution phase shifts to optimally configure the RIS. Additionally, BSs are typically positioned at elevated locations with plentiful space in the surrounding environment, making deploying a large RIS surface possible. A large-size RIS provides significant beamforming/multiplexing/array gain, reducing the overall path loss while maintaining cost-effective and energy-efficient hardware.

To illustrate the potential of BS-side RIS applications, we present two examples highlighting its advantages in alignment with the anticipated 6G requirements in terms of energy/spectral efficiency enhancement.

1. *Enhanced energy efficiency*: In [103], a BS-side RIS design is proposed to reduce the required number of RF chains at the BS side. This approach involves implementing the RIS to redesign the classical Alamouti's scheme with a single RF chain instead of the traditional two, reducing cost and power consumption on the transmitter side. The advantage of such an approach in designing the BS is more evident in the generalized scenario of Alamouti's scheme: a large-scale RIS-assisted space-time block code (STBC) MIMO system, leading to considerable power saving and enhanced energy efficiency.

2. *Enhanced spectral efficiency*: Integrating passive RISs directly into the BS structure can facilitate passive beamforming/multiplexing cost-effectively [104], as illustrated in the Scenario 1 in Fig. 6.1. This novel design lets us directly reconfigure the signals incoming/outgoing from the BS without encountering substantial path loss due to the extremely short distance between BS and RIS. In this regard, the authors demonstrated that deploying an integrated RIS with the BS yields superior performance in terms of spectral efficiency compared to the conventional system without RIS.

6.4 UE-Side RIS Deployment

Another practical approach for RIS deployment is to place it near a single UE or a cluster of UEs where the UE-RIS channel is more stable than BS-RIS, and UE has control over the RIS.

Due to UEs' mobility, they may end up in regions with weak/no network coverage. The conventional solution of adding more BSs/relays to address this issue can be practically costly and energy inefficient [14]. Specifically, this challenge becomes more prominent when higher frequencies (like mmWave and terahertz bands) are adopted in future 6G networks, causing manifold dead zones due to the vulnerability to signal blockages. Since a BS-side RIS may encounter similar obstacles as the BS alone, deploying the RIS on the UE side is a more favorable solution to address the coverage issue. Thus, the RIS can establish an alternative link to the main blocked one by providing reflection paths reaching the dead zone. By strategically positioning each RIS in UE proximity, a reliable LOS link between the RIS and BS/UE can be guaranteed [105]. A relatively more reliable control link (compared to the BS-RIS link) enables the UE to control the RIS independently from the BS.

Here, we present two examples from the current literature to provide concrete context to the concept of UE-side RIS and its impact on the 6G requirements.

1. *Enhanced reliability:* As discussed in [11], a primary use-case for RIS is extending the coverage to the cell edge and dead zone when the direct link between

the BS and UE is weak or blocked, as illustrated in Scenarios 4, 6, and 7 in Fig. 6.1. Another attractive scenario is the coverage extension in an outdoor-to-indoor (O2I) setup where the BS is implemented outdoors while the UE is located indoors and receives weak/no signals [109], as depicted in the Scenario 5 in Fig. 6.1.

2. *Enhanced user-experienced data rate:* Enabling a large-scale antenna array at the UE has been seen as unfeasible due to size, energy consumption, and cost limitations [107]. Nevertheless, the recent study of [107] has introduced a UE-side RIS design that leverages multi-layer RIS surfaces to achieve a system performance similar to that obtained using a large-scale antenna array. Consequently, an amplified beamforming/array gain can be realized, raising the user-experienced data rate.

6.5 Key Considerations in RIS Tuning

In order to achieve optimal performance in an RIS-assisted system, a dynamic RIS configuration based on I-CSI is required. The responsible terminal calculates the optimal phase shift profile and conveys this information to the RIS's control unit. Inefficient control and configuration can negatively affect the system's overall performance by limiting the functionality of the RIS. In what follows, we explore the key considerations involved in RIS tuning, focusing specifically on the practical aspects of control link management and phase shift configuration for both BS-side and UE-side scenarios.

6.5.1 Control Link

In order to guarantee optimal RIS tuning, a robust control link with sufficient capacity to transmit control information from the responsible terminal to the RIS needs to be established. Based on the operating scenario and RIS deployment strategy, selecting a control link medium can encompass various options, such as fiber-optic cables, metal-based wiring, or wireless links.

For BS-side RIS deployments, where both the BS and RIS have fixed locations, fiber-optic cabling can be the optimal choice for the control link regarding capacity and reliability. Nevertheless, a wireless link can be an alternative option for more flexible RIS placement/orientation to achieve optimum tuning.

In contrast, when deploying the RIS on the UE side, the cabling/wiring solution is often impractical due to UE mobility. Establishing a dedicated wireless control link is the most feasible solution. The only exception is when the RIS is integrated within the UE, as the stationary positions of the UE and RIS relative to each other make metal-based wiring a viable option for creating a dedicated control link [107].

6.5.2 Phase Shift Profile Design

One of the main and essential functions of RISs is their ability to focus the reflected signal into a specific spatial direction without using active RF components (passive beamforming). This is realized by adjusting the phase shifts of individual RIS elements relying on the CSI. Phase shift adjustment can be continuous or discrete. Continuous phase shifting results in superior performance enhancement, while discrete phase shift adjustment is cost-effective and less complex.

Considering the availability of sophisticated hardware and the feasibility of implementing a high-capacity control link at the BS, configuring BS-side RIS with continuous (high-resolution) phase shifts is feasible, enabling optimal RIS tuning. On the other hand, since the UEs typically suffer from limited hardware, and the UE-RIS control link cannot guarantee high-capacity communication, implementing low-complexity RIS configuration schemes in the UE-side RIS is essential; accordingly, control signaling is preferred to be simple to prevent high signaling overhead and long latency. The first simulation in Fig. 6.3 shows that as control link bandwidth (B_c) increases, the ratio of control signaling time (T_F) to the total time block (T) decreases. This indicates that a high-capacity control link can transmit high-resolution control signals with minimal time allocation. The simulation assumes an RIS of size 10×10. Relevant parameters and formulas are given in [110]. Besides, heuristic approaches can be exploited to design a low-complex phase-shift configura-

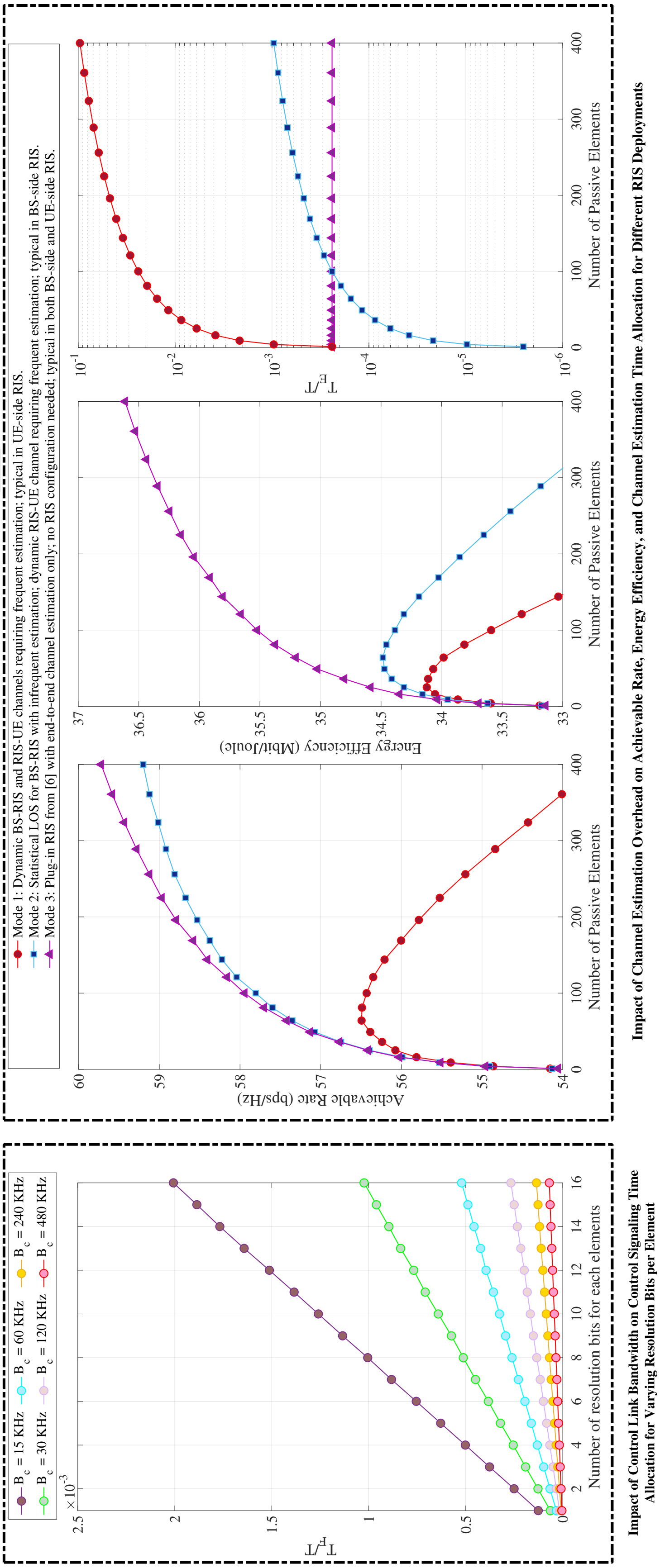

Figure 6.3: Effects of control link bandwidth, control signaling, and channel estimation overhead on RIS performance metrics. The necessary formulas and parameters for these simulations can be found in [110].

tion scheme [111]. Another alternative can be adopting codebook-based schemes to decrease overall complexity and signaling overhead between the UE and RIS while maintaining satisfactory performance [94].

6.6 Design Aspects for Peak Performance

After optimizing the RIS tuning parameters, the focus must shift to key design considerations aimed at further mitigating multiplicative path loss and enhancing RIS beamforming gain. In this context, we examine two fundamental design parameters: RIS size and element type.

6.6.1 RIS Size

A key to mitigating the multiplicative path loss— the major challenge in RIS-based communication— is using an RIS with a large number of elements. However, deploying a large RIS requires sufficient physical space (e.g., a 10×10 planar RIS with half-wavelength spacing at 2.4 GHz spans approximately 56 cm $\times$ 56 cm) and adequate resources to support channel estimation and the joint optimization of active BS/UE beamforming and passive RIS beamforming to ensure peak performance.

BS-side deployments generally offer ample space for larger RIS structures. Additionally, the advanced hardware at the BS can handle the computational complexity of large-scale RIS setups, including channel estimation and joint active-passive beamforming optimization. Furthermore, placing the RIS near the BS and leveraging the fixed positions of both allows for a stable statistical LOS channel, reducing the need for frequent BS-RIS channel estimation. This reduction in channel estimation overhead decreases time/power allocation to the pilot signals, significantly improving performance.

Unlike BS-side RIS deployments, UE-side RIS implementations often face space constraints for large arrays. This limitation is evident in integrated RIS setups on the UE side. To address this, a multi-layer RIS structure was proposed in [107]. Similarly, in O2I coverage extension scenarios where a transparent RIS is embedded in a window [109], space limitations can reduce the RIS size, potentially providing inadequate passive array gain to counteract multiplicative path loss. However, exceptions exist; for example, deploying large RIS surfaces on building facades near dead zones, such as in street canyons, can provide substantial passive array gain to overcome multiplicative path loss. Additionally, in UE-side RIS designs, the dynamic channels demand frequent estimation. UEs also lack the advanced hardware and resources available in BS-side deployments, limiting optimal RIS operation. These limitations lead to poorer performance for UE-side RIS, compared to BS-side RIS.

Fig. 6.3 shows how reduced channel estimation overhead affects channel estimation time T_E, achievable rate, and energy efficiency across RIS deployments. In order to have a fair comparison, we considered three different modes:

- *Mode 1*: Represents dynamic BS-RIS and RIS-UE channels that require frequent channel estimation, typical for *UE-side RIS* deployments where both links are highly dynamic.

- *Mode 2*: Assumes a statistical LOS for the BS-RIS channel with infrequent estimation and a dynamic RIS-UE channel needing frequent updates, typical for *BS-side RIS* deployments.

- *Mode 3*: Refers to the Plug-in RIS [105] with end-to-end channel estimation only, without requiring RIS configuration; applicable to both *BS-side* and *UE-side* deployments, offering minimal overhead.

In Mode 1, frequent channel estimation for both BS-RIS and RIS-UE links results in high overhead, reducing performance after a peak. Mode 2 benefits from a statistical LOS BS-RIS channel, requiring less frequent estimation, thus improving efficiency. Mode 3, with end-to-end estimation only, has minimal overhead, achieving the highest rate and efficiency consistently.

As shown in Fig. 6.3, innovative designs like Plug-in RIS can overcome the overhead problem and improve performance. Developing such structures is crucial for addressing the practical challenges of RIS implementation.

6.6.2 Element Type

Deploying large RIS panels is not always feasible due to space constraints and the significant overhead load. As shown in Fig. 6.3, increasing the number of RIS elements initially enhances the achievable rate and energy efficiency, but beyond a certain point, further increases lead to performance degradation due to the growing time and power demands for pilot signals. Thanks to the BS's advanced capabilities, BS-side RIS can maintain higher performance with lower resource allocation, as explained in the previous sub-section and demonstrated by Mode 2. In contrast, UE-side RIS faces more challenges due to dynamic channels from UE mobility and limited resources (shown via Mode 1 in Fig. 6.3). In such cases, integrating active RIS elements can offer a solution by amplifying the reflected signal [83].

6.7 Advancing Towards 6G: How RISs Shape the Requirements of 6G Networks

This section highlights different features associated with both BS-side and UE-side RIS deployments, with a particular emphasis on meeting the requirements of 6G networks. These requirements include high energy/spectral efficiency, low latency, massive connectivity, ultra-reliability, and high data rates. Specifically, we discuss how each RIS deployment can enhance various 6G requirements.

6.7.1 Integrated or Separated RIS: Which Serves 6G Requirements Better?

BS/UE-side integrated RIS results in the minimum path loss. Hence, we can maximize data rate and spectral efficiency while minimizing the communication latency. Furthermore, by integrating RIS into each terminal, we can replace active components with passive elements, resulting in enhanced energy efficiency. However, the BS/UE-side integrated design does not have flexibility in RIS placement; hence, it cannot circumvent blockages and provide redundant paths. Therefore, BS/UE-separated design is recommended to increase connection density and network reliability.

Table 6.1: 6G Requirements and RIS Deployment Types for BS-side and UE-side RIS

6G Requirement	RIS Deployment	Recommended Strategy	Contributing Factors	Impact Level
Latency	BS-side	Integrated	Stable Control link; High Beamforming Gain	High
	UE-side		Beamforming Gain; Channel Estimation Overhead; Resource and Deployment Limitations	Medium
Spectral Efficiency	BS-side	Integrated	High Beamforming Gain	High
	UE-side		Beamforming Gain; Resource and Deployment Limitations	Medium
Energy Efficiency	BS-side	Integrated	Passive Element Utilization; Reduced Active Components	High
	UE-side		Passive Nature; Resource and Deployment Limitations	Medium
User Experience Data Rate	BS-side	Integrated	High Beamforming Gain; Robust Control	High
	UE-side		Beamforming Gain; Compact and Efficient Designs; Resource and Deployment Limitations	Medium
Peak Data Rate	BS-side	Integrated	High Beamforming Gain	High
	UE-side		Beamforming Gain; Flexible Placement; Resource and Deployment Limitations	Medium
Reliability	BS-side	Separated	Limited Placement Flexibility	Low
	UE-side		High Placement Flexibility	High
Connection Density	BS-side	Separated	Limited Placement Flexibility	Low
	UE-side		High Placement Flexibility	High

In conclusion, in a realistic network, both integrated and separated RIS designs should be adopted concurrently to meet the high standards of 6G networks.

6.7.2 Towards 6G: The Strategic Role of BS-Side RIS

Generally, BSs are placed within an environment to provide broad coverage. When an RIS is deployed near the BS, it inherits this wide coverage capability. This feature allows us to leverage the RIS as a passive beamformer, reducing costs, conserving power, and enhancing energy efficiency at the BS, as fewer active components like RF chains and phase shifters are required. Furthermore, a large passive BS-side RIS can significantly increase beamforming gain, enhancing user-experienced/peak data rate and spectral efficiency, and reducing communication latency. As explained earlier, by placing RIS separated from the BS, the transmitted signal can circumvent the environmental blockages. However, to circumvent a faraway blockage, we may increase the BS-RIS distance, which increases multiplicative path loss. On the other hand, to keep the multiplicative path loss under a certain threshold, minimum BS-RIS distance should be maintained. In this point of view, BS-side RIS has minor flexibility in enhancing connection density and communication reliability. Table 6.1 summarizes the influences of RIS on 6G requirements.

6.7.3 UE-Side RIS: A Flexible Solution for 6G Network Requirements

Unlike BS, UEs generally do not have fixed positions and can move freely in the environment, potentially ending with dead zones. As explained in the last sub-section, BS-side RIS deployment might not effectively circumvent the blockages due to the limited placing flexibility (see Scenario 3 in Fig. 6.1). Therefore, as depicted in the Scenario 4 in Fig. 6.1, the RIS can be positioned near the dead zone to circumvent the blockage more effectively while keeping the multiplicative path loss under a certain threshold. In this context, UE-side RIS can enhance connection density and communication reliability by reserving virtual LOS to the dead zone. On the other hand, integrating RIS within the UE realizes a large array at the UE [107], which can considerably enhance beamforming/array gain, directly increasing the user-experienced/peak data rate and spectral efficiency while reducing communication latency.

However, deploying large RIS near the UE, either integrated into or separated from the UE, presents a unique challenge: the overhead associated with cascaded channel estimation and RIS configuration [11]. Given the UE's limited computational/power resources, these overheads can increase system latency, as illustrated in Fig. 6.3. Accordingly, striking a balance between the RIS size and the signaling overhead while considering efficient channel estimation and RIS configuration strategies (like codebook-based configuration) is of great importance [110]. Adopting novel designs like plug-in RIS [105], which simplifies channel estimation and RIS configuration, can facilitate UE-side RIS deployment with higher energy efficiency and lower latency. Fig. 6.3 demonstrates the superiority of Plug-in RIS over traditional RIS design.

Table. 6.1 summarizes the effect of each RIS deployment on 6G requirements. Generally, RIS positively impacts the 6G requirements; however, practical limitations should be considered for each deployment. For some 6G requirements, BS-side RIS provides higher performance enhancements, while UE-side RIS deployment is better for the other requirements. In a complete network, the hybrid implementation of these two deployments can complement the network needs.

6.8 Conclusion and Future Horizon

RISs have demonstrated great potential in shaping intelligent radio environments for wireless communications tailored to meet the demands of future networks, such as ultra-reliable, low-latency communication and massive connectivity. To fully leverage RIS-assisted networks, it is essential to explore practical deployment strategies and their impacts. To this end, this chapter examined two practical RIS designs—BS-side and UE-side RIS—and proposed a framework with various design parameters. Moreover, we have highlighted how these applications influence the requirements of 6G networks, showcasing their potential to revolutionize future communications. Fig. 6.4 outlines these RIS deployment strategies, highlighting

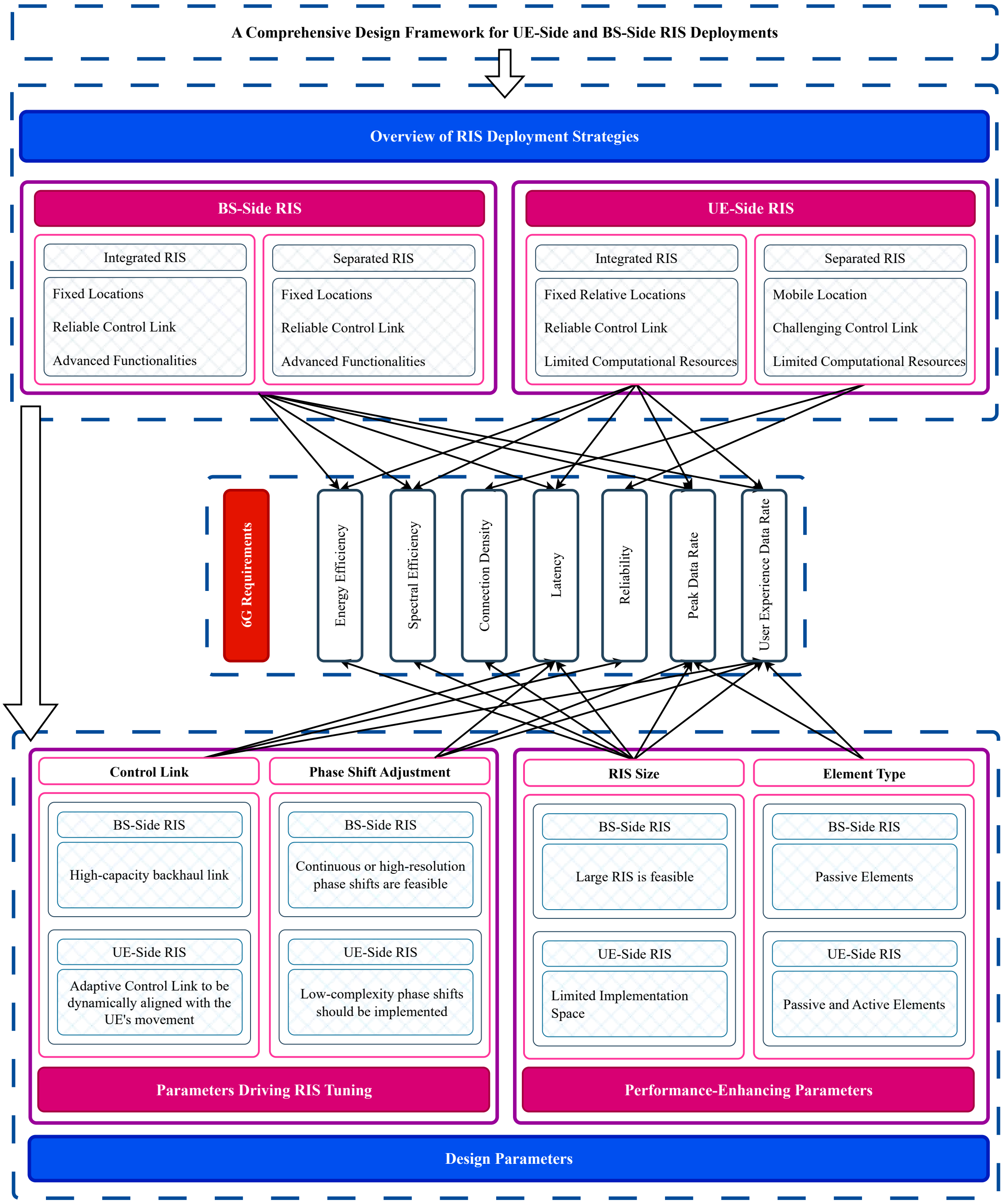

Figure 6.4: Proposed design framework for BS-Side and UE-Side RIS deployments.

key design parameters and their impact on 6G network performance.

Despite significant progress, RIS technology faces practical challenges that need to be addressed for cost-effective and efficient integration into next-generation networks. Fig. 6.5 outlines the future directions for BS/UE-side RIS deployments, highlighting key areas where innovation is crucial to unlock the full potential of RIS in future wireless communications. For the BS-side RIS, challenges include managing large-size RIS configurations, optimizing multi-user setups, and minimizing computational and signaling overhead. For the UE-side RIS, the challenges are categorized into integrated, separated, and hybrid configurations, emphasizing the need for enhanced beamforming, efficient channel estimation, and reliable control mechanisms. These challenges highlight the need for innovative designs and optimization strategies to maximize the benefits of RIS technology in future 6G networks.

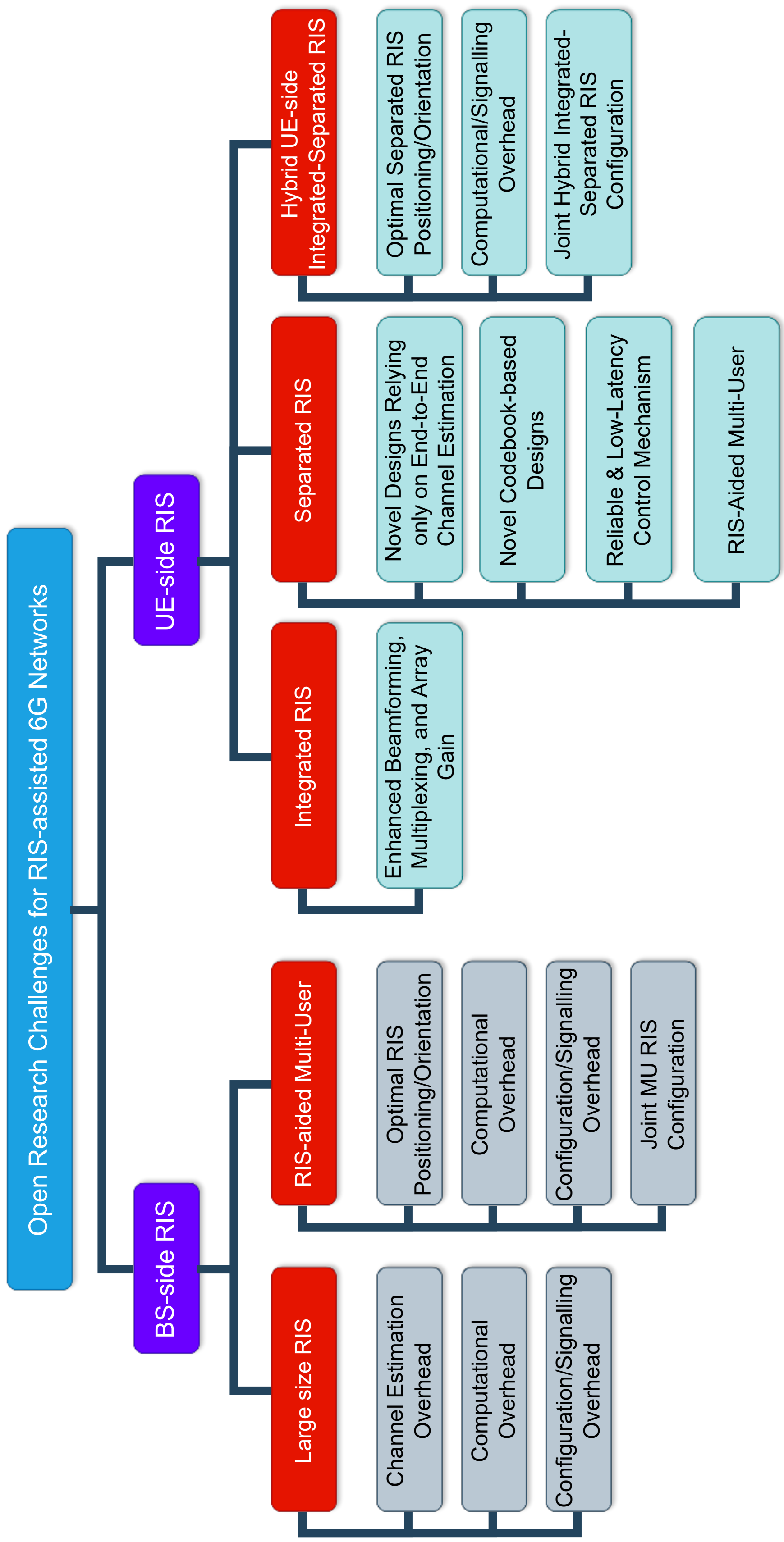

Figure 6.5: Open challenges for BS-side/UE-side RIS-aided 6G networks.

Chapter 7

MODERN BASE STATION ARCHITECTURE: ENABLING PASSIVE BEAMFORMING WITH BEYOND DIAGONAL RIS

7.1 Introduction

The rapid evolution of wireless communication systems is driven by the ever-increasing demand for enhanced network access and capacity. Given the growing need for frequency spectrum to support emerging applications, utilizing higher frequency bands, such as the millimeter-wave (mmWave) spectrum, continues to be a vital enabler for advanced communication systems, including sixth-generation (6G) networks [87, 43, 48]. The abundant bandwidth available in the mmWave spectrum enables high data rate and low latency communication, aligning well with 6G requirements. Additionally, the short wavelength of mmWave signals allows the integration of a large number of antennas, facilitating the formation of highly directional beams. While the primary goal of these beams is to overcome the significant path loss inherent in mmWave environments, their directional nature can be effectively leveraged in multi-user systems to minimize inter-user interference and facilitate massive connectivity in 6G networks [68, 90].

Despite the advantages of mmWave systems, the required equipment for their implementation is both costly and power-intensive [10], which is misaligned with the stringent energy efficiency requirements of 6G networks. To tackle this challenge, hybrid beamforming is proposed as an alternative to fully digital beamforming, reducing the number of radio frequency (RF) chains at transceivers by employing a network of analog phase shifters following baseband precoding. However, the analog network still relies on a large number of high-precision active phase shifters, which can pose challenges to the practical implementation of large antenna arrays [10].

Reconfigurable intelligent surfaces (RISs) have recently emerged as a promising solution to enhance wireless communication systems by dynamically controlling the propagation environment [14, 112]. However, beyond their conventional role as auxiliary reflectors, an intriguing question arises: Can RISs serve as primary beamformers at the base station (BS) or user equipment (UE)? Such an approach would leverage the passive and cost-effective nature of RISs, significantly reducing hardware complexity and power consumption compared to traditional active analog beamforming. This consideration opens new avenues for exploring BS/UE-integrated RISs, where RISs are seamlessly embedded into transceiver designs to enable passive beamforming.

7.1.1 Related Works

Hybrid beamforming has gained significant attention as a cost-effective alternative to fully digital beamforming in mmWave systems. In this context, [86] introduces an angular-based hybrid precoding and combining approach for mmWave massive MIMO systems, focusing on minimizing channel state information (CSI) overhead. [68] evaluates three-dimensional (3D) antenna array structures for hybrid precoder design in multi-user mmWave massive MIMO. The authors in [90] proposes a two-stage angular-based hybrid precoding method, grouping users by angular similarity. To further reduce system costs, [10] presents a fixed phase shifter design that reduces the number of phase shifters in hybrid precoding architectures, offering a cost-efficient solution. Although the adoption of analog phase shifters significantly reduces the number of RF chains, implementing massive MIMO still requires a large number of phase shifters, which can lead to increased cost, complexity, and power consumption [10].

Programmable metasurfaces have gained attention for their passive nature and ability to enable low-cost arrays that direct incident electromagnetic (EM) waves. Explored types include passive RIS [14], active RIS [83], simultaneously transmitting and receiving (STAR) RIS [113], stacked intelligent metasurface (SIM), and beyond diagonal (BD) RIS [17]. Some studies propose RISs as primary beamformers at the BS or UE to simplify massive MIMO deployment [114, 112]. Furthermore, integrating RIS directly within transceivers mitigates the multiplicative path loss challenges typically associated with conventional RIS-assisted systems [112].

User-side RIS integration has been specifically explored in [115, 107] as a means to realize cost- and energy-efficient large-scale arrays. The authors in [104] propose integrating an RIS within the radome of a BS as an auxiliary passive array, enabling real-time reconfiguration to enhance system performance cost-effectively. In [116], a hybrid beamforming approach is proposed, targeting sidelobe suppression and main-lobe optimization through a least squares-based cost function applied to BS digital beamforming and intelligent transmissive surface phase configurations. A notable advancement in this domain is SIM, which seamlessly integrates RIS technology within the BS or UE to enable the passive implementation of advanced MIMO functionalities. By employing multiple layers of low-cost meta-atoms, SIM facilitates the deployment of large arrays at transceivers using passive components [114, 117, 118, 119, 120].

BD-RIS represents an advanced evolution of RIS technology, offering enhanced flexibility by enabling the manipulation of both the phase and amplitude of impinging signals without introducing amplification or attenuation [17, 18, 16]. Unlike traditional diagonal RIS (D-RIS), BD-RIS incorporates inter-element connectivity, which allows for amplitude adjustment across RIS elements, significantly enhancing its beamforming capabilities. This advanced functionality makes BD-RIS a compelling choice for integration at transceivers, where its ability to passively perform analog beamforming can replace conventional analog phase shifters, simplifying the transceiver design while maintaining high performance. As discussed in [121], BD-RIS outperforms D-RIS when the magnitudes of the individual elements of the BS-RIS and RIS-UE channels are linearly independent. This implies that rich-scattered channels, such as those modeled by Rayleigh fading, create favorable conditions for BD-RIS to surpass D-RIS. Moreover, increasing the number of UEs enriches the channel, further benefiting BD-RIS. However, as the channel becomes more scattered, the performance gap between BD-RIS and D-RIS narrows.

Initial efforts have been invested to evaluate the potential of BD-RIS. The work of [122] explores a reflective BD-RIS integrated within the BS, focusing on the sub-6 GHz spectrum. The study considers a multi-user system and shows that BD-RIS outperforms D-RIS by more effectively mitigating inter-user interference. [123] investigates an integrated sensing and communication (ISAC) system with a BD-RIS integrated into the BS. Although the study focuses on the mmWave band, it models the NLOS channel component using a Rayleigh distribution, which does not accurately capture the spatially sparse scattering nature of mmWave environments. Additionally, the adoption of a multi-user system further enriches the channel, thereby amplifying the performance advantage of the BD-RIS over the traditional D-RIS. The study in [124] examines a SIM structure implemented with BD-RIS and demonstrates that a single-layer SIM with BD-RIS outperforms any SIM based on D-RIS, highlighting the significant potential of BD-RIS in RIS-integrated systems. However, the RIS-UE channel is modeled as rich-scattered using a Rayleigh distribution, creating favorable conditions for BD-RIS to surpass the performance of conventional D-RIS. It has been demonstrated in [125] that integrating a linear BD-RIS at the BS significantly enhances beamforming gain compared to D-RIS, but it focuses solely on linear configurations and localization parameter estimation limiting the application scenario.

7.1.2 Motivations and Contributions

The primary motivation for deploying large arrays and massive MIMO is their ability to form narrow beams toward intended targets, effectively mitigating severe path loss and high attenuation in high-frequency communication systems. However, the aforementioned studies do not investigate the performance of BS-integrated BD-RIS under spatially sparse scattering channels, which more accurately represent realistic channel conditions in the high-frequency spectrum. Moreover, the impact of BS-integrated BD-RIS on beamforming gain remains unexamined, despite narrow beamforming being a fundamental feature of mmWave communication. Additionally, these studies fail to provide a comprehensive analysis of how various design parameters, such as array size and BS-RIS separation, affect system performance in such environments. This analysis is crucial as it paves the way for the practical implementation of infrastructures supporting promising 6G applications, such as radio localization, sensing, non-terrestrial networks, and other use cases that rely on large arrays to achieve narrow beams. With this in mind, the main contributions of this chapter are summarized as follows:

- We investigate a BS-integrated BD-RIS system model that facilitates passive beamforming at the BS by emulating a multiple-input single-output (MISO) configuration through a single-input single-output (SISO)-assisted BD-RIS. Using the widely-adopted geometric cluster-based channel model, which accurately represents the spatially sparse scattered nature of mmWave environments, we demonstrate the BD-RIS's ability to form narrow beams for efficient directional communications in a point-to-point (P2P) mmWave scenario. Notably, our analysis reveals that BD-RIS delivers high performance gains even in sparse scattering channels, proving that its effectiveness is not restricted to rich scattering environments. To configure the BD-RIS, we employ a simple algorithm based on Takagi's decomposition, which effectively achieves beamforming gains comparable to those of active analog beamforming antenna arrays.

- We demonstrate that the internal geometry of the BS-integrated BD-RIS is pivotal in minimizing the circuit complexity of the proposed system. Achieving maximum beamforming gain does not require a fully-connected BD-RIS structure. Instead, by dividing the BD-RIS elements into groups that exhibit symmetry around the active antenna, it is possible to maintain the maximum beamforming gain, as the channel amplitude variations within each group are identical and match those of the entire BD-RIS. Notably, this approach is flexible and can be applied to any desired number of groups. Specifically, as long as symmetry around the active antenna is preserved within a group, that group can be further subdivided into smaller groups without compromising performance.

- We evaluate the beamforming gain of the proposed BS-integrated BD-RIS configured as a uniform planar array, benchmarking its performance against traditional D-RIS and active analog beamforming antenna arrays. By introducing a novel metric, termed *channel amplitude variations*, we pinpoint and address the beamforming limitations inherent in BS-integrated D-RIS architectures. Our findings reveal that the proposed BS-integrated BD-RIS achieves a beamforming gain and beam pattern comparable to the performance of active analog beamforming antenna arrays. In contrast, D-RIS exhibits limited beamforming capability and wider beam patterns. To the best of our knowledge, this study is the first to explore BS-integrated RIS configurations from the perspectives of beamforming gain and beam pattern performance in a spatially sparse scattered environment. Besides, we conducted various simulations to evaluate the bit error rate (BER) and validate the results with the theoretical upper bound, along with a comprehensive achievable rate analysis across various parameters under various conditions.

The remainder of this chapter is structured as follows: Section 7.2 introduces the system, channel, and signal models. Section 7.3 provides an in-depth discussion of the BD-RIS architecture and the configuration algorithm for both fully-connected and group-connected modes. Section 7.4 derives the theoretical upper bound for the average BER (ABER). Section 7.5 examines the fundamental differences between BD-RIS and conventional D-RIS, as well as the impact of design parameters on system performance. Section 7.6 presents comprehensive simulation results, comparing the proposed BS-integrated BD-RIS with established benchmarks. Finally, Section 7.7 summarizes the findings and concludes the chapter.

7.2 System, Channel, and Signal Model

In this section, we begin by presenting the system model, outlining the architecture of the proposed BS-integrated BD-RIS, the arrangement of its passive elements, and its role in enabling passive beamforming for efficient directional communication in the mmWave environment. Next, we detail the channel model, capturing the interaction between the active antenna and the BD-RIS, as well as the propagation characteristics of the wireless channel between the BD-RIS and the UE. We then describe the signal model, explaining the transmission of symbols, passive beamforming by the BD-RIS, and the formulation and detection of the received signal at the UE.

7.2.1 System Model

Fig. 7.1 illustrates the proposed system model and the BS structure designed for deployment in a mmWave environment. Building upon the motivations discussed in Section 7.1, we consider a P2P SISO system where the BS is equipped with a single active antenna and a passive BD-RIS integrated into the BS as depicted in Fig. 7.1(a). This configuration enables passive beamforming, effectively forming the beams to combat the severe path loss and attenuation characteristic of the mmWave spectrum [87, 85, 112]. Fig. 7.1(b) provides a 3D view of the BD-RIS side facing the active antenna, with the opposite side, which faces outward, having an identical structure. Each side of the BD-RIS is referred to as a sector, as illustrated in Fig. 7.1(c). For the proposed application, the BD-RIS operates exclusively in the transmissive mode (signals are sending to sector 2), with its reflective mode deactivated [18].

To facilitate exclusive transmissive operation, the passive elements on each side are organized into a uniform planar array with M_x columns and M_y rows. Each back-to-back pair of passive elements from the two sectors of the BD-RIS constitutes a single cell, enabling seamless coordination between the two sectors. This arrangement comprises a total of $M = M_x \times M_y$ cells, allowing the integrated BD-

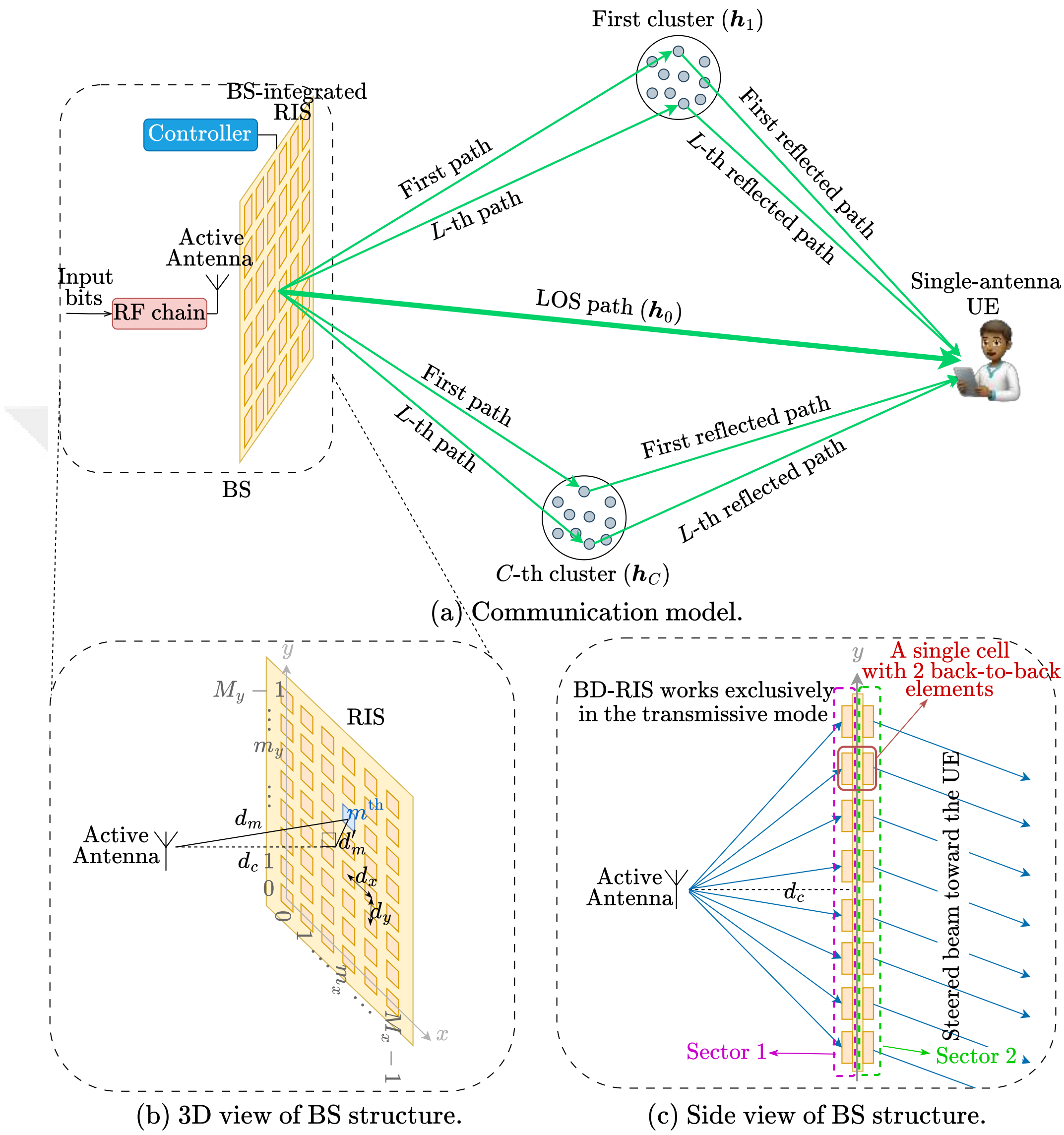

Figure 7.1: System model: (a) Communication model showcasing the BS-integrated BD-RIS and single-antenna UE, illustrating the LOS path and NLOS clusters with multipath components; (b) 3D view of the BS structure, highlighting the BD-RIS geometry, BS-RIS separation (d_c), and the active antenna-to-RIS element distances (d_m); (c) Side view of the BS structure, demonstrating the BD-RIS operation in transmissive mode, where Sector 1 receives the incident wave, and Sector 2 transmits the steered beam toward the UE.

RIS to effectively steer the EM wave radiated by the active antenna toward the UE. To maintain focus on the proposed system model, the details of the BD-RIS circuit are provided separately in Section 7.3.

The spacing between adjacent columns along the x-axis is d_x, while the spacing between adjacent rows along the y-axis is d_y. The m-th cell ($0 \leq m \leq M-1$) is located at the intersection of the m_y-th row ($0 \leq m_y \leq M_y - 1$) and m_x-th column ($0 \leq m_x \leq M_x - 1$), where the index m is given by $m = m_y M_x + m_x$. The active antenna is positioned along an axis perpendicular to the RIS plane, passing through the geometric center of the RIS surface at a distance of d_c, as shown in Fig. 7.1(b). Additionally, the distance between the active antenna and the m-th cell is denoted as d_m and defined as follows:

$$d_m = \sqrt{d_c^2 + d_m'^2}, \tag{7.1}$$

where d_m' represents the distance between the m-th element and the center of the BD-RIS, defined as:

$$d_m' = \frac{1}{2}\sqrt{(d_x|2m_x - M_x + 1|)^2 + (d_y|2m_y - M_y + 1|)^2}. \tag{7.2}$$

7.2.2 Channel Model

In the proposed system, the channel between the active antenna and the BD-RIS plays a critical role in shaping the performance of passive beamforming. The integration of the BD-RIS within the BS introduces unique propagation characteristics, as the EM wave emitted by the active antenna interacts with each BD-RIS cell, arriving with distinct amplitudes and phases. To capture this interaction, the transmission coefficient vector from the active antenna to the BD-RIS is derived using the Rayleigh-Sommerfeld diffraction theory for near-field propagation [126, 127, 128, 129, 120]. The transmission coefficient vector, denoted as $\boldsymbol{g} \in \mathbb{C}^{M\times 1}$, is expressed as follows [126, 127, 128, 129, 120]:

$$[\boldsymbol{g}]_m = \frac{A d_c}{d_m^2}\left(\frac{1}{2\pi d_m} - \frac{\jmath}{\lambda}\right) e^{\jmath 2\pi d_m/\lambda}, \tag{7.3}$$

where A represents the area of each passive element, and λ represents the wavelength of the carrier signal.

After traversing the BD-RIS, the signal propagates through the wireless channel between the BD-RIS and the UE. In the mmWave environment, such channels are characterized by significant propagation challenges, including penetration loss, severe path loss, and attenuation, which create a sparsely scattered propagation environment. To capture these conditions accurately, the widely recognized clustered geometric channel model is employed. This model accounts for the combined effect of a LOS path and multiple non-LOS (NLOS) clusters, as illustrated in Fig. 7.1(a). Specifically, the channel between the BD-RIS and UE, denoted as $\boldsymbol{h} \in \mathbb{C}^{M\times 1}$, is modeled as a superposition of these paths and is expressed as follows [87, 85, 4, 7]:

$$\begin{aligned} \boldsymbol{h} &= \sqrt{\frac{M}{CL+1}}\Bigg(\underbrace{\alpha \boldsymbol{a}^{\mathsf{H}}(\varphi_0,\vartheta_0)}_{\boldsymbol{h}_0^{\mathsf{T}}} + \sum_{c=1}^{C}\underbrace{\sum_{\ell=1}^{L}\beta_{c,\ell}\boldsymbol{a}^{\mathsf{H}}(\varphi_{c,\ell},\vartheta_{c,\ell})}_{\boldsymbol{h}_c^{\mathsf{T}}}\Bigg)^{\mathsf{T}} \\ &= \sqrt{\frac{M}{CL+1}}\Bigg(\underbrace{\boldsymbol{h}_0}_{\text{LOS component}} + \underbrace{\sum_{c=1}^{C}\boldsymbol{h}_c}_{\text{NLOS component}}\Bigg), \end{aligned} \tag{7.4}$$

where C represents the number of NLOS clusters and L denotes the number of NLOS paths in each cluster. The parameters $\alpha \sim \mathcal{CN}(0,\sigma_\alpha^2)$, $\varphi_0 \sim \mathcal{U}[-\pi,\pi]$, and $\vartheta_0 \sim \mathcal{U}[0,\frac{\pi}{2}]$ denote the complex path gain, azimuth angle of departure (AOD), and elevation AOD for the LOS path, respectively [87, 85]. For the ℓ-th path in the c-th cluster, the corresponding parameters are $\beta_{c,\ell} \sim \mathcal{CN}(0,\sigma_\beta^2)$, $\varphi_{c,\ell} \sim \mathcal{L}(\varphi_c,\varsigma_c)$, and $\vartheta_{c,\ell} \sim \mathcal{L}(\vartheta_c,\varsigma_c)$, representing the complex path gain, azimuth AOD, and elevation AOD, respectively [87, 85, 26]. Here, $\varphi_c \sim \mathcal{U}[-\pi,\pi]$ and $\vartheta_c \sim \mathcal{U}[0,\frac{\pi}{2}]$ are the mean azimuth and elevation AODs while ς_c denotes the angular spread in both the azimuth and elevation dimensions for the c-th cluster [87, 85, 26]. The variances of the LOS and NLOS path gains are defined by $\sigma_i^2 = 10^{-0.1\mathrm{PL}_i(d)}$, $i \in \{\alpha,\beta\}$, where $\mathrm{PL}_i(d)$ represents the path loss between the BD-RIS and UE, and d denotes the distance between them. In addition, $\boldsymbol{a}(\phi,\theta) \in \mathbb{C}^{M\times 1}$ represents the array response (steering) vector at the BD-RIS transmit terminal, indicating that the corresponding path is directed toward the azimuth angle ϕ and elevation angle θ. The mathematical expression for $\boldsymbol{a}(\phi,\theta)$ is given as follows:

$$\boldsymbol{a}(\phi,\theta) = \frac{1}{\sqrt{M}}[e^{\jmath \boldsymbol{k}^\mathsf{T}\boldsymbol{p}_0}, e^{\jmath \boldsymbol{k}^\mathsf{T}\boldsymbol{p}_1}, \ldots, e^{\jmath \boldsymbol{k}^\mathsf{T}\boldsymbol{p}_{M-1}}]^\mathsf{T}, \tag{7.5}$$

where $\boldsymbol{k}$ represents the wave-number vector, which characterizes the direction of the corresponding path, and $\boldsymbol{p}_m$, $0 < m < M-1$, denotes the position vector of the m-th cell, specifying its location on the BD-RIS. These vectors are mathematically expressed as:

$$\boldsymbol{k} = \frac{2\pi}{\lambda}[\sin\theta\cos\phi, \sin\theta\sin\phi]^\mathsf{T}, \tag{7.6}$$

$$\boldsymbol{p}_m = [m_x d_x, m_y d_y]^\mathsf{T}. \tag{7.7}$$

Notably, in (7.4), the channel model is decomposed into the LOS sub-channel, represented by $\boldsymbol{h}_\mathbf{0}$, and the summation of NLOS sub-channels, $\sum_{c=1}^{C}\boldsymbol{h}_c$.

7.2.3 Signal Model

This chapter focuses on P2P communication, where a single stream of information bits is transmitted to a single-antenna UE. The transmitted symbol s is chosen from an $\mathcal{M}$-ary constellation set of order $\mathcal{M}$ and transmits to the BD-RIS through the transmission channel $\boldsymbol{g}$. As a result, the system's spectral efficiency is defined as $\eta = \log_2\mathcal{M}$ bits per channel use (bpcu). The BD-RIS applies a configuration scattering matrix $\boldsymbol{\Omega} \in \mathbb{C}^{M\times M}$ to the incoming EM wave from the active antenna, effectively steering it toward the UE through the mmWave channel $\boldsymbol{h}$. The BD-RIS configuration strategy is detailed in Section 7.3. The received signal at the UE can be expressed as:

$$y = \sqrt{P}\boldsymbol{h}^\mathsf{T}\boldsymbol{\Omega}\boldsymbol{g}s + n = \sqrt{P}\boldsymbol{h}^\mathsf{T}\boldsymbol{\zeta}s + n, \tag{7.8}$$

where P is the BS transmitted power, and $n \in \mathcal{CN}(0,\sigma_n^2)$ is the additive noise component at the UE. Here, we define $\boldsymbol{\zeta} \in \mathbb{C}^{M\times 1}$ as $\boldsymbol{\zeta} = \boldsymbol{\Omega}\boldsymbol{g}$, representing the effective passive beamforming at the transmit terminal of BD-RIS.

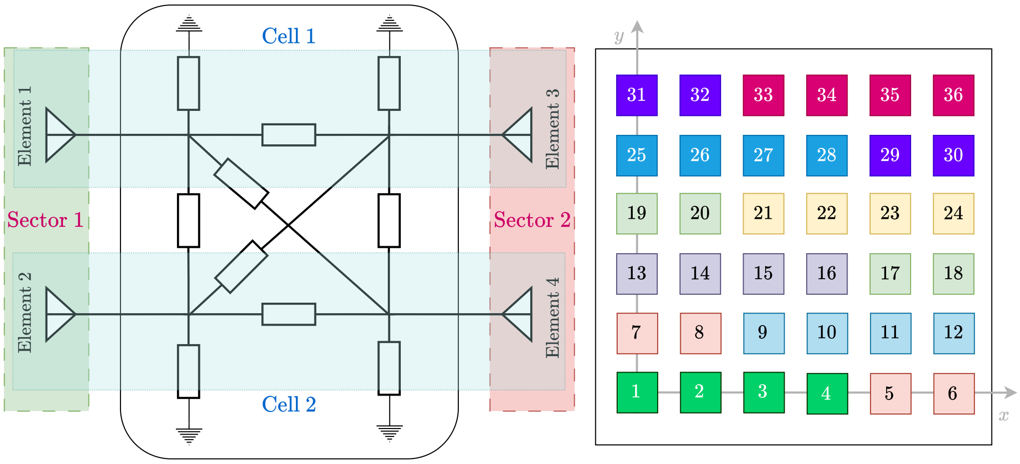

Figure 7.2: (a) A simplified example of the circuit structure for a fully-connected BD-RIS with two cells, illustrating inter-element connections for amplitude and phase manipulation. (b) A visualization of the group-connected structure with $M = 36$, $G = 9$, and $\bar{M} = 4$, showing the division of cells into groups for balancing performance and circuit complexity.

Ultimately, a maximum-likelihood (ML) detector is employed in the UE to extract the transmitted symbols from the received signal y. The detection process is expressed as:

$$\hat{s} = \arg\min_{s} |y - \sqrt{P} h_{\text{eff}} s|^2, \tag{7.9}$$

where $\hat{s}$ denotes the estimated $\mathcal{M}$-ary symbol and $h_{\text{eff}} = \boldsymbol{h}^{\mathsf{T}} \boldsymbol{\Omega} \boldsymbol{g}$ represents the effective SISO channel gain. It is worth mentioning that CSI can be acquired using existing channel estimation methods developed for SIM and holographic MIMO systems [120, 114, 117, 130, 131].

7.3 BD-RIS Structure and Configuration

In this section, we explore the circuit structure and configuration strategy of the BD-RIS, concentrating on its design to enable efficient passive beamforming. A simplified example of the circuit structure for the fully-connected BD-RIS is presented in [18] and illustrated in Fig. 7.2(a). As detailed in Section 7.2.1, the BD-RIS elements are divided into two sectors: sector 1, facing the active antenna, captures the incident EM wave, while sector 2, facing outward, transmits the directed signal toward the UE. Each pair of back-to-back elements from the two sectors forms a single cell, as depicted in Fig. 7.2(a).

To enable manipulation of both the amplitude and phase of the impinging EM wave, inter-element connections are crucial [17, 18]. Extending the two-cell structure in Fig. 7.2(a) to an M-cell fully-connected BD-RIS significantly increases circuit complexity. To balance performance and circuit complexity, a G-group-connected structure can be adopted by dividing the M cells into G groups, with each group containing $\bar{M} = M/G$ cells. In this configuration, full connectivity is implemented within each group, while no connections exist between different groups [18]. For simplicity, we assume that all groups consist of an equal number of cells $\bar{M}$.[1] The set of cell indices for the q-th group is defined as $\mathcal{G}_q = \{(q-1)\bar{M}+1, \dots, q\bar{M}\}$, where each group contains $\bar{M}$ consecutive cells. This grouping approach is referred to as the linear permutation throughout this chapter. To aid visualization, Fig. 7.2(b) illustrates a BD-RIS configuration with $M = 36$, $G = 9$, and $\bar{M} = 4$. Two notable special cases arise from this framework:

- When $G = M$, the structure corresponds to a traditional transmissive RIS with a diagonal configuration scattering matrix, allowing only phase manipulation of the impinging signal, which limits its passive beamforming capabilities.

- Conversely, when $G = 1$, the configuration transitions to a fully-connected BD-RIS, offering the highest degree of freedom for designing the configuration scattering matrix and enabling superior passive beamforming performance.

The configuration scattering matrix of the q-th group, $\mathbf{\Omega}_q \in \mathbb{C}^{\bar{M}\times\bar{M}}$, is a full

[1] It is worth noting that varying grouping strategies with dynamic group sizes can lead to different trade-offs between performance and circuit complexity [132, 133]. However, investigating these strategies and their impact on passive beamforming performance lies beyond the scope of this thesis and is deferred to future work.

matrix that satisfies the following unitary and symmetry constraints:

$$\boldsymbol{\Omega}_q^{\mathsf{H}}\boldsymbol{\Omega}_q = \boldsymbol{I}_{\bar{M}}, \tag{7.10}$$

$$\boldsymbol{\Omega}_q^{\mathsf{T}} = \boldsymbol{\Omega}_q. \tag{7.11}$$

The unitary constraint ensures that each group operates without power loss, while the symmetry constraint reduces hardware complexity by requiring only a single component between each pair of distinct elements.

The BS maintains direct access to the BD-RIS, enabling it to transmit control signals to an embedded controller for configuring the BD-RIS. To ensure compliance with the unitary and symmetry constraints for BD-RIS configuration as specified in (7.10) and (7.11), we utilize Takagi's decomposition as outlined in [134]. Hence, utilizing the BS-RIS channel $\boldsymbol{g}$, the effective beamforming vector $\boldsymbol{b} \in \mathbb{C}^{M\times 1}$ corresponding to the RIS-UE channel, and employing singular value decomposition (SVD) technique, the BD-RIS configuration for the general case of G groups is detailed in Algorithm 4.

7.4 ABER Theoretical Analysis

This section presents the derivation of a closed-form expression for the theoretical upper bound on the ABER, serving as a validation for the ABER analysis. The upper bound is expressed as

$$\text{ABER} \leq \frac{1}{\eta\mathcal{M}} \sum_{s^\star} \sum_{\hat{s}} d_H(s^\star, \hat{s}) \mathbb{P}(s^\star \rightarrow \hat{s}), \tag{7.12}$$

where $s^\star$ denotes the correct symbol considered for transmission, $d_H(s^\star, \hat{s})$ represents the Hamming distance between the binary representations of $s^\star$ and $\hat{s}$, and $\mathbb{P}(s^\star \rightarrow \hat{s})$ indicates the unconditional pairwise error probability (UPEP). To compute UPEP, we begin by deriving the conditional pairwise error probability (CPEP) under the assumption that the channel parameter set $\mathcal{C} = \{\alpha, \varphi_0, \vartheta_0, \beta_{c,\ell}, \varphi_{c,\ell}, \vartheta_{c,\ell}\}, \forall c, \ell$ is

Algorithm 4: BD-RIS Configuration for Linear Permutation

Determine the beamforming vector $\boldsymbol{b}$ from the RIS-UE channel using one of the possible approaches outlined in Section 7.6.1;
for *each group of cells* $q \in \{1, \ldots, G\}$ **do**
  Constitute $\boldsymbol{a}_q = \boldsymbol{b}_{[(q-1)\bar{M}+1:q\bar{M}]}$;
  Constitute $\boldsymbol{g}_q = \boldsymbol{g}_{[(q-1)\bar{M}+1:q\bar{M}]}$;
  Calculate $\boldsymbol{u}_q = \boldsymbol{g}_q / \|\boldsymbol{g}_q\|$;
  Compute $\boldsymbol{v}_q = \boldsymbol{b}_q / \|\boldsymbol{b}_q\|$;
  Derive the symmetric matrix $\boldsymbol{A}_q = \boldsymbol{v}_q \boldsymbol{u}_q^{\mathsf{H}} + (\boldsymbol{v}_q \boldsymbol{u}_q^{\mathsf{H}})^{\mathsf{T}}$;
  Decompose $\boldsymbol{A}_q$ using SVD as $\boldsymbol{A}_q = \boldsymbol{U}_q \boldsymbol{\Sigma}_q \boldsymbol{V}_q^{\mathsf{H}}$;
  Calculate $\boldsymbol{\nu}_q = \operatorname{diag}(\boldsymbol{U}_q^{\mathsf{H}} \boldsymbol{V}_q^{*})$;
  Determine $\boldsymbol{\rho}_q = \angle \boldsymbol{\nu}_q / 2$;
  Compute $\boldsymbol{\mathcal{Q}}_q = \boldsymbol{U}_q \operatorname{diag}(e^{(\jmath \boldsymbol{\rho}_q)})$;
  Takagi's decomposition: $\boldsymbol{A}_q = \boldsymbol{\mathcal{Q}}_q \boldsymbol{\Sigma}_q \boldsymbol{\mathcal{Q}}_q^{\mathsf{T}}$;
  Scattering matrix for the q-th group: $\boldsymbol{\Omega}_q = \boldsymbol{\mathcal{Q}}_q \boldsymbol{\mathcal{Q}}_q^{\mathsf{T}}$;
end
Assemble the overall BD-RIS scattering matrix as $\boldsymbol{\Omega} = \operatorname{blkdiag}(\boldsymbol{\Omega}_1, \ldots, \boldsymbol{\Omega}_G)$;

known, as follows:

$$\mathbb{P}(s^{\star} \rightarrow \hat{s} | \mathcal{C}) = \mathbb{P}(|y - \sqrt{P} \boldsymbol{h}^{\mathsf{T}} \boldsymbol{\Omega} \boldsymbol{g} s^{\star}|^2 > |y - \sqrt{P} \boldsymbol{h}^{\mathsf{T}} \boldsymbol{\Omega} \boldsymbol{g} \hat{s}|^2). \tag{7.13}$$

By substituting the signal model from (7.8) into (7.13), the CPEP can be reformulated as:

$$\mathbb{P}(s^{\star} \rightarrow \hat{s} | \mathcal{C}) = \mathbb{P}(|n|^2 > |n + \sqrt{P} \boldsymbol{h}^{\mathsf{T}} \boldsymbol{\Omega} \boldsymbol{g} (s^{\star} - \hat{s})|^2). \tag{7.14}$$

After performing the necessary mathematical manipulations, the CPEP can be expressed as follows [87, 105]:

$$\mathbb{P}(s^{\star} \rightarrow \hat{s} | \mathcal{C}) = Q\left(\frac{|\sqrt{P} \boldsymbol{h}^{\mathsf{T}} \boldsymbol{\Omega} \boldsymbol{g} (s^{\star} - \hat{s})|}{\sqrt{2} \sigma_n} \right). \tag{7.15}$$

Finally, taking the expectation over sufficiently many channel realizations yields the UPEP as

$$\mathbb{P}(s^\star \to \hat{s}) = \mathbb{E}_{\mathcal{C}}\left[Q(\frac{|\sqrt{P}\boldsymbol{h}^\mathsf{T}\boldsymbol{\Omega}\boldsymbol{g}(s^\star - \hat{s})|}{\sqrt{2}\sigma_n}) \right]. \tag{7.16}$$

7.5 Channel Amplitude Variation: A Key Design Metric for BS-Integrated RIS Performance

In this section, we take a closer look at the design parameters of the BS-integrated BD-RIS and analyze how these parameters impact system performance compared to traditional structures. Specifically, we focus on the BS-RIS channel, a deterministic component of the BS's internal architecture, shaped by the BS's design parameters.

According to the Rayleigh-Sommerfeld diffraction theory for near-field propagation, as presented in (7.3), the amplitude of the channel coefficient corresponding to each element is inversely proportional to d_m^3, emphasizing a rapid decay in channel gain amplitude with increasing distance. Unlike traditional D-RIS, which is limited to phase compensation, BD-RIS can adjust both phase and amplitude variations. Consequently, when the signal emitted by the active antenna reaches the BD-RIS, it achieves alignment in both phase and amplitude across RIS elements. The primary performance degradation in BS-integrated BD-RIS compared to active analog beamforming antenna arrays arises from the multiplicative path loss due to the BS-RIS distance. In contrast, D-RIS, with its phase-only adjustment capability, cannot align the amplitude variations across RIS elements. This limitation introduces additional performance degradation beyond the multiplicative path loss, as amplitude misalignment further reduces system efficiency. This enhanced capability of BD-RIS provides greater flexibility in beamforming design, whereas the performance of D-RIS remains fundamentally constrained by its limited adjustment capabilities.

Since amplitude variations across RIS elements play a crucial role, we focus on this aspect in the remainder of this section. As previously mentioned, the amplitude of the channel gain corresponding to the m-th element is inversely proportional to d_m^3. The variations in d_m are significantly affected by two key factors: the array aperture and the BS-RIS separation (d_c). The array aperture, directly proportional to the number of RIS elements, plays a crucial role—larger RIS arrays incorporate more elements, resulting in greater variations in d_m and, consequently, more pronounced discrepancies in channel amplitudes across the elements. In contrast, as the BS-RIS separation (d_c) increases, the relative variations in d_m decrease, leading to reduced differences in channel amplitudes among the RIS elements.

To quantify and visualize the relative spread of channel amplitude variations between the active antenna and the RIS elements, we introduce a novel metric called *channel amplitude variation* (CAV). CAV quantifies the variability in channel amplitudes relative to their mean and is specifically defined for the BS-RIS transmission channel vector $\boldsymbol{g}$. Mathematically, CAV is computed as the standard deviation of the channel amplitude components normalized by their mean, expressed as

$$\mathrm{CAV} = \frac{\sqrt{\frac{1}{M}\sum_{m=1}^{M}(|[\boldsymbol{g}]_m| - \mu_{|\boldsymbol{g}|})^2}}{\mu_{|\boldsymbol{g}|}}, \tag{7.17}$$

where $\mu_{|\boldsymbol{g}|}$ represents the mean amplitude of the channel gains between the active antenna and the RIS elements, and is formally expressed as

$$\mu_{|\boldsymbol{g}|} = \frac{1}{M}\sum_{m=1}^{M}|[\boldsymbol{g}]_m|. \tag{7.18}$$

The normalization by the mean ensures that the CAV metric provides a dimensionless and scale-invariant representation of amplitude variability, making it suitable for comparisons across different system configurations and BS-RIS separations.

Fig. 7.3 depicts the CAV as a function of both the array size and the BS-RIS separation (d_c). As previously discussed, the CAV increases with larger array sizes and smaller d_c. It is important to note that the primary motivation for integrating RIS within the BS is to enable the implementation of larger arrays to achieve narrower beams, thereby reducing cost and power consumption. Additionally, minimizing the BS-RIS separation (d_c) is crucial to mitigate the impact of multiplicative path loss. Consequently, designing a system that aligns with these two characteristics is critical, underscoring the necessity of adopting BD-RIS to effectively manage amplitude variations. Notably, as d_c decreases, placing the RIS closer to the active

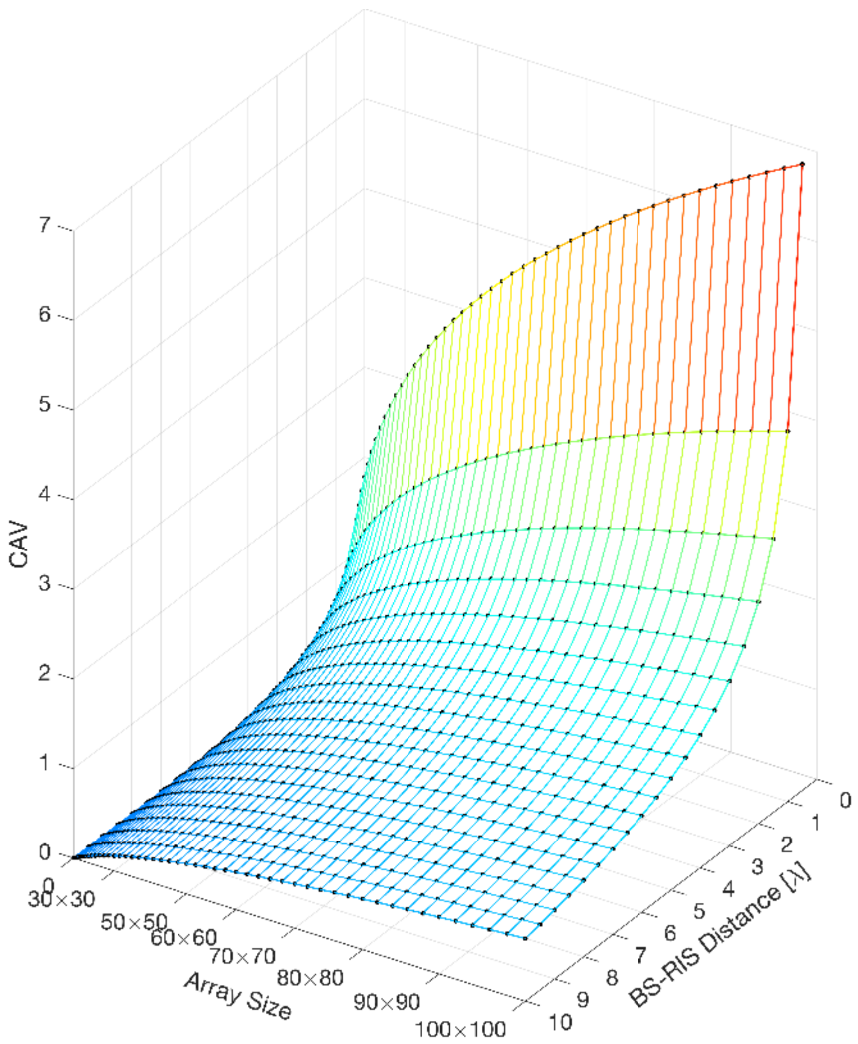

Figure 7.3: CAV for different array sizes and BS-RIS separations.

antenna, the CAV exhibits greater sensitivity, further underlining the importance of advanced designs like BD-RIS to mitigate these effects.

7.6 Simulation Results and System Evaluation

This section presents the computer simulation results for the proposed BS-integrated BD-RIS, offering a comparative evaluation against considered benchmarks. The simulation setup is first outlined for a realistic mmWave street canyon environment. Next, the beamforming performance is assessed, demonstrating the potential of the

BD-RIS to outperform the traditional D-RIS structure and closely rival the performance of active analog beamforming antenna arrays. ABER and achievable rate analyses are conducted under diverse circumstances to comprehensively evaluate the system's performance from multiple perspectives. Finally, it is shown that dividing the BD-RIS cells into groups according to their geometric symmetry around the active antenna allows for a reduction in circuit complexity while maintaining system performance.

7.6.1 Simulation Setup

We consider a P2P scenario in the street canyon environment which the distance between the BS-integrated BD-RIS and UE is considered $d = 20$ m. We consider the carrier frequency $f_c = 28$ GHz; hence, we have a mmWave environment with a spatially sparse-scattered channel described in (7.4). Due to the highly dynamic nature of urban environments and the susceptibility of mmWave signals to blockages, the presence of a LOS path cannot be consistently guaranteed. To comprehensively evaluate the system's performance under varying conditions, we consider two distinct scenarios:

- *Scenario 1*: A dominant LOS component is present alongside several NLOS clusters.
- *Scenario 2*: The LOS is blocked, and communication relies solely on the NLOS clusters to ensure connectivity.

The path loss model for $i \in \{\text{LOS}, \text{NLOS}\}$ path is defined as follows [4]:

$$\text{PL}_i(d)\,[\text{dB}] = a_i + 10\, b_i \log_{10}(d) + \xi_i, \tag{7.19}$$

where a_i represents the reference path loss at the reference distance, b_i is the path loss exponent that determines the rate of signal attenuation with distance, and $\xi_i \sim \mathcal{N}(0, \sigma^2_{\xi,i})$ models the effect of shadowing, with $\sigma_{\xi,i}$ indicating the shadow fading severity. The practical values for the parameters a_i, b_i, and $\sigma_{\xi,i}$ are provided

Table 7.1: Simulation Parameters.

Parameter	**Description**	**Value**
f_c	Carrier frequency	28 GHz
B	Communication bandwidth	100 MHz
d	Communication range	20 m
$d_x = d_y$	Inter-element spacing across x and y axis	$\lambda/2$
d_c	BS-RIS separation	$\lambda/2$
A	Area of each passive elements	$(\lambda/2)^2$
M	BS Array size	10×10
C	Number of clusters	8
L	Number of paths per cluster	10
ς_c	Angular spread in c-th cluster	$7.5°$
P	BS transmitted power	20 dBm
$\mathcal{M}$	$\mathcal{M}$-ary constellation order	2
a_{LOS}	Reference LOS path loss	61.4 dB
a_{NLOS}	Reference NLOS path loss	72 dB
b_{LOS}	LOS path loss exponent	2
b_{NLOS}	NLOS path loss exponent	2.92
$\sigma_{\xi,\text{LOS}}$	LOS shadow fading severity	5.8 dB
$\sigma_{\xi,\text{NLOS}}$	NLOS shadow fading severity	8.7 dB
Noise PSD	Noise power spectrum density	-174 dBm

in Table 7.1, derived from an experimental campaign conducted in a dense urban environment in New York City [4]. The noise power spectral density (PSD) is assumed to be $-174\,\text{dBm/Hz}$ [87, 105], and the system bandwidth (BW) is set to $B = 100\,\text{MHz}$ [87, 105]. Consequently, the noise power is calculated as $\sigma_n^2 = \text{PSD} + 10\log_{10}(B) = -94\,\text{dBm}$. The number of NLOS clusters and paths is set to $C = 8$ and $L = 10$, respectively, following the parameters in [87, 26]. The angular spread of the NLOS clusters is assumed to be $\varsigma_c = 7.5°$ as specified in [87].

Additionally, a binary phase shift keying (BPSK) signaling scheme is employed for ABER analysis. Unless specified otherwise, the default BD-RIS configuration in all simulations is fully-connected, showcasing the maximum potential of BD-RIS. A summary of the default system parameter values is presented in Table 7.1.

A critical factor influencing the BD-RIS configuration and overall system performance is the stochastic nature of the RIS-UE channel. To ensure effective performance, the BS must access the efficient beamforming vector $\boldsymbol{b} \in \mathbb{C}^{M\times 1}$ which aligns with the RIS-UE channel during each time block. Obviously, the availability of CSI (full or partial) is crucial for deriving such an effective beamforming vector. In this chapter, we evaluate the performance of the proposed system under three different cases based on CSI availability:

1. *Case 1 (Full CSI is available at the BS)*: The BS, equipped with a large antenna array, can estimate the RIS-UE channel by processing pilot signals transmitted by the UE during the uplink phase [120, 130, 131]. The optimal *unconstrained* beamforming vector for the channel $\boldsymbol{h}$ is determined as $\boldsymbol{b} = \boldsymbol{v}_1$, where $\boldsymbol{v}_1 \in \mathbb{C}^{M\times 1}$ represents the first column of the unitary matrix $\boldsymbol{V} \in \mathbb{C}^{M\times M}$ [26]. This matrix is obtained via the ordered SVD of the channel, expressed as $\boldsymbol{h}^{\mathsf{T}} = \boldsymbol{\Sigma}\boldsymbol{V}^{\mathsf{H}}$, where $\boldsymbol{\Sigma}$ is a $1 \times M$ vector of singular values with non-negative elements. The beamforming vector $\boldsymbol{v}_1$ encapsulates the optimal complex weights—comprising both phase and magnitude—for the BD-RIS elements to maximize beamforming gain. However, in systems with constant modulus constraints, such as BS-integrated D-RIS or active analog beamforming antenna arrays utilizing analog phase shifter networks, only the phase information from $\boldsymbol{v}_1$ can be exploited.

2. *Case 2 (Full CSI is available at the UE)*: In general, the UE may handle channel estimation;[2] however, feedbacking the full CSI to the BS, particularly in

[2]Although we focus on a MISO system in this work, the extension to a MIMO system incorporating a UE-integrated BD-RIS is straightforward. In such a scenario, the UE also has the capability to estimate the channel.

systems with massive MIMO, is often impractical and can result in significant overhead [26]. To address this, the UE can utilize the spatially sparse precoding (SSP) scheme proposed in [26]. With this approach, the UE identifies the best match for the channel's dominant eigenmode $\boldsymbol{v}_1$ from a predefined codebook. As the codebook is shared between the BS and UE, the UE only needs to transmit the index of the selected codeword, significantly reducing feedback overhead. Here, we utilize a codebook consisting of beams corresponding to equally spaced angles [26], defined as follows:

$$\mathcal{B} = \{\boldsymbol{a}(\phi, \theta) | \phi \in [-\pi : \frac{\pi}{36} : \pi], \theta \in [0 : \frac{\pi}{36} : \frac{\pi}{2}]\}. \tag{7.20}$$

The optimal beam alignment with $\boldsymbol{v}_1$ is determined by identifying the beam index that maximizes the correlation, computed as:

$$\{i^\star, j^\star\} = \max_{i,j} \|\boldsymbol{a}^{\mathsf{H}}(\phi_i, \theta_j)\boldsymbol{v}_1\|, \tag{7.21}$$

where ϕ_i and θ_j represent the i-th and j-th quantized azimuth and elevation angles within the ranges $\phi = [-\pi : \frac{\pi}{36} : \pi]$ and $\theta = [0 : \frac{\pi}{36} : \frac{\pi}{2}]$, respectively. Subsequently, the UE transmits the indices $\{i^\star, j^\star\}$ to the BS via limited feedback link, allowing the BS to compute the beamforming vector as $\boldsymbol{b} = \boldsymbol{a}(\phi_{i^\star}, \theta_{j^\star})$.

3. *Case 3 (Partial CSI is available)*: In certain scenarios, full CSI may be unavailable, or obtaining partial CSI is preferred to minimize channel estimation overhead [90, 86]. Angular channel information can be extracted using AoD estimation algorithms [71], allowing the identification of an effective transmission direction.[3] Subsequently, the effective channel h_{eff}, required for detection, can be readily estimated.

[3] In order to emulate this process, we search across the available LOS and NLOS directions to maximize the transmitted signal in the target sub-channel while minimizing the leakage power into unintended sub-channels. Mathematically, the optimal direction $c^\star$ is determined by solving $c^\star = \max_{c=0,\ldots,C} \frac{|\boldsymbol{h}_c^{\mathsf{T}}\boldsymbol{a}(\varphi_c,\vartheta_c)|}{|(\sum_{i\neq c}\boldsymbol{h}_i^{\mathsf{T}})\boldsymbol{a}(\varphi_c,\vartheta_c)|}$; hence, the effective beamforming vector can be obtained as $\boldsymbol{b} = \boldsymbol{a}(\varphi_{c^\star}, \vartheta_{c^\star})$. It is worth noting that the direction of the c-th NLOS cluster is assumed to align with its best effective path, as defined in [87, equation (13)].

To assess the performance of the proposed BS-integrated BD-RIS, we consider two benchmarks as outlined below:

- *Benchmark 1 (D-RIS)*: A traditional transmissive RIS integrated at the BS [107, 115, 116, 135, 126, 114, 119, 127, 136, 128, 18] features a diagonal phase shift matrix as its defining characteristic. In this benchmark, the phase shift matrix is given by $\mathbf{\Omega} = \text{diag}\left(e^{-\jmath \arg(\boldsymbol{g} \odot \boldsymbol{b}^*)}\right)$.

- *Benchmark 2 (Active Analog Beamforming Antenna Array)*: A BS configured with a planar active analog beamforming antenna array comprising $M_x \times M_y$ elements connected to a network of analog single phase shifters [10]. In this configuration, the analog beamforming vector is directly applied to the phase shift network. It is important to note that the analog phase shift network imposes a constant modulus constraint on the beamforming weights. Consequently, when employing SVD, a phase-only beamforming vector is used, calculated as $\boldsymbol{b} = e^{\jmath \arg(\boldsymbol{v}_1)}$. The signal model corresponding to this benchmark can be expressed as:

$$y = \sqrt{P}\boldsymbol{h}^{\mathsf{T}}\boldsymbol{b}s + n. \tag{7.22}$$

7.6.2 Beamforming Performance Analysis

This subsection evaluates the beamforming performance of the proposed BS-integrated BD-RIS under various system configurations, serving as a foundation for understanding the system's behavior from other perspectives. As stated in (7.8), $\boldsymbol{\zeta} = \mathbf{\Omega}\boldsymbol{g}$ represents the effective beamforming vector at the RIS's transmit terminal. Here, the matrix $\mathbf{\Omega}$ not only defines the RIS type (D-RIS or BD-RIS) but also specifies the grouping strategy employed in the BD-RIS configuration. To simplify the analysis, we consider a directional beam focused at $\phi = \theta = 0$ as the beamforming vector for configuring the BD-RIS/D-RIS, defined as $\boldsymbol{b} = \boldsymbol{a}(0, 0)$.

Fig. 7.4 presents the beamforming gain of the proposed BS-integrated BD-RIS compared with the benchmarks, i.e., the D-RIS and the active analog beamforming antenna array. Overall, increasing the array size results in sharper beams with

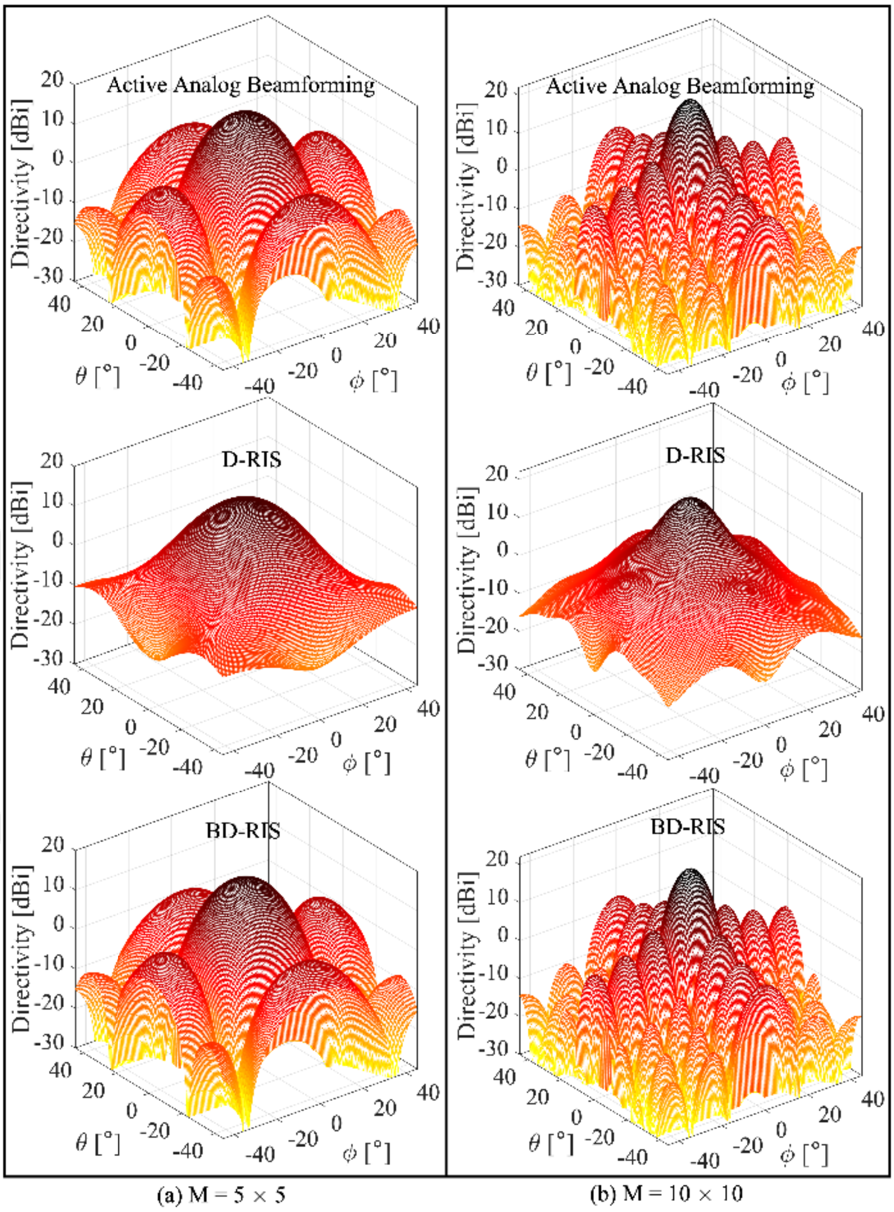

Figure 7.4: Beamforming performance of different BS structures: (a) beam patterns for $M = 5 \times 5$ array, (b) beam patterns for $M = 10 \times 10$ array.

Table 7.2: Beamforming Performance Metrics for Different BS Structures

	Active Analog Beamforming		**D-RIS**		**BD-RIS**	
	5 × 5	**10 × 10**	**5 × 5**	**10 × 10**	**5 × 5**	**10 × 10**
PP Directivity [dBi]	15.1975	21.548	13.5771	17.6019	15.1975	21.548
HPP Directivity [dBi]	12.1186	18.6688	10.4215	14.6447	12.1186	18.6688
HPBW [°]	21	10	27	15	21	10

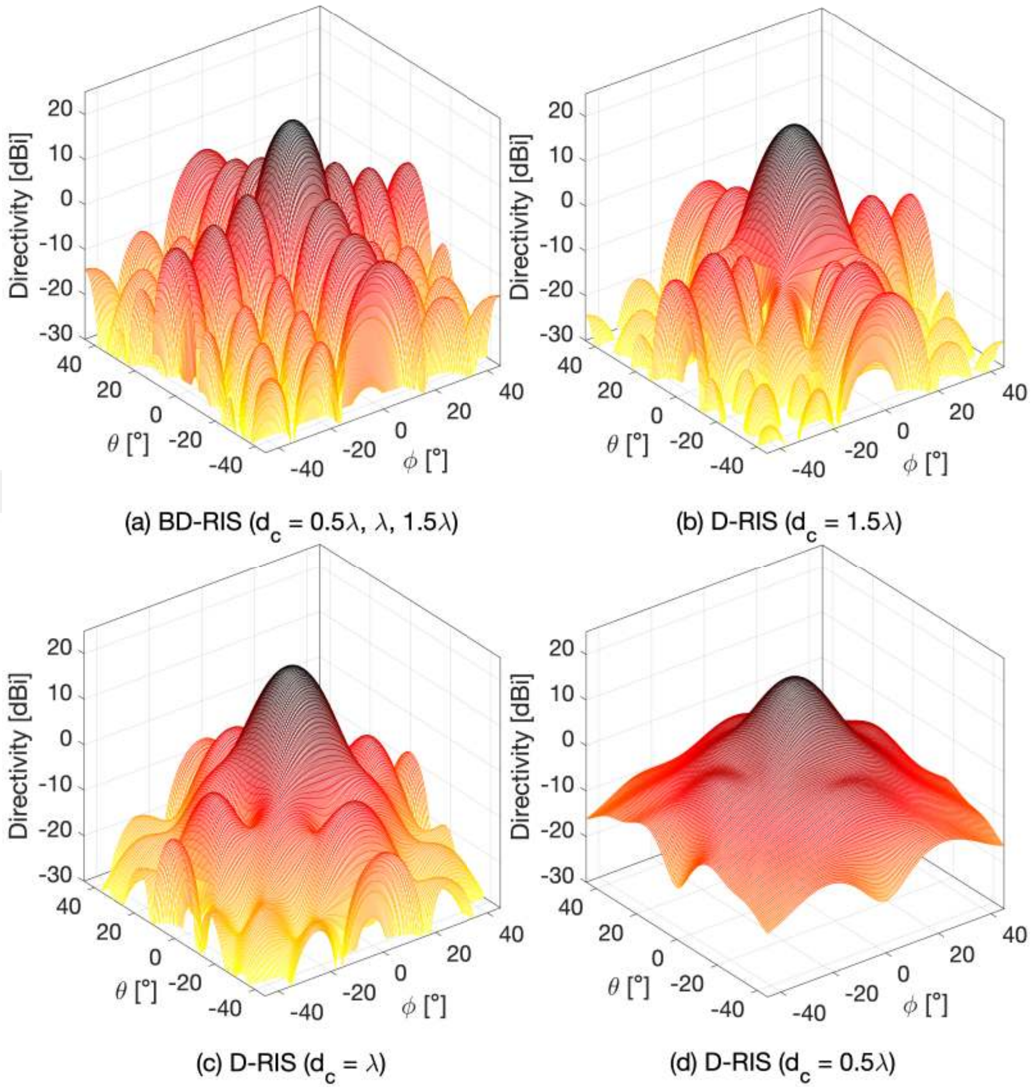

Figure 7.5: Beamforming performance comparison between BS-integrated BD-RIS and D-RIS for varying BS-RIS separations (d_c): a) BD-RIS with $d_c = 0.5\lambda, \lambda, 1.5\lambda$, (b) D-RIS with $d_c = 1.5\lambda$, (c) D-RIS with $d_c = \lambda$, and (d) D-RIS with $d_c = 0.5\lambda$.

Table 7.3: Beamforming Performance Metrics for Different BS-RIS Separations

	D-RIS			**BD-RIS**
	$\boldsymbol{d_c = 0.5\lambda}$	$\boldsymbol{d_c = \lambda}$	$\boldsymbol{d_c = 1.5\lambda}$	$\boldsymbol{d_c = 0.5\lambda, \lambda, 1.5\lambda}$
PP Directivity [dBi]	17.6019	20.0124	20.8684	21.548
HPP Directivity [dBi]	14.6447	17.0038	17.8702	18.6688
HPBW (°)	15	13	12	10

higher directivity across all structures. However, the D-RIS exhibits lower directivity and broader beams compared to its counterparts, while the BD-RIS achieves a beamforming performance comparable to that of the active analog beamforming antenna array. This superior performance of the BD-RIS is attributed to its fully-connected structure, which enables it to effectively compensate for the CAV. The numerical metrics, including peak point (PP) directivity, half-power point (HPP) directivity, and half-power beamwidth (HPBW), extracted from Fig. 7.4 for various BS structures, are summarized in Table 7.2.

Fig. 7.5 illustrates the beamforming gain of the BS-integrated BD-RIS and D-RIS for varying BS-RIS separations (d_c). Thanks to its ability to adjust both phase and amplitude, the BD-RIS maintains a consistent beam pattern regardless of d_c, while the D-RIS demonstrates reduced directivity and increased HPBW as d_c decreases. As shown in Fig. 7.3, the CAV increases as d_c decreases, posing a challenge for D-RIS since it cannot compensate for the elevated CAV. The key beamforming metrics for these configurations are summarized in Table 7.3. It is crucial to highlight that as d_c increases, the multiplicative path loss becomes more pronounced, which detrimentally affects the overall system performance. Therefore, ensuring a high beamforming gain while minimizing d_c is essential for optimizing performance, as elaborated in Section 7.6.4.

7.6.3 ABER Analysis

This subsection analyzes the ABER performance of the proposed BS-integrated BD-RIS across different LOS availability scenarios and three distinct precoding schemes. The results are benchmarked against D-RIS and active analog beamforming antenna arrays. Furthermore, as illustrated in Fig. 7.6, the theoretical bound derived in Section 7.4 provides a tight upper limit, validating the accuracy of our ABER simulations.

As shown in Fig. 7.6, the BD-RIS achieves performance close to that of the active analog beamforming antenna array across all evaluated scenarios and cases, demonstrating its robustness in delivering efficient beamforming gain under varying

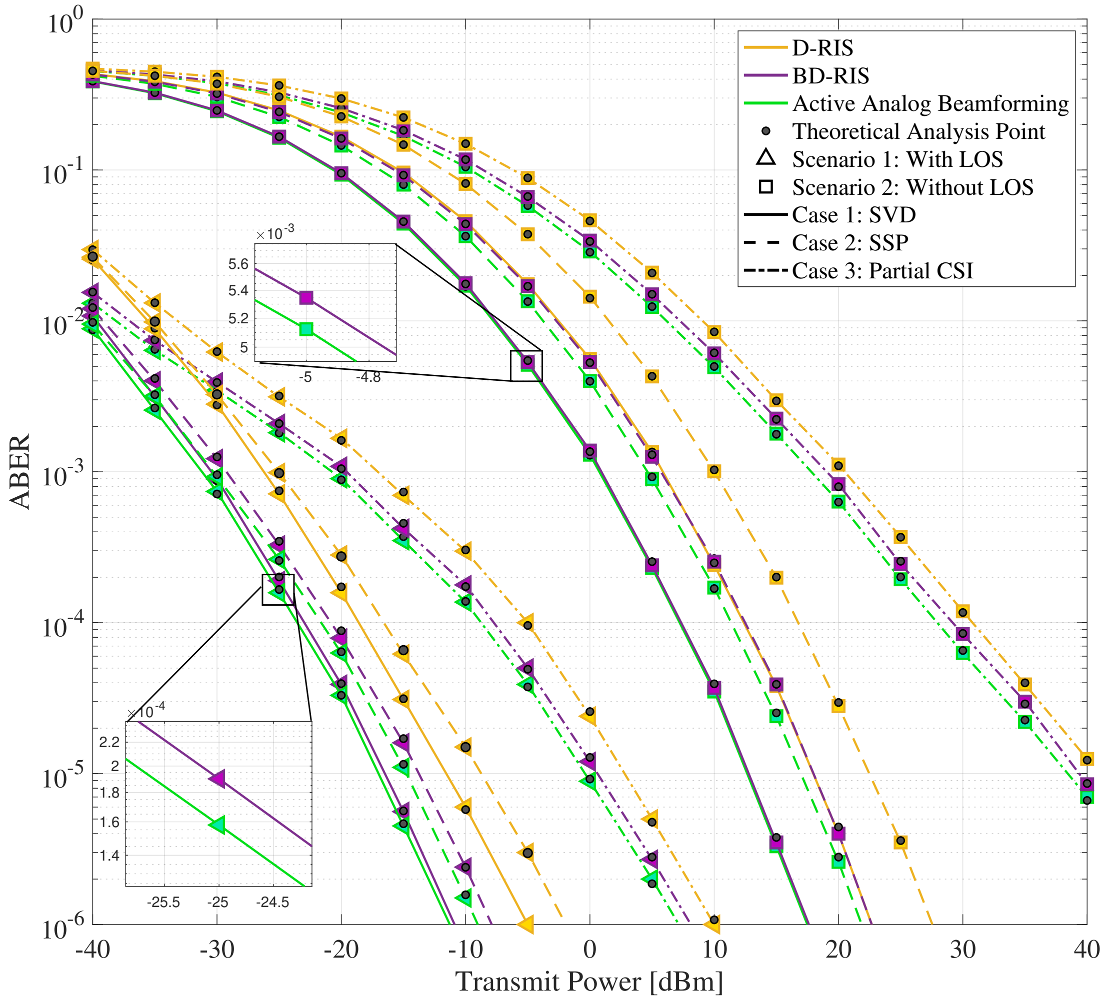

Figure 7.6: ABER performance of the BS-integrated BD-RIS compared to D-RIS and active analog beamforming antenna array under varying LOS conditions and precoding schemes, with theoretical validation.

conditions. As outlined in Algorithm 4, the beamforming vector $\boldsymbol{b}$ is employed in the BD-RIS configuration as a representation of the channel $\boldsymbol{h}$. Notably, in Case 1, $\boldsymbol{b}$ incorporates both the amplitude and phase variations. However, only the BD-RIS can fully utilize these amplitude and phase variations, whereas the benchmarks, including the active analog beamforming antenna array, are restricted to exploiting only the phase components of $\boldsymbol{b}$. This capability provides the BD-RIS with one more advantage in Case 1, resulting in ABER performance that is closer to that of the active analog beamforming antenna array compared to other cases. In Scenario 2, where the channel $\boldsymbol{h}$ is entirely composed of NLOS components, the amplitude variations across the RIS elements are more pronounced. This further improves the ABER performance of the BD-RIS in Case 1, narrowing the gap with the active analog beamforming antenna array even more compared to Scenario 1. In other cases, the performance gap between the BD-RIS and the active analog beamforming antenna array is solely attributed to the multiplicative path loss caused by the physical distance between the active antenna and the RIS elements.

On the other hand, the D-RIS, constrained to phase-only manipulation of the impinging signal, exhibits greater ABER performance degradation across various scenarios and cases due to both multiplicative path loss and reduced beamforming gain. As illustrated in Fig. 7.4 and summarized in Table 7.2, the D-RIS generates wider beams, leading to increased signal leakage into unintended paths. Consequently, as a part of signal experiences higher fading in these unintended paths, the ABER increases for the D-RIS configuration.

These results highlight the limitations of D-RIS and underscore the significant advantages of BD-RIS in achieving efficient beamforming gain and improved ABER performance.

7.6.4 Achievable Rate Analysis

This subsection provides a detailed analysis of the achievable rate performance as a function of transmit power, array size, and BS-RIS separation (d_c). The achievable rate is calculated as follows:

$$R = \mathbb{E}_{\boldsymbol{h}}\left[\log_2\left(1+\frac{|\sqrt{P}\boldsymbol{h}^{\mathsf{T}}\boldsymbol{\zeta}x|^2}{\sigma_n^2}\right)\right], \tag{7.23}$$

where $x \sim \mathcal{CN}(0,1)$ is the transmitted symbol following a complex normal distribution with unit variance, allowing the analysis to be generalized for any potential constellation.

Fig. 7.7(a) illustrates the achievable rate as a function of transmit power across various scenarios and precoding cases. In all simulations, the BD-RIS demonstrates

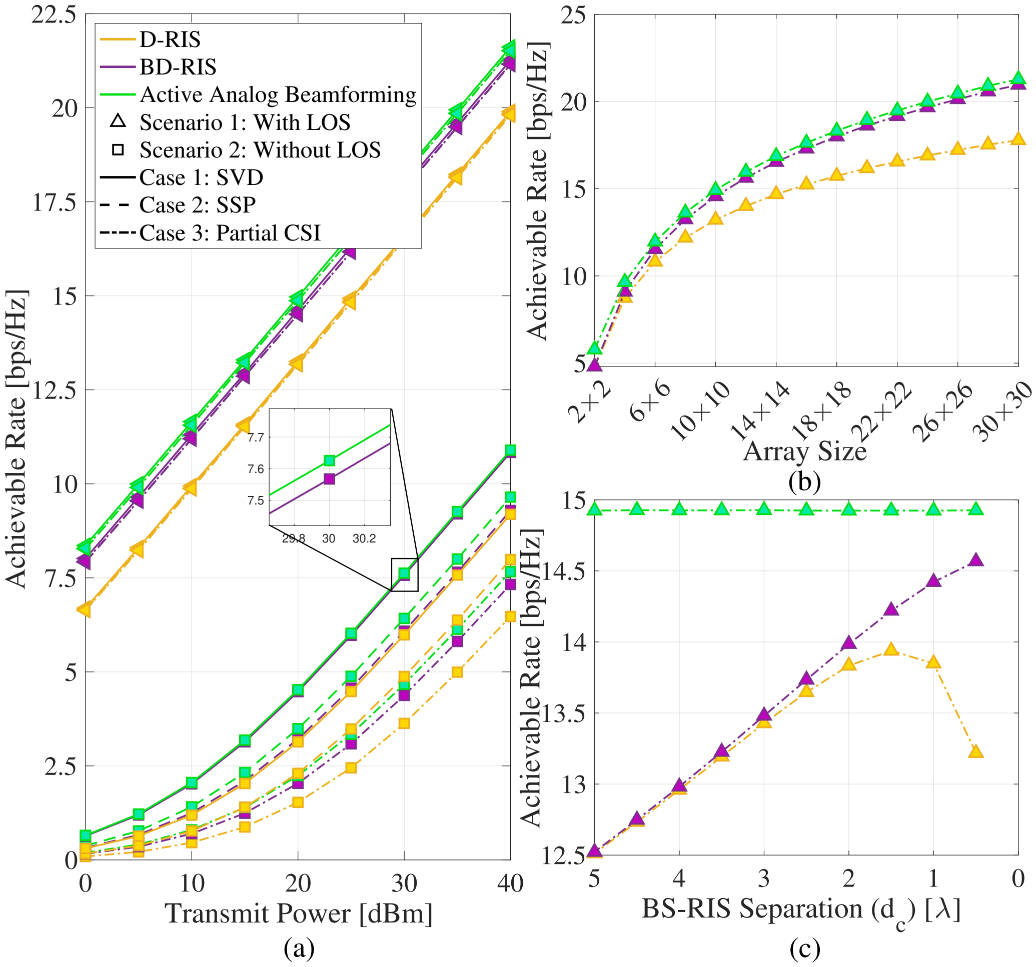

Figure 7.7: Achievable rate analysis for the proposed BS-integrated BD-RIS and benchmarks under various scanrios and precoding cases: (a) varying transmit power, (b) varying array size, (c) varying BS-RIS separation (d_c).

performance close to that of the active analog beamforming antenna array. Notably, in Scenario 2, where LOS is unavailable, and under Case 1, the BD-RIS achieves an achievable rate comparable to the active analog beamforming antenna array. As discussed in the previous subsection, the BD-RIS's ability to manipulate both the phase and amplitude enables it to leverage the optimal phase and amplitude provided by $\boldsymbol{v}_1$. In contrast, the active analog beamforming antenna array is limited to utilizing only the phase information from the dominant eigenmode $\boldsymbol{v}_1$. This additional capability of the BD-RIS enhances its beamforming performance, allowing it to compensate for the multiplicative path loss and achieve comparable performance to the active analog beamforming antenna array in Scenario 2. Similar to the ABER performance, the reduced beamforming gain of the D-RIS leads to degraded achievable rate performance across all simulations.

It is worth noting that in the presence of a dominant LOS, as in Scenario 1, the achievable rate is identical across all precoding cases, as illustrated in Fig. 7.7(a). For the remainder of this chapter, we focus on simulations conducted under Scenario 1 using Case 3, the less complex beamforming method. Fig. 7.7(b) illustrates the achievable rate as a function of array size, comparing the performance of the proposed BS-integrated BD-RIS with the benchmarks. For a small RIS array of size 2×2, the BD-RIS and D-RIS exhibit identical performance. This is because, in this configuration, the distances between the active antenna and all RIS elements (d_m) are equal, resulting in uniform channel gain amplitudes across the elements; hence CAV $= 0$ and there is no need for amplitude compensation. However, as the array size increases, the channel gain amplitudes across the RIS elements start to vary, as explained in Section 7.5. As shown in Fig. 7.3, larger array sizes lead to increased CAV, introducing greater discrepancies in channel gain amplitudes across RIS elements and emphasizing the need to compensate for these variations. Since the D-RIS cannot address amplitude variations, the performance gap between the D-RIS and the active analog beamforming antenna array widens with increasing array size. In contrast, the BD-RIS, with its ability to compensate for both amplitude and phase variations, maintains a constant performance gap compared to the active analog beamforming antenna array as the array size increases. As previously discussed, this constant gap is attributed to the multiplicative path loss.

The BS-RIS separation (d_c) is another critical factor influencing the CAV, as outlined in Section 7.5. As shown in Fig. 7.7(c), at sufficiently large separations, a reduction in d_c generally leads to an increase in the achievable rate due to reduced multiplicative path loss. However, as d_c decreases further, the D-RIS begins to exhibit noticeable performance degradation compared to the BD-RIS. This behavior arises because the increasing CAV at smaller d_c values demands compensation to maintain effective beamforming gain. While the BD-RIS, with its inter-element connections, can effectively mitigate amplitude variations, the D-RIS lacks this capability. As shown in Fig. 7.7(c), when d_c falls below a certain threshold ($d_c < 1.5\lambda$ in the configuration considered here), the achievable rate performance of the D-RIS starts to decline with further decreasing d_c. According to Fig. 7.5, the beamforming performance of the D-RIS deteriorates with decreasing d_c, resulting in wider beams and reduced directivity. This suboptimal beamforming performance for $d_c < 1.5\lambda$ leads to a decrease in the achievable rate for the D-RIS, as the negative impact of poor beamforming gain outweighs the positive effect of reduced multiplicative path loss. In contrast, the BD-RIS consistently demonstrates enhanced performance as d_c decreases, attributed to its ability to effectively compensate for significant CAV and sustain robust beamforming. This enables the BD-RIS to fully capitalize on the reduced multiplicative path loss associated with smaller d_c.

7.6.5 Group-Connected BD-RIS Structure

In this subsection, we examine the impact of the group-connected BD-RIS, which features a less complex circuit architecture compared to the fully-connected structure, on the achievable rate performance and beamforming gain of the proposed system. Fig. 7.8(a) illustrates the achievable rate performance for different numbers of groups. As the number of groups increases, the inter-element connections within each group decrease, as each fully-connected group comprises fewer elements. This reduction in inter-element connections lowers the circuit complexity but also reduces the degrees of freedom required to effectively compensate for the CAV, resulting in a degradation in achievable rate performance. However, certain special cases in Fig. 7.8(a) reveal an exception to this trend. Specifically, the performance remains identical for $G = 1$ and $G = 2$, as well as for $G = 10$ and $G = 20$.

The reason for this behavior is illustrated in the beam patterns in Figs. 7.8(b) and (c). For $G = 1$ and $G = 2$ (Fig. 7.8(b)), the beam patterns are identical, and a similar observation holds for $G = 10$ and $G = 20$ (Fig. 7.8(c)). This phenomenon can be attributed to the geometric symmetry in the group configurations, as shown

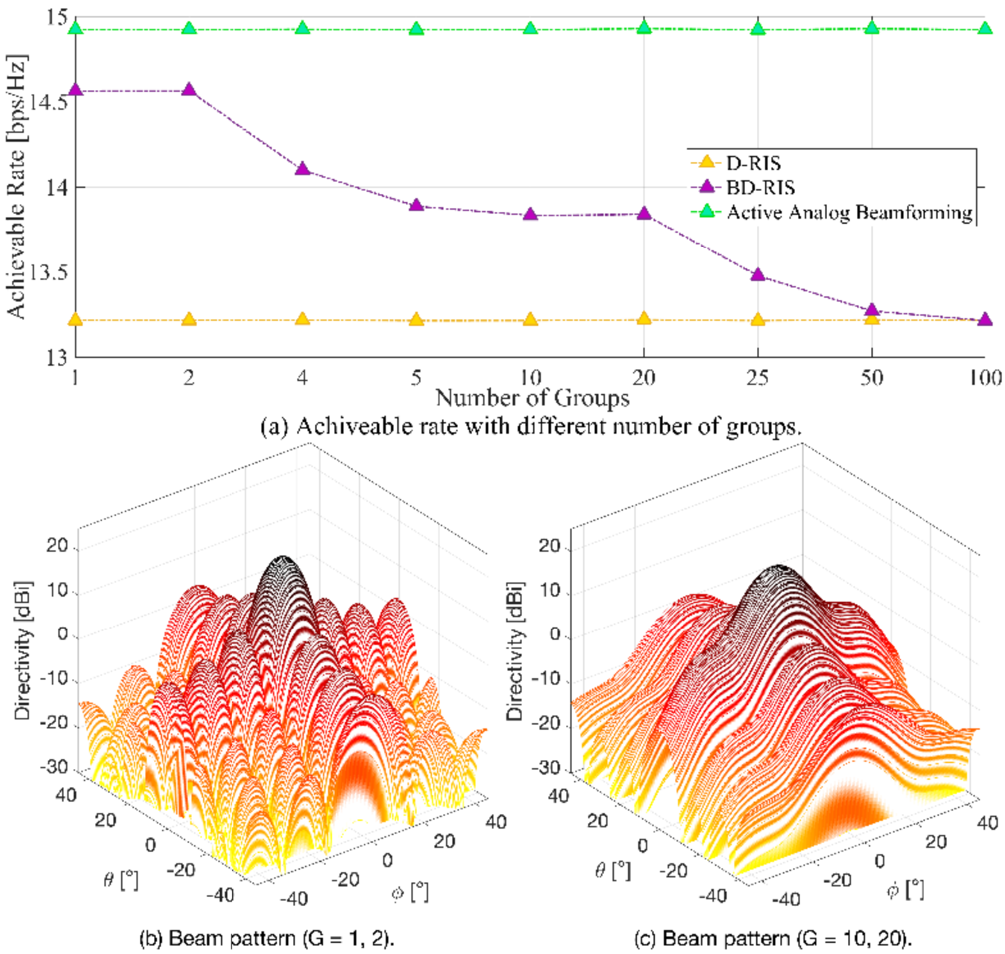

Figure 7.8: Achievable rate and beam pattern comparison of the BS-integrated BD-RIS under different group configurations: (a) Achievable rate performance for varying numbers of groups; (b) beam pattern comparison for fully-connected BD-RIS ($G = 1$) and group-connected BD-RIS ($G = 2$); (c) beam pattern comparison for group-connected BD-RIS configurations with $G = 10$ and $G = 20$.

in Fig. 7.9. The blue circle in Fig. 7.9 denotes the location of the active antenna array, which is positioned at the back of the RIS at a distance d_c from its center. In Fig. 7.9(a), a fully-connected structure is depicted, capable of compensating for CAV across the entire BD-RIS. However, this fully-connected structure can be divided into two groups for a 2-group-connected configuration, where one group is highlighted with solid colors, and the other is represented with cross-hatches. These groups

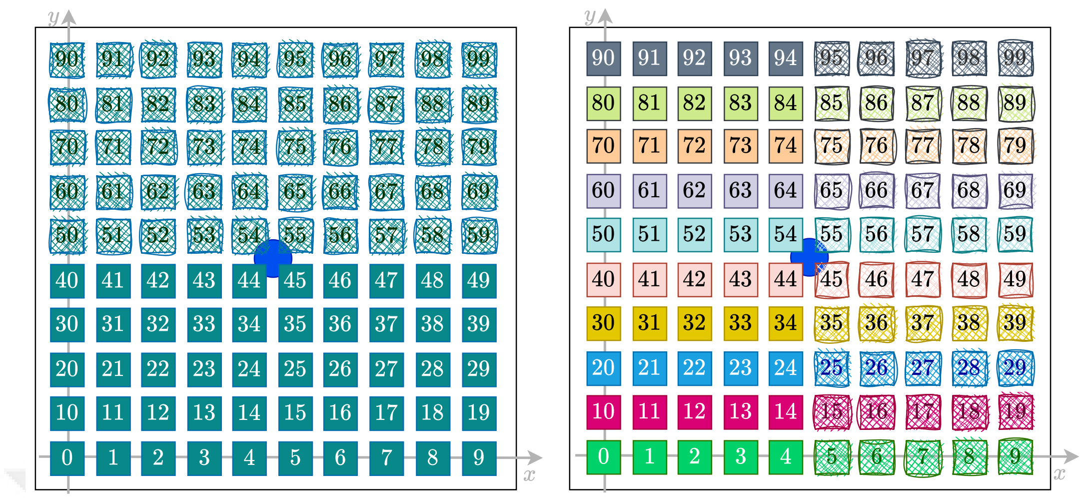

(a) (b)

Figure 7.9: Grouping configurations of the BD-RIS: (a) a fully-connected structure transitioning to a 2-group-connected structure ($G = 2$) without performance loss; (b) a 10-group-connected structure transitioning to a 20-group-connected structure ($G = 20$) while maintaining performance integrity.

exhibit geometric symmetry around the active antenna. Hence, it is evident that the set of $[\boldsymbol{g}]_m$ values for each group is identical, leading to an equivalent CAV value for both groups. Furthermore, when these two sets are combined, the CAV of the entire BD-RIS remains equal to the CAV of each individual group. Consequently, a 2-group-connected BD-RIS structure with linear permutation suffices to effectively compensate for CAV across the entire BD-RIS.[4] Similarly, Fig. 7.9(b) illustrates a 10-group-connected structure, where the elements in each row are assigned to the same group. This structure can be further divided into two symmetric sub-groups around the active antenna, ensuring that the CAV values for each sub-group remain identical and equivalent to the original group. Consequently, inter-element

[4] Clearly, the 2-group-connected structure can be further divided into a 4-group-connected structure while maintaining identical CAV values due to the symmetry around the active antenna. However, achieving this requires more advanced permutations beyond the linear approach, which will be explored in our future work.

connections can be minimized without compromising performance in such symmetric configurations.

It is worth noting that, as depicted in Fig. 7.9(b), the 10-group-connected structure incorporates inter-element connections exclusively along one dimension (the x-axis), with no connections along the y-axis. This configuration leads to a narrow HPBW in the elevation dimension while maintaining a broader beam in the azimuth dimension, as demonstrated in Fig. 7.8(b).

7.7 Conclusion

This chapter studied a novel array architecture that enables passive beamforming at the BS, achieving beamforming gains comparable to those of active analog beamforming antenna arrays. By integrating a BD-RIS within the BS, a SISO system can emulate the performance of a MISO system, leveraging the superior passive beamforming capability of the BD-RIS. Our analysis demonstrated that the beamforming gain of the BS-integrated BD-RIS is robust to variations in RIS dimensions and BS-RIS separation, owing to its inter-element connection structure. In contrast, the performance of traditional D-RIS is highly sensitive to these critical design parameters. Consequently, the only notable performance degradation in the BS-integrated BD-RIS arises from the multiplicative path loss, which can be minimized by reducing the BS-RIS separation without concerns about beamforming degradation at short separations. To address circuit complexity, we proposed a simple grouping strategy that reduces the number of inter-element connections while maintaining equivalent beamforming performance. Comprehensive simulation results validated the efficiency of the proposed BS-integrated BD-RIS architecture and demonstrated its superiority over traditional D-RIS systems. Furthermore, it was shown that the proposed architecture achieves performance levels close to those of active analog beamforming antenna arrays, offering an affordable alternative in terms of cost and power consumption.

Chapter 8

EFFICIENT LOCALIZATION WITH BASE STATION-INTEGRATED BEYOND DIAGONAL RIS

8.1 Introduction

In sixth-generation (6G) communication systems, high-precision localization is expected to be achieved with a single anchor, enabled by advances in millimeter wave (mmWave) communication and large antenna arrays [137, 138]. Such technologies allow base stations (BSs) or user equipments (UEs) to measure angles of departure (AoD) and arrival (AoA) more precisely. Reconfigurable intelligent surfaces (RISs) offer a promising, cost-effective alternative to large antenna arrays by enabling passive beamforming within transceivers [114]. For instance, the stacked intelligent metasurface (SIM) transceiver design [126, 114, 119, 127] demonstrates the potential of passive beamforming with benefits such as ultra-fast processing, reduced cost and complexity, and lower energy consumption. Beyond diagonal RIS (BD-RIS) advances RIS technology by enabling control over both the amplitude and phase of impinging waves, offering higher flexibility in passive beamforming [17, 121]. Notably, unlike active or absorptive RIS [139], BD-RIS controls both phase and amplitude of the impinging signal under a unitary constraint, without amplification or absorption.

The fundamental limits of mmWave multiple-input multiple-output (MIMO) systems with large RISs, focusing on channel estimation, localization, and orientation error bounds, are studied in [137]. The study of [122] investigates the use of a BD-RIS at the transmitter for massive MIMO, using manifold optimization to enhance spectral efficiency with fewer active antennas. Similarly, [140] shows that BD-RIS enhances both communication and sensing performance in mmWave integrated sensing and communication (ISAC) systems, significantly reducing power consumption and presenting a promising solution for future applications. RIS-aided near-field (NF) localization is further explored in [141, 142], showing the potential for NF localization by exploiting spherical wavefront. A SIM-aided ISAC system, with shared elements for communication and sensing, is proposed in [127], while the role of SIM for direction-of-arrival (DoA) estimation is examined in [136, 128].

In scenarios such as those studied in [141, 127, 136, 128], where part or all of the channel operates in the NF, the signal undergoes amplitude variations across different RIS elements alongside phase changes. Diagonal RIS (D-RIS), however, only enables phase adjustment, whereas BD-RIS allows control over both amplitude and phase. Despite this added flexibility, the localization potential of BD-RIS remains unexplored. This gap in the literature motivates our investigation of BD-RIS's potential for precision localization in such scenarios. The main contributions of this chapter are as follows:

1. We propose a BS-enabled passive beamforming system using a BD-RIS for downlink efficient localization, a scenario that has not been previously explored.

2. We analyze the beamforming gain of the proposed system, demonstrating the superiority of BD-RISs over traditional structures. Additionally, Cramér-Rao lower bound (CRLB) analysis in both NF and far-field (FF) scenarios is performed.

3. We conduct a comprehensive analysis, evaluating localization performance across various system parameters. This detailed analysis offers new insights into the potential of BD-RIS, highlighting its capability to enhance precision localization from multiple perspectives.

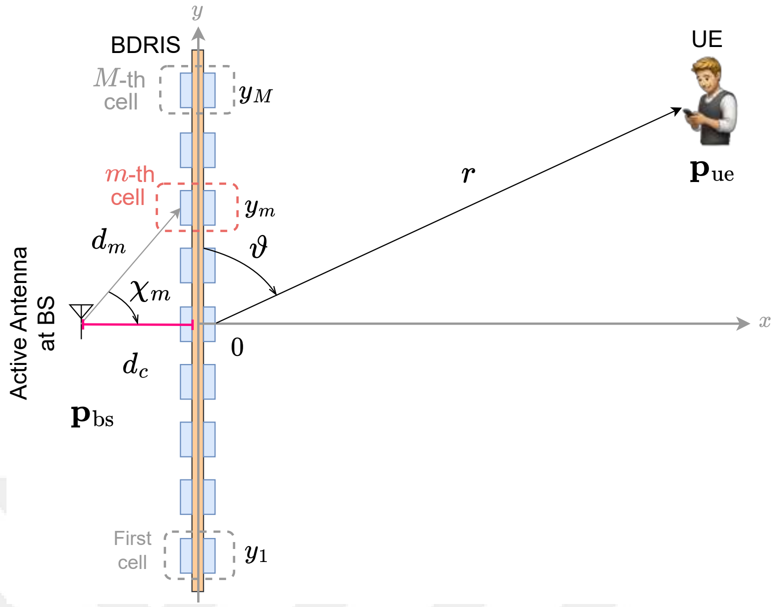

Figure 8.1: System model for the proposed BS-integrated BD-RIS.

8.2 System, Channel, and Signal Model

This section outlines the proposed system, channel, and signal model, which leverages BS-enabled passive beamforming assisted by a BD-RIS to facilitate downlink localization.

8.2.1 System Model

Fig. 8.1 illustrates the proposed system designed to enable passive beamforming at the BS in a single-input single-output (SISO) communication system, where a linear fully-connected BD-RIS is integrated with the BS to emulate a multiple-input single-output (MISO) system.[1] The BD-RIS consists of M cells, each containing two elements: one faces the active antenna, while the other on the opposite side transmits signals toward the UE [18]. The inter-element spacing on both sides of

[1]This work is the first to explore the integration of fully-connected BD-RIS at the BS for passive beamforming in localization. We focus on 2D localization to simplify the analysis and provide a clear understanding of the system's behavior, reserving the more complex 3D analysis for future research.

the BD-RIS is $\delta = \lambda/2$, where λ denotes the wavelength of the carrier frequency. Accordingly, the array aperture of BD-RIS can be calculated as $D = (M-1)\delta$. All elements are internally connected, forming a fully-connected BD-RIS structure [17]. For passive beamforming to occur at the BS, the total energy of the signal emitted by the active antenna must pass through the BD-RIS. As a result, the BD-RIS operates exclusively in transmissive mode, with its reflective mode inactive [18].

For simplicity, we assume that the center of the BD-RIS is located at the origin of the reference Cartesian system, i.e., $\boldsymbol{p}_{\text{ris}} = [0,0]^\mathsf{T}$, and is aligned along the y-axis. Therefore, the position of the m-th cell is given by $\boldsymbol{p}_m = [0, y_m]^\mathsf{T}$, where $y_m = m - \frac{M+1}{2}$. The BS is positioned at $\boldsymbol{p}_{\text{bs}} = [-d_c, 0]^\mathsf{T}$, where d_c denotes the distance between the BS's active antenna and the center of the BD-RIS and is on the order of a few wavelengths. The location of the UE, $\boldsymbol{p}_{\text{ue}}$, is unknown and must be estimated. Accordingly, the distance between the RIS and the UE is expressed as $r = \|\boldsymbol{p}_{\text{ue}} - \boldsymbol{p}_{\text{ris}}\|$. As illustrated in Fig. 8.1, the UE is located at an angular position of $\vartheta = \arcsin\left(([\boldsymbol{p}_{\text{ue}}]_1 - [\boldsymbol{p}_{\text{ris}}]_1)/r\right)$ relative to the y-axis.

8.2.2 Channel Model

In the proposed system model, two distinct communication channels are defined: $\boldsymbol{g}[n] \in \mathbb{C}^{M\times 1}$ for the BS-RIS channel (also known as transmission coefficient vector [126, 114, 119, 127]) and $\boldsymbol{h}[n] \in \mathbb{C}^{1\times M}$ for the RIS-UE channel. Here, $n \in [-K, K]$ is an integer representing the n-th subcarrier of the employed orthogonal frequency division multiplexing (OFDM) system, with a total of $N = 2K+1$ subcarriers.

BS-RIS Channel Model

Given the close proximity of the RIS to the BS's active antenna, the BS-RIS channel requires a distinct model to capture its unique propagation characteristics. The channel coefficient between the active antenna and the m-th RIS element at the central frequency is modeled using Rayleigh-Sommerfeld diffraction theory for NF propagation as $[\boldsymbol{g}[0]]_m = \frac{A\cos\chi_m}{d_m}\left(\frac{1}{2\pi d_m} - \frac{\jmath}{\lambda}\right)e^{\jmath 2\pi d_m/\lambda}$ [126, 114, 119, 127], where $A = (\lambda/2)^2$ represents the area of each passive element, d_m is the distance between the active antenna and the m-th cell, and χ_m is the angular displacement between the line connecting the active antenna at the BS and the m-th cell of the BD-RIS, and the axis perpendicular to the BD-RIS surface. Accordingly, the BD-RIS channel model for the n-th subcarrier is as [119]

$$[\boldsymbol{g}[n]]_m = \frac{A\cos\chi_m}{d_m}\left(\frac{1}{2\pi d_m} - \frac{\jmath}{\lambda}\right)e^{\jmath 2\pi d_m\left(\frac{1}{\lambda}-\frac{n\Delta_f}{c}\right)}, \tag{8.1}$$

where $\Delta_f = B/N$ denotes the subcarrier spacing with B is the total bandwidth, and c is the speed of light.

RIS-UE Channel Model

The RIS-UE channel depends on the RIS-UE distance r and may be either NF or FF. Notably, the NF model remains valid universally, automatically simplifying to the FF model at far distances. In this chapter, however, we treat them separately to allow for analysis of both models.

- *Scenario 1 (NF Channel Model)*: If $0.62\sqrt{D^3/\lambda} < r < 2D^2/\lambda$, the UE is located in the Fresnel (radiative) NF region of the RIS [142, 141]. In this case, the RIS-UE channel is modeled as a line-of-sight (LoS) narrowband channel ($n = 0$ and $N = 1$), as follows [143]:[2]

  $$\boldsymbol{h}_1[0] = \boldsymbol{h}_1 = \beta_1\boldsymbol{a}_1^{\mathsf{H}}(r,\vartheta), \tag{8.2}$$

  where $\beta_1 = \frac{\lambda}{4\pi r}e^{-\jmath\frac{2\pi}{\lambda}r}$ represents the complex channel gain[142]. The term $\boldsymbol{a}_1(r,\vartheta) \in \mathbb{C}^{M\times 1}$ denotes the NF array response vector at the RIS, defined as [143]:

  $$[\boldsymbol{a}_1(r,\vartheta)]_m = \frac{1}{\sqrt{M}}e^{-\jmath\frac{2\pi}{\lambda}(r_m(r,\vartheta)-r)}, \tag{8.3}$$

  where $r_m(r,\vartheta) = \sqrt{r^2 + y_m^2\delta^2 - 2ry_m\delta\cos(\vartheta)}$ is the distance between the UE and the m-th cell.

[2]To improve readability, we omit the subcarrier index when exclusively discussing Scenario 1 throughout this chapter (i.e., $\boldsymbol{h}_1[0]$ becomes $\boldsymbol{h}_1$).

- *Scenario 2 (FF Channel Model)*: If $r > 2D^2/\lambda$, the UE is located in the FF region [138]. In this case, we model the RIS-UE channel as a LoS wideband channel. The channel for the n-th subcarrier is expressed as follows [137, 144]:

$$\boldsymbol{h}_2[n] = \beta_2 e^{-\jmath 2\pi\tau n\Delta_f} \boldsymbol{a}_2^{\mathsf{H}}(\vartheta), \tag{8.4}$$

where $\beta_2 = \frac{\lambda}{4\pi r} e^{\jmath\varphi}$ represents the complex channel gain, with $\varphi \sim \mathcal{U}(0, 2\pi)$ [145]. Here, $\tau = r/c$ is time of arrival (ToA) for RIS-UE channel,[3] and $\boldsymbol{a}_2(\vartheta) \in \mathbb{C}^{M\times 1}$ is the array response (steering) vector at the RIS, defined as follows [144, 137, 85]:

$$[\boldsymbol{a}_2(\vartheta)]_m = \frac{1}{\sqrt{M}} e^{\jmath 2\pi(m-1)\frac{\delta}{\lambda}\cos\vartheta}. \tag{8.5}$$

8.2.3 Signal Model

To facilitate downlink localization, the BS systematically sweeps the environment, transmitting T_i pilot signals to various zones within the area of interest over sequential time slots in the i-th scenario. Without loss of generality, we assume a unit transmit pilot symbol. Thus, the received signal at the UE for the n-th subcarrier in Scenario i during the t-th time slot is as

$$y_{i,t}[n] = \sqrt{P}\boldsymbol{h}_i[n]\boldsymbol{\Omega}_{i,t}\boldsymbol{g}[n] + w_{i,t}[n], \tag{8.6}$$

where P is the transmitted power, and $w_{i,t} \sim \mathcal{CN}(0, \sigma^2)$ represents the additive noise component during the t-th time slot in the i-th scenario. Here, $\boldsymbol{\Omega}_{i,t} \in \mathbb{C}^{M\times M}$ is the RIS phase shift matrix during t-th time slot in the i-th scenario. To ensure that the BD-RIS is power-lossless, its phase shift matrix should satisfy unitary constraint, i.e., $\boldsymbol{\Omega}_{i,t}^{\mathsf{H}}\boldsymbol{\Omega}_{i,t} = \boldsymbol{I}_M$. Additionally, the phase shift matrix must be symmetric, i.e., $\boldsymbol{\Omega}_{i,t} = \boldsymbol{\Omega}_{i,t}^{\mathsf{T}}$, ensuring identical phase adjustments between each pair of passive elements, allowing a single phase shifter per element pair. Ultimately, for the purpose of the

[3] To simplify analysis, we assume tight synchronization between the BS and UE, leaving asynchronous scenario for the future work.

Algorithm 5: Pre-defined codebook for BD-RIS configuration

1: Define T_i uniformly distributed sweeping points/angles for NF/FF:

(NF) Define T_1 sweeping points as $\{\boldsymbol{s}_1, \boldsymbol{s}_2, \dots, \boldsymbol{s}_{T_1}\}$ with $\{\boldsymbol{s}_t = [r_t, \vartheta_t]^\mathsf{T} | r_t \in [\varrho_{\min} : \Delta_r : \varrho_{\max}],$ $\vartheta_t \in [0 : \Delta_\vartheta : 180°]\}$, where $\varrho_{\min} > 0.62\sqrt{\frac{D^3}{\lambda}}$ and $\varrho_{\max} < \frac{2D^2}{\lambda}$.

(FF) Define T_2 sweeping angles as $\{\vartheta_1, \vartheta_2, \dots, \vartheta_{T_2}\}$ with $\vartheta_t \in [0 : \Delta_\vartheta : 180°]$.

2: Compute the transmit steering vector at the transmit terminal of BD-RIS for the t-th codeword (associated with the t-th time slot):

(NF) Compute toward location $\boldsymbol{s}_t$ using (8.3).

(FF) Compute toward direction ϑ_t using (8.5).

3: Calculate $\boldsymbol{u}_T = \boldsymbol{g}[0]/\|\boldsymbol{g}[0]\|$; set $\boldsymbol{u}_R = \boldsymbol{a}_1(r_t, \vartheta_t)$ for NF or $\boldsymbol{u}_R = \boldsymbol{a}_2(\vartheta_t)$ for FF.

4: Calculate the symmetric matrix $\boldsymbol{A}$ and decompose it using standard singular value decomposition (SVD) as $\boldsymbol{A} = \boldsymbol{u}_R \boldsymbol{u}_T^\mathsf{H} + (\boldsymbol{u}_R \boldsymbol{u}_T^\mathsf{H})^\mathsf{T} = \boldsymbol{U\Sigma V}^\mathsf{H}$.

5: Compute $\boldsymbol{\nu} = \mathrm{diag}(\boldsymbol{U}^\mathsf{H}\boldsymbol{V}^*)$, followed by $\boldsymbol{\phi} = \angle\boldsymbol{\nu}/2$.

6: After computing $\boldsymbol{Q} = \boldsymbol{U}\,\mathrm{diag}(\exp(\jmath\boldsymbol{\phi}))$, Takagi's decomposition can be expressed as $\boldsymbol{A} = \boldsymbol{Q\Sigma Q}^\mathsf{T}$; thus, the t-th codeword for the i-th scenario is obtained as $\boldsymbol{\Omega}_{i,t} = \boldsymbol{QQ}^\mathsf{T}$.

CRLB analysis, we define the noiseless component of the received signal as

$$\mu_{i,t}[n] = \boldsymbol{h}_i[n]\boldsymbol{\Omega}_{i,t}\boldsymbol{g}[n] = \boldsymbol{h}_i[n]\boldsymbol{\zeta}_{i,t}[n], \tag{8.7}$$

where $\boldsymbol{\zeta}_{i,t}[n] = \boldsymbol{\Omega}_{i,t}\boldsymbol{g}[n]$.

8.2.4 Pre-defined Codebook for BD-RIS Configuration

In each scenario, a pre-defined codebook enables systematic environmental sweeping, with different codewords selected in each time slot to ensure full coverage. Since T_i symbols are required, the codebook must contain T_i codewords, each satisfying the unitary and symmetry constraints outlined above. Takagi's decomposition, as described in [134], is used to construct this codebook, with detailed steps provided in Algorithm 5.

8.3 Fisher Information Analysis

In this section, we calculate the position error bound (PEB), which represents a theoretical lower bound on the achievable accuracy of position estimation. The positional parameters for scenario i are expressed as $\boldsymbol{\xi}_{po,i} = [\boldsymbol{p}_{\mathrm{ue},i}^{\mathsf{T}}, \Re(\beta_i), \Im(\beta_i)]^{\mathsf{T}}$. However, before proceeding, we must first derive the CRLB for the channel parameters. In the i-th scenario, the Fisher information matrix (FIM), $\boldsymbol{\mathcal{F}}_{ch,i} \in \mathbb{R}^{4\times4}$, with respect to the channel parameters set $\boldsymbol{\xi}_{ch,i}$ is obtained using the Slepian-Bangs formula [146] as follows:

$$\boldsymbol{\mathcal{F}}_{ch,i} = \frac{2P}{\sigma^2} \sum_{t=1}^{T_i} \sum_{n=-K}^{K} \Re\left\{ \left(\frac{\partial \mu_{i,t}[n]}{\partial \boldsymbol{\xi}_{ch,i}}\right) \left(\frac{\partial \mu_{i,t}[n]}{\partial \boldsymbol{\xi}_{ch,i}}\right)^{\mathsf{H}} \right\}. \tag{8.8}$$

The channel parameter vector for NF and FF scenarios are defined as $\boldsymbol{\xi}_{ch,1} = [r, \vartheta, \Re(\beta_1), \Im(\beta_1)]^{\mathsf{T}}$ and $\boldsymbol{\xi}_{ch,2} = [\tau, \vartheta, \Re(\beta_2), \Im(\beta_2)]^{\mathsf{T}}$, respectively. The mathematical derivations for obtaining $\boldsymbol{\mathcal{F}}_{ch,i}$ are provided in Appendix C.1. Consequently, the CRLB for $[\boldsymbol{\xi}_{ch,i}]_\ell$ is calculated as:

$$\eta_\ell = \mathrm{CRLB}\left([\boldsymbol{\xi}_{ch,i}]_\ell\right) = \sqrt{[\boldsymbol{\mathcal{F}}_{ch,i}^{-1}]_{\ell,\ell}}. \tag{8.9}$$

Once $\boldsymbol{\mathcal{F}}_{ch,i}$ is calculated, the FIM of the positional parameters can be obtained as $\boldsymbol{\mathcal{F}}_{po,i} = \boldsymbol{\mathcal{J}}_i^{\mathsf{T}} \boldsymbol{\mathcal{F}}_{ch,i} \boldsymbol{\mathcal{J}}_i$, where $\boldsymbol{\mathcal{J}}_i \in \mathbb{R}^{4\times4}$ is the Jacobian matrix, defined as $[\boldsymbol{\mathcal{J}}_i]_{\ell,s} = \partial\left[\boldsymbol{\xi}_{ch,i}\right]_\ell / \partial\left[\boldsymbol{\xi}_{po,i}\right]_s$. The mathematical derivation of $\boldsymbol{\mathcal{J}}_i$ is provided in Appendix C.2. Ultimately, the PEB for Scenario i is calculated as follows:

$$\mathrm{PEB}_i = \sqrt{\tau\left([\boldsymbol{\mathcal{F}}_{po,i}^{-1}]_{1:2,1:2}\right)}. \tag{8.10}$$

8.4 Simulation Results and Analytical Insights

This section presents the CRLB analysis of the proposed architecture. The assumed values for various parameters are listed in Table 8.1, unless stated otherwise. For comparison, we evaluate two different benchmarks:

- *Benchmark 1 (D-RIS)*: A cell-wise single-connected BD-RIS operating in transmissive mode. It is also called simultaneously transmitting and reflecting RIS

Table 8.1: Computer simulation parameters.

Parameter	**Value**	**Parameter**	**Value**
$\boldsymbol{p}_{\text{ris}}$	$[0, 0]^\mathsf{T}$	T_1	500
$\boldsymbol{p}_{\text{ue},1}$	$[12, 8]^\mathsf{T}$ m	T_2	100
$\boldsymbol{p}_{\text{ue},2}$	$[60, 40]^\mathsf{T}$ m	Δ_r	10 m
d_c	0.5λ [114, 126]	Δ_ϑ	$1.8°$
M	101	$\varrho_{\min}$	5 m
P	20 dBm	$\varrho_{\max}$	45 m
c	3×10^8 m/s	N_1	1
$f_c = c/\lambda$	28 GHz	N_2	501
Δ_f	120 KHz	B	$N_i \Delta_f$
δ	$\lambda/2$ m	σ^2	$-174 + 10\log(B)$ dBm

(STAR-RIS) [18]. When integrated within a BS, it functions as a single-layer stacked intelligent metasurface [126, 114, 119, 127, 136, 128, 18]. Due to its single-connected structure and diagonal phase shift matrix, which aligns with the characteristics of traditional D-RIS, we refer to it as D-RIS in this chapter for clarity and to highlight its diagonal structure.

- *Benchmark 2 (AAA)*: The BS equipped with a linear active antenna array (AAA) with M antenna elements.

In each benchmark, a pre-defined codebook is constructed for beam-sweeping to facilitate UE localization. For both benchmarks, steps $1-3$ in Algorithm 5 are first performed. In Benchmark 1, the t-th codeword is generated as $\boldsymbol{\Omega}_{i,t} = \operatorname{diag}\left(e^{-\jmath \arg(\boldsymbol{u}_T \odot \boldsymbol{u}_R^*)}\right)$ [134], while $\boldsymbol{u}_R$ is used to create the t-th codeword for Benchmark 2.

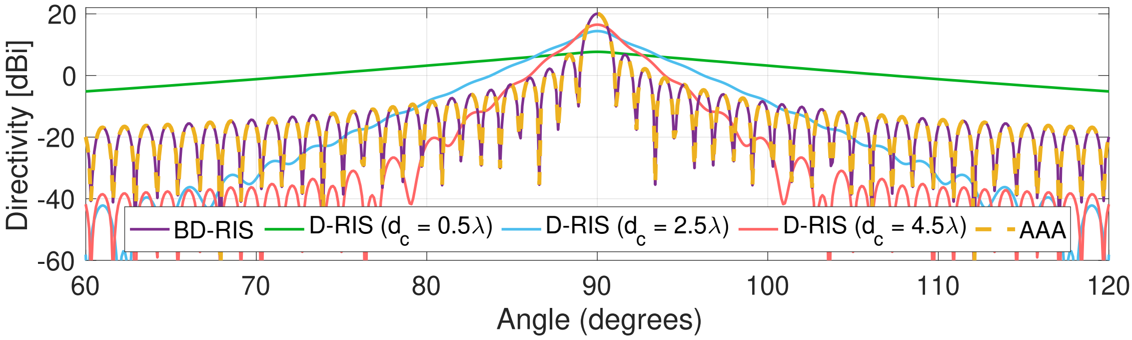

Figure 8.2: Transmit beamforming patterns for BD-RIS and benchmark configurations, calculated using the effective passive beamforming vector $\boldsymbol{\zeta} = \boldsymbol{\Omega}\boldsymbol{g}[0]$.

8.4.1 Beamforming Performance Analysis

Placing the RIS closer to the BS reduces the multiplicative path loss in the overall BS-UE channel [112]. However, as shown in Fig. 8.2, D-RIS exhibits reduced beamforming performance as d_c decreases. This decline occurs because the BS-RIS channel vector $\boldsymbol{g}$ shows greater variations in both magnitude and phase with a shorter d_c. Since D-RIS can only adjust the phase, it cannot compensate for these magnitude variations, thereby limiting its beamforming capability [121]. In contrast, the fully-connected BD-RIS can adjust both phase and amplitude of impinging waves, allowing it to sustain high beamforming gain even at close proximity to the BS. As shown in Fig. 8.2, this capability enables BD-RIS to achieve beamforming performance comparable to the AAA structure. Although BD-RIS matches AAA in beamforming gain, AAA is still expected to outperform it due to reduced path loss, as it lacks the cascaded channels effect. Next, we evaluate BD-RIS performance against the benchmarks in terms of PEB and CRLB on channel parameters.

8.4.2 CRLB Analysis for the NF Scenario

The CRLB analysis for Scenario 1 (NF) is shown in Fig. 8.3. Figs. 8.3(a) and (b) present the CRLB for r, ϑ, and the PEB across different transmitted power levels,

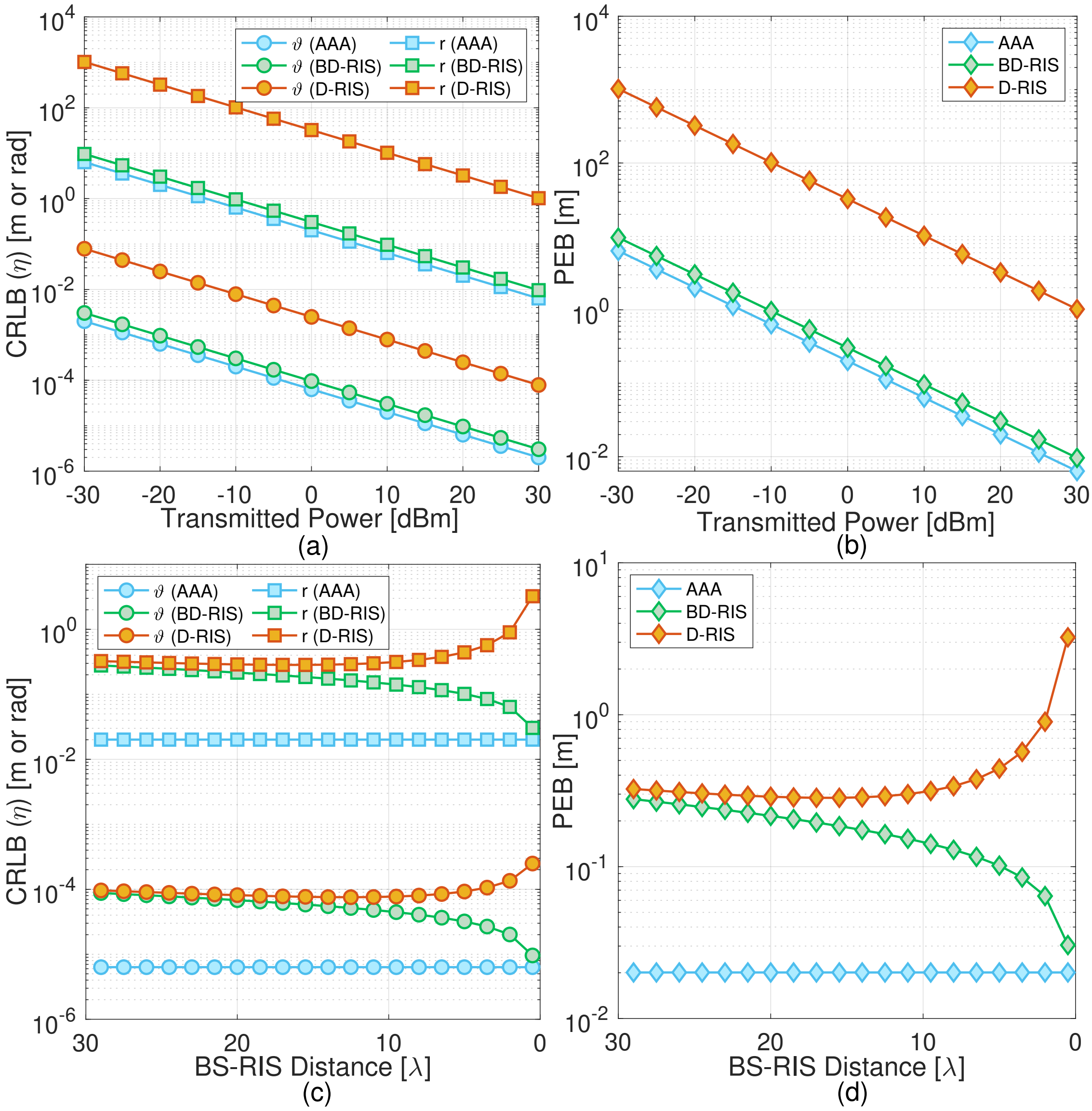

Figure 8.3: CRLB and PEB analysis for Scenario 1 (NF): (a) CRLB for r and ϑ vs. transmitted power, (b) PEB vs. transmitted power, (c) CRLB for r and ϑ vs. BS-RIS distance, and (d) PEB vs. BS-RIS distance.

respectively. While a significant performance gap exists between D-RIS and AAA, BD-RIS achieves performance close to AAA due to similar beamforming capabilities. Figs. 8.3(c) and (d) show the CRLB for channel parameters and PEB as a function of BS-RIS distance (d_c), respectively. When the RIS is positioned far from the BS, BD-RIS and D-RIS exhibit similar CRLB performance. This similarity arises from the comparable beamforming gains of both structures at larger d_c, as illustrated in Fig. 8.2. As d_c decreases, BD-RIS performance improves due to reduced multiplicative path loss, with its fully-connected structure maintaining beamforming gain. In contrast, D-RIS initially benefits from reduced d_c, but beyond a critical threshold, the loss in beamforming gain outweighs path loss reduction, leading to a substantial CRLB and PEB performance drop.

8.4.3 CRLB Analysis for the FF Scenario

Fig. 8.4 presents the CRLB analysis for Scenario 2 (FF), comparing BD-RIS, D-RIS, and AAA across various parameters. In Fig. 8.4(a), D-RIS significantly underperforms in ϑ estimation compared to BD-RIS and AAA, which achieve higher angular resolution due to their sharp beams. Conversely, D-RIS achieves τ estimation comparable to BD-RIS and AAA due to its broad beam pattern, which disperses energy over a wide range. This wide dispersion allows the UE to receive pilot signals even when the BS beam is not precisely aimed at it. Notably, τ estimation primarily relies on the frequency diversity of the wideband channel rather than a sharp, narrow beam, making D-RIS's broad coverage beneficial for this purpose. This advantage is also reflected in the CRLB trends for τ in Figs. 8.4(c) and (e). Despite this advantage in τ, D-RIS's weaker angular estimation negatively impacts its PEB, while BD-RIS attains performance close to AAA, thanks to its flexibility in beam design, as shown in Fig. 8.4(b).

Figs. 8.4(c) and (d) show the CRLB performance of the channel parameters and the PEB performance as a function of BS-RIS distance (d_c), respectively. The trends for ϑ and PEB closely mirror those in Scenario 1 (NF) (see Figs. 8.3(c) and (d)). As d_c decreases, the CRLB on τ improves for both D-RIS and BD-RIS, driven by reduced multiplicative path loss and enhanced SNR, underscoring SNR's importance in τ estimation. Note that, AAA's performance remains stable, unaffected by d_c, due to its independent MISO structure.

Figs. 8.4(e) and (f) respectively show the CRLB performance for channel param-

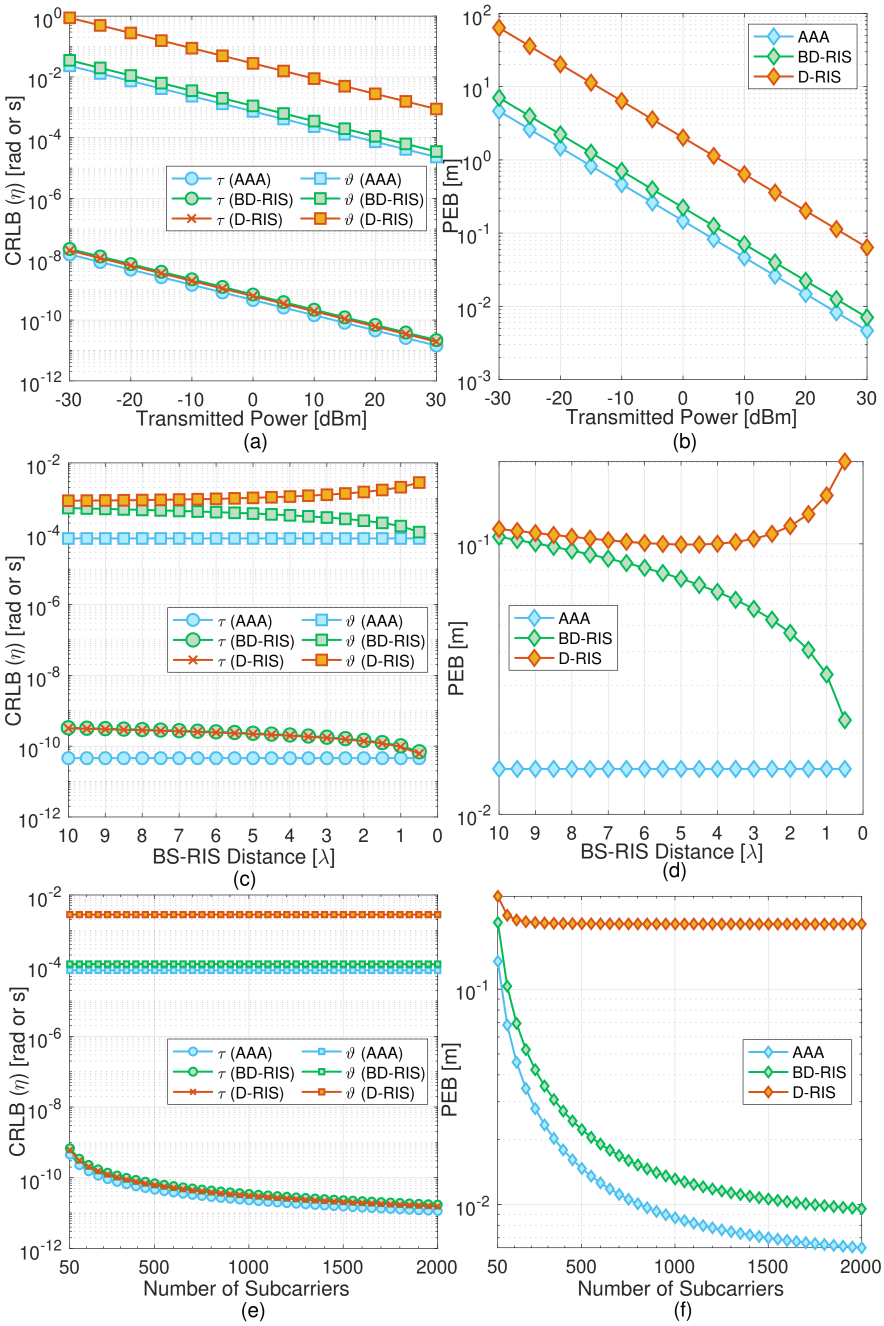

Figure 8.4: CRLB and PEB analysis in Scenario 2 (FF): (a) CRLB for τ and ϑ vs. transmitted power, (b) PEB vs. transmitted power, (c) CRLB for τ and ϑ vs. BS-RIS distance, (d) PEB vs. BS-RIS distance, (e) CRLB for τ and ϑ vs. number of subcarriers, and (f) PEB vs. number of subcarriers.

eters and PEB as the number of subcarriers increases. In Fig. 8.4(e), ϑ estimation remains unaffected by the number of subcarriers, as it depends primarily on beamforming gain. Conversely, τ estimation benefits from the frequency diversity of OFDM, showing improved CRLB performance across all setups as the number of subcarriers increases. In Fig. 8.4(f), D-RIS's PEB performance plateaus after only a few subcarriers, while BD-RIS and AAA continue to improve significantly before reaching their own performance ceilings at much higher subcarrier counts. This early ceiling for D-RIS is due to its limited beamforming capability and correspondingly poorer ϑ estimation. In contrast, the lower CRLB on ϑ for BD-RIS and AAA indicates a greater capacity to leverage frequency diversity across a larger number of subcarriers, thereby enhancing PEB.

8.4.4 PEB Visualization for the Area of Interest

Figs. 8.5(a) and (b) show the PEB on a logarithmic scale for various UE positions in NF and FF scenarios, respectively. In the NF scenario, the same RIS configuration listed in Table 8.1 is applied. BD-RIS achieves performance comparable to AAA, while D-RIS provides sub-meter level accuracy only for UEs within a few meters of the RIS. For the FF scenario illustrated in Fig. 8.5(b), we assume $\Delta_\vartheta = 5°$ (instead of $\Delta_\vartheta = 1.8°$, for better visualization of the beams). Similar to NF scenarios, D-RIS shows relatively poor performance, whereas BD-RIS's performance remains close to AAA. Furthermore, Fig. 8.5(b) illustrates enhanced PEB along paths where the sweeping beam aligns with the positions of UEs in both BD-RIS and AAA configurations, underscoring the critical role of high-resolution codebooks in achieving precise localization. While a direct comparison between NF (Fig. 8.5(a)) and FF (Fig. 8.5(b)) is challenging due to the higher number of samples in FF from the OFDM structure, it is evident that BD-RIS provides a more substantial improvement over D-RIS in NF than in FF. In NF scenarios, where beamforming gain is critical for estimating positional parameters r and ϑ, BD-RIS significantly reduces the PEB compared to D-RIS. In contrast, this enhancement is less pronounced in FF, where ToA estimation benefits more from frequency diversity rather than beam-

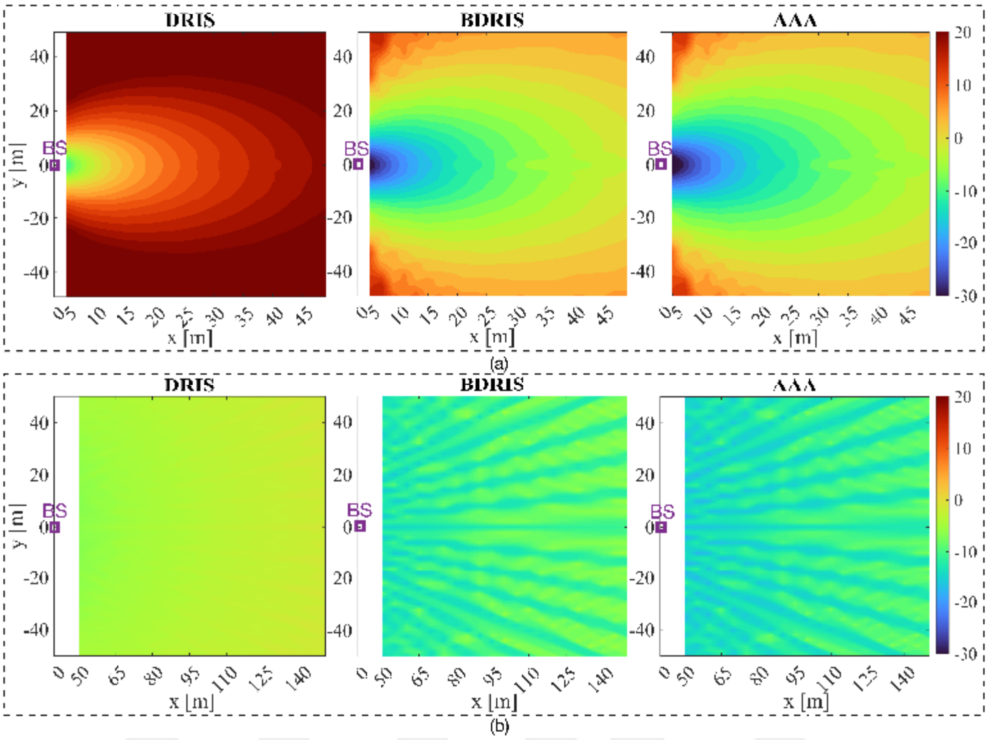

Figure 8.5: $10\log_{10}(\text{PEB})$ for different UE positions. (a) Scenario 1 (NF); (b) Scenario 2 (FF).

forming precision.

8.5 Conclusion

This chapter has proposed a novel BS architecture integrating fully-connected BD-RIS to enable enhanced passive beamforming for efficient localization. This design offers a promising alternative to existing benchmarks, achieving localization accuracy comparable to active analog beamforming with traditional antenna arrays. Through comprehensive CRLB analysis in both NF and FF scenarios, we have demonstrated that BD-RIS offers substantial improvements over traditional D-RIS. Notably, BD-RIS shows comparable performance to AAA, establishing it as a viable solution for high-accuracy positioning in 6G networks and beyond. Our findings underline the potential of BD-RIS to bridge the gap between active and passive localization methods, paving the way for efficient, scalable localization solutions in future networks.

Chapter 9

CONCLUSION

This thesis has presented a comprehensive investigation into novel system designs for mmWave communication networks, addressing critical challenges posed by next-generation wireless networks, particularly in the context of 6G. With the ambitious goals of 6G demanding higher data rates, increased energy efficiency, and broader coverage, this work has explored innovative approaches such as cluster index modulation, reconfigurable intelligent surfaces, and advanced antenna array configurations. These contributions collectively aim to enhance communication performance in realistic environments, providing a foundation for scalable, energy-efficient solutions.

The research introduced CIM as a robust and adaptable modulation scheme for mmWave environments. By leveraging the spatial separation of clusters and indexing best propagation paths, CIM demonstrated significant improvements in bit error rate and spectral efficiency, especially when combined with hybrid beamforming and RIS. This work further explored RIS as a transformative technology for addressing the inherent limitations of mmWave systems, particularly path loss and signal blockage.

To address the cost and complexity associated with large antenna arrays, this thesis proposed the Plug-In RIS, a fully passive solution that enhances coverage in dead zones without requiring continuous reconfiguration or end-to-end channel decoupling. Additionally, a comprehensive framework for both BS-side and UE-side RIS deployments was developed, providing insights into practical design considerations that support efficient and flexible RIS implementations tailored to different deployment scenarios.

The thesis also introduced the Beyond-Diagonal RIS (BD-RIS), a cutting-edge RIS structure integrated at the base station to enable efficient passive beamforming. BD-RIS offers a high beamforming gain comparable to active antennas but with reduced power consumption and implementation cost, aligning with the energy efficiency demands of 6G. Moreover, the study demonstrated the suitability of BD-RIS for applications in single-anchor localization, where precise beam control is crucial for accurate positioning.

In summary, this thesis has contributed to the advancement of system design by proposing new modulation schemes, energy-efficient RIS designs, and high-performance beamforming techniques for mmWave systems. The research findings not only address the immediate challenges in mmWave communications but also pave the way for future studies in scalable and cost-effective wireless solutions. As 6G technology continues to evolve, the methodologies and insights presented in this work provide a valuable resource for developing next-generation communication networks capable of meeting the stringent requirements of coverage, efficiency, and performance.

Appendix A

A.1 Proof of Lemma 1

Different whitening procedures with benefits and detriments are discussed in [147]. We prefer standardized zero-phase components analysis (ZCA-cor) whitening transformation due to its unique ability to keep the whitened noise $\mathbf{F}_r\mathbf{n}$ maximally similar to the effective noise $\mathbf{W}^H\mathbf{n}$ [147]. As a result, while we whiten the effective noise, we keep it as similar as possible to its colored version.

A.2 Proof of Lemma 2

Assume that $\mathbf{x}_1$ and $\mathbf{x}_2$ are two complex vectors with the same dimension. It is straightforward to prove that the following equation is correct.

$$||\mathbf{x}_1 + \mathbf{x}_2||^2 = ||\mathbf{x}_1||^2 + ||\mathbf{x}_2||^2 + 2\Re\{\mathbf{x}_1^H\mathbf{x}_2\}. \tag{A.1}$$

Using (A.1), we can update (4.18) as follows:

$$\begin{aligned}&\mathbb{P}(\{c^*, s^*\} \to \{c^*, \hat{s}\}|\alpha_0, \beta_{1,1}, \ldots, \beta_{C_R,L_R}) \\ &\quad = \mathbb{P}(2\Re\{\sqrt{P}\mathbf{n}^H\mathbf{f}_{r,c^*}\mathbf{f}_{r,c^*}^H\mathbf{H}_{\mathbf{eff}}^{\mathbf{b}^*}\mathbf{f}_t(s^* - \hat{s})\} + |\sqrt{P}\mathbf{f}_{r,c^*}^H\mathbf{H}_{\mathbf{eff}}^{\mathbf{b}^*}\mathbf{f}_t(s^* - \hat{s})|^2 < 0).\end{aligned} \tag{A.2}$$

Let us define $\zeta = 2\Re\{\sqrt{P}\mathbf{n}^H\mathbf{f}_{r,c^*}\mathbf{f}_{r,c^*}^H\mathbf{H}_{\mathbf{eff}}^{\mathbf{b}^*}\mathbf{f}_t(s^* - \hat{s})\} + |\sqrt{P}\mathbf{f}_{r,c^*}^H\mathbf{H}_{\mathbf{eff}}^{\mathbf{b}^*}\mathbf{f}_t(s^* - \hat{s})|^2$. Since $\mathbf{n}^H$ has complex normal distribution with variance σ^2, its real part has normal distribution with variance $\frac{\sigma^2}{2}$, i.e., $\Re\{\mathbf{n}^H\} \sim \mathcal{N}(0, \frac{\sigma^2}{2})$. Hence, it is easy to see that ζ has normal distribution with mean μ_ζ and variance σ_ζ, i.e., $\zeta \sim \mathcal{N}(\mu_\zeta, \sigma_\zeta^2)$, wherein

$$\mu_\zeta = |\sqrt{P}\mathbf{f}_{r,c^*}^H\mathbf{H}_{\mathbf{eff}}^{\mathbf{b}^*}\mathbf{f}_t(s^* - \hat{s})|^2,$$

$$\sigma_\zeta^2 = 2\sigma^2||\sqrt{P}\mathbf{f}_{r,c^*}\mathbf{f}_{r,c^*}^H\mathbf{H}_{\mathbf{eff}}^{\mathbf{b}^*}\mathbf{f}_t(s^* - \hat{s})||^2.$$

Subsequently, we can derive the CPEP as

$$\mathbb{P}(\{c^*, s^*\} \rightarrow \{c^*, \hat{s}\}|\alpha_0, \beta_{1,1}, \ldots, \beta_{C_R,L_R}) = Q\Big(\frac{|\mathbf{f}_{r,c^*}^H \mathbf{H}_{\mathbf{eff}}^{\mathbf{b}^*} \mathbf{f}_t (s^* - \hat{s})|^2}{\sqrt{2}\sigma||\mathbf{f}_{r,c^*} \mathbf{f}_{r,c^*}^H \mathbf{H}_{\mathbf{eff}}^{\mathbf{b}^*} \mathbf{f}_t (s^* - \hat{s})||}\Big). \tag{A.3}$$

Finally, by taking expectation over enough number of channel realizations, the UPEP expression can be obtained as in (4.19).

A.3 Proof of Lemma 3

Let us define

$$\chi_1 = \frac{|\mathbf{f}_{r,c^*}^H \mathbf{n}|^2}{\sigma^2/2}, \tag{A.4}$$

$$\chi_2 = \frac{|\mathbf{f}_{r,\hat{c}}^H \mathbf{n} + \sqrt{P}\mathbf{f}_{r,\hat{c}}^H (\mathbf{H}_{\mathbf{eff}}^{\mathbf{b}^*} s^* - \mathbf{H}_{\mathbf{eff}}^{\hat{\mathbf{b}}} \hat{s})\mathbf{f}_t|^2}{\sigma^2/2}, \tag{A.5}$$

where χ_1 and χ_2 are central and non-central chi-squared random variables with two degrees of freedom, respectively. Notice that, χ_2 has a non-centrality parameter as:

$$\Lambda = \frac{2|\sqrt{P}\mathbf{f}_{r,\hat{c}}^H (\mathbf{H}_{\mathbf{eff}}^{\mathbf{b}^*} s^* - \mathbf{H}_{\mathbf{eff}}^{\hat{\mathbf{b}}} \hat{s})\mathbf{f}_t|^2}{\sigma^2}. \tag{A.6}$$

The PDF of central and non-central random variable with i degrees of freedom and non-centrality parameter of Λ is as follows, respectively:

$$f_{\chi_1}(x_1) = \frac{1}{2^{\frac{i}{2}}\Gamma(\frac{i}{2})} x_1^{\frac{i}{2}-1} \exp{(-\frac{x_1}{2})}, \tag{A.7}$$

$$f_{\chi_2}(x_2) = \frac{1}{2} \exp{(-\frac{x_2 + \Lambda}{2})} (\frac{x_2}{\Lambda})^{\frac{k}{4}-\frac{1}{2}} I_{\frac{k}{2}-1}(\sqrt{\Lambda x_2}), \tag{A.8}$$

where $I_\nu(y)$ is the Bessel function of the first kind and it is defined as:

$$I_\nu(y) = (\frac{y}{2})^\nu \sum_{i=0}^{\infty} \frac{(y^2/4)^i}{i!\Gamma(\nu + i + 1)}. \tag{A.9}$$

Accordingly, for two degrees of freedom, the PDF of χ_1 and χ_2 can be obtained as follows, respectively:

$$f_{\chi_1}(x_1) = \frac{1}{2} \exp{(-\frac{x_1}{2})}. \tag{A.10}$$

$$f_{\chi_2}(x_2) = \frac{1}{2}\exp\left(-\frac{x_2+\Lambda}{2}\right)\sum_{i=0}^{\infty}\frac{(\frac{\Lambda x_2}{4})^i}{(i!)^2}. \tag{A.11}$$

Thanks to the whitening filter, χ_1 and χ_2 are independent; therefore, we can constitute their joint PDF as follows:

$$f_{\chi_1,\chi_2}(x_1,x_2) = f_{\chi_1}(x_1)f_{\chi_2}(x_2) = \frac{1}{4}\exp\left(-\frac{x_1+x_2+\Lambda}{2}\right)\sum_{i=0}^{\infty}\frac{(\frac{\Lambda x_2}{4})^i}{(i!)^2}. \tag{A.12}$$

Subsequently, we can derive the CPEP expression for the case of erroneous cluster index detection as follows:

$$\begin{aligned}
&\mathbb{P}(\{c^*, s^*\} \to \{\hat{c}, \hat{s}\}|\alpha_0, \beta_{1,1}, \ldots, \beta_{C_R,L_R}) = \mathbb{P}(\chi_1 > \chi_2)\\
&= \int_0^{\infty}\int_{x_2}^{\infty} f_{\chi_1,\chi_2}(x_1,x_2)dx_1dx_2 = \frac{1}{4}\int_0^{\infty}\exp\left(-\frac{x_2+\Lambda}{2}\right)\\
&\times \sum_{i=0}^{\infty}\frac{(\frac{\Lambda x_2}{4})^i}{(i!)^2}\left\{\int_{x_2}^{\infty}\exp\left(-\frac{x_1}{2}\right)dx_1\right\}dx_2 = \frac{\exp\left(-\frac{\Lambda}{2}\right)}{2}\int_0^{\infty}\exp(-x_2)\sum_{i=0}^{\infty}\frac{(\frac{\Lambda x_2}{4})^i}{(i!)^2}dx_2\\
&= \frac{\exp\left(-\frac{\Lambda}{2}\right)}{2}\sum_{i=0}^{\infty}\left\{\frac{(\frac{\Lambda}{4})^i}{(i!)^2}\int_0^{\infty}x_2^i\exp(-x_2)dx_2\right\} = \frac{\exp\left(-\frac{\Lambda}{2}\right)}{2}\sum_{i=0}^{\infty}\frac{(\frac{\Lambda}{4})^i}{i!} = \frac{\exp\left(-\frac{\Lambda}{4}\right)}{2}\\
&= \frac{1}{2}\exp\left(-\frac{|P\mathbf{f}_{r,\hat{c}}^H(\mathbf{H}_{\mathbf{eff}}^{\mathbf{b}^*}s^* - \mathbf{H}_{\mathbf{eff}}^{\hat{\mathbf{b}}}\hat{s})\mathbf{f}_t|^2}{2\sigma^2}\right).
\end{aligned} \tag{A.13}$$

It is worth mentioning that during solving process of (A.13), we used Maclaurin series for e^x, i.e., $\sum_{i=0}^{\infty}\frac{x^i}{i!} = e^x$, and $\int_0^{\infty}x^ie^{-x}dx = i!$; the latter can be obtained by extending the factorial to a continuous function using definition of Gamma function. Ultimately, by taking expectation over enough channel realizations, we can obtain the UPEP as (4.21).

Appendix B

B.1 Proof of Corollary 1

By substituting $\theta_0 = 0$ into (5.16), we can simplify it as:

$$\text{EFD} = 2d \times \tan\left(\frac{\text{HPBW}}{2}\right). \tag{B.1}$$

On the other hand, the tangent function can be expanded using the MacLaurin series as follows:

$$\tan(x) = x + \frac{x^3}{3} + \frac{2x^5}{15} + \ldots; \quad \text{if} \quad |x| < \frac{\pi}{2}, \tag{B.2}$$

whereas when x is of a small magnitude, it can be approximated as $\tan(x) \approx x$. Note that $\frac{\text{HPBW}}{2}$ becomes relatively small when implementing a large array at the BS. Consequently, the approximation formula remains applicable here, and we can further simplify (B.1) to (5.17).

B.2 Proof of Lemma 6

By exploiting [87, equation (24)] and after some mathematical manipulations, (5.19) can be updated as

$$\begin{aligned} \mathcal{P}(s^* \to \hat{s}|\alpha_k, \beta_k) = \mathcal{P}(&|\sqrt{P}G_t G_r \mathbf{f}_r^H \mathbf{H}_{\text{eff},k} \mathbf{f}_t (s^* - \hat{s})|^2 \\ &+ 2\mathcal{R}\{\sqrt{P}G_t G_r \mathbf{n}^H \mathbf{f}_r \mathbf{f}_r^H \mathbf{H}_{\text{eff},k} \mathbf{f}_t (s^* - \hat{s}) < 0\}). \end{aligned} \tag{B.3}$$

As the elements of $\mathbf{n}^H$ follow a complex normal distribution with variance σ^2, its real component also conforms to a normal distribution with variance $\frac{\sigma^2}{2}$, represented as $\mathcal{R}\{\mathbf{n}^H\} \sim \mathcal{N}(\mathbf{0}_{N_r}, \frac{\sigma^2}{2}\mathbf{I}_{N_r})$. Accordingly, calculating (5.20) is straightforward.

Appendix C

C.1 Detailed Derivations of $\boldsymbol{\mathcal{F}}_{ch,i}$

This section presents the detailed calculation of $\boldsymbol{\mathcal{F}}_{ch,i}$ by evaluating $\frac{\partial \mu_{i,t}[n]}{\partial [\boldsymbol{\xi}_{ch,i}]_\ell}$. Consequently, $\boldsymbol{\mathcal{F}}_{ch,i}$ is obtained using (8.8).

Scenario 1: The calculations for Scenario 1 are as follows:

$$[\frac{\partial \mu_{1,t}}{\partial r}, \frac{\partial \mu_{1,t}}{\partial \vartheta}]^{\mathsf{T}} = \beta_1 [\dot{\boldsymbol{a}}_{1,r}(r,\vartheta), \dot{\boldsymbol{a}}_{1,\vartheta}(r,\vartheta)]^{\mathsf{H}} \boldsymbol{\zeta}_{1,t}[0], \tag{C.1}$$

$$[\frac{\partial \mu_{1,t}}{\partial \Re(\beta_1)}, \frac{\partial \mu_{1,t}}{\partial \Im(\beta_1)}] = [1, \jmath] \boldsymbol{a}_1^{\mathsf{H}}(r,\vartheta) \boldsymbol{\zeta}_{1,t}[0], \tag{C.2}$$

where

$$[\dot{\boldsymbol{a}}_{1,r}(r,\vartheta), \dot{\boldsymbol{a}}_{1,\vartheta}(r,\vartheta)] = [\boldsymbol{d}_r, \boldsymbol{d}_\vartheta] \odot [\boldsymbol{a}_1(r,\vartheta), \boldsymbol{a}_1(r,\vartheta)], \tag{C.3}$$

with

$$[\boldsymbol{d}_r]_m = -\jmath \frac{2\pi}{\lambda} \left(\frac{r - y_m \delta \cos\vartheta}{\sqrt{r^2 + y_m^2 \delta^2 - 2 r y_m \delta \cos\vartheta}} - 1 \right), \tag{C.4}$$

$$[\boldsymbol{d}_\vartheta]_m = -\jmath \frac{2\pi}{\lambda} \frac{r y_m \delta \sin\vartheta}{\sqrt{r^2 + y_m^2 \delta^2 - 2 r y_m \delta \cos\vartheta}}. \tag{C.5}$$

Scenario 2: The calculations in this case are as follows:

$$\frac{\partial \mu_{2,t}[n]}{\partial \tau} = -\jmath 2\pi n \Delta_f \beta_2 e^{-\jmath 2\pi \tau n \Delta_f} \boldsymbol{a}_2^{\mathsf{H}}(\vartheta) \boldsymbol{\zeta}_{2,t}[n], \tag{C.6}$$

$$\frac{\partial \mu_{2,t}[n]}{\partial \vartheta} = \beta_2 e^{-\jmath 2\pi \tau n \Delta_f} \dot{\boldsymbol{a}}_{2,\vartheta}^{\mathsf{H}}(\vartheta) \boldsymbol{\zeta}_{2,t}[n], \tag{C.7}$$

$$[\frac{\partial \mu_{2,t}[n]}{\partial \Re(\beta_2)}, \frac{\partial \mu_{2,t}[n]}{\partial \Im(\beta_2)}] = [1, \jmath] e^{-\jmath 2\pi \tau n \Delta_f} \boldsymbol{a}_2^{\mathsf{H}}(\vartheta) \boldsymbol{\zeta}_{2,t}[n], \tag{C.8}$$

where $\dot{\boldsymbol{a}}_{2,\vartheta}(\vartheta) = -\jmath 2\pi \frac{\delta}{\lambda} \cos\vartheta \, \mathrm{diag}(0, \ldots, M-1) \boldsymbol{a}_2(\vartheta)$.

C.2 Detailed Derivations of Jacobian Matrix $\boldsymbol{\mathcal{J}}_i$

Each channel parameter in $\boldsymbol{\xi}_{ch,i}$ must be expressed as a function of the positional parameters $\boldsymbol{\xi}_{po,i}$, after which the derivatives are readily computed.

Scenario 1: The derivatives are as follows:

$$\frac{\partial r}{\partial[\boldsymbol{p}_{\mathrm{ue}}]_1} = \frac{[\boldsymbol{p}_{\mathrm{ue}}]_1 - [\boldsymbol{p}_{\mathrm{ris}}]_1}{\|\boldsymbol{p}_{\mathrm{ue}} - \boldsymbol{p}_{\mathrm{ris}}\|}, \frac{\partial r}{\partial[\boldsymbol{p}_{\mathrm{ue}}]_2} = \frac{[\boldsymbol{p}_{\mathrm{ue}}]_2 - [\boldsymbol{p}_{\mathrm{ris}}]_2}{\|\boldsymbol{p}_{\mathrm{ue}} - \boldsymbol{p}_{\mathrm{ris}}\|} \tag{C.9}$$

$$\frac{\partial \vartheta}{\partial[\boldsymbol{p}_{\mathrm{ue}}]_1} = -\frac{[\boldsymbol{p}_{\mathrm{ue}}]_2 - [\boldsymbol{p}_{\mathrm{ris}}]_2}{\|\boldsymbol{p}_{\mathrm{ue}} - \boldsymbol{p}_{\mathrm{ris}}\|^2}, \frac{\partial \vartheta}{\partial[\boldsymbol{p}_{\mathrm{ue}}]_2} = \frac{[\boldsymbol{p}_{\mathrm{ue}}]_1 - [\boldsymbol{p}_{\mathrm{ris}}]_1}{\|\boldsymbol{p}_{\mathrm{ue}} - \boldsymbol{p}_{\mathrm{ris}}\|^2}. \tag{C.10}$$

Scenario 2: The derivatives are as follows:

$$\frac{\partial \tau}{\partial[\boldsymbol{p}_{\mathrm{ue}}]_1} = \frac{[\boldsymbol{p}_{\mathrm{ue}}]_1 - [\boldsymbol{p}_{\mathrm{ris}}]_1}{c\|\boldsymbol{p}_{\mathrm{ue}} - \boldsymbol{p}_{\mathrm{ris}}\|}, \frac{\partial \tau}{\partial[\boldsymbol{p}_{\mathrm{ue}}]_2} = \frac{[\boldsymbol{p}_{\mathrm{ue}}]_2 - [\boldsymbol{p}_{\mathrm{ris}}]_2}{c\|\boldsymbol{p}_{\mathrm{ue}} - \boldsymbol{p}_{\mathrm{ris}}\|}, \tag{C.11}$$

$$\frac{\partial \vartheta}{\partial[\boldsymbol{p}_{\mathrm{ue}}]_1} = -\frac{[\boldsymbol{p}_{\mathrm{ue}}]_2 - [\boldsymbol{p}_{\mathrm{ris}}]_2}{\|\boldsymbol{p}_{\mathrm{ue}} - \boldsymbol{p}_{\mathrm{ris}}\|^2}, \frac{\partial \vartheta}{\partial[\boldsymbol{p}_{\mathrm{ue}}]_2} = \frac{[\boldsymbol{p}_{\mathrm{ue}}]_1 - [\boldsymbol{p}_{\mathrm{ris}}]_1}{\|\boldsymbol{p}_{\mathrm{ue}} - \boldsymbol{p}_{\mathrm{ris}}\|^2}. \tag{C.12}$$

In both scenarios, it is evident that $\frac{\partial \Re(\beta_i)}{\partial \Re(\beta_i)} = \frac{\partial \Im(\beta_i)}{\partial \Im(\beta_i)} = 1$. All other entries in the Jacobian matrix $\boldsymbol{\mathcal{J}}_i$ are zero.

BIBLIOGRAPHY

[1] L Huawei et al. "6G: The Next Horizon From Connected People and Things to Connected Intelligence". In: *Huawei, White Paper* (2022).

[2] Fjolla Ademaj et al. "A Spatial Consistency Model for Geometry-Based Stochastic Channels". In: *IEEE Access* 7 (2019), pp. 183414–183427. DOI: 10.1109/ACCESS.2019.2958154.

[3] Ming Xiao et al. "Millimeter wave communications for future mobile networks". In: *IEEE Journal on Selected Areas in Communications* 35.9 (2017), pp. 1909–1935.

[4] Mustafa Riza Akdeniz et al. "Millimeter wave channel modeling and cellular capacity evaluation". In: *IEEE journal on selected areas in communications* 32.6 (2014), pp. 1164–1179.

[5] Stefano Buzzi and Carmen D'Andrea. "On clustered statistical MIMO millimeter wave channel simulation". In: *arXiv preprint arXiv:1604.00648* (2016).

[6] Weiqiang Tan et al. "Analysis of Different Planar Antenna Arrays for mmWave Massive MIMO Systems". In: *2017 IEEE 85th Vehicular Technology Conference (VTC Spring), Sydney, NSW, Australia.* June 2017, pp. 1–5. DOI: 10.1109/VTCSpring.2017.8108586.

[7] Keke Ying et al. "GMD-based hybrid beamforming for large reconfigurable intelligent surface assisted millimeter-wave massive MIMO". In: *IEEE Access* 8 (2020), pp. 19530–19539.

[8] Sung Hyuck Hong et al. "Hybrid beamforming for intelligent reflecting surface aided millimeter wave MIMO systems". In: *IEEE Transactions on Wireless Communications* (2022).

[9] Renwang Li et al. “Joint Design of Hybrid Beamforming and Reflection Coefficients in RIS-Aided mmWave MIMO Systems”. In: *IEEE Trans. Commun.* 70.4 (Jan. 2022), pp. 2404–2416. DOI: 10.1109/TCOMM.2022.3144986.

[10] Xianghao Yu, Jun Zhang, and Khaled B Letaief. “A hardware-efficient analog network structure for hybrid precoding in millimeter wave systems”. In: *IEEE Journal of Selected Topics in Signal Processing* 12.2 (2018), pp. 282–297.

[11] Ertugrul Basar and Ibrahim Yildirim. “Reconfigurable intelligent surfaces for future wireless networks: A channel modeling perspective”. In: *IEEE Wireless Commun.* 28.3 (Apr. 2021), pp. 108–114.

[12] Ertugrul Basar. “Index modulation techniques for 5G wireless networks”. In: *IEEE Communications Magazine* 54.7 (2016), pp. 168–175.

[13] Ertugrul Basar et al. “Index modulation techniques for next-generation wireless networks”. In: *IEEE access* 5 (2017), pp. 16693–16746.

[14] Ertugrul Basar et al. “Wireless communications through reconfigurable intelligent surfaces”. In: *IEEE Access* 7 (Aug. 2019), pp. 116753–116773.

[15] Changsheng You et al. “How to Deploy Intelligent Reflecting Surfaces in Wireless Network: BS-Side, User-Side, or Both Sides?” In: *J. commun. inf. netw.* 7.1 (Mar. 2022), pp. 1–10. DOI: 10.23919/JCIN.2022.9745477.

[16] Hongyu Li, Shanpu Shen, and Bruno Clerckx. “Beyond Diagonal Reconfigurable Intelligent Surfaces: A Multi-Sector Mode Enabling Highly Directional Full-Space Wireless Coverage”. In: *IEEE Journal on Selected Areas in Communications* 41.8 (2023), pp. 2446–2460. DOI: 10.1109/JSAC.2023.3288251.

[17] Hongyu Li et al. “Reconfigurable intelligent surfaces 2.0: Beyond diagonal phase shift matrices”. In: *IEEE Commun. Mag.* 62.3 (Nov. 2023), pp. 102–108.

[18] Hongyu Li, Shanpu Shen, and Bruno Clerckx. “Beyond Diagonal Reconfigurable Intelligent Surfaces: From Transmitting and Reflecting Modes to

Single-, Group-, and Fully-Connected Architectures". In: *IEEE Trans. Wireless Commun.* 22.4 (Oct. 2023), pp. 2311–2324.

[19] Hongyu Li et al. "Beyond Diagonal Reconfigurable Intelligent Surfaces With Mutual Coupling: Modeling and Optimization". In: *IEEE Communications Letters* 28.4 (2024), pp. 937–941. DOI: 10.1109/LCOMM.2024.3361648.

[20] Pei Zhou et al. "IEEE 802.11 ay-based mmWave WLANs: Design challenges and solutions". In: *IEEE Communications Surveys & Tutorials* 20.3 (2018), pp. 1654–1681.

[21] Shu Sun et al. "MIMO for millimeter-wave wireless communications: Beamforming, spatial multiplexing, or both?" In: *IEEE Communications Magazine* 52.12 (2014), pp. 110–121.

[22] Theodore S Rappaport et al. *Millimeter wave wireless communications.* Pearson Education, 2015.

[23] Yong Niu et al. "A survey of millimeter wave communications (mmWave) for 5G: opportunities and challenges". In: *Wireless networks* 21.8 (2015), pp. 2657–2676.

[24] Nemanja Stefan Perović et al. "Receive spatial modulation for LOS mmWave communications based on TX beamforming". In: *IEEE Communications Letters* 21.4 (2016), pp. 921–924.

[25] Robert W Heath et al. "An overview of signal processing techniques for millimeter wave MIMO systems". In: *IEEE Journal of selected topics in signal processing* 10.3 (2016), pp. 436–453.

[26] Omar El Ayach et al. "Spatially sparse precoding in millimeter wave MIMO systems". In: *IEEE transactions on wireless communications* 13.3 (2014), pp. 1499–1513.

[27] Ahmed Raafat et al. "Energy efficient transmit-receive spatial modulation for uplink-downlink large-scale MIMO systems". In: *2018 IEEE Globecom Workshops (GC Wkshps).* IEEE. 2018, pp. 1–6.

[28] Hongyu Li et al. "Dynamic hybrid beamforming with low-resolution PSs for wideband mmWave MIMO-OFDM systems". In: *IEEE Journal on Selected Areas in Communications* 38.9 (2020), pp. 2168–2181.

[29] Asil Koc, Ahmed Masmoudi, and Tho Le-Ngoc. "3D angular-based hybrid precoding and user grouping for uniform rectangular arrays in massive MU-MIMO systems". In: *IEEE Access* 8 (2020), pp. 84689–84712.

[30] Merve Yüzgeçcioğlu and Eduard Jorswieck. "Hybrid beamforming with spatial modulation in multi-user massive MIMO mmWave networks". In: *2017 IEEE 28th Annual International Symposium on Personal, Indoor, and Mobile Radio Communications (PIMRC)*. IEEE. 2017, pp. 1–6.

[31] Yacong Ding et al. "Spatial scattering modulation for uplink millimeter-wave systems". In: *IEEE Communications Letters* 21.7 (2017), pp. 1493–1496.

[32] Ali Mokh et al. "Analytical performance of hybrid beam index modulation". In: *IEEE Wireless Communications Letters* (2019).

[33] Yajun Fan et al. "Pre-Compensation-Assisted Generalized Beam Index Modulation (PC-GBIM) for mmWave Massive MIMO Over Doubly Selective Channels". In: *IEEE Wireless Communications Letters* 10.2 (2020), pp. 411–415.

[34] Wei Wang and Wei Zhang. "Spatial modulation for uplink multi-user mmWave MIMO systems with hybrid structure". In: *IEEE Transactions on Communications* 68.1 (2019), pp. 177–190.

[35] Shijian Gao, Xiang Cheng, and Liuqing Yang. "Spatial multiplexing with limited RF chains: Generalized beamspace modulation (GBM) for mmWave massive MIMO". In: *IEEE Journal on Selected Areas in Communications* 37.9 (2019), pp. 2029–2039.

[36] Constantine A Balanis. *Antenna theory: analysis and design.* John wiley & sons, 2015.

[37] Asil Koc and Tho Le-Ngoc. "Full-Duplex mmWave Massive MIMO Systems: A Joint Hybrid Precoding/Combining and Self-Interference Cancellation Design". In: *IEEE Open Journal of the Communications Society* 2 (2021), pp. 754–774.

[38] Zhi Zheng et al. "Efficient beamspace-based algorithm for two-dimensional DOA estimation of incoherently distributed sources in massive MIMO systems". In: *IEEE Transactions on Vehicular Technology* 67.12 (2018), pp. 11776–11789.

[39] Ting Wang et al. "Two-dimension direction-of-arrival estimation for massive MIMO systems". In: *IEEE Access* 3 (2015), pp. 2122–2128.

[40] Xiaoyi Zhu et al. "A Deep Learning and Geospatial Data based Channel Estimation Technique for Hybrid Massive MIMO Systems". In: *IEEE Access* 9 (2021), pp. 145115–145132.

[41] Ertugrul Basar. "On multiple-input multiple-output OFDM with index modulation for next generation wireless networks". In: *IEEE Transactions on Signal Processing* 64.15 (2016), pp. 3868–3878.

[42] G Muraleedharan, C Guedes Soares, and Claudia Lucas. "Characteristic and moment generating functions of generalised extreme value distribution (GEV)". In: *Sea Level Rise, Coastal Engineering, Shorelines and Tides.* Nova, 2011, pp. 269–276.

[43] Peilan Wang et al. "Joint transceiver and large intelligent surface design for massive MIMO mmWave systems". In: *IEEE Trans. Wireless. Commun.* 20.2 (Oct. 2020), pp. 1052–1064.

[44] Peilan Wang et al. "Intelligent reflecting surface-assisted millimeter wave communications: Joint active and passive precoding design". In: *IEEE Trans. Veh. Technol.* 69.12 (Oct. 2020), pp. 14960–14973.

[45] Asil Koc, Ahmed Masmoudi, and Tho Le-Ngoc. "Full-duplex non-coherent communications for massive MIMO systems with analog beamforming". In: *2022 IEEE Int. Conf. Commun. (ICC), Seoul, South Korea* (May 2022).

[46] Yan Jiang et al. “Generalized 3-D Spatial Scattering Modulation”. In: *IEEE Trans. Wireless Commun.* 21.3 (Aug. 2021), pp. 1570–1585.

[47] Yuliang Tu et al. “Generalized spatial scattering modulation for uplink millimeter wave MIMO system”. In: *Proc. IEEE Int. Conf. Commun. China (ICCC), Beijing, China*. Feb. 2018, pp. 22–27.

[48] M Raeisi et al. “Cluster Index Modulation for mmWave Communication Systems”. In: *Front. Comms. Net.* (Feb. 2022).

[49] Mobeen Mahmood, Asil Koc, and Tho Le-Ngoc. “Energy-efficient MU-massive-MIMO hybrid precoder design: Low-resolution phase shifters and digital-to-analog converters for 2D antenna array structures”. In: *IEEE Open J. Commun. Soc.* 2 (Aug. 2021), pp. 1842–1861.

[50] Mobeen Mahmood, Asil Koc, and Tho Le-Ngoc. “Massive-MIMO hybrid precoder design using few-bit DACs for 2D antenna array structures”. In: *ICC 2021-IEEE International Conference on Communications, Montreal, QC, Canada*. IEEE. June 2021, pp. 1–5.

[51] Mobeen Mahmood, Asil Koc, and Tho Le-Ngoc. “2D antenna array structures for hybrid massive MIMO precoding”. In: *2020 IEEE Global Commun. Conf. (GLOBECOM), Taipei, Taiwan*. Dec. 2020.

[52] Haochen Liu et al. “Machine learning assisted adaptive index modulation for mmWave communications”. In: *IEEE Open J. Commun. Soc.* 1 (Sept. 2020), pp. 1425–1441.

[53] Qingfeng Ding et al. “Hybrid precoding for mmWave massive MIMO systems with different antenna arrays”. In: *China Communications* 16.10 (Oct. 2019), pp. 45–55. DOI: 10.23919/JCC.2019.10.003.

[54] Xiaoyong Wu, Norman C. Beaulieu, and Danpu Liu. “On Favorable Propagation in Massive MIMO Systems and Different Antenna Configurations”. In: *IEEE Access* 5 (Apr. 2017), pp. 5578–5593. DOI: 10.1109/ACCESS.2017.2695007.

[55] Jintao Wang, Longzhuang He, and Jian Song. "Towards higher spectral efficiency: Spatial path index modulation improves millimeter-wave hybrid beamforming". In: *IEEE J. Sel. Top. Signal Process.* 13.6 (May 2019), pp. 1348–1359.

[56] Boyu Ning et al. "Terahertz multi-user massive MIMO with intelligent reflecting surface: Beam training and hybrid beamforming". In: *IEEE Trans. Veh. Technol.* 70.2 (Jan. 2021), pp. 1376–1393.

[57] Jiangfeng Hu, Haifan Yin, and Emil Björnson. "MmWave MIMO Communication with Semi-Passive RIS: A Low-Complexity Channel Estimation Scheme". In: *2021 IEEE Global Communications Conference (GLOBECOM), Madrid, Spain.* Dec. 2021, pp. 01–06. DOI: 10.1109/GLOBECOM46510.2021.9685434.

[58] Randy L Haupt. "Optimized element spacing for low sidelobe concentric ring arrays". In: *IEEE Trans. Antennas Propag.* 56.1 (Jan. 2008), pp. 266–268.

[59] Konstantinos Ntontin et al. "Reconfigurable Intelligent Surface Optimal Placement in Millimeter-Wave Networks". In: *IEEE open j. Commun. Soc.* 2 (Mar. 2021), pp. 704–718. DOI: 10.1109/OJCOMS.2021.3068790.

[60] Bei Guo, Renwang Li, and Meixia Tao. "Joint Design of Hybrid Beamforming and Phase Shifts in RIS-Aided mmWave Communication Systems". In: *Proc. IEEE Wireless Commun. Netw. Conf. (WCNC).* Mar. 2021, pp. 1–6.

[61] Ibrahim Yildirim, Ali Uyrus, and Ertugrul Basar. "Modeling and analysis of reconfigurable intelligent surfaces for indoor and outdoor applications in future wireless networks". In: *IEEE Trans. Commun.* 69.2 (Nov. 2020), pp. 1290–1301.

[62] Sarath Gopi, Sheetal Kalyani, and Lajos Hanzo. "Intelligent reflecting surface assisted beam index-modulation for millimeter wave communication". In: *IEEE Trans. Wireless Commun.* 20.2 (Oct. 2020), pp. 983–996.

[63] Qingqing Li et al. "Polarized spatial scattering modulation". In: *IEEE Commun. Lett.* 23.12 (Sept. 2019), pp. 2252–2256.

[64] Shengzhen Ruan et al. "Diversity analysis for spatial scattering modulation in millimeter wave MIMO system". In: *Proc. 11th Int. Conf. Wireless Commun. Signal Process. (WCSP)*. Dec. 2019, pp. 1–5.

[65] Ruiqi Liu et al. "Simulation and Field Trial Results of Reconfigurable Intelligent Surfaces in 5G Networks". In: *IEEE Access* 10 (Nov. 2022), pp. 122786–122795. DOI: 10.1109/ACCESS.2022.3223447.

[66] Shicong Liu et al. "Deep denoising neural network assisted compressive channel estimation for mmWave intelligent reflecting surfaces". In: *IEEE Trans. Veh. Technol.* 69.8 (June 2020), pp. 9223–9228.

[67] Peilan Wang et al. "Compressed Channel Estimation for Intelligent Reflecting Surface-Assisted Millimeter Wave Systems". In: *IEEE Signal Process. Lett.* 27 (May 2020), pp. 905–909. DOI: 10.1109/LSP.2020.2998357.

[68] Mobeen Mahmood, Asil Koc, and Tho Le-Ngoc. "3-D Antenna Array Structures for Millimeter Wave Multi-User Massive MIMO Hybrid Precoder Design: A Performance Comparison". In: *IEEE Commun. Lett.* (Mar. 2022).

[69] Asil Koc and Tho Le-Ngoc. "Full-Duplex mmWave Massive MIMO Systems: A Joint Hybrid Precoding/Combining and Self-Interference Cancellation Design". In: *IEEE open j. Commun. Soc.* 2 (Mar. 2021), pp. 754–774. DOI: 10.1109/OJCOMS.2021.3069672.

[70] *5G: Study on Channel Model for Frequencies From 0.5 to 100 GHz.* document 3GPP TR 38.901, Ver. 16.1.0, 2020.

[71] Asil Koc, Ahmed Masmoudi, and Tho Le-Ngoc. "3D Angular-Based Hybrid Precoding and User Grouping for Uniform Rectangular Arrays in Massive MU-MIMO Systems". In: *IEEE Access* 8 (May 2020), pp. 84689–84712. DOI: 10.1109/ACCESS.2020.2992713.

[72] Deepak Mishra and Håkan Johansson. "Channel Estimation and Low-complexity Beamforming Design for Passive Intelligent Surface Assisted MISO Wireless Energy Transfer". In: *IEEE Int. Conf. Acoust. Speech Signal Process.*

(ICASSP), Brighton, UK. May 2019, pp. 4659–4663. DOI: 10.1109/ICASSP.2019.8683663.

[73] Jie Chen et al. "Channel Estimation for Reconfigurable Intelligent Surface Aided Multi-User mmWave MIMO Systems". In: *IEEE Trans. Wirel. Commun.* 22.10 (Feb. 2023), pp. 6853–6869. DOI: 10.1109/TWC.2023.3246264.

[74] Tian Lin et al. "Channel Estimation for Intelligent Reflecting Surface-Assisted Millimeter Wave MIMO Systems". In: *IEEE Glob. Commun. Conf. (GLOBECOM), Taipei, Taiwan*. Dec. 2020, pp. 1–6. DOI: 10.1109/GLOBECOM42002.2020.9322519.

[75] Zhen-Qing He and Xiaojun Yuan. "Cascaded Channel Estimation for Large Intelligent Metasurface Assisted Massive MIMO". In: *IEEE Wireless Commun. Lett.* 9.2 (Oct. 2020), pp. 210–214. DOI: 10.1109/LWC.2019.2948632.

[76] Chen Hu et al. "Two-Timescale Channel Estimation for Reconfigurable Intelligent Surface Aided Wireless Communications". In: *IEEE Trans. Commun.* 69.11 (Apr. 2021), pp. 7736–7747. DOI: 10.1109/TCOMM.2021.3072729.

[77] Ziwei Wan, Zhen Gao, and Mohamed-Slim Alouini. "Broadband Channel Estimation for Intelligent Reflecting Surface Aided mmWave Massive MIMO Systems". In: *IEEE Int. Conf. Commun. (ICC), Dublin, Ireland*. June 2020, pp. 1–6. DOI: 10.1109/ICC40277.2020.9149146.

[78] Jiancheng An et al. "Low-Complexity Channel Estimation and Passive Beamforming for RIS-Assisted MIMO Systems Relying on Discrete Phase Shifts". In: *IEEE Trans. Commun.* 70.2 (Nov. 2022), pp. 1245–1260. DOI: 10.1109/TCOMM.2021.3127924.

[79] Jiancheng An et al. "Joint Training of the Superimposed Direct and Reflected Links in Reconfigurable Intelligent Surface Assisted Multiuser Communications". In: *IEEE Trans. Green Commun. Netw.* 6.2 (Jan. 2022), pp. 739–754. DOI: 10.1109/TGCN.2022.3143226.

[80] Abdelrahman Taha, Muhammad Alrabeiah, and Ahmed Alkhateeb. "Enabling Large Intelligent Surfaces With Compressive Sensing and Deep Learning". In: *IEEE Access* 9 (Mar. 2021), pp. 44304–44321. DOI: 10.1109/ACCESS.2021.3064073.

[81] Yu Jin et al. "Channel Estimation for Semi-Passive Reconfigurable Intelligent Surfaces With Enhanced Deep Residual Networks". In: *IEEE Trans. Veh. Technol.* 70.10 (Sept. 2021), pp. 11083–11088. DOI: 10.1109/TVT.2021.3109937.

[82] Feng Zheng, Haoxiang Liu, and Liangang Chi. "A Semi-Passive RIS Channel Estimation Method based on Super-Resolution Network". In: *IEEE 8th Int. Conf. Comput. Commun. (ICCC), Chengdu, China.* Mar. 2022, pp. 17–21. DOI: 10.1109/ICCC56324.2022.10065831.

[83] Zijian Zhang et al. "Active RIS vs. Passive RIS: Which Will Prevail in 6G?" In: *IEEE Trans. Commun.* 71 (Dec. 2022), pp. 1707–1725. DOI: 10.1109/TCOMM.2022.3231893.

[84] *Reconfigurable Intelligent Surfaces (RIS); Communication Models, Channel Models, Channel Estimation and Evaluation Methodology.* ETSI GR RIS 003 V1.1.1, May 2023.

[85] Mahmoud Raeisi et al. "Antenna Array Structures for Enhanced Cluster Index Modulation". In: *Joint Eur. Conf. Netw. Commun. & 6G Summit (EuCNC/6G Summit), Gothenburg, Sweden.* June 2023, pp. 102–107. DOI: 10.1109/EuCNC/6GSummit58263.2023.10188340.

[86] Asil Koc and Tho Le-Ngoc. "Hybrid millimeter-wave massive MIMO systems with low CSI overhead and few-bit DACs/ADCs". In: *IEEE 92nd Veh. Technol. Conf. (VTC2020-Fall).* Dec. 2020, pp. 1–5.

[87] Mahmoud Raeisi et al. "Cluster Index Modulation for Reconfigurable Intelligent Surface-Assisted mmWave Massive MIMO". In: *IEEE Trans. Wireless Commun.* 23.2 (July 2023), pp. 1581–1591. DOI: 10.1109/TWC.2023.3290618.

[88] P Hannan. "The element-gain paradox for a phased-array antenna". In: *IEEE Trans. Antennas Propag.* 12.4 (July 1964), pp. 423–433.

[89] Hadi Sarieddeen, Mohamed-Slim Alouini, and Tareq Y Al-Naffouri. "Terahertz-band ultra-massive spatial modulation MIMO". In: *IEEE J. Sel. Areas Commun.* 37.9 (Sept. 2019), pp. 2040–2052.

[90] Asil Koc, Ahmed Masmoudi, and Tho Le-Ngoc. "Angular-Based 3D Hybrid Precoding for URA in Multi-User Massive MIMO Systems". In: *IEEE 90th Veh. Technol. Conf. (VTC2019-Fall), Honolulu, HI, USA*. Sept. 2019, pp. 1–5. DOI: 10.1109/VTCFall.2019.8891298.

[91] Harry L Van Trees. *Optimum Array Processing: Part IV of Detection, Estimation, and Modulation Theory.* John Wiley & Sons, 2002.

[92] Ertugrul Basar. "Transmission Through Large Intelligent Surfaces: A New Frontier in Wireless Communications". In: *Eur. Conf. on Netw. and Commun. (EuCNC), Valencia, Spain.* June 2019, pp. 112–117. DOI: 10.1109/EuCNC.2019.8801961.

[93] Yuetian Zhou and Fang Nan. "Performance Evaluation between the RIS and Full/Half-Duplex Relay". In: *2023 International Wirel. Commun. Mob. Comput. (IWCMC).* June 2023, pp. 550–555. DOI: 10.1109/IWCMC58020.2023.10183245.

[94] Jiancheng An et al. "Codebook-Based Solutions for Reconfigurable Intelligent Surfaces and Their Open Challenges". In: *IEEE Wirel. Commun.* 31 (Nov. 2022), pp. 1–8. DOI: 10.1109/MWC.010.2200312.

[95] Xing Jia et al. "Environment-Aware Codebook for Reconfigurable Intelligent Surface-Aided MISO Communications". In: *IEEE Wirel. Commun. Lett.* 12.7 (Apr. 2023), pp. 1174–1178. DOI: 10.1109/LWC.2023.3265399.

[96] *Reconfigurable Intelligent Surfaces (RIS); Use Cases, Deployment Scenarios and Requirements.* ETSI GR RIS 001 V1.1.1, Apr. 2023.

[97] Xilong Pei et al. "RIS-Aided Wireless Communications: Prototyping, Adaptive Beamforming, and Indoor/Outdoor Field Trials". In: *IEEE Trans. Commun.* 69.12 (Sept. 2021), pp. 8627–8640. DOI: 10.1109/TCOMM.2021.3116151.

[98] Roi Méndez-Rial et al. "Hybrid MIMO Architectures for Millimeter Wave Communications: Phase Shifters or Switches?" In: *IEEE Access* 4 (Jan. 2016), pp. 247–267. DOI: 10.1109/ACCESS.2015.2514261.

[99] Jianhua Mo et al. "Hybrid Architectures With Few-Bit ADC Receivers: Achievable Rates and Energy-Rate Tradeoffs". In: *IEEE Trans. Wireless Commun.* 16.4 (Mar. 2017), pp. 2274–2287. DOI: 10.1109/TWC.2017.2661749.

[100] *5G: Study on Channel Model for Frequencies from 0.5 to 100 GHz.* document 3GPP TR 38.901, Ver. 17.0.0, Apr. 2022.

[101] Rui Peng and Yafei Tian. "Robust Wide-Beam Analog Beamforming With Inaccurate Channel Angular Information". In: *IEEE Commun. Lett.* 22.3 (Mar. 2018), pp. 638–641. DOI: 10.1109/LCOMM.2017.2782322.

[102] Parisa Ramezani, Yong Zeng, and Abbas Jamalipour. "Optimal Resource Allocation for Multiuser Internet of Things Network With Single Wireless-Powered Relay". In: *IEEE Internet Things J.* 6.2 (Nov. 2018), pp. 3132–3142. DOI: 10.1109/JIOT.2018.2879373.

[103] Aymen Khaleel and Ertugrul Basar. "Reconfigurable Intelligent Surface-Empowered MIMO Systems". In: *IEEE Syst. J.* 15.3 (Aug. 2021), pp. 4358–4366. DOI: 10.1109/JSYST.2020.3011987.

[104] Yuwei Huang, Lipeng Zhu, and Rui Zhang. "Integrating Intelligent Reflecting Surface Into Base Station: Architecture, Channel Model, and Passive Reflection Design". In: *IEEE Trans. Commun.* 71.8 (2023), pp. 5005–5020. DOI: 10.1109/TCOMM.2023.3282592.

[105] Mahmoud Raeisi et al. "Plug-In RIS: A Novel Approach to Fully Passive Reconfigurable Intelligent Surfaces". In: *IEEE Trans. Wireless Commun.* (July 2024). Early Access. DOI: 10.1109/TWC.2024.3418969.

[106] Björn Sihlbom, Marios I. Poulakis, and Marco Di Renzo. "Reconfigurable Intelligent Surfaces: Performance Assessment Through a System-Level Simulator". In: *IEEE Wireless Commun.* 30.4 (2023), pp. 98–106. DOI: 10.1109/MWC.015.2100668.

[107] Kunzan Liu et al. "Compact User-Specific Reconfigurable Intelligent Surfaces for Uplink Transmission". In: *IEEE Trans. Commun.* 70.1 (Nov. 2022), pp. 680–692. DOI: 10.1109/TCOMM.2021.3124953.

[108] Yanqing Ren et al. "On Deployment Position of RIS in Wireless Communication Systems: Analysis and Experimental Results". In: *IEEE Wireless Commun. Lett.* 12.10 (July 2023), pp. 1756–1760. DOI: 10.1109/LWC.2023.3292125.

[109] Xie Xie et al. "Joint Precoding for Active Intelligent Transmitting Surface Empowered Outdoor-to-Indoor Communication in mmWave Cellular Networks". In: *IEEE Trans. Wireless Commun.* 22.10 (Feb. 2023), pp. 7072–7086. DOI: 10.1109/TWC.2023.3247906.

[110] Alessio Zappone et al. "Overhead-Aware Design of Reconfigurable Intelligent Surfaces in Smart Radio Environments". In: *IEEE Trans. Wireless Commun.* 20.1 (2021), pp. 126–141. DOI: 10.1109/TWC.2020.3023578.

[111] Hao Zhou et al. "A Survey on Model-Based, Heuristic, and Machine Learning Optimization Approaches in RIS-Aided Wireless Networks". In: *IEEE Commun. Surveys Tutor.* (Dec. 2023). Early Access, doi: 10.1109/COMST.2023.3340099. DOI: 10.1109/COMST.2023.3340099.

[112] Mahmoud Raeisi et al. "A Comprehensive Design Framework for UE-side and BS-Side RIS Deployments". In: *arXiv preprint arXiv:2404.16607* (2024).

[113] Waqas Khalid et al. "Simultaneous Transmitting and Reflecting-Reconfigurable Intelligent Surface in 6G: Design Guidelines and Future Perspectives". In: *IEEE Network* (Dec. 2022), pp. 1–9. DOI: 10.1109/MNET.129.2200389.

[114] Jiancheng An et al. "Stacked Intelligent Metasurface-Aided MIMO Transceiver Design". In: *IEEE Wireless Commun.* 31.4 (Apr. 2024), pp. 123–131.

[115] Kunzan Liu, Zijian Zhang, and Linglong Dai. "User-Side RIS: Realizing Large-Scale Array at User Side". In: *IEEE Glob. Commun. Conf. (GLOBECOM)*. Dec. 2021, pp. 01–06. DOI: 10.1109/GLOBECOM46510.2021.9685418.

[116] Wannian Du et al. "Hybrid Beamforming Design for ITS-Assisted Wireless Networks". In: *IEEE Wireless Commun. Lett.* 12.3 (Mar. 2023), pp. 451–455. DOI: 10.1109/LWC.2022.3230095.

[117] Qingchao Li et al. "Stacked Intelligent Metasurfaces for Holographic MIMO-Aided Cell-Free Networks". In: *IEEE Trans. Commun.* 72.11 (May 2024), pp. 7139–7151. DOI: 10.1109/TCOMM.2024.3403499.

[118] Jiancheng An et al. "Stacked Intelligent Metasurfaces for Multiuser Beamforming in the Wave Domain". In: *IEEE Int. Conf. Commun. (ICC), Rome, Italy*. May 2023, pp. 2834–2839.

[119] Zheao Li, Jiancheng An, and Chau Yuen. "Stacked Intelligent Metasurfaces for Fully-Analog Wideband Beamforming Design". In: *IEEE VTS Asia Pac. Wireless Commun. Symp. (APWCS), Singapore*. Aug. 2024.

[120] Xianghao Yao et al. "Channel Estimation for Stacked Intelligent Metasurface-Assisted Wireless Networks". In: *IEEE Wireless Commun. Lett.* 13.5 (Feb. 2024), pp. 1349–1353. DOI: 10.1109/LWC.2024.3369874.

[121] Shanpu Shen, Bruno Clerckx, and Ross Murch. "Modeling and Architecture Design of Reconfigurable Intelligent Surfaces Using Scattering Parameter Network Analysis". In: *IEEE Trans. Wireless Commun.* 21.2 (Aug. 2022), pp. 1229–1243.

[122] Anup Mishra et al. "Transmitter Side Beyond-Diagonal Reconfigurable Intelligent Surface for Massive MIMO Networks". In: *IEEE Wireless Commun. Lett.* 13.2 (Nov. 2024), pp. 352–356.

[123] Kexin Chen and Yijie Mao. "Transmitter Side Beyond-Diagonal RIS for mmWave Integrated Sensing and Communications". In: *IEEE 25th Int. Workshop Signal Process. Adv. Wireless Commun. (SPAWC)*. Sept. 2024, pp. 951–955. DOI: 10.1109/SPAWC60668.2024.10693959.

[124] Matteo Nerini and Bruno Clerckx. "Physically Consistent Modeling of Stacked Intelligent Metasurfaces Implemented With Beyond Diagonal RIS". In: *IEEE Commun. Lett.* 28.7 (May 2024), pp. 1693–1697. DOI: 10.1109/LCOMM.2024.3401580.

[125] Mahmoud Raeisi et al. "Efficient Localization with Base Station-Integrated Beyond Diagonal RIS". In: *arXiv preprint arXiv:2411.13295* (2024).

[126] Jiancheng An et al. "Stacked Intelligent Metasurfaces for Efficient Holographic MIMO Communications in 6G". In: *IEEE J. Sel. Areas Commun.* 41.8 (June 2023), pp. 2380–2396.

[127] Haoxian Niu et al. "Stacked Intelligent Metasurfaces for Integrated Sensing and Communications". In: *IEEE Wireless Commun. Lett.* 13.10 (Aug. 2024), pp. 2807–2811.

[128] Jiancheng An et al. "Two-Dimensional Direction-of-Arrival Estimation Using Stacked Intelligent Metasurfaces". In: *IEEE J. Sel. Areas Commun.* 42.10 (June 2024), pp. 2786–2802.

[129] Hao Liu et al. "DRL-Based Orchestration of Multi-User MISO Systems with Stacked Intelligent Metasurfaces". In: *IEEE Int. Conf. Commun. (ICC).* June 2024, pp. 4991–4996. DOI: 10.1109/ICC51166.2024.10622385.

[130] Özlem Tuğfe Demir, Emil Björnson, and Luca Sanguinetti. "Channel Modeling and Channel Estimation for Holographic Massive MIMO With Planar Arrays". In: *IEEE Wireless Commun. Lett.* 11.5 (Feb. 2022), pp. 997–1001. DOI: 10.1109/LWC.2022.3152600.

[131] Mingyao Cui and Linglong Dai. "Channel Estimation for Extremely Large-Scale MIMO: Far-Field or Near-Field?" In: *IEEE Trans. Commun.* 70.4 (Jan. 2022), pp. 2663–2677. DOI: 10.1109/TCOMM.2022.3146400.

[132] Matteo Nerini et al. "Beyond Diagonal Reconfigurable Intelligent Surfaces Utilizing Graph Theory: Modeling, Architecture Design, and Optimization". In: *IEEE Trans. Wireless Commun.* 23.8 (Feb. 2024), pp. 9972–9985. DOI: 10.1109/TWC.2024.3367631.

[133] Hongyu Li, Shanpu Shen, and Bruno Clerckx. "A Dynamic Grouping Strategy for Beyond Diagonal Reconfigurable Intelligent Surfaces With Hybrid Transmitting and Reflecting Mode". In: *IEEE Trans. Veh. Technol.* 72.12 (June 2023), pp. 16748–16753. DOI: 10.1109/TVT.2023.3288690.

[134] Ignacio Santamaria et al. "SNR Maximization in Beyond Diagonal RIS-Assisted Single and Multiple Antenna Links". In: *IEEE Signal Process. Lett.* 30 (July 2023), pp. 923–926.

[135] Özlem Tuğfe Demir and Emil Björnson. "User-Centric Cell-Free Massive MIMO With RIS-Integrated Antenna Arrays". In: *IEEE 25th Int. Workshop Signal Process. Adv. Wireless Commun. (SPAWC).* Sept. 2024, pp. 546–550. DOI: 10.1109/SPAWC60668.2024.10694297.

[136] Jiancheng An et al. "Stacked Intelligent Metasurface Performs a 2D DFT in the Wave Domain for DOA Estimation". In: *IEEE Int. Conf. Commun. (ICC).* June 2024, pp. 3445–3451.

[137] Jiguang He et al. "Large Intelligent Surface for Positioning in Millimeter Wave MIMO Systems". In: *IEEE Veh. Technol. Conf. (VTC-Spring), Antwerp, Belgium.* May 2020.

[138] Henk Wymeersch. "A Fisher Information Analysis of Joint Localization and Synchronization in near Field". In: *IEEE Int. Conf. Commun. Workshops. (ICC Workshops), Dublin, Ireland.* June 2020.

[139] Fangzhou Wang and A. Lee Swindlehurst. "Applications of Absorptive Reconfigurable Intelligent Surfaces in Interference Mitigation and Physical Layer Security". In: *IEEE Trans. Wireless Commun.* 23.5 (Sept. 2024), pp. 3918–3931.

[140] Kexin Chen and Yijie Mao. "Transmitter Side Beyond-Diagonal RIS for mmWave Integrated Sensing and Communications". In: *arXiv preprint arXiv:2404.12604* (2024).

[141] Cuneyd Ozturk et al. "RIS-Aided Near-Field Localization Under Phase-Dependent Amplitude Variations". In: *IEEE Trans. Wireless Commun.* 22.8 (Jan. 2023), pp. 5550–5566.

[142] Pinjun Zheng et al. "Near Field Sidelink Positioning Through A Single Active RIS". In: *IEEE Glob. Commun. Conf. (GLOBECOM), Kuala Lumpur, Malaysia*. Dec. 2023, pp. 2511–2516.

[143] Zhaolin Wang, Xidong Mu, and Yuanwei Liu. "Near-Field Integrated Sensing and Communications". In: *IEEE Commun. Lett.* 27.8 (May 2023), pp. 2048–2052.

[144] Jiguang He et al. "Adaptive Beamforming Design for mmWave RIS-Aided Joint Localization and Communication". In: *IEEE Wirel. Commun. Netw. Conf. (WCNC) Workshops., Seoul, South Korea*. Apr. 2020.

[145] Kamran Keykhosravi et al. "SISO RIS-Enabled Joint 3D Downlink Localization and Synchronization". In: *IEEE Int. Conf. Commun. (ICC), Montreal, QC, Canada*. Aug. 2021.

[146] Steven M Kay. *Fundamentals of Statistical Signal Processing: Estimation Theory*. 1993.

[147] Agnan Kessy, Alex Lewin, and Korbinian Strimmer. "Optimal whitening and decorrelation". In: *Amer. Stat.* 72.4 (Jan. 2018), pp. 309–314.